CONDITION-BASED MONITORING OF NATURAL DRAUGHT WET-COOLING TOWER PERFORMANCE-RELATED PARAMETERS

by
Frederik Coenrad Ehlers

Thesis presented in partial fulfilment of the requirements for the degree of Master of Science in the Faculty of Engineering at the Stellenbosch University

Thesis supervisor: Prof. H.C.R. Reuter
Faculty of Engineering
Department of Mechanical and Mechatronic Engineering

December 2011

DECLARATION

By submitting this thesis electronically, I declare that the entirety of the work contained therein is my own, original work, that I am the sole author thereof (save to the extent explicitly otherwise stated), that reproduction and publication thereof by Stellenbosch University will not infringe any third party rights and that I have not previously in its entirety or in part submitted it for obtaining any qualification.

December 2011

ABSTRACT

The meteorological conditions at Eskom's Majuba Power Station are measured, evaluated and trended in this dissertation. The results are used to evaluate the current natural draught wet-cooling tower (NDWCT) design- and performance test specifications and to compare these to the original design- and performance test specifications. The evaluation reveals that the design parameters for the NDWCTs at Majuba Power Station, a cooling system that was originally designed optimally, could have been determined differently and arguably more accurately by using the wet-bulb temperature (T_{awb}) as the main design variable instead of the dry-bulb temperature (T_a). A new technique to determine optimal NDWCT design and performance test conditions is consequently proposed. In order to satisfy the atmospheric conditions required for a successful NDWCT performance test, it is also proposed that the tests be undertaken between 12:00 and 14:00 during Summer. It is found that the NDWCT inlet T_{awb}, measured at specific heights, does not compare well to the far-field T_{awb} measured at the same heights when a T_{awb} accuracy of 0.1 K is required. It is proposed that a more representative far-field T_{awb} measuring height of 10 m should be used in future NDWCT designs as the NDWCT design temperature reference height. The industry-standard reference height should, however, still be used during temperature profile calculations.

A parametric study of the water-steam cycle and wet-cooling system at Majuba indicates that during full load conditions, the generated output (P_{st}) is primarily dependent on the condenser saturation pressure (p_c). The latter is reliant on T_{awb}, the temperature lapse rate (LR_T) that is represented by the temperature profile exponent (b_T), the main cooling water flow rate (m_{cw}), atmospheric pressure (p_a), and wind speed (V_W). Using historical plant data relatively simple methods, enabling the quick and effective determination of these relationships, are proposed. The plant-specific and atmospheric parameters required for these analyses are also tabulated.

Two NDWCT effectiveness models, one mathematical (Kröger, 1998) and one statistical artificial neural network (ANN) model are presented and evaluated. ANNs, which are not often used to evaluate NDWCT effectiveness, provide accurate NDWCT temperature approach results within 0.5 K of measured values for varying dependent variables. This motivates that an ANN, if set up and used correctly, can be an effective condition-monitoring tool and can be used to improve the accuracy of more empirical NDWCT performance models. The one-dimensional mathematical effectiveness model provides accurate results under NDWCT design conditions.

The dependency of Majuba's NDWCT to the rain zone mean drop diameter (d_d) is evaluated by means of the one-dimensional mathematical model. A reduction in d_d from 0.0052 m to 0.0029 m can reduce the NDWCT re-cooled water temperature (T_{cwo}) so that the rated p_c is reduced by 0.15 kPa, which relates to a combined financial saving during peak and off-peak periods of R1.576M in 2013 and R1.851M in 2016.

Similar improvements can result in higher savings at other wet-cooled stations in the Eskom fleet due to less optimally-designed wet-cooling systems. The proposed techniques should be considered in future economic evaluations of wet-cooling system improvements at different power stations.

OPSOMMING

Die meteorologiese toestande by Eskom se Majuba-kragstasie is deur die navorser gemeet en -evalueer. Die resultate word gebruik om die Natuurlike-trek, Nat koeltoring (NTNKT) se ontwerp- en werkverrigting toetsspesifikasies te evalueer en vergelyk met die oorspronklike toetsspesifikasies. Die resultate dui daarop dat die ontwerpsparameters vir die NTNKTs by Majuba-kragstasie, 'n verkoelings-sisteem wat aanvanklik optimaal ontwerp is, op 'n ander, selfs meer akkurate manier bepaal kon word deur die natbol-temperatuur (T_{awb}) te gebruik as die hoof-ontwerpsparameter inplaas van die droëbol temperatuur (T_a).'n Nuwe tegniek wat gebruik kan word om akkurate NTNKT ontwerp- en werkverrigting toetsspesifikasies te bepaal word voorgestel. Die tydperk vir die mees optimale atmosferiese toestande, wanneer NTNKT-toetse uitgevoer moet word, word vasgestel as tussen 12:00 en 14:00 tydens Somermaande. Dit word bewys, vir 'n T_{awb} akkuraatheid van 0.1 K, dat die NTNKT inlaat-T_{awb}, gemeet by verskillende hoogtes, nie vergelykbaar is met T_{awb} wat ver van die NTNKT af op dieselfde hoogtes gemeet word nie. 'n Meer aanvaarbare hoogte van 10 m word voorgestel as die NTNKT ontwerpstemperatuur verwysingshoogte vir toekomstige NTNKT ontwerpe wanneer die T_{awb} ver van die NTNKT af meet word. Die industrie-standaard temperatuur verwysingshoogte moet wel steeds gebruik word tydens temperatuur-profielberekeninge.

'n Parametriese studie van die turbine se water-stoom siklus en die nat-verkoelingstelsel by Majuba dui daarop dat die generator se uitset (P_{st}) hoofsaaklik afhanklik is van die kondensator se druk (p_c) gedurende vol-vrag toestande. Druk (p_c) is weer afhanklik van T_{awb}, die temperatuur vervaltempo (LR_T) wat voorgestel word deur die temperatuur profiel eksponent (b_T), die verkoelingswater-vloeitempo (m_{cw}), atmosferiese druk (p_a) en windspoed (V_W). Deur die gebruik van historiese data word redelike eenvoudige metodes voorgestel om dié verhoudings doeltreffend te bepaal. Die atmosferiese- en stasie-spesifieke parameters wat benodig word vir dié ontleding is ook getabuleer.

Twee modelle vir NTNKT-effektiweit, 'n wiskundige (gebaseer op Kröger, 1998) en statistiese kunsmatige neurale-netwerk (KNN) model, word aangebied en geëvalueer. KNNe, wat nie gereeld gebruik word om NTNKTe se effektiwiteit te evalueer nie, lewer akkurate NTNKT temperatuur-benadering resultate binne 0.5 K van die gemete resultate vir wisselende afhanklike parameters. Dié resultate motiveer dat 'n KNN wat korrek opgestel is doeltreffend gebruik kan word om die toestand van NTNKTs te bepaal en om die akkuraatheid van ander NTNKT-modelle te verbeter. Die een-dimensionele, wiskundige model lewer akkurate resultate onder NTNKT ontwerpspesifikasies.

'n Wiskundige NTNKT-model word gebruik om die afhanklikheid van Majuba-kragstasie se NTNKTe tot die reënsone druppelgrootte (d_d) te bereken. 'n Vermindering in d_d van 0,0052 tot 0,0029 m kan die NTNKT se afgekoelde watertemperatuur (T_{cwo}), van só 'n aard verlaag dat p_c verminder met 0,15 kPa. Só kan 'n gesamentlike vol- en gedeeltelike vrag finansiële besparing van R1.576M in 2013 en R1.851M in 2016 behaal word.

Soortgelyke verbeterings aan verkoelingstelsels sal lei tot meer en hoër besparings by ander Eskom nat-verkoelde stasies. Dié tegnieke moet in ag geneem word tydens toekomstige ekonomiese evaluasies van verbeterings tot nat-verkoelingstelsels by ander kragstasies.

ACKNOWLEDGEMENTS

Thank you to our heavenly Father for giving me the ability to complete this thesis;

My supervisor, Prof. H.C.R. Reuter, for his support, guidance and technical experience during the past four years;

My wife, mom and dad for their continuous loving support and motivation;

Markus Jonker (Eskom's Majuba Power Station Turbine Engineering Manager), for his continuous support and understanding;

Marlon Perumal and Thokozani Ntuli (Majuba turbine engineering) for their valuable inputs;

Majuba Maintenance staff, Andre Rossouw, Carel Buitendag and in particular Lean Meyburgh for their help with the conducted experiments;

Francois du Preez and Johannes Pretorius (Eskom Generation Business Engineering) for their technical experience and inputs;

All my friends for their support during the past four years.

TABLE OF CONTENTS

LIST OF FIGURES

LIST OF TABLES

LIST OF SYMBOLS

A	Area, m^2
A_{fr}	Frontal area of the fill, m^2
a_{fi}	Area density - wetted area divided by the fill volume, m^{-1}
b_H	Humidity profile exponent
b_T	Temperature profile exponent
b_W	Wind profile exponent
$b_{W,ma}$	Wind profile exponent – monthly average
C_D	Coefficient of drag
C_{IL}	Implementation cost limit, R
C_{RZ}	Rain zone correction factor
c_{pa}	Specific heat of dry air at constant pressure, J/kgK
c_{pw}	Specific heat of water at constant pressure, J/kgK
c_{pwi}	Specific heat of the water evaluated at T_{wi}, J/kgK
c_{pwo}	Specific heat of the water evaluated at T_{wo}, J/kgK
D	Diffusion coefficient, m^2/s
D_W	Wind direction
$D_{W,r}$	Wind direction at reference height of 10 m
d	Diameter, m
d_d	Rain zone drop diameter, m
d_z	Incremental height, m
e	Error
Fr	Froude number
G	Mass velocity, kg/m^2s
g	Gravitational acceleration, m/s^2
H	Height, m
H_{abl}	Height of the ABL, m
H_i	Height of the NDWCT inlet, m
H_{inv}	Inversion height, m
H_r	Height from which the NDWCT draws in air, m
H_s	Height of the NDWCT, m
h_d	Mass transfer coefficient, kg/m^2s
h_0	ISA reference height for atmospheric measurements, 0 m
i_{fgw}	Latent heat of vaporisation, kJ/kg
i_{ma}	Enthalpy of main air stream, J/kg
i_{ma1}	Enthalpy of air at elevation H_1, J/kg
i_{ma5}	Enthalpy of air at elevation H_5, J/kg
i_{masw}	Enthalpy of saturated air at air-water interface, J/kg
K	Loss coefficient
k	Thermal conductivity, W/mK
L_{fi}	Height of the fill, m
LR_T	Temperature Lapse Rate
LR_W	Wind Lapse Rate
M	Molecular mass, kg/mole
Me	Merkel number
m_a	Dry air mass flow rate, kg/s
m_{av}	Air-vapour mass flow rate, kg/s

m_{coal}	Coal mass flow rate, kg/s
m_{CRH}	Cold re-heat mass flow rate, kg/s
m_{cw}	Cooling water mass flow rate, kg/s
m_{HP}	High pressure turbine mass flow rate, kg/s
m_w	Inlet water mass flow rate, kg/s
n_d	Number of the day of the year (1 Jan = 1 & 31 Dec = 365)
n_m	Number of the month of the year (Jan = 1 & Dec = 12)
P_{aux}	Auxiliary power, MW
P_{st}	Steam Turbine output, MW
p_a	Atmospheric pressure, kPa
p_c	Condenser saturation pressure, kPa
p_{HP}	High pressure turbine pressure, MPa
p_{sat}	Saturation pressure, kPa
p_v	Saturated water vapour pressure, N/m^2
p_{wc}	Saturated liquid water critical pressure, N/m^2
p_0	ISA reference height atmospheric pressure, 101.325 kPa
Q_{in}	Total heat input, MW
$Q_{in,steam}$	Total heat input to steam, MW
Q_{out}	Total heat rejected, MW
$q_{moisture}$	Heat required to remove moisture from coal, MW/kg
R	Gas constant, J/kgK
RH	Relative Humidity, %
Ry	Characteristic flow number
r	Rounding diameter, m
Sc	Schmidt number
S_O	Operational saving, R
SR	Solar Radiation, W/m^2
S_R	Revenue saving, R
s	Entropy, J/K
T	Temperature, K
T_a	Dry-bulb temperature, K
T_{awb}	Wet-bulb temperature, K
T_{cwi}	NDWCT inlet cooling water temperature, K
T_{cwo}	NDWCT outlet cooling water temperature, K
T_{dp}	Dew-point temperature, K
T_H	Heat source reservoir temperature, K
T_L	Heat sink reservoir temperature, K
T_r	Temperature at a reference height, K
T_{sat}	Saturation temperature, K
T_w	Bulk water temperature, K
T_0	ISA reference height dry-bulb temperature, 273.15 K
t_c	Civil time
t_{EOT}	Equation of time (value in minutes)
t_{LST}	Local solar time
V_W	Wind speed, m/s
$V_{W,r}$	Wind speed at reference height of 1.2 m, m/s
W_{net}	Net work output, MW
W_{gross}	Gross work output, MW

z	Height AGL, m
z_{it}	Height at the top of an inversion, m
z_r	Reference height AGL, m
$z_{T,r}$	Temperature reference height AGL, m
$z_{W,r}$	Wind reference height AGL, m
α_{e6}	Kinetic energy coefficient
ΔT_i	Temperature difference across an inversion, K
ε	Effectiveness
η_{th}	Water-steam cycle thermal efficiency, %
η_{boiler}	Boiler Thermal efficiency, %
μ	Dynamic viscosity, kg/sm
ρ	Density, kg/m^3
ω	Humidity ratio, kg/kg dry air

ABBREVIATIONS

ABC	Above basin curb
ABL	Atmospheric boundary layer
AGL	Above ground level
ANN	Artificial neural network
BP	Back propagation
BS	British standard
CRH	Cold re-heat
CTI	Cooling Technology Institute
CV	Calorific value
CW	Cooling water
DALR	Dry-adiabatic lapse rate
DL	Data logger
EOL	End of life
GMT	Greenwich mean time
HP	High pressure
HR	Heat rate
HRH	Hot re-heat
HRR	Heat rejection rate
ICAO	International civil aviation organization
IP	Intermediate pressure
IRR	Internal rate of return
ISA	International standard atmosphere
ISO	International organization of standardization
KNN	Kunsmatige neurale netwerk
LHV	Lower heating value
LMTD	Log mean temperature difference
LP	Low pressure
MCR	Maximum continuous rating
MSE	Mean square error
NDWCT	Natural draught wet-cooling tower
NTNKT	Nutuurlike-trek nat koeltoring
OEM	Original equipment manufacture
OSHAct	Occupational health and safety act
PBL	Planetary boundary layer
PA	Primary air
PF	Pulverised fuel
RF	Rainfall
SBL	Surface boundary layer
UHV	Upper heating value
UTC	Coordinated universal time

CHAPTER 1
INTRODUCTION

1.1. GENERAL OVERVIEW AND MOTIVATION

South Africa's main power utility, Eskom, is in the process of expanding its capacity as result of capacity shortfalls and consequent load-shedding in parts of the country since 2006. The projected load demand is increasing; a tendency that further motivates the need for Eskom to expand capacity by building new and upgrading existing power stations.

As at 2010 Eskom has a fleet of 23 power stations of which 11 are coal-fired stations. These 11 stations have a total of 63 NDWCTs. During a natural draught wet-cooling tower's (NDWCT) life cycle, its internal elements, including the packing, sprayers and drift eliminators, need to be refurbished and/or replaced as result of obsolescence and expiry. A total of 32 NDWCTs in the Eskom fleet are fitted with asbestos cement-fill packs. Legislation regulating the use of asbestos requires that these packs be replaced (retrofitted) by 2033 (section 43 of the Occupational Health and Safety Act 85 of 1993).

Eskom consequently needs to determine the performance and effectiveness of the NDWCTs accurately before and after retrofitting. The power utility must also predict the performance increase that new technologies will provide with the corresponding return on investment. The ability to predict and evaluate the performance of NDWCTs effectively will invariably also assist Eskom in verifying that performance tests conducted on NDWCTs are accurate.

The tests conducted during this investigation were all completed at Eskom's Majuba Power Station (Majuba Power Station) that is located near Amersfoort in Mpumalanga, South Africa. It is the only station in the Eskom fleet that utilises both direct dry-cooling as well as wet-cooling as their main cooling mechanism. The first three units are dry-cooled units whereas the last three units are wet-cooled by means of a common wet-cooling system. The station was designed to generate 4110 MW, with the dry-cooled units generating 657 MW each and the wet-cooled units generating 713 MW each.

In order to accurately design NDWCTs and to predict the performance and effectiveness of NDWCTs, the atmospheric conditions in the vicinity of the NDWCT need to be evaluated and trended. This includes determining what ranges of atmospheric conditions should be used during NDWCT designs and performance tests and how these specifications should be determined, where these conditions should be measured, the relationship between far-field and NDWCT inlet conditions and determining what times are suitable to conduct NDWCT performance tests. These objectives are evaluated and discussed in chapter 2 and chapter 3.

The effectiveness of NDWCTs is not only affected by the atmospheric conditions but also by the plant-specific conditions such as the generated load (P_{st}) and the cooling water mass-flow rate (m_{CW}). These parameters influence the effectiveness

of the condenser, and thus p_c, which is the link between the turbo-generator set and the NDWCTs. It is thus vital to comprehend the functional dependence between these parameters and to be able to model the effect of changes in these parameters on P_{st}. This parametric study is conducted and discussed in chapter 4, which provides relatively simple methods to determine these relationships. The plant-specific parameters required for this study are also tabulated. Two other NDWCT-models, one mathematical and one statistical, are discussed and evaluated in chapter 5.

The results from the above are used to determine the financial impact of a reduction in the NDWCT mean rain-zone drop diameter (d_d). This relates to an increase in the NDWCT effectiveness, a consequent reduction in the condenser saturation pressure (p_c) and increase in P_{st}, and thus to a reduction in the life cycle cost of Majuba Power Station. This is discussed in chapter 6, after which the main conclusion and recommendations are provided in chapter 7.

1.2. OBJECTIVES

The overview and motivation above provide a holistic view of the objectives, which are elaborated on below:

Chapter 2: Meteorological conditions at Majuba Power Station

- To measure and log meteorological parameters that influence the effectiveness of NDWCTs, including dry-bulb temperature (T_a), wet-bulb temperature (T_{awb}), wind speed (V_W) and direction (D_W), relative humidity (RH), rainfall (RF), solar radiation (SR) and atmospheric pressure (p_a) at Majuba Power Station over a period of 1 calendar year.
- To evaluate and trend the local meteorological parameters as functions of time, daily and seasonally.

Chapter 3: Ambient NDWCT design and performance test conditions

- To determine new/ current design and performance test ambient conditions for Majuba Power Station (2009-2010) and to compare these results with the original conditions.
- To evaluate the method and standard (British Standards, 1988) used to determine the original NDWCT design and performance test conditions.

Chapter 4: Water-steam cycle η_{th} and p_c functional dependence

- To understand and determine the water-steam cycle thermal efficiency (η_{th}) functional dependence at Majuba Power Station with historical plant data in order to calculate the relationship between η_{th} and plant parameters such as p_c (with the least amount of parameters).
- To understand and determine the p_c functional dependence at Majuba Power Station with historical plant data.
- To use these functional dependants to develop a simple method to quickly and effectively determine the relationships and to state which parameters are required to conduct such a functional dependence.

Chapter 5: Modelling of Majuba Power Station's NDWCTs

- To set up a 1-D mathematical model – presented by Kröger (1998) – for Majuba Power Station's NDWCTs and evaluate its accuracy.
- To set up and train an artificial neural network (ANN) of Majuba Power Station's NDWCTs and evaluate its accuracy as a performance prediction tool
- To compare the two models' results and to use these results to motivate improvements to the different models

Chapter 6: Financial impact of reducing the condenser saturation temperature

- To determine and financially quantify the advantages that a reduction in p_c will have on the η_{th} at Majuba Power Station.

CHAPTER 2
METEOROLOGICAL CONDITIONS AT MAJUBA POWER STATION

2.1. INTRODUCTION

Power plant cooling systems are dependent on local meteorological conditions including T_a, V_W, D_W, p_a, RH, SR, RF, temperature profiles, humidity profiles and wind profiles. These conditions have been investigated inter alia by Moore (1976) and Herberholz & Schultz (1979). As confirmed by Merkel (1925), temperature inversions may be a cause of apparent inconsistencies in NDWCT performance predictions (discussed in chapter 3). In order to determine and/ or evaluate the performance of NDWCTs it is thus necessary to understand and quantify these local meteorological conditions and the effect thereof on NDWCT effectiveness and therefore performance.

Equations and empirical correlations from literature are generally used to predict the effect that local meteorological conditions have on the overall performance of NDWCTs. According to Kröger (2004) most of these studies, however, focus on the lower atmosphere (below 50 km) and not specifically on the atmospheric boundary layer (ABL - below two km) and surface boundary layer (SBL - below 200 m), which are the layers from which cooling towers draws its cooling air.

This is depicted in Figure 2-1, where H_{abl} is the height of the ABL, H_s is the tower height, H_i is the tower inlet height, m_{av} is the inlet air-vapour mass flow rate and H_r is the height from which air is drawn into the tower, as presented by Kloppers & Kröger (2005).

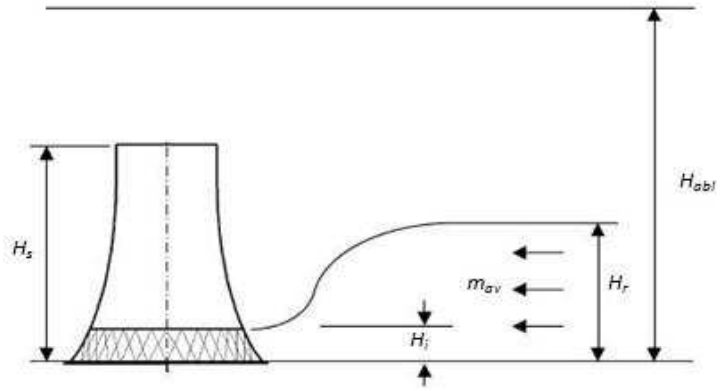

Figure 2-1: Schematic depicting the height from which air is drawn into a NDWCT (Kloppers, 2005).

In this chapter the researcher focuses on the evaluation of the atmospheric conditions at Majuba Power Station within this ABL from measurement data with the main objectives as stated in section 1.2.

The outline of this chapter is as follows:

- Meteorological parameter theory and literature;

- Description of the weather mast at Majuba Power Station and the measuring techniques;
- Reference height analyses;
- Temperature profile characteristics;
- Humidity characteristics;
- Wind profile characteristics; and
- Conclusion.

2.2. METEOROLOGICAL PARAMETER THEORY AND LITERATURE

2.2.1. The atmosphere

The atmosphere is divided into a number of contiguous regions, including the troposphere (0 – 20 km), stratosphere (20 – 50 km), mesosphere (50 – 85 km), thermosphere (85 – 690 km) and exosphere (690 – 10000 km). The air in these regions is mainly composed of nitrogen, oxygen and argon which together constitute the major gases of the atmosphere, as presented by Lutgens & Tarbuck (1995). Other trace gases such as water vapour, carbon dioxide, methane, nitrous oxide and ozone also exist in smaller quantities. The temperature in the stratosphere remains primarily constant with height, whereas the temperature profile in the troposphere is linear with height. The boundary between the troposphere and the stratosphere is known as the tropopause and is defined by this change in temperature profiles.

For the study of weather data in the power generation industry the focus area is mainly the troposphere, of which the ABL is part. Its thickness may differ with landform and the time of day, but it is normally defined by the first 2 kilometres from above ground level (AGL). The ABL is characterised by large vertical gradients in wind velocity, air temperature and humidity that is more pronounced in the first 200 m or SBL. These gradients are caused by friction with the Earth's surface. The transport of energy in this layer is accomplished by means of eddy diffusion and the physical state of the layer is dependent on the surface fluxes of momentum, heat and moisture (Kröger, 2004).

As noted by Hoffmann (1997), these vertical gradients and thus profiles change throughout the day and year. The hourly variation is attributed to surface heating, *SR*, and other variables, whilst the daily variation can be attributed to the change in the angle of the Earth's rotational axis; the cause of seasons. This axis is tilted 23.5^{o} with respect to the plane of its orbit around the Sun. Winter in the Southern Hemisphere is characterised by the South end of the axis of rotation that is tilted away from the Sun, while Summers are characterised by this axis that is tilted towards the Sun. The day during which the axis is tilted the most towards the Sun is called "Summer solstice" (23 December) while the "Winter Solstice" is known as the day during which the axis is tilted the furthest away from the Sun (21 June). On 22 March and 22 September the tilt is in a plane tangential to the Earth's orbit around the Sun. These days are called the "Autumn-" and "Spring Equinoxes" respectively. Due to the eccentricity of the Sun with respect to the Earth's orbit,

the Earth is closer to the Sun when it is Summer in the Southern Hemisphere and there is a tendency for seasonal variations in temperature to be greater in the Southern- than in the Northern Hemisphere (Kloppers, 2003).

2.2.2. Temperature profiles

As explained in section 2.2.1, temperatures vary significantly with height in the SBL. The following theoretical discussion focuses on instantaneous profiles rather than hourly and daily variation in these profiles; which is entirely dependent on the measurement location, the time of day as well as the seasons. The investigation into these profile changes is discussed in section 2.5.

The International Organization of Standardization (ISO) presents a standardised atmospheric model for temperature amongst other atmospheric parameters, namely International Standard Atmosphere (ISA). This model provides guidelines to the changes of temperature over a wide range of mid-latitudes and is compiled with a reference height (h_0), -temperature (T_0) and –pressure (p_0) of 0 m, 288.15 K and 101325 Pa respectively, as presented in ISO 2533 (1975).

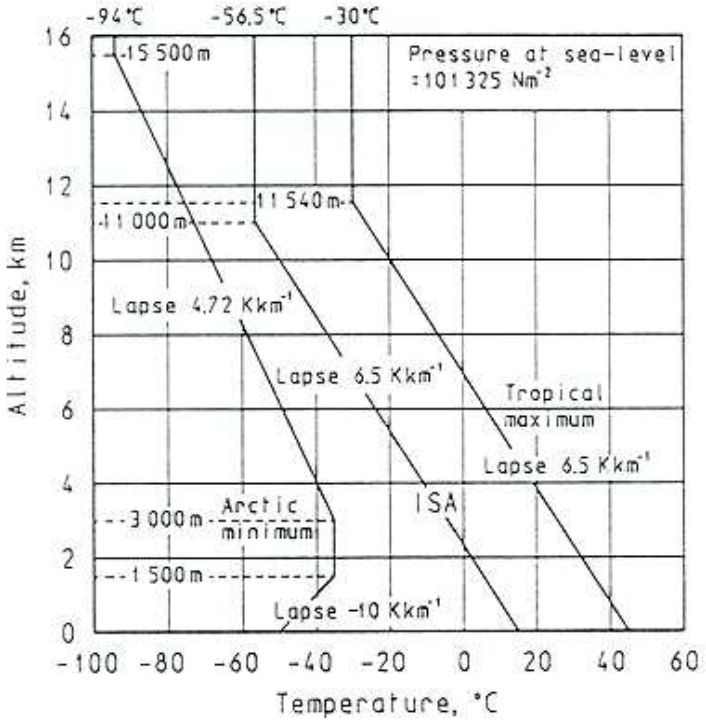

Figure 2-2: Graph showing different temperature lapse rate models (Kröger, 2004).

Figure 2-2 depicts the ISA rate of change in temperature with height together with the Tropical Maximum- and Arctic Minimum Atmosphere rate of change. According to the ISA 2533 guidelines (1975), the dry-adiabatic change in temperature (K) with heights (z) up to 11 km is:

$$T = T_0 - z\frac{dT}{dz} = 288.15 - 0.0065z \quad \textbf{(2-1)}$$

Kröger (2004) states that, a small parcel of air moving adiabatically up and down in the atmospheric pressure field will experience an isentropic change in temperature as a result of the change in pressure. With this in mind the author finds that the dry-adiabatic temperature lapse rate (DALR) can be stated as follows:

$$T = T_0 - z\frac{dT}{dz} = T_0 - 0.0095z \quad \textbf{(2-2)}$$

The difference between ISA and DALR is due to the simplifying assumptions associated with the ISA. The ISA is an average temperature lapse rate that is based on average conditions at mid-Latitudes as well as a stationary- (no wind or turbulence), dust-free atmosphere that contains no moisture, and is formalised with reference conditions at sea level as presented in ISO 2533 (1975) and by Talay (1975). These conditions are not suitable for the applications in this study, which motivates that the DALR equation (2-2), presented by Kröger is preferred. This equation is independent of the location and can be used when the ground level temperature is available. This equation can also be used for the calculation of values in the upper regions of the ABL. The limitations of this equation are, however, discussed below.

Surface heating takes place in the first 2 metres of the SBL. The first 20 m of the SBL is characterised by much higher gradients than the areas above it, partly because of this heating caused by the Earth's surface as well as the surface friction evident in this region. Equation (2-2) does thus not reflect the true relationship for temperature in this region because of its linear nature. In general, the distributions in the SBL can be expressed approximately using a model developed by Kloppers & Kröger (2005). These researchers present a simple empirical equation to predict the approximate temperature distribution in ambient air within the SBL. The equation is used for periods of adiabatic lapse rates as well as periods of temperature inversions, where only two temperature measurements and their corresponding elevations are required, i.e.:

$$T = (T_{r(^0C)} + 273.15)\left(z/z_r\right)^{b_T} \quad \textbf{(2-3)}$$

The value for the temperature profile exponent (b_T) is determined by regression.

Temperature inversions

Temperature inversions reduce the effectiveness of NDWCTs (Kloppers, 2003) due to the potential driving force or pressure differential that is less, and the effective NDWCT inlet T_a is higher compared to conditions where adiabatic lapse rates prevail (Kröger, 2004).

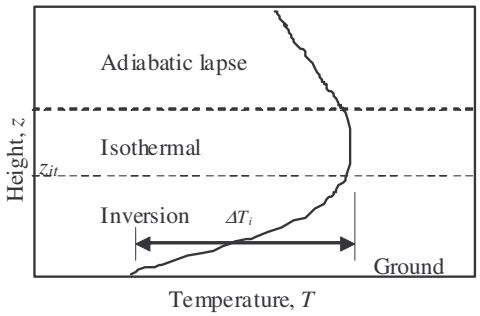

Figure 2-3: Temperature distribution of the stable boundary layer (Kloppers, 2003), showing the inversion, isothermal and adiabatic lapse rate regions.

Temperature inversions, which exhibit an increase in temperature with height in the SBL, are contiguous with the surface of the Earth and are capped by an isothermal region that is occasionally accompanied by a wind jet. Above the isothermal region the atmosphere exhibits an adiabatic lapse rate. This is depicted in Figure 2-3.

There are two parameters that influence the stability of an inversion layer. These are the temperature difference between ground level and the top of the inversion, ΔT_i, and the inversion height (z_{it}) - defined as the height at which the actual temperature gradient first becomes 0, or where the isothermal region is first established (Kröger, 2004).

A number of factors influence the evolution of temperature inversion during the nocturnal stable boundary regime. These include drainage flows, which originates when air adjacent to a sloping surface cools and becomes more dense than the free air at the same elevation (as presented by Soler, Infante & Buenestado (2002)); mixing induced by conduction between the ground and the vegetative canopy; mixing induced by nocturnal low-level jets as well as radiative heating and –cooling of the Earth's surface, as presented by Kröger (2004) and Ohya & Uchida (2004).

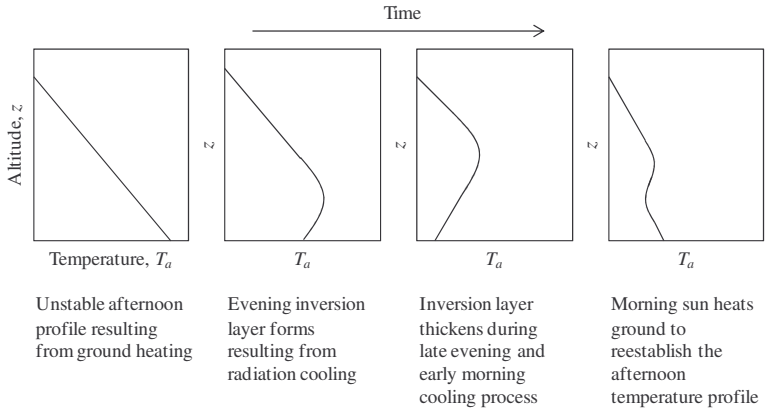

Figure 2-4: Typical diurnal variations in atmospheric air temperature profiles (Kröger, 2004).

The mentioned factors cause significant diurnal variations in the air temperature near the surface, as explained in Figure 2-4. In the afternoon the Sun heats the surface of the Earth to a temperature much higher than the average air temperature. This results in a net heat transfer from the surface to the air near the surface. Convectively unstable conditions might be experienced when the temperature drops more sharply than predicted by the DALR (Kröger, 1998). During the transition from day to night, radiation begins to cool the surface especially when the sky is clear. The surface temperature may drop below the average air temperature near the surface, which results in a net heat flux from the first few metres of air to the ground. This forms a temperature inversion as depicted in Figure 2-4. The cooling of the surface may continue throughout the night, thickening the inversion layer. This process occurs until the Sun starts to rise and when solar radiation again transfers heat from the Sun to the ground, forming a transition profile as shown in Figure 2-4. After sufficient heating this cycle is repeated.

Temperature inversion profile and height calculation methods

Numerous theoretical studies have been conducted in order to predict the nocturnal atmospheric temperature profile from ground-based measurements. The methods that are introduced by these studies include methods from Anfossi *et al.* (1975) and Surridge (1986). The Anfossi method fails to correlate the data particularly well but gives a reasonable indication of the inversion height. Surridge's method, on the other hand, does follow the particular data closely over a specific part of the inversion, but under-predicts the inversion height (Kloppers, 2003). It is thus apparent that both of these rather cumbersome methods have its limitations.

In the light of these limitations Kröger (2004) shows that equation (2-3) can be used to predict the temperature profiles of atmospheric air during inversion periods (only applicable in the stable boundary layer), while an extended version of equation (2-3) is preferred near the top of the inversion where the temperature gradient is 0. This extended version represents the transition between the inversion and the adiabatic lapse rate above it and is presented as follows:

$$T = (T_{r(^0C)} + 273.15)\left(z/z_r \right)^{b_T} - 0.00975 \cdot z \qquad \textbf{(2-4)}$$

In order to calculate an approximate value for the inversion height, it is required to differentiate equation (2-4) and to set it equal to 0.

$$\frac{dT}{dz} = b_T (T_{r(^0C)} + 273.15)\left(\frac{z_{it}}{z_r} \right)^{b_T - 1} - 0.00975 = 0 \qquad \textbf{(2-5)}$$

This is the point at which the inversion subsides and the adiabatic lapse rate commences, known as the isothermal region. Rearranging this equation provides

the following equation for calculating the inversion height once the temperature profile exponent, b_T, is known (Kloppers, 2003):

$$z_{it} = \left[0.00975 / \left\{b_T \left(T_1 + 273.15\right)\right\}\right]^{1/(b_T - 1)} \quad \textbf{(2-6)}$$

2.2.3. Wind profiles

Elliot *et al.* (1986) and Peterson & Hennessey (1978) show that the variation of wind speed with height can generally be estimated by means of a wind profile power law that is widely used in industry for wind power assessments and determining wind profiles (equation (2-7):

$$\frac{V_W}{V_{Wr}} = \left(\frac{z}{z_r}\right)^{b_W} \quad \textbf{(2-7)}$$

This relationship can be used to determine V_W in the atmospheric boundary layer once the wind profile exponent (b_W) is known. This exponent is generally taken as 0.143 for stable atmospheric conditions over open land surfaces, as stated by Hsu *et al.* (1994). Using a constant b_W can, however, occasionally yield inaccurate results as it does not account for the surface roughness, the displacement of calm winds from the surface due to the presence of obstacles, or the stability of the atmosphere, all of which influence b_W dramatically as noted by Touma (1977) and Counihan (1975).

In quantifying the effect of wind on the performance of NDWCTs, it is important to have a sound knowledge of the variation of V_W, D_W and b_W on a daily and seasonal basis. These variations at Majuba Power Station are discussed in section 2.8.

2.2.4. Humidity profiles

Atmospheric humidity influences the heat- and mass transfer as well as the draught through a NDWCT (Kloppers, 2003). A number of empirical methods have been developed to predict humidity profiles as a function of altitude (Shoda *et al.* (1975) and Gorchakov *et al.* (1975)) but these methods all focus on the lower atmosphere (below 50 km) and not on the ABL and SBL, which is the area of interest for NDWCT performance predictions. These methods can thus accurately predict the humidity profiles in the lower atmosphere, where the diurnal variations are small, but struggle to predict these profiles in the boundary layer, where the diurnal variations are more pronounced.

During sunrise, evapotranspiration ensures that water vapour is added to the lower atmosphere. This causes a sharp increase in the air's humidity. The lapse condition that prevails becomes the most pronounced at the time of maximum surface heating due to convective mixing and the subsequent intensity of the vapour concentration in the lower atmosphere. In the afternoon the convective mixing diminishes as the air near the ground becomes stable. During this time

evaporation continues, but the intensity of the vapour concentration slows down and the lapse rate is similar to isothermal conditions. During nocturnal hours radiative cooling causes dew formation and the subsequent extraction of water vapour from the atmosphere. This causes a sharp decrease in the humidity near the surface that leads to the formation of an inversion in the water vapour- and thus the humidity profiles.

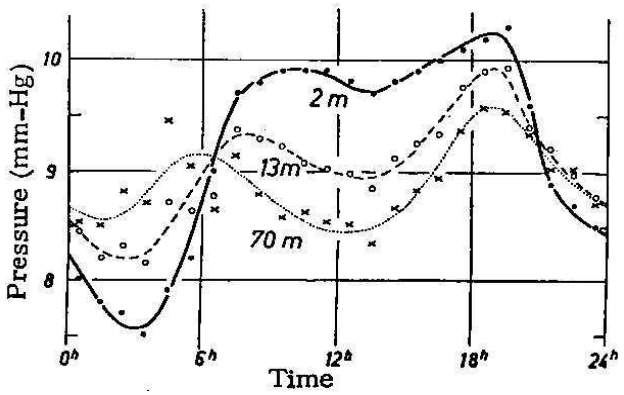

Figure 2-5: Diurnal variation of water vapour pressure at Quickborn, Germany on a clear July day (Oke, 1987).

Figure 2-5 depicts the variation in vapour pressure measured at three different heights in Quickborn, Germany on a clear day in July (Oke, 1987). The inversion formation in the vapour pressure profile is clear in this figure. The depth and strength of the inversion is determined by the downward flux of water vapour in a suitably turbulent environment. The level of turbulence is imperative. If too low, dew ceases to form as the ground cannot be replenished by water vapour from above. If the level of turbulence is too high, mixing inhibits surface radiative cooling to sub-dew-point temperatures. During early afternoon hours, turbulence transfers moisture from the surface at such a rate that specific humidity usually falls to an early-afternoon minimum, even during periods of strong evapotranspiration (Kloppers, 2003).

Oke (1987) states that although the vapour flux is at a peak during the early afternoon, the humidity concentration drops slightly. This is the result of the convective activity penetrating to such heights in the ABL that the vapour concentration becomes diluted by mixing with descending masses of drier air. In the late afternoon surface cooling is strong and the lower layer becomes stable. The ability to transport vapour to higher layers is thus lower than the rate at which it continues to be added from the surface. Moisture converges into the lowest layers and a second humidity maximum is observed (Kloppers, 2003). This well-known double wave of vapour pressure is recognised in Figure 2-5. This tendency appears at all levels, but the amplitude of fluctuations increase closer to the ground. In all of these layers the evening peak is higher than the morning value. Figure 2-5 is, however, dependent on the season, the weather conditions and the location of measurement.

2.3. DESCRIPTION OF THE WEATHER MAST AT MAJUBA POWER STATION

2.3.1. Location

In 1994 a 65 m lattice-type mast, depicted in Figure 2-6 and Figure 2-7, was erected 1200 m from the power station (S 27.09341°, E 29.77431°). The purpose was to measure and monitor atmospheric conditions, including T_a, p_a, V_W and D_W, RH, RF and SR, at different heights above the standard meteorological height of 1.2 m for T_a and 10 m for V_W and D_W (Louth, 1996). The aim was to study the effect of atmospheric weather conditions on the main cooling systems at Majuba Power Station.

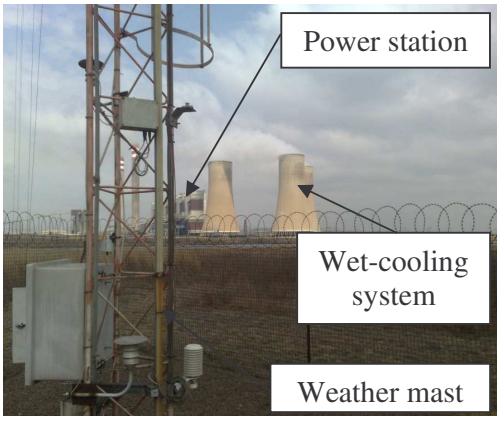

Figure 2-6: View of Majuba Power Station from the base of the station's weather mast.

Figure 2-6 depicts the base of the weather mast with Majuba Power Station and the wet-cooling system in the background, whereas Figure 2-7 depicts the structure of the mast with its support cabling.

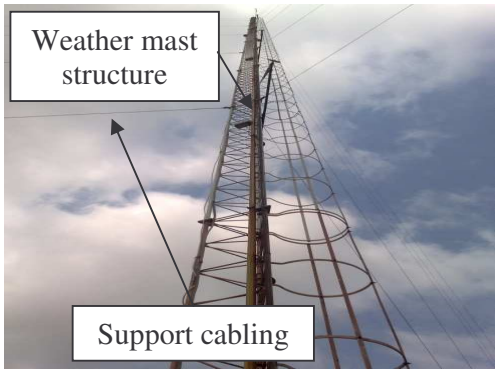

Figure 2-7: View of Majuba Power Station's weather mast structure and cabling.

The mast site was chosen firstly to be far enough from the power station, and the 153 m high NDWCTs, for its micro climate to have no effect on the installed measurement equipment. Secondly, the site was chosen in order for the mast to be on the same height above sea level as the station's reference height. The other reasons for the location were to ensure that the station does not influence the wind

measurements from the nominal wind direction and to ensure that the mast is located on a flat plane (Louth, 1996). The geographic map showing the location of the mast in relation to the power station and the NDWCTs is depicted in Figure 2-8. The NDWCTs are not explicitly shown, but the location is accurate.

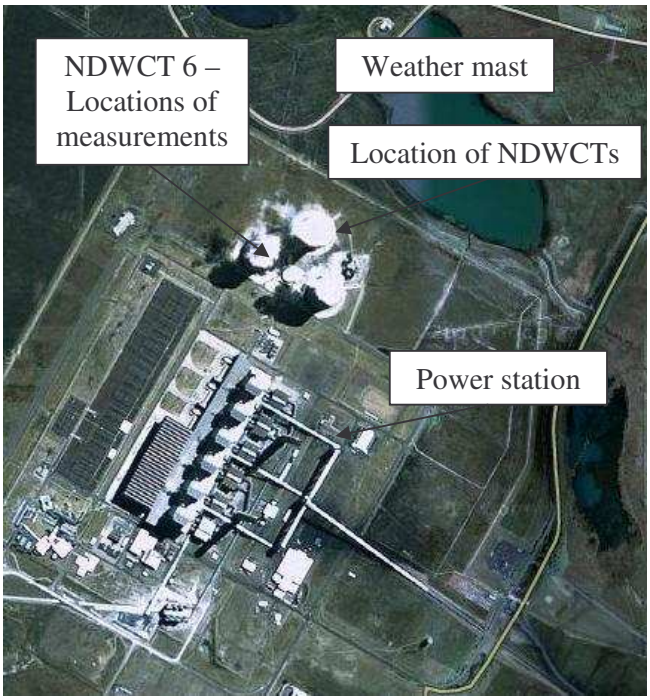

Figure 2-8: Map showing the weather mast location relative to Majuba Power Station.

2.3.2. Instrumentation and data capturing

As shown in Figure 2-9, the mast consists of 7 temperature thermistors (T_a) that are mounted at heights of 1.2 m, 2.5 m, 5 m, 10 m, 20 m, 40 m and 65 m AGL. V_W and D_W are measured at 10 m, 20 m, 40 m and 65 m AGL by means of anemometers. *RH*, *SR* and p_a are measured at 1.2 m. *RF* is measured by a tipping rain-bucket that is fixed to the foot of the mast. A data logger, located at the foot of the mast, averages every 60 measurements taken at a frequency of 10 seconds that represents a 10 minute interval. The logged data from 09:55 to 10:05 is averaged to represent 10:00. Seasonal data is presented in terms of the four seasons, which are explained below:

- Summer = 1 December – 28/29 February;
- Autumn = 1 March – 31 May;
- Winter = 1 June – 31 August; and
- Spring = 1 September – 30 November.

This basis is used throughout (the study) for all the measured data.

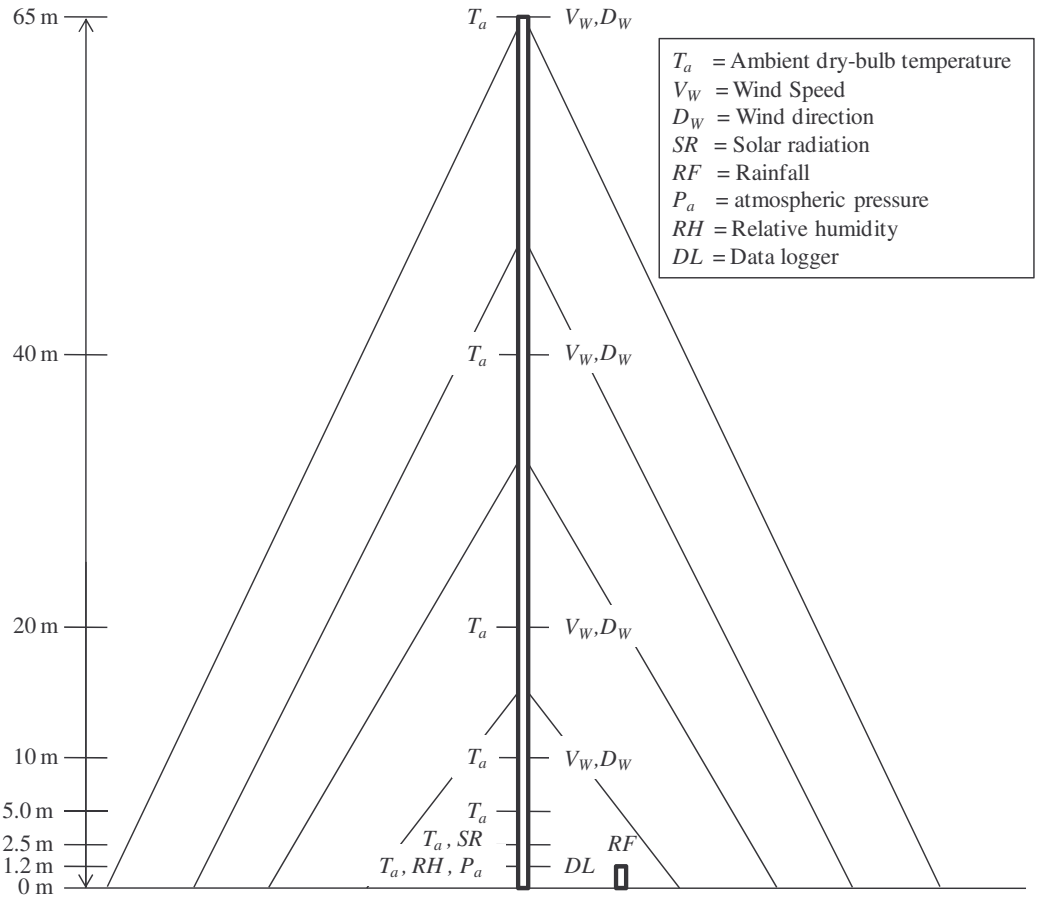

Figure 2-9: Schematic representation of Majuba Power Station's weather mast.

In Table 2-1 the researcher summarises the specifications of the equipment installed on the mast. The calibration certificates, together with photos of the equipment, can be viewed in appendix D.

Table 2-1: Majuba Power Station's weather mast - measuring equipment specifications.

Measurement	Equipment	Accuracy (95% confidence)
Dry-bulb temperature	YSI 44203 thermistors with radiation shields	+/- 0.394 ºC
Wind speed and direction	RM Young 05103 wind monitors	+/- 0.2032 m/s and +/- 6.06 º
Atmospheric pressure	RM Young 61101 SENTRA transducer	+/- 2.08 mB
Relative humidity	RM Young 41372 humidity sensor	+/- 6.0 % RH
Rainfall	Texas Electronics tipping bucket guage	+/- 0.04 mm/5 mm rain
Data logger	Campbell Scientific CR10 data logger	N/A

In addition to the equipment discussed above, data loggers were installed in order to determine the humidity profiles due to reasons provided in section 2.2.4 and to establish the differential temperatures and *RH* between far-field and NDWCT inlet measurements (Section 3.2). These data loggers are manufactured by TinyTag ®. Ten data loggers were used with an average standard deviation of 0.221 ^{o}C. The data loggers show comparable temperature and humidity

resolutions and accuracies when compared to the equipment installed on the weather mast - Table 2-1, as depicted below in Figure 2-10 and Figure 2-11. The accuracies are motivated by the differential measurements in both the figures. The specifications for these data loggers are provided in appendix D.

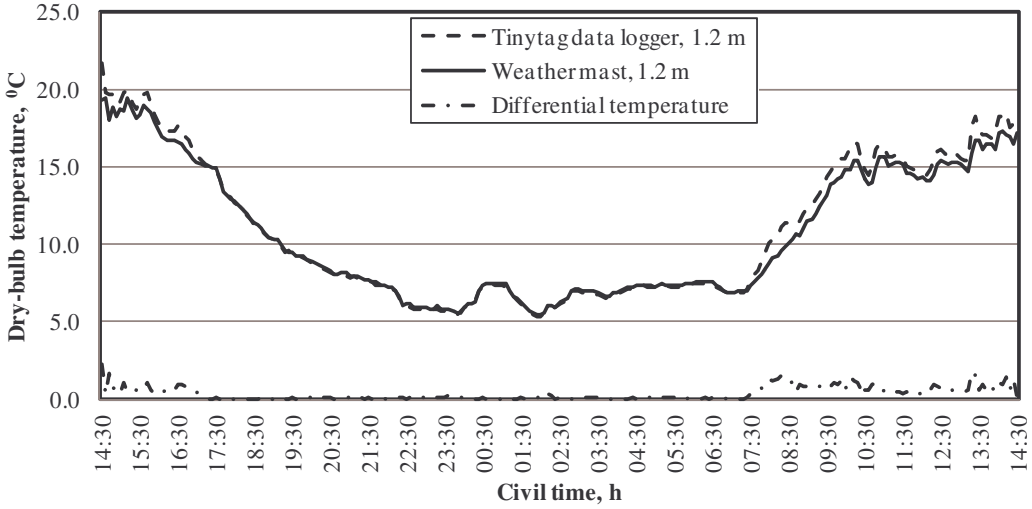

Figure 2-10: Comparative test results between an installed thermistor on Majuba Power Station's weather mast and a TinyTag ® data logger for a 24-hour period.

The two measurements compare well overall but it is found that during daytime periods, when *SR* is evident, the data loggers do not compare as well to the installed equipment as is the case during nocturnal hours.

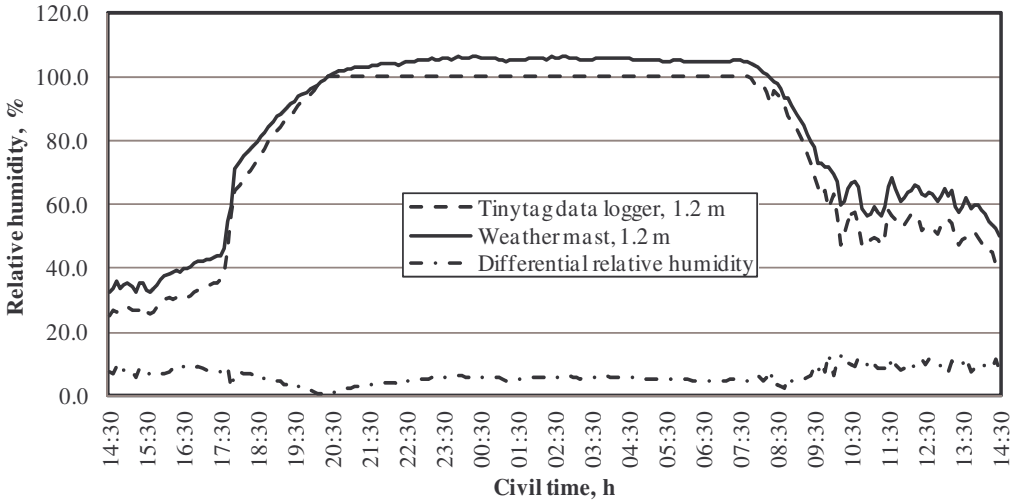

Figure 2-11: Comparative test results between an installed *RH*-sensor on Majuba Power Station's weather mast and a TinyTag ® data logger for a 24-hour period.

The comparisons depicted above are best achieved after the TinyTag loggers have been improved significantly by installing thermal shields around them, as depicted in Figure 2-12.

Figure 2-12: TinyTag data loggers (3) installed at Majuba Power Station's weather mast at 1.2 m AGL with the middle data logger shielded from *SR*.

2.3.3. Data grouping and validation

For the purpose of the study (section 2.4 - 2.8), data from the weather mast was collected over a period of 12 months from August 2009 to July 2010. All instruments were calibrated before this period. The calibrated TinyTag® data loggers were only used for 2 weeks during June 2011.

As is the case with any measuring instrument, not all the measured data will be accurate. Reasons for these discrepancies are calibration faults as well as instrument failure. To ensure that all the data used for analysis are in fact accurate, all individual instrument data are analysed separately in order to exclude datasets that are not representative and have one or more incorrect measurements.

Specific sections of data are used during the following investigations. The composition of these datasets is explained in the relevant sections. All datasets are, however, collected with reference to civil time, which refers to the statutory time scales designated by authorities or, simply defined, to local time indicated by clocks (Civil, 2010).

In order to compare ambient conditions at different locations more accurately it is recommended that the data be presented in terms of local solar time, which is time defined by the position of the Sun. The solar day is the time it takes for the Sun to

return to the same meridian in the sky. When the centre of the Sun is on an observer's meridian, the observer's local solar time is 0 hours (noon). Because the Earth moves with varying speed in its orbit at different times of the year and because the plane of the Earth's equator is inclined to its orbital plane, the length of the solar day is different depending on the time of year. Mean solar time is the average of local solar time and may be thought of as being measured relative to an imaginary Sun (the mean Sun) that lies in the Earth's equatorial plane and around which the Earth orbits with constant speed. Every mean solar day is of the same length. The difference between the local solar time and the mean solar time at a given location is known as the equation of time (t_{EOT}). Tables used by navigators list the t_{EOT} for different times of year so that an observer can calculate his mean solar time from his local solar time. Mean solar time is the basis for civil time as described by the Columbia Encyclopaedia (Solar, 2010), and is the time scale used throughout this report. Calculating local solar time (t_{LST}) from civil time (t_c) is done by means of the equation (2-8):

$$t_{LST} = t_C - (12:00 - t_{EOT}) \qquad \textbf{(2-8)}$$

Representing time with reference to local solar time will ensure that data comparison is conducted using the same time scale, thus improving the accuracy of the comparison.

The monthly sunrise and sunset times for the period from August 2009 to July 2010 is depicted in Figure 2-13 below. This figure indicates that Summer months are defined by earlier sunrises and longer days and *vice versa* for Winter months. The data depicted in this figure will be used throughout this report and will be referenced accordingly.

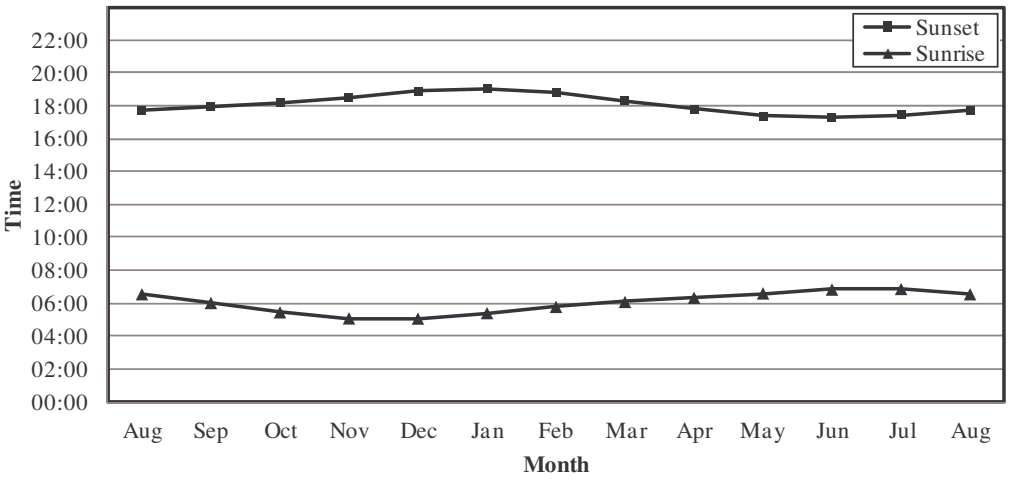

Figure 2-13: Monthly sunrise and sunset times at Majuba Power Station.

2.4. REFERENCE HEIGHT ANALYSIS

The industry-standard temperature- and wind reference heights according to Louth (1996) are 1.2 m and 10 m respectively. According to BS 4485 (1988), the reference height for T_a and T_{awb} is 1.5 m to 2.0 m above basin curb (ABC) which relates to approximately 3 m AGL. The temperature reference heights stipulated by Louth (1996) are, however, used throughout this dissertation in order to make representative comparisons between design and current meteorological conditions due to its use in the initial meteorological conditions study conducted in 1996.

Standard reference heights are, however, not always used – for various reasons. This section serves as a motivation to use the industry-standard reference heights to obtain reliable and comparative results. The sensitivity of different reference heights on the dry-bulb b_T is determined. A similar study is completed for the wet-bulb b_T, the b_W as well as the humidity profile exponent (b_H).

Table 2-2: Measured T_a (°C) at Majuba Power Station's weather mast – 04/09/2009.

Time	Measurement height						
	1.2	2.5	5	10	20	40	65
18:00	18.08	19.01	20.16	20.87	21.23	22.23	22.14
19:00	15.21	15.67	16.34	16.88	17.18	17.62	17.68
20:00	12.58	12.89	13.39	13.98	14.46	15.36	16.12
21:00	11.16	11.78	12.69	13.86	14.36	15.40	15.95
22:00	9.43	10.50	11.95	12.99	13.28	13.66	14.22
23:00	8.86	9.58	10.98	12.16	12.88	14.02	14.33

In order to quantify the sensitivity of the reference height a set of T_a data is used that represents a cloudless and relatively windless day at Majuba Power Station. The data is depicted in Table 2-2. The basis for this data is explained in section 2.3.2.

The temperature profiles during the inception and first few hours of the inversion period are depicted in Figure 2-14, using the data provided in Table 2-2. The b_T for each hourly interval is determined by regression. The inversion lapse rate periods are used in order to determine the correct reference height as well as to show that equation (2-3) can accurately predict the temperature inversion lapse rates.

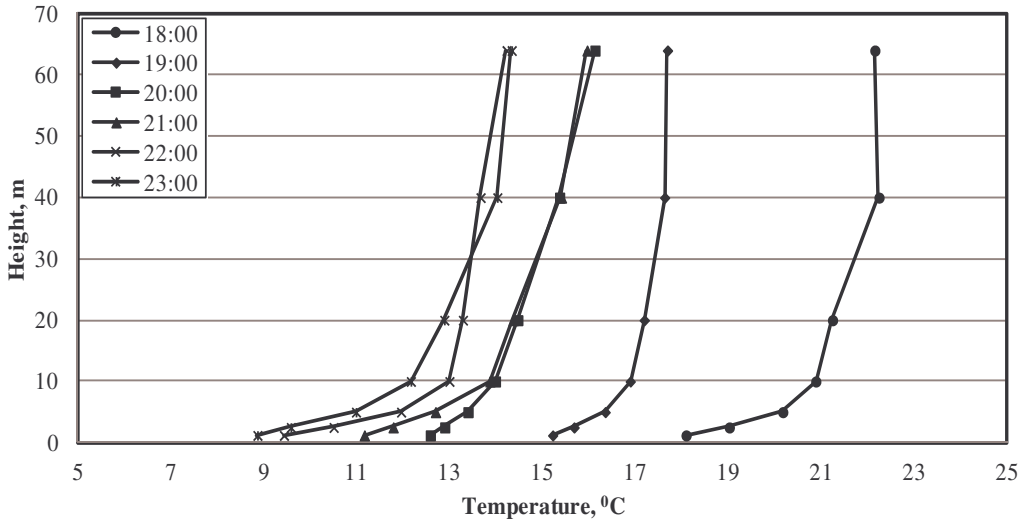

Figure 2-14: Hourly measured dry-bulb temperature profiles from 18:00 to 23:00 on 2009/09/04.

The b_T-values corresponding to the profiles in Figure 2-14 are presented in Table 2-3. All the exponent values are found to differ for different reference heights at a fixed time interval. It is thus necessary to know which reference height provides the most accurate temperature profiles.

Table 2-3: Hourly best-fit values for b_T from 18:00 to 23:00 on 2009/09/04 for different reference heights.

Time	1.2 m	2.5 m	5.0 m	10 m
18:00	0.004035	0.003953	0.003382	0.003488
19:00	0.002374	0.002427	0.002122	0.002689
20:00	0.002761	0.003101	0.003295	0.002744
21:00	0.004201	0.004481	0.004448	0.004458
22:00	0.004237	0.004018	0.003111	0.005253
23:00	0.005031	0.005580	0.005118	0.005487
Average	0.003773	0.003927	0.003579	0.004020

Figure 2-15 depicts the measured temperatures at 21:00 as well as the corresponding predicted temperature profiles at 21:00 for different reference heights. The profiles for reference heights of 1.2 m, 2.5 m and 5.0 m are all found to represent the measured data accurately. The temperature profile for the 10 m reference height deviates from the measured data as the height increases and should thus not be considered as a reference height.

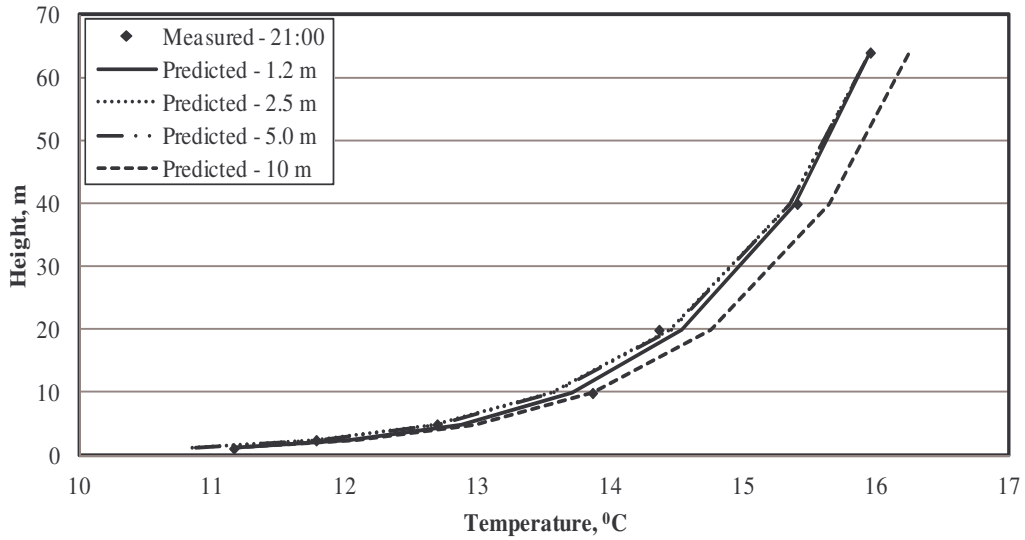

Figure 2-15: Measured and predicted dry-bulb temperature profiles for 21:00 on 2009/09/04

It should be noted that the vegetation near ground level does influence the ground level temperature. This effect is, however, small at Majuba Power Station's weather mast, where the vegetation largely consists of open savannah and fully grown root crops.

Table 2-4: Roughness lengths for various surfaces (Kröger, 2004).

Surface configuration	Roughness length, m	Surface configuration	Roughness length, m
Urban areas		Flat relief, vegetated	
Central business district	8.00	Uncut grass	0.070
High density residential	4.50	Crop stubble	0.020
Low density residential	2.00	Snow and short grass	0.002
Rolling relief		Flat relief, unvegetated	
Coastal bush	1.00	Natural snow (temporary)	0.00100
Open savanna	0.80	Bare sand	0.00040
Full grown root crops	0.25	Open sea	0.00020
Shrubs	0.15	Water	0.00010

The surface roughness lengths corresponding to these two categories is depicted in Table 2-4 and are 0.8 m and 0.25 m respectively – below any of the reference heights discussed in this section. Figure 2-16 depicts the vegetation at Majuba's weather mast during the four seasons.

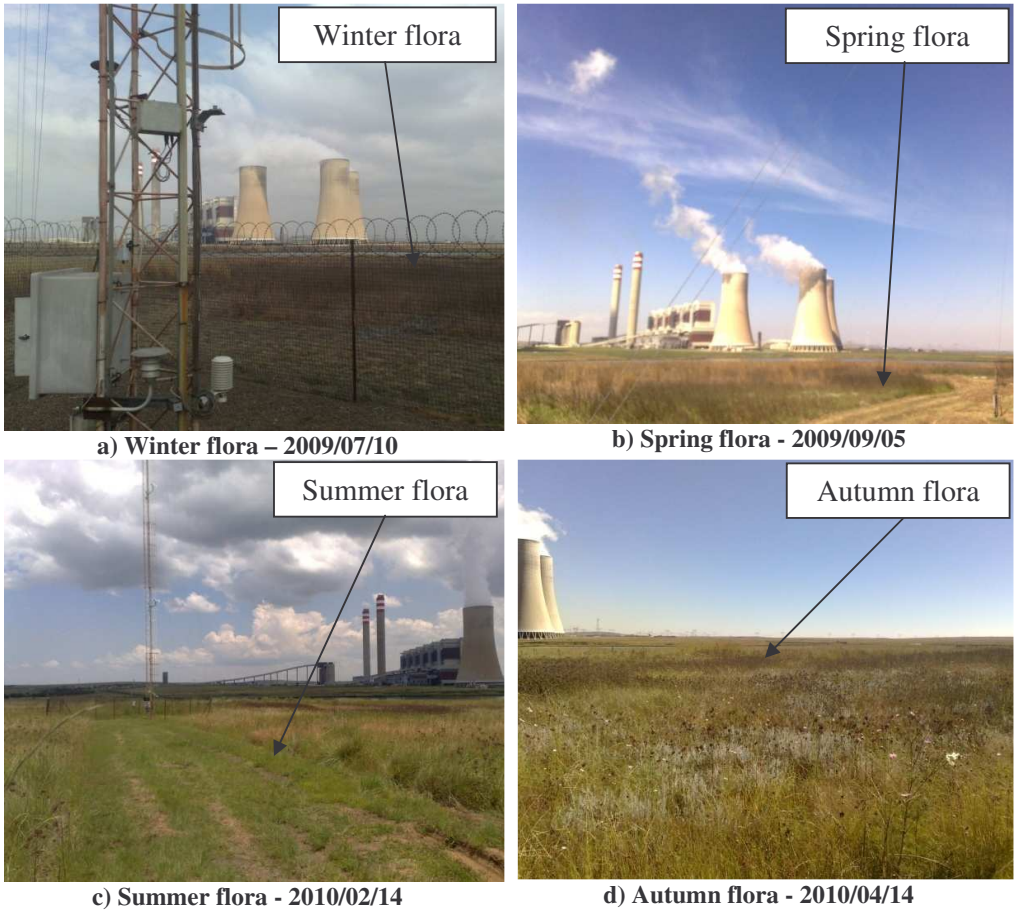

a) Winter flora – 2009/07/10

b) Spring flora - 2009/09/05

c) Summer flora - 2010/02/14

d) Autumn flora - 2010/04/14

Figure 2-16: Seasonal variation in the flora at Majuba Power Station.

The flora is found to remain short throughout the year, which confirms that it falls within the specific classes mentioned above.

The above discussion and results, together with the fact that the industry standard is the same as one of these heights in question, and that a height of 1.2 m is easily reachable to meteorologists (Kloppers, 2003), motivates that the industry-standard reference height of 1.2 m for temperature is the preferred reference height to use for all T_a-related calculations and measurements. As noted in paragraph 1 of section 2.4, the temperature reference height stipulated in BS 4485 (1988) could also be used as motivated by the results depicted in Figure 2-15. However, due to the reasons provided in this paragraph, the reference height stipulated by Louth (1996) will be used throughout this dissertation.

A similar reference height sensitivity analysis was completed for the T_{awb}-profiles, the ω-profiles as well as the wind profiles. The results from these analyses show that the industry-standard temperature and humidity reference height of 1.2 m, as well as the wind reference height of 10 m, should be used in all calculations and measurements. Heights above 1.2 m for temperature and humidity, and above 10 m for wind, produce less accurate and even erroneous results. The accuracy

decreases with height as is the case with the above temperature profile sensitivity analysis.

2.5. TEMPERATURE AND TEMPERATURE PROFILE CHARACTERISTICS

In section 2.2.2 the theory behind temperature profiles is discussed. In this section the researcher discusses the daily and seasonal variations in temperature profiles during specific time periods, as measured at Majuba Power Station's weather mast in an attempt to understand the temperature profile characteristics.

2.5.1. Daily variations in temperature profiles at Majuba Power Station

The stable ABL in Mpumalanga is characterised by strong nocturnal inversions and thus large temperature profile changes within a 24-hour period. In order to determine these temperature profiles, a calm, relatively windless day with minimal cloud cover is used. The turbulence associated with the strong winds enhances mixing in the ABL, which results in a more subdued temperature profile according to Kröger (2004). Golder (1972) furthermore states that wind velocities above 8 m/s will invariably result in an adiabatic (neutral) atmosphere. The clearness of the day also contributes to the formation of an inversion layer as clouds reflect most of the Earth's radiation back to the surface. This reduces the rate of cooling of the surface after sunset and thus suppresses the formation of the inversion layer.

Keeping the above characteristics in mind, a relatively cloudless 24-hour period was chosen with reference height V_W of less than 8 m/s to eliminate the effect of strong winds and irregular solar radiation.

The calmness of the day can be verified in Figure 2-17, which depicts the reference height V_W for the date 04/09/2009. The maximum V_W during this period is approximately 6 m/s.

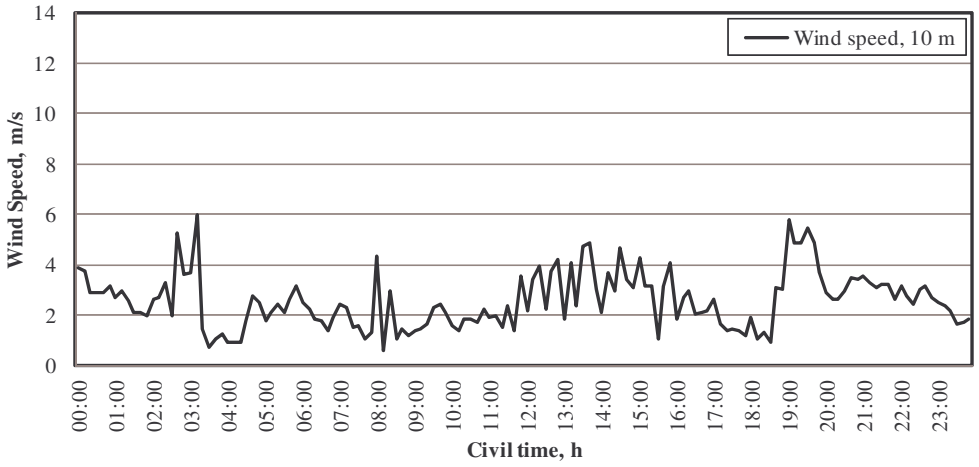

Figure 2-17: Measured reference height wind speed – 2009/09/04.

It is found that the periods after sunrise (from 06:00) and after sunset (from 18:00) is characterised by higher V_W values due to the transformation from inversion lapse rates to adiabatic lapse rates and *vice versa*, as explained in section 2.2.2.

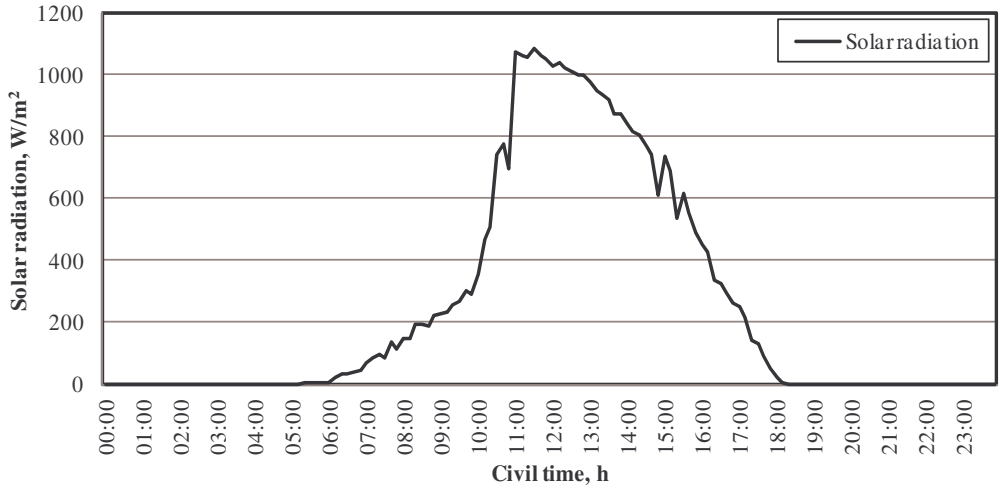

Figure 2-18: Measured S*R* at Majuba Power Station – 2009/09/04.

Figure 2-18 presents the *SR* for the 24-hour period. It is found that the applicable day was relatively cloudless. It is, however, noted that the period from sunrise (06:00) to approximately 10:00 is characterised by a much more subdued initial increase in solar radiation compared to the decrease in the afternoon. This was caused by intermittent cloud cover that subsided at approximately 10:00, after which the *SR* increased rapidly until noon, which is characterised by the highest *SR*. The *SR* steadily decreases after noon, with some intermittent cloud cover between 14:30 and 15:30 and until sunset (18:00).

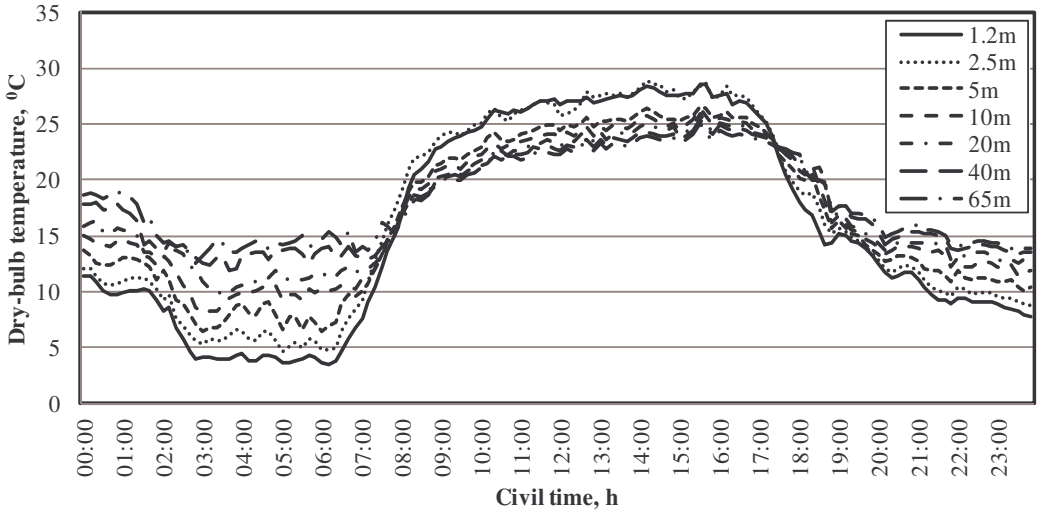

Figure 2-19: Measured T_a-values at Majuba Power Station – 2009/09/04.

In Figure 2-19 T_a-values are depicted with reference to civil time at different heights for 04/09/2009. The inversion layer that prevails during the nocturnal hours (18:00 to 06:00) is portrayed where T_a increases with height, as well as the adiabatic lapse rate that exists during the daytime (08:00 to 16:00). During this time T_a decreases with increasing height. The morning transition period is found to prevail from 06:00 to 08:00 and the evening transition occurs between 16:30 and 17:30. These transition periods tend towards isothermal conditions, with clear isothermal conditions prevailing for a short period of time, and correspond well to literature, together with the sunrise and sunset times depicted in Figure 2-13.

The hourly T_a-profiles are depicted in Figure 2-20. The period from 00:00 to 05:00 depicts the time in which the inversion layer thickens during early mornings as result of the radiation cooling process and net heat flux from the ground to the air above it. As the Sun rises it heats the ground and re-establishes an adiabatic lapse rate temperature profile. This is depicted by the period from 06:00 to 11:00. The unstable afternoon T_a-profile resulting from the solar ground heating is depicted from 12:00 to 17:00 while the evening inversion layer caused by radiation from the Earth's surface to the atmosphere and space is displayed from 18:00 to 23:00.

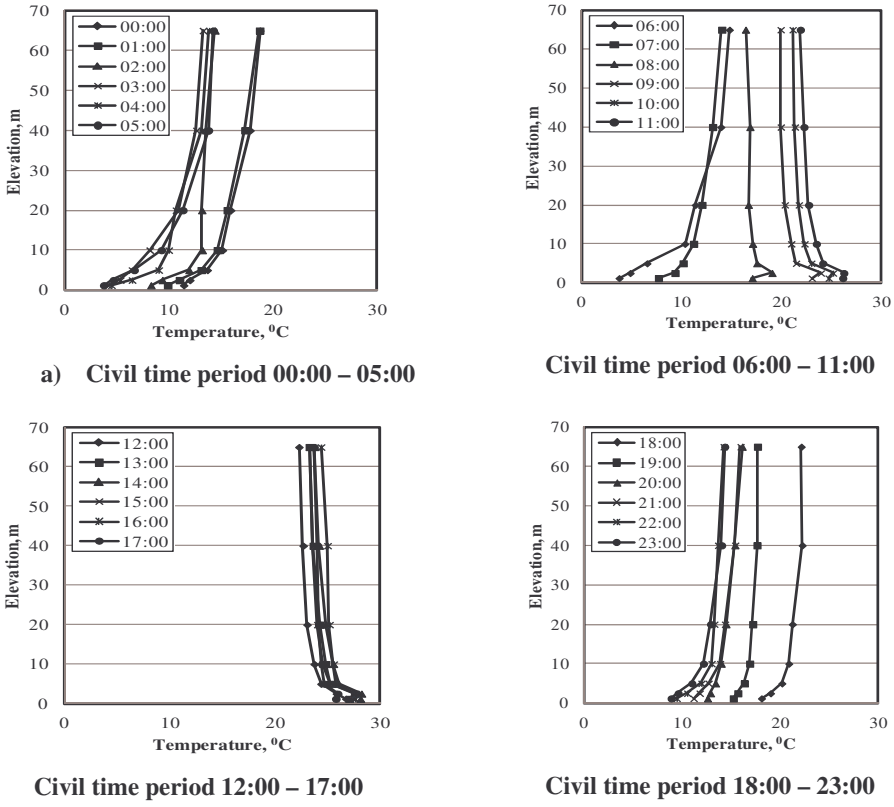

Figure 2-20: Measured T_a-profiles for different civil time intervals – 2009/09/04.

An uncommon phenomenon was noticed during the first few hours after sunrise (08:00 to 11:00) where the T_a at a height of 1.2 m is lower compared to the corresponding height at 2.5 m. This phenomenon is explained in section 2.5.2. The T_a-profile data does overall compare well to data published by (Kröger, 1998).

From the data presented in Figure 2-17 to Figure 2-19 it is established that the chosen 24-hour period has relatively low reference-height V_W-values, minimal cloud cover and well-developed temperature profiles throughout, which aids in the analysis of the T_a-profiles below.

The measured T_a-values displayed in Figure 2-19 are used to calculate the T_a-profiles using equation (2-3). The basis for the measured data is explained in section 2.3.2. As explained in section 2.4, a reference height ($z_{T,r}$) of 1.2 m is used in determining b_T. The results can be viewed in Table 2-5 which depicts the calculated T_a for 04/09/2009 as well as the deviations from the corresponding, measured T_a.

Table 2-5: Calculated T_a-values and the deviations from the measured T_a-values at Majuba Power Station – 2009/09/04.

Time	Calculated dry-bulb temperatures							Deviations from measured dry-bulb temperatures						
	Measurement heights													
	1.2m	2.5m	5.0m	10m	20m	40m	65m	1.2m	2.5m	5.0m	10m	20m	40m	65m
00:00	11.40	12.73	14.00	15.26	16.54	17.82	18.72	0.00	0.74	0.33	0.14	0.62	0.04	0.00
01:00	9.86	11.46	12.99	14.52	16.06	17.61	18.70	0.00	0.46	-0.10	-0.12	0.47	0.32	0.00
02:00	8.25	9.37	10.43	11.50	12.57	13.64	14.40	0.00	0.02	-1.48	-1.68	-0.57	0.10	0.00
03:00	4.09	5.75	7.33	8.92	10.52	12.13	13.26	0.00	0.45	0.89	0.78	-0.37	-0.50	0.00
04:00	4.46	6.16	7.78	9.41	11.05	12.69	13.85	0.00	-0.27	-1.22	-0.55	0.38	-0.47	0.00
05:00	3.71	5.62	7.43	9.26	11.09	12.94	14.24	0.00	0.98	0.80	0.01	-0.23	-0.84	0.00
06:00	3.72	5.71	7.61	9.53	11.45	13.39	14.76	0.00	0.90	1.11	-0.77	0.10	-0.52	0.00
07:00	7.66	8.82	9.91	11.01	12.11	13.22	14.00	0.00	-0.50	-0.23	-0.17	0.10	0.14	0.00
08:00	17.05	16.93	16.81	16.69	16.58	16.46	16.38	0.00	-2.10	-0.70	-0.39	-0.08	-0.36	0.00
09:00	23.02	22.44	21.90	21.36	20.82	20.28	19.90	0.00	-1.48	0.46	0.41	0.51	0.37	0.00
10:00	24.71	24.04	23.41	22.79	22.16	21.54	21.10	0.00	-1.10	0.45	0.50	0.44	0.21	0.00
11:00	26.11	25.33	24.59	23.85	23.12	22.38	21.87	0.00	-0.89	0.48	0.38	0.42	0.15	0.00
12:00	26.73	25.90	25.12	24.35	23.57	22.80	22.26	0.00	0.07	0.76	0.63	0.54	0.14	0.00
13:00	27.04	26.34	25.68	25.03	24.37	23.72	23.26	0.00	-1.23	0.37	0.25	0.16	0.08	0.00
14:00	28.10	27.30	26.55	25.80	25.05	24.30	23.78	0.00	-0.90	0.52	0.28	0.26	0.11	0.00
15:00	27.50	26.71	25.97	25.24	24.50	23.76	23.25	0.00	-0.76	0.68	0.74	0.48	0.13	0.00
16:00	27.60	27.00	26.44	25.87	25.31	24.75	24.36	0.00	-0.62	0.70	0.30	0.15	-0.23	0.00
17:00	25.77	25.39	25.02	24.66	24.30	23.94	23.69	0.00	-0.55	0.31	0.22	0.15	-0.08	0.00
18:00	18.08	18.82	19.52	20.23	20.94	21.64	22.14	0.00	-0.19	-0.64	-0.64	-0.29	-0.59	0.00
19:00	15.21	15.66	16.09	16.52	16.95	17.38	17.68	0.00	-0.01	-0.25	-0.36	-0.23	-0.24	0.00
20:00	12.58	13.23	13.84	14.45	15.07	15.69	16.12	0.00	0.34	0.45	0.47	0.61	0.33	0.00
21:00	11.16	12.03	12.86	13.69	14.53	15.36	15.95	0.00	0.25	0.17	-0.17	0.17	-0.04	0.00
22:00	9.43	10.30	11.13	11.96	12.80	13.63	14.22	0.00	-0.20	-0.82	-1.03	-0.48	-0.03	0.00
23:00	8.86	9.86	10.80	11.75	12.70	13.66	14.33	0.00	0.28	-0.18	-0.41	-0.18	-0.36	0.00

The deviations depicted in Table 2-5 indicate that the calculated T_a values compare well with the measured values. Some of the calculated values, displayed in Table 2-5 above, are plotted in Figure 2-21 to aid in displaying the similarity between the measured and calculated data and thus the accuracy of equation (2-3).

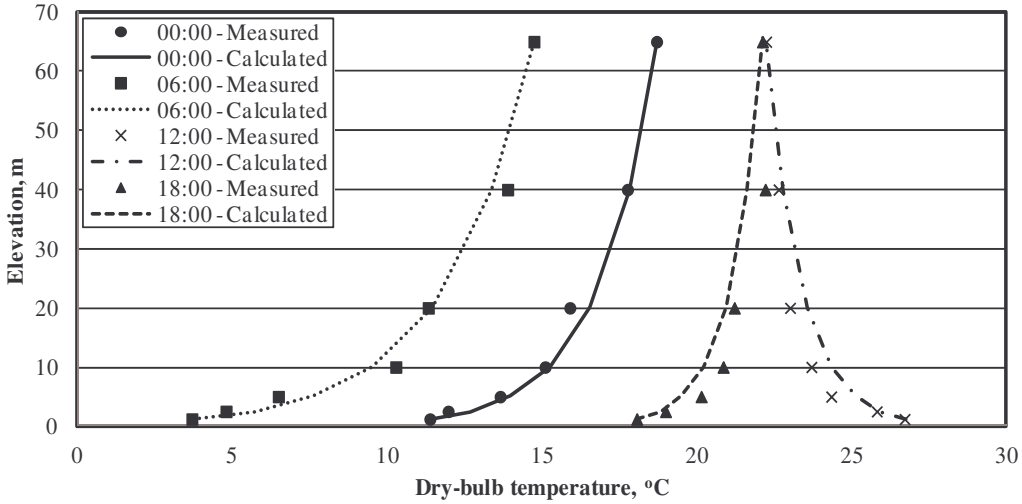

Figure 2-21: Measured and calculated T_a-profiles at Majuba Power Station for four different time periods – 2009/09/04.

In Figure 2-21 it is shown that the adiabatic lapse rates as well as the inversion lapses are correlated well with the use of equation (2-3). This is motivated by the deviations depicted in Table 2-5. These results indicate that the equation is suitable for calculating all T_a-profiles, as stated in section 2.2. This daily variation in b_T for 04/09/2009 is displayed in Figure 2-22.

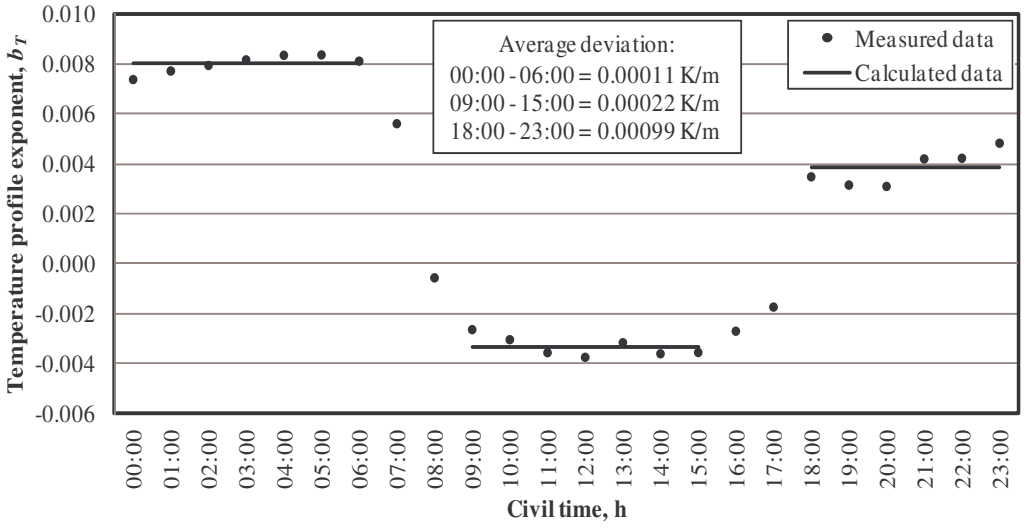

Figure 2-22: Variation in the calculated b_T at Majuba Power Station – 2009/09/04

The measured data depicted in Figure 2-22 indicates that b_T is relatively constant during nocturnal hours before sunrise (00:00 – 06:00). For this reason the exponent has been approximated by means of a single value for the period. This choice of approximation is motivated by the low average deviation depicted in Figure 2-22. Nocturnal hours after sunset (18:00 – 23:00) show a bigger scatter and is characterised by lower b_T-values, but are also approximated and motivated in a similar manner as explained above. The reason for the use of a single value is explained in section 2.5.2 and the reason for the difference between 00:00 and 23:00 can be attributed to the fact that this data only represents a single day. This means that a number of parameters such as V_W, RH, SR and T_a, will have an effect on the b_T. This applies to the two days prior and after the day discussed above as well.

The daytime b_T-values (09:00 – 15:00) are also approximated by means of a single value as shown in Figure 2-22. The approximation technique is again motivated with the average deviation, which is low.

The transition periods between the daytime and nocturnal hours are not approximated because these periods are not of interest. The reason for this is explained in section 3.5, where it is noted that a stable temperature lapse rate is required for NDWCT performance tests.

The average seasonal hourly variation in b_T provides a more stable approximation of the hourly variation in b_T. The averages minimise the effect of independent parameters, discussed in the previous paragraph, on b_T. The average values are determined by averaging the specific time intervals over the 4 different three-month periods explained in section 2.3.2.

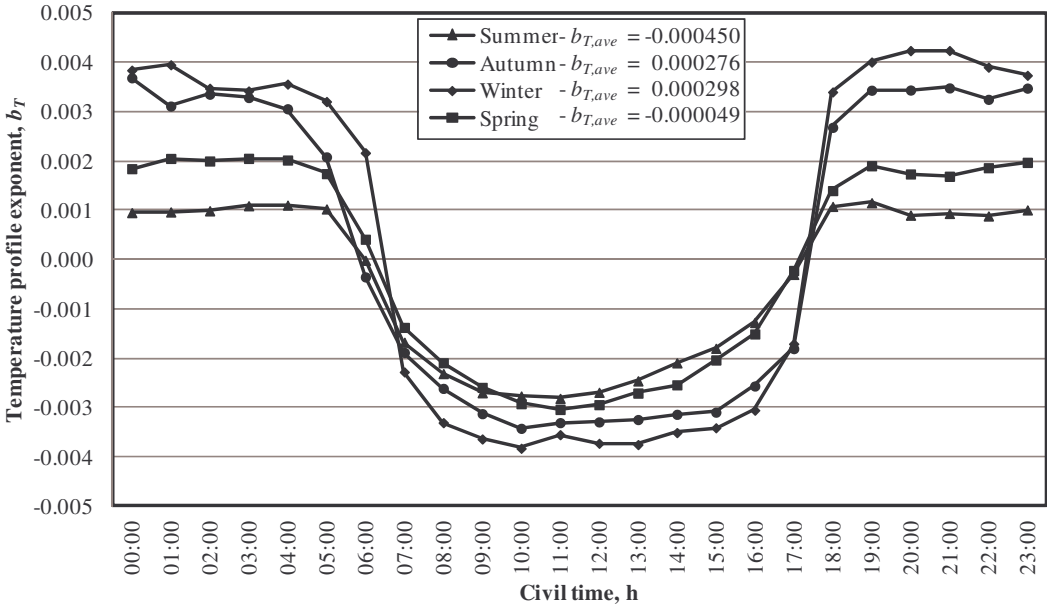

Figure 2-23: Measured hourly variation in b_T for the four seasons at Majuba Power Station.

Figure 2-23 depicts the hourly variation in the average b_T for the four seasons. This figure indicates that the daily variation in this exponent follows the same trend throughout the year. Summer is characterised by less intense temperature inversions before sunrise and after sunset compared to that of Winter. Summer months are also typified by more subdued adiabatic lapse rates after sunrise and before sunset compared to Winter. The measurements for Autumn and Spring depict the gradual decrease and increase in average values from Summer to Winter.

The hourly variation in the b_T for the four seasons can be approximated in two different sections by means of single values (Figure 2-24). More accurate approximations are possible, but for the purpose of this investigation the singular value approximation is sufficient. The use of single value approximations is motivated above and in section 3.5 below.

Figure 2-24 depicts the nocturnal (18:00 - 05:00) b_T singular value approximation for the four seasons as well as the daytime (08:00 - 15:00) b_T singular approximation values. The transition periods from 05:00 to 08:00 and 15:00 to 18:00 are not approximated, as motivated above. These single-value approximations provide the reader with a guide to daytime and night-time approximations for b_T throughout the year at Majuba Power Station.

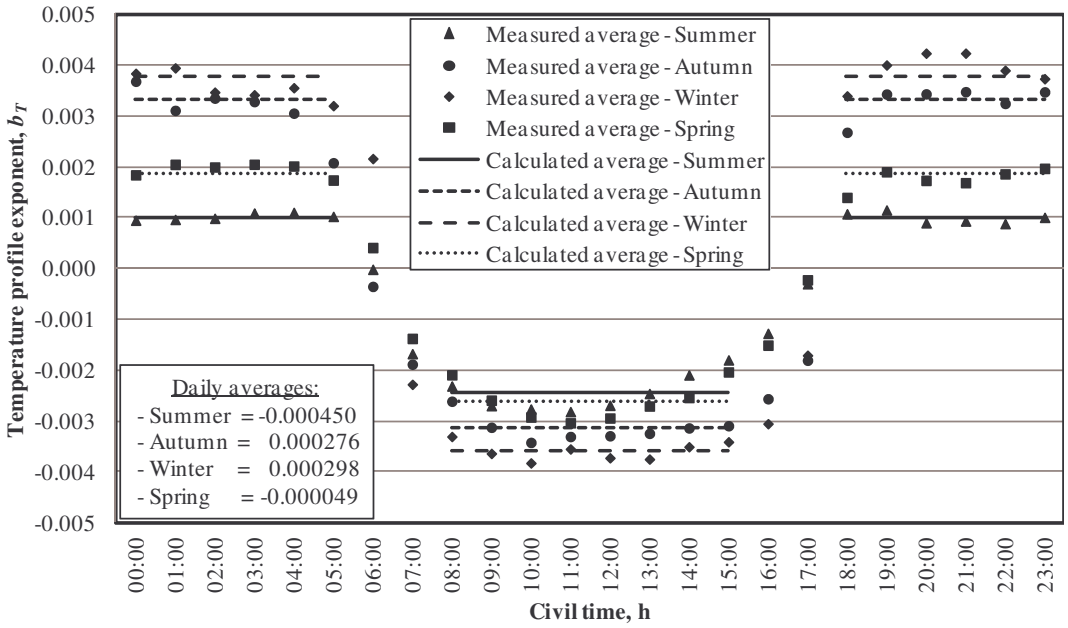

Figure 2-24: Measured hourly variation in b_T for the four seasons at Majuba Power Station with hourly approximations.

The calculated hourly variations in b_T during daytime and nocturnal hours as well as the daily averages for the four different seasons, depicted above, are provided in Table 2-6:

Table 2-6: Calculated b_T for the periods 08:00 – 15:00, 18:00 to 05:00 and the daily averages for the four seasons at Majuba Power Station.

Season	08:00 - 15:00	18:00 - 05:00	Daily average
Summer	-0.0024491	0.0010111	-0.0004461
Autumn	-0.0031473	0.0033196	0.0002760
Winter	-0.0035830	0.0037916	0.0002982
Spring	-0.0026019	0.0018598	-0.0000487

From Figure 2-23, Figure 2-24 and Table 2-6 it is found that the hourly variation in b_T also varies on an annual cycle. This is evident where b_T-values vary for specific time intervals during the different seasons. The annual variation in b_T is discussed in section 2.5.2 below.

2.5.2. Seasonal variation in temperature profiles at Majuba Power Station

The seasonal changes in the tilt of the Earth's rotational axis cause the atmospheric conditions to change, as explained in section 2.2.1. The b_T–values also changes on a seasonal basis. As shown by Kloppers (2003), this data should show a sinusoidal behaviour, depicted in Figure 2-25 below.

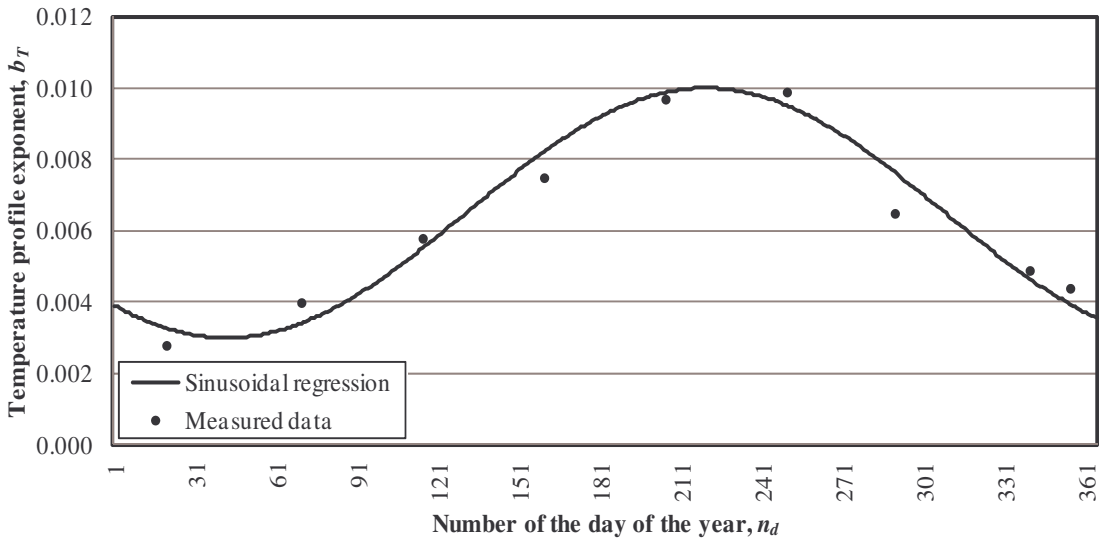

Figure 2-25: Annual variation in the average b_T from 19:00 to 07:00 at Lephalale (Kloppers, *et al.*, 2005).

Figure 2-25 illustrates that the annual variation in the average b_T during inversion periods, from 19:00 to 07:00, in Lephalale (Ellisras; S 23.6667°, E 27.78333°) can be approximated by means of a sinusoidal function of which the equation is as follows:

$$b_T = 0.0035\sin(0.0177n_d - 2.32392) + 0.0065 \quad \textbf{(2-9)}$$

From Figure 2-25 it is clear that strong inversions exist from 19:00 to 07:00 throughout the year. The lowest average value occurs between days 31 and 61, which is between January and February (Summer), whilst the largest average value occurs between days 211 and 241, which correspond to July and August (Winter). The data presented in Figure 2-25, however, focuses on the average value for the entire inversion period from 19:00 to 07:00. This increases the complexity of the data and makes the data unusable when focusing on the seasonal variation of a specific hourly b_T-value. This figure is thus only used to depict the general seasonal sinusoidal behaviour of b_T at Lephalale and should not be used otherwise.

The seasonal variation in b_T at Majuba is evaluated with specific time period seasonal variations. This reduces the complexity of the data and eliminates the errors that may occur when averaging b_T-values for a couple of hours during the day and month and evaluating the seasonal variation of these average values.

As result of atmospheric parameters that differ between the two locations, this annual variation in b_T at Majuba Power Station is not similar to the variation at Lephalale. Examples of differing parameters include T_a, RH, V_W, evapotranspiration, the albedo of vegetation or surface cover (Kloppers, 2003) and the use of specific time intervals and not average values as explained above.

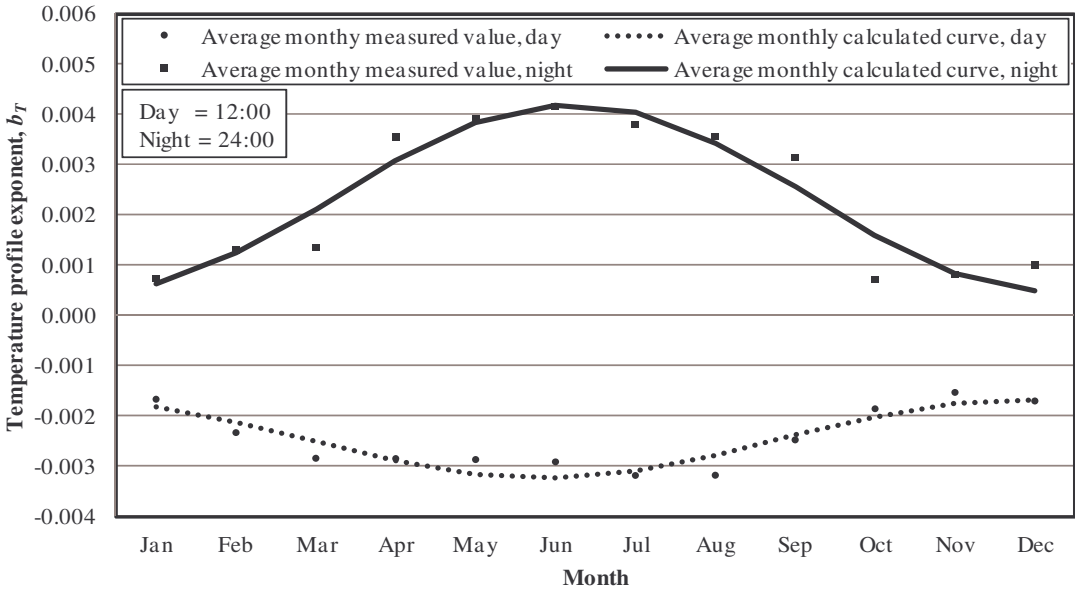

Figure 2-26: Monthly variation of b_T during daytime (12:00) and nocturnal hours (24:00) at Majuba Power Station.

Figure 2-26 depicts the monthly variation in the average b_T for two time periods (12:00 and 24:00) at Majuba Power Station. The date format used in Figure 2-25 has been replaced by the use of a monthly average values that are calculated by averaging the daily values for the specific time intervals for the different months.

These daily values are determined by using data loggers, as explained in section 2.3.2 above. These hourly-specific average values produce a more accurate representation of the monthly variation in b_T for specific time intervals. The annual daytime (12:00) monthly variation in b_T at Majuba Power Station is approximated with a sinusoidal regression curve with equation (2-10), where n_m is the number of the month:

$$b_T = -0.00077\sin(0.16667\pi \cdot n_m - 1.484) - 0.02452 \quad \textbf{(2-10)}$$

The equivalent nocturnal variation is approximated with equation (2-11):

$$b_T = -0.00185\sin(0.16667\pi \cdot n_m + 1.457) + 0.0023 \quad \textbf{(2-11)}$$

The above figures provide the reader with a method to quickly and effectively determine the daily and nocturnal b_T by either reading it straight from Figure 2-26 or by using the two equations above.

2.5.3. Daily and seasonal variation in T_a at Majuba Power Station

Figure 2-27 below presents the monthly variation in the average reference height T_a at Majuba Power Station. February (Summer) is characterised by the highest reference height T_a during daytime and nocturnal hours, while June is characterised by the lowest average T_a throughout the day.

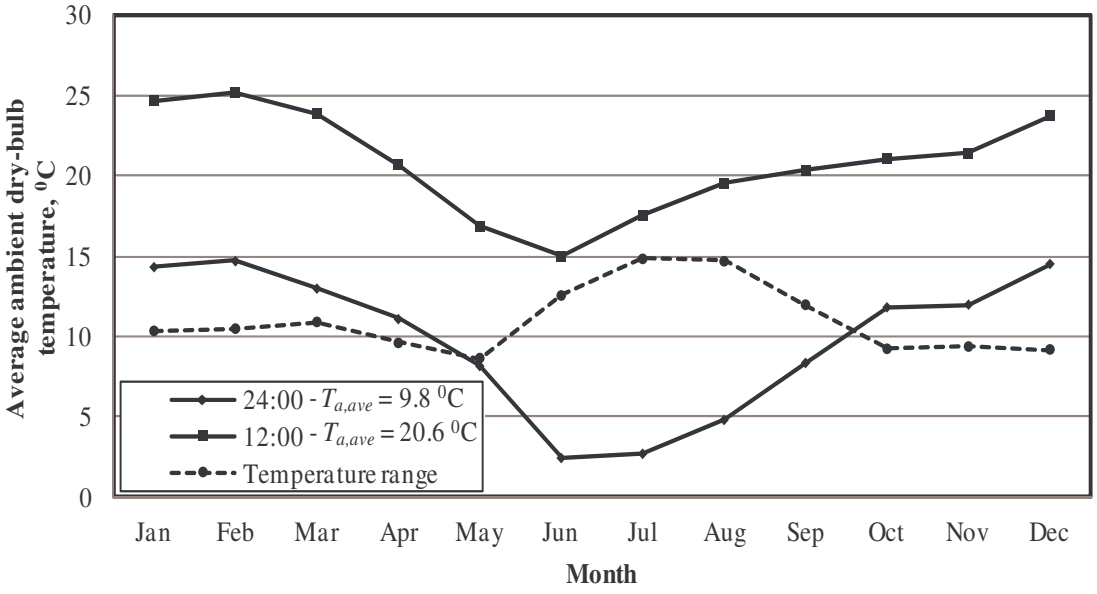

Figure 2-27: Monthly variation in the average reference height T_a at Majuba Power Station for 12:00 and 24:00.

During Summer, Autumn and Spring the difference between the average daytime and night time reference height T_a, or temperature range, remains relatively constant. The temperature range in Winter is, however, greater. Reasons for this phenomenon include the reduced amount of cloud cover during Winter compared to the other seasons, which increases the amount of reflective- and sky radiation (Winter is the dry season at Majuba Power Station). This is also evident in the monthly variation in the average reference height $T_{awb,}$ depicted in Figure 2-28.

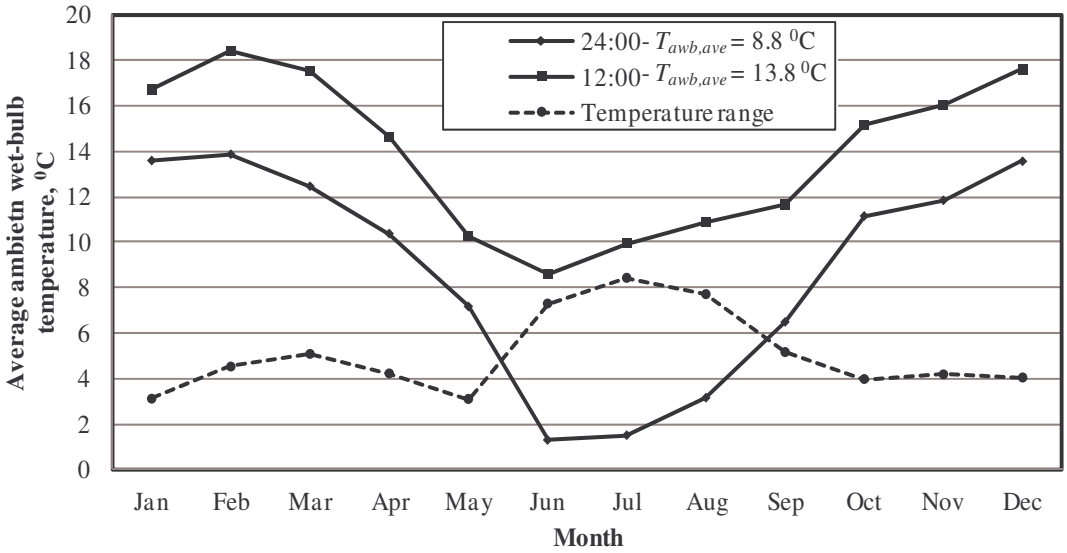

Figure 2-28: Monthly variation in the average reference height T_{awb} at Majuba Power Station for 12:00 and 24:00.

The transition between these two extremes of the T_a range is furthermore of interest. The average T_a measured at different heights during Summer at Majuba Power Station is displayed in Figure 2-29. The maximum average T_a of 24^{o}C occurs roughly between 12:00 and 13:00 at a height of 2.5 m, while the lowest average T_a of 14^{o}C is present approximately between 04:00 and 05:00 at 1.2 m height.

This data compares well with data presented by Lander (1991) for Eskom's Matimba- and Kendal power stations. The averages at Majuba Power Station are, however, much lower compared to the averages at Matimba power station in Lephalale because of the geographical location and the related atmospheric conditions.

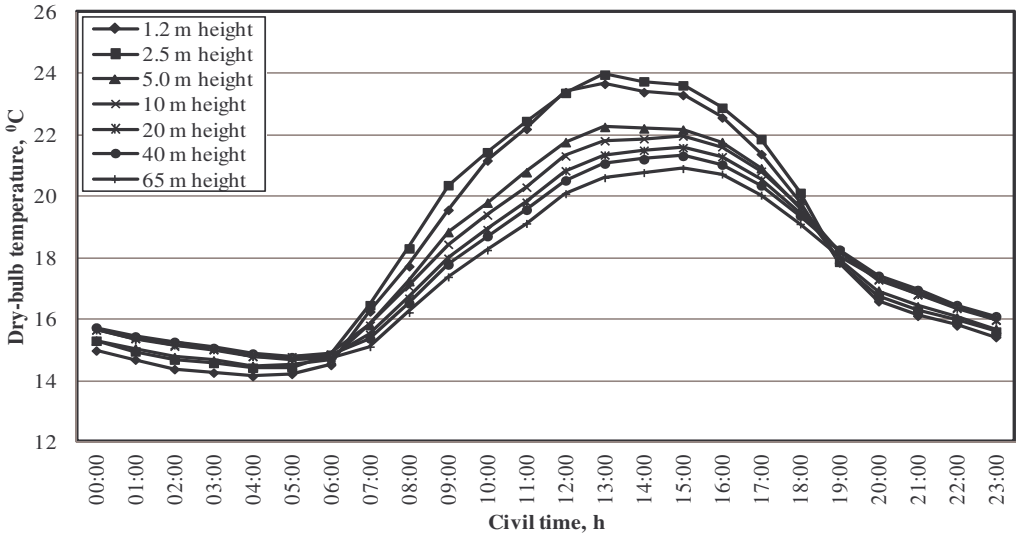

Figure 2-29: Average T_a measured at seven heights during Summer at Majuba Power Station.

A similar phenomenon to that present in Figure 2-20 is also present in Figure 2-29, where the temperature at 2.5 m is higher during the first few hours after sunrise compared to the corresponding temperature at 1.2 m. This uncommon phenomenon is partly attributed to the local layer of crusher stone surrounding the weather mast within the mast's fencing, and also to incorrect thermocouple readings. This equipment is calibrated yearly (appendix D) but tends to lose accuracy with time and can therefore produce incorrect readings. The layer of stone can be viewed in Figure 2-30. The layer of stone takes more time to be heated and cooled respectively compared to the surrounding soil. This substantiates the lower temperatures at 1.2 m height during the first few hours after sunrise.

Figure 2-30: Crusher stone local to Majuba Power Station's weather mast.

Figure 2-31 depicts the average T_a during Winter. The temperature profiles are found to be much more elaborate during nocturnal hours in Winter compared to Summer months (Figure 2-29), as shown above in Figure 2-26. Much larger temperature gradients and inversion layers are also present during sunrise times.

The reason for this is explained earlier in this section and in section 2.2.1. This data does, however, compare well to that of Lander (1991).

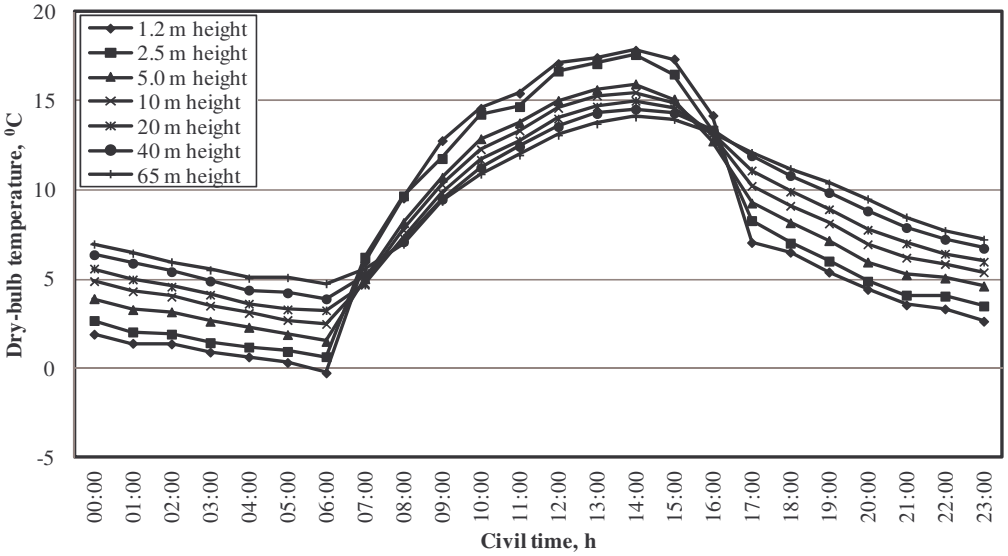

Figure 2-31: Average T_a at seven different heights during Winter at Majuba Power Station.

Although the nocturnal hour temperature distributions during Winter are much more pronounced compared with similar times in Summer (Figure 2-29), the daytime temperature distributions during Summer and Winter are found to be similar. This more pronounced temperature distribution during nocturnal hours in Winter substantiates the more distinct temperature range (Figure 2-27) during Winter, discussed above.

2.5.4. Seasonal variation in temperature inversion heights

Temperature inversions are accompanied by an inversion height (H_{inv}), which is explained in section 2.2.2 above. This height is dependent on T_a measured at 1.2 m AGL as well as b_T. A larger positive value for b_T will result in a thicker temperature inversion layer during windless conditions. NDWCTs draw their inlet air from an approximate height of half the tower's height, as stated by Kloppers & Kröger (2005), which is approximately 75 m for Majuba Power Station's NDWCT. Any inversion will naturally affect the potential driving force of the tower, but H_{inv}-values that are higher than this value from which the air is drawn into the tower will affect the driving force even more adversely. This is due to the increased average T_a across the air-inlet height. For this reason it is necessary to plot the annual variation in H_{inv}-values at Majuba Power Station to quantify the effect of these heights on the NDWCT effectiveness.

The monthly H_{inv}-values at Majuba Power Station are determined by using equation (2-6) following the process explained in Section 2.2.2. The average nocturnal (24:00) b_T expressed in Figure 2-26, together with the T_a measured at 1.2 m height, are used in the calculation of this height. The temperatures are collected at 24:00 in order to ensure that the inversion has formed completely to

ensure reliable results. Figure 2-32 depicts the results obtained from the inversion height calculations.

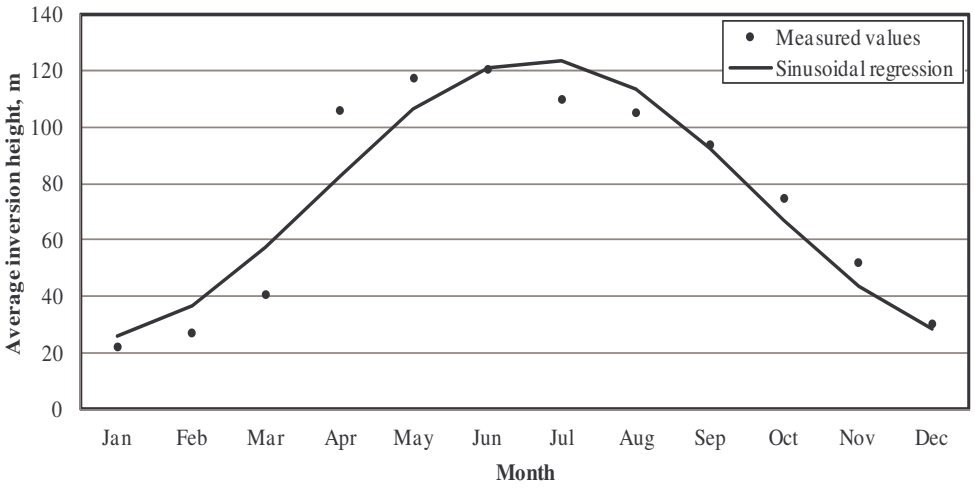

Figure 2-32: Annual variation in the inversion height at Majuba Power Station for 24:00.

Figure 2-32 indicates that the H_{inv}-values follow a sinusoidal trend relatively closely. H_{inv} increases from 25 m during the seasonal change from Summer to Autumn and thickens throughout Autumn to reach a peak value of 122 m in July (Winter). The layer subsides as the seasons change from Winter to Spring and reaches a minimum value in Summer, after which the cycle is repeated. Equation (2-12) represents the sinusoidal regression curve depicted in Figure 2-32:

$$H_{inv} = -49.44\sin(0.16667\pi \cdot n_m + 1.21) + 49.91 \quad \textbf{(2-12)}$$

With this correlation and Figure 2-32 it is possible to determine the average monthly H_{inv} at 24:00 at Majuba Power Station. This data is important to quantify the effect of varying H_{inv}-values on Majuba Power Station's NDWCT effectiveness. Winter months are expected to have a more adverse effect on the effectiveness of the NDWCTs due to the higher average H_{inv} compared to Summer.

2.6. HUMIDITY CHARACTERISTICS

Humidity profiles are imperative in quantifying the performance of a NDWCT, as explained in section 2.2.4 above. It is thus important to understand the variations in these profiles. In this section the researcher discusses the variations in *RH* as well as ω at Majuba Power Station. The only humidity measurement that is measured on the weather mast is the *RH* at 1.2 m, as explained in section 2.3.2. The ω at 1.2 m is, however, calculated and the humidity profiles are measured by means of the additionally installed data loggers discussed in section 2.3.2.

2.6.1. *RH* characteristics

The average hourly variation in the *RH* for the four seasons at Majuba Power Station is depicted in Figure 2-33.

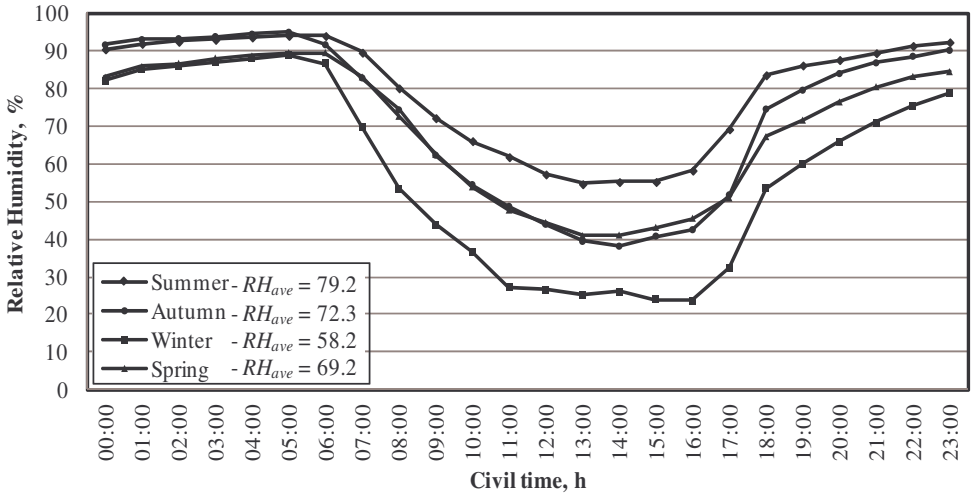

Figure 2-33: Average daily variation in *RH* measured at 1.2 m AGL for the four seasons at Majuba Power Station.

As is shown in Figure 2-33, the *RH* varies dramatically from day to day for the four seasons. Summer is characterised by the smallest variation in *RH* on a daily basis, with a maximum *RH* of 93 % occurring just before sunrise, between 05:00 and 06:00, and a minimum *RH* of 55 % occurring during the afternoon between 13:00 and 15:00. The average daily *RH* during Summer is 79.2 %, which is the highest average for the four seasons (Summer is the rainy season in this province).

Winter months are characterised by a much larger variation in *RH* on a daily basis as depicted in Figure 2-33 above. The maximum *RH* of 89 % occurs between 05:00 and 06:00 before sunrise, as is the case with Summer months. The minimum *RH* during Winter is 23 %, which occurs just before sunset. The daily *RH* average during Winter months amounts to 58.2 %, which is the lowest average for the four seasons (Winter being the dry season in this province).

Autumn and Spring months are characterised by fairly similar *RH* values throughout the day. The biggest difference between these two seasons occurs during nocturnal hours, when Autumn months have a slightly higher *RH* reading. From Figure 2-33 it is also clear that the variation in *RH* between the four seasons is much smaller during nocturnal hours than in daytime hours, especially during the last few hours before sunrise. This phenomenon is motivated by the following factors:

The *RH* during all four seasons is characterised by large gradients between sunrise and sunset. The most stable *RH* periods occur between 00:00 and 05:00 before sunrise - where the *RH* values for Summer and Autumn, and Winter and Spring

are essentially the same - and between 12:00 and 16:00 during the afternoon throughout the seasons.

It is also found that the *RH* drops significantly after sunrise and increases sharply shortly before sunset. This phenomenon is caused by the rate/ extent of evapotranspiration and the rate of the change in saturated air-vapour pressure, which is dependent on T_a AGL. As T_a increases after sunrise, the saturated air-vapour pressure of air increases, while evapotranspiration removes some of the moisture from the Earth's surface. This evapotranspiration is the most pronounced during this period, as explained in section 2.2.4. The rate of evapotranspiration is, however, lower than the rate of T_a increase and thus the rate of increase in the saturated air-vapour pressure, which leads to the decrease in *RH*.

The opposite scenario is evident in late afternoon, where evapotranspiration continues but the intensity of the vapour concentration slows down. During nocturnal hours radiative cooling causes dew formation and the subsequent extraction of water vapour from the atmosphere. The rate of evapotranspiration during this period is again slower than the rate of decrease in the saturated air-vapour pressure due to the decrease in T_a during these periods. This causes the sharp increase in *RH*.

This seasonal variation in the average *RH* for 24:00 and 12:00 is depicted in Figure 2-34. Nocturnal hours are found to be characterised by higher *RH* readings throughout the year compared to daytime hours, as explained above. The *RH* ranges from 29 % to 62 % during daytime hours throughout the year, whereas the nocturnal *RH* varies from 78 % to 94 %. Nocturnal hours are also characterised by smaller variations in *RH* throughout the year compared with daytime hours. This is caused by the smaller variation in T_a at 1.2 m AGL during nocturnal hours throughout the year compared to Summer (Figure 2-29 and Figure 2-31). This, together with the explanation of the rate of evapotranspiration relative to the saturated air-vapour pressure presented earlier, constitutes the smaller variations in *RH* during nocturnal hours.

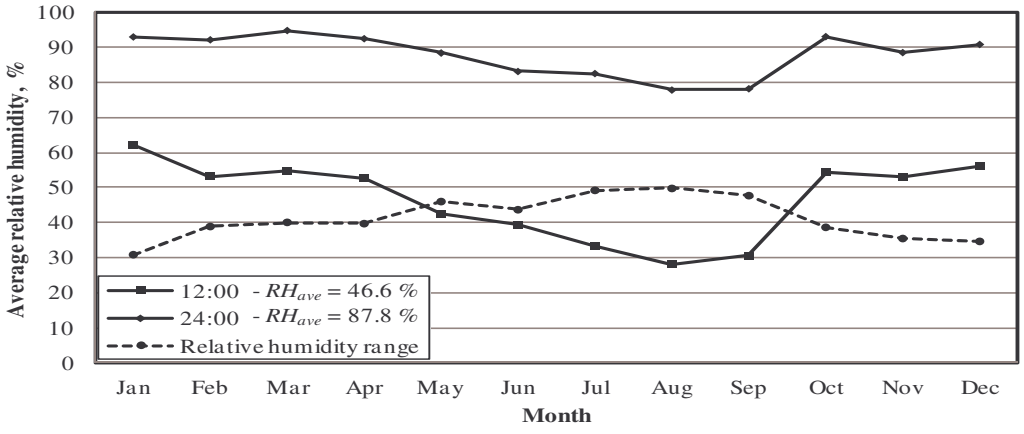

Figure 2-34: Monthly variation in the average reference height *RH* at Majuba Power Station for 12:00 and 24:00.

Summer months (December to February) are characterised by high *RH* readings on average during the daytime and nocturnal hours. The *RH* drops throughout Autumn to reach minimum values during Winter months. The *RH* increases dramatically during Spring to reach the Summer values explained above. It is, however, found that *RH* does not show a true reflection of the air's vapour content due to the dependence on T_a. It is thus required to evaluate ω.

2.6.2. ω characteristics

Figure 2-35 presents the average daily variation in the ω for different heights at Majuba Power Station for the period discussed in section 2.3.3.

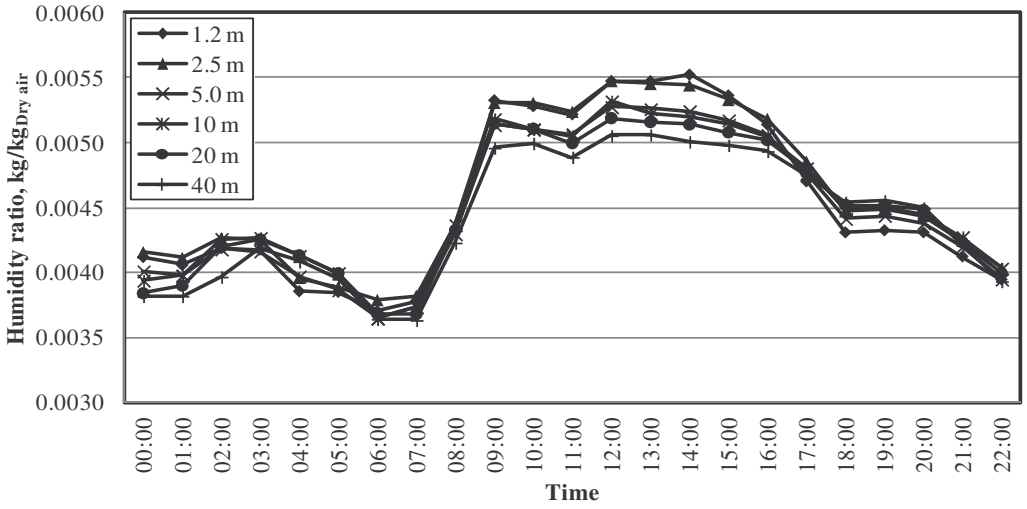

Figure 2-35: Average daily variation in ω at Majuba Power Station from 16 June 2011 – 28 June 2011.

Figure 2-35 makes it clear that the double wave effect discussed in section 2.2.4 is also present at Majuba Power Station. The ω also follows the same trend, as it increases sharply during early morning hours and *vice versa* during the afternoon, as discussed. This figure thus provides the reader with some insight into the daily variation in the ω for different heights, and also the means of validating the data with reference to literature.

Similarly to Figure 2-20, the average ω as a function of height is depicted in Figure 2-36. During early morning nocturnal hours it is noted that the ω remains relatively constant with increasing height. A small variation is noticeable below 10 m.

The reference height ω decreases from 00:00 to 05:00, as is depicted in Figure 2-35. During early morning hours around sunrise (between 07:00 and 11:00) the ω decreases slightly with height. The reference height ω increases until close to the afternoon (10:00), after which it decreases slightly to 12:00. It remains relatively constant thereafter and until 15:00, after which it decreases again. This relates well to the double wave effect depicted in Figure 2-35. During mid-day (from 12:00 to 15:00) the ω decreases with height.

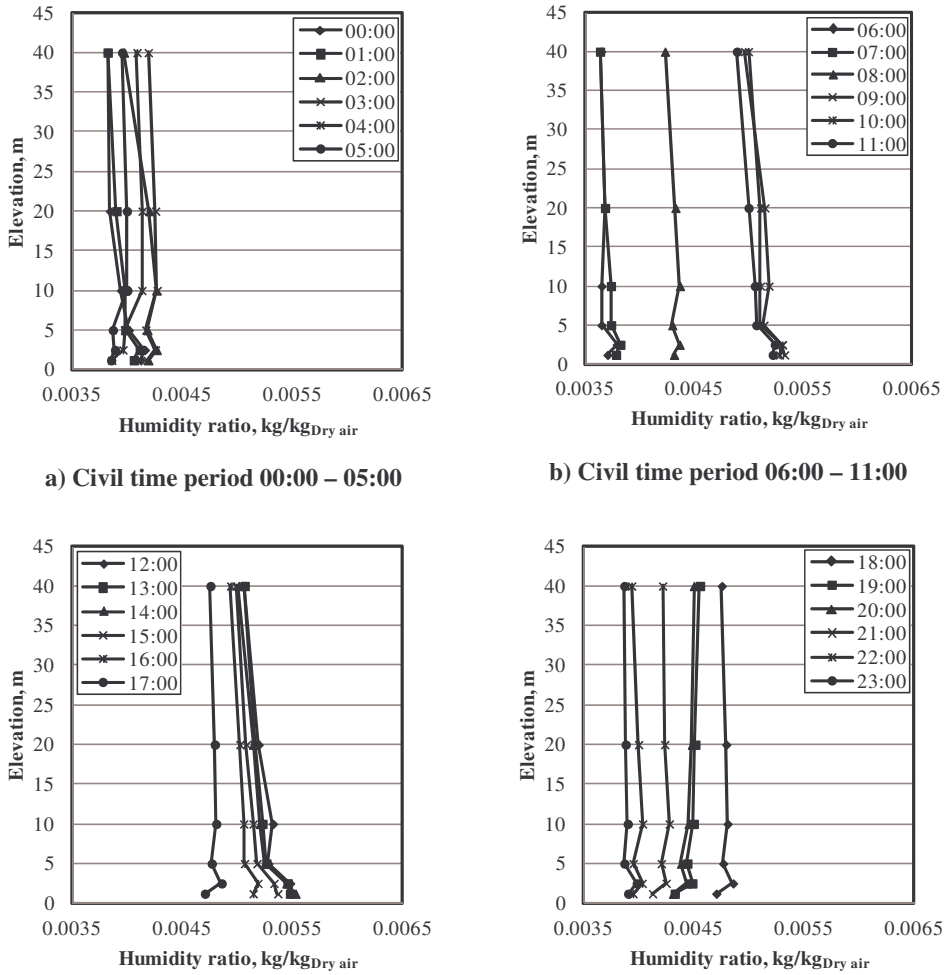

a) Civil time period 00:00 – 05:00

b) Civil time period 06:00 – 11:00

c) Civil time period 12:00 – 17:00

d) Civil time period 18:00 – 23:00

Figure 2-36: Average measured ω-profiles for different civil time intervals – 16/06/2011 – 28/06/2011.

After 15:00 the reference height ω decreases rapidly to 17:00, while it remains relatively constant with height. During sunset (17:00) the ω again tends to move/ migrate towards the constant state with height as explained above. The reference height ω decreases until 23:00. The explanation provided by Figure 2-35 and Figure 2-36 relates well to literature, as explained in section 2.2.4. These results will be used throughout this thesis and will be referenced accordingly.

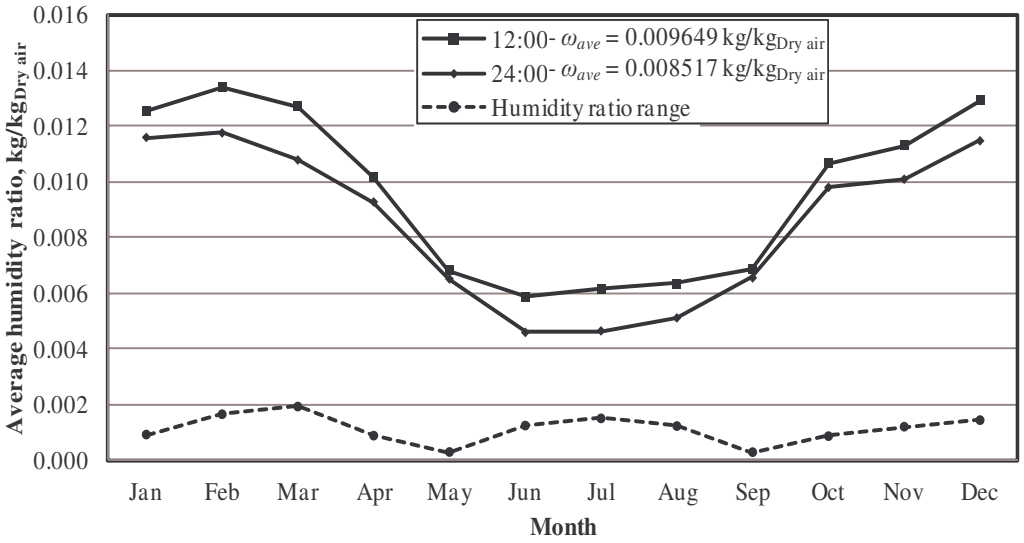

Figure 2-37: Monthly variation in the calculated average reference height ω at Majuba Power Station for 12:00 and 24:00.

Figure 2-37 depicts the monthly variation in the calculated ω during noon and midnight at Majuba Power Station. This figure indicates that the change in water vapour present in the air is small between noon and midnight throughout the year. The small difference that is present is caused by the evapotranspiration in the morning hours and the subsequent increase in vapour content in the air, as explained in section 2.2.4, together with the rate of dew formation during nocturnal hours.

The difference in daytime and night-time ω is found to change/vary slightly throughout the year. The months March and December are characterised by the largest difference between daytime and nocturnal hour ω, while May and September are characterised by very similar ω values throughout the day. Summer months are characterised by a larger variation between noon and midnight due to the increased rate of evapotranspiration during daytime compared to the rate of condensation at night; and Winter is also characterised by a large variation due to the increased rate of condensation (frost) compared to the rate of daytime evapotranspiration.

The end of Autumn (May) and the start of Spring are furthermore found to be characterised by very similar daytime and night-time ω due to the equilibrium between the rate of evapotranspiration and condensation. Figure 2-37 provides the reader with an effective means of approximating the average daytime (12:00) and nocturnal (24:00) ω throughout the year.

2.7. AMBIENT PRESSURE CHARACTERISTICS

The monthly variation in p_a at Majuba Power Station is depicted in Figure 2-38. In this figure the similarity between daytime and nocturnal hour p_a-values throughout the year is portrayed. It is, however, found that night-time hours have

a slightly higher p_a-value throughout. This is caused by the colder temperatures during these periods, which increases the density of air and therefore increases the atmospheric pressure at ground level.

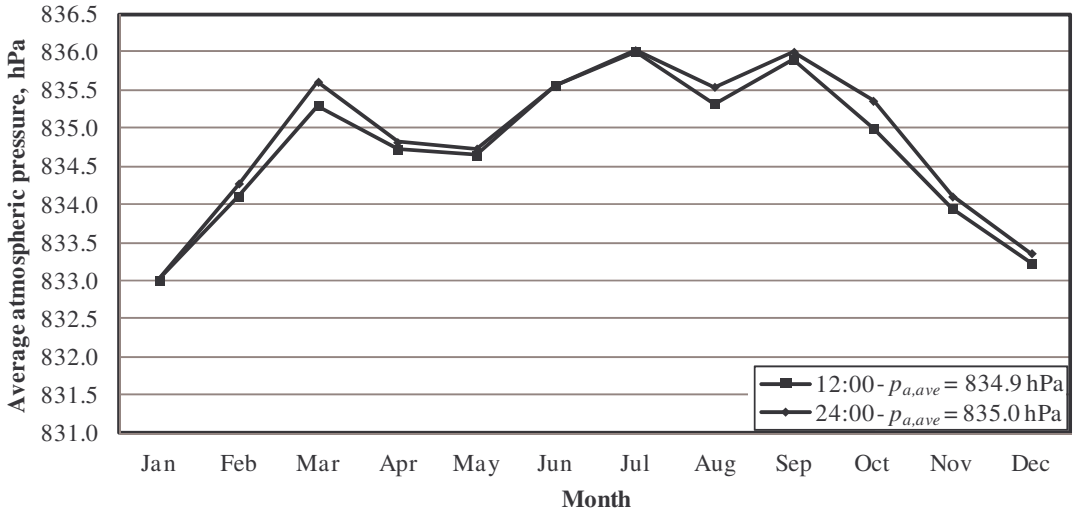

Figure 2-38: Monthly variation in the average reference height p_a at Majuba Power Station for 12:00 and 24:00

Summer months are characterised by the lowest average p_a due to the higher average T_a values. Similarly Winter months are characterised by the highest average atmospheric pressure due to the lower average T_a values during this period.

The variation in reference height p_a indicates that Majuba Power Station is characterised by variations between 833 hPa and 836 hPa on an annual basis. This information is used in section 4.3 where the influence of p_a on NDWCT effectiveness is discussed.

Due to the single installed p_a measurement device (section 2.3.2) it is not possible to determine the p_a profiles. These are, however, calculated where required by means of equation (2-13), presented by Kloppers & Kröger (2005):

$$p_{a1} - p_{az} = p_{a1}\left\{1 - \exp\left[-g \cdot z_1^{\,b_T} / \left\{(273.15 + T_1)R(1 - b_T)\right\} \cdot \left(z^{(1-b_T)} - z_1^{\,(1-b_T)}\right)\right]\right\} \quad \textbf{(2-13)}$$

2.8. WIND PROFILE CHARACTERISTICS

Wind profiles are dependent on, *inter alia*, V_W and D_W for specific locations. Other parameters that influence the wind profiles, including surface roughness and atmospheric stability, will not be addressed directly in this section, but do form an integral part of the following discussions as motivated in section 2.2.3.

The variation in V_W and D_W on an annual and seasonal basis at Majuba Power Station is discussed in this section after which the dependence of wind profiles with respect to these parameters is evaluated. The effect of V_W on b_W will be

discussed first, followed by a discussion of the effect of D_W on b_W. A discussion of the dependence of wind profiles to the daily hour and variation in the monthly average b_W for 12:00 and 24:00 concludes the section.

2.8.1. Annual and seasonal variation in V_W and D_W at Majuba Power Station

The variations in V_W and D_W at Majuba Power Station are imperative in understanding the effects of V_W and D_W on b_W. The variation in V_W and D_W is depicted by means of, amongst other things, wind roses using the software *Lakes Environmental's WRPlot*. It should be noted that, for this study, calm conditions ("calms") are characterised by reference height V_W values of less than 1 m/s and the term wind speed relates to the reference height V_W. The average annual distribution of V_W and D_W, which is averaged throughout the day and year, is plotted in Figure 2-39 below.

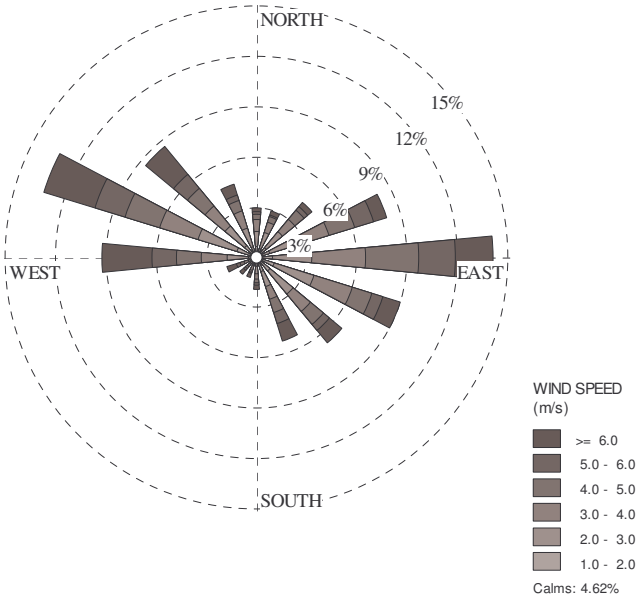

Figure 2-39: Annual distribution in V_W and D_W at Majuba Power Station.

In the above figure a dominant Easterly D_W is indicated, closely followed by a West-North-Westerly D_W. The latter D_W is characterised by the highest percentage of V_W values above 6 m/s. The South to South-West D_W is the least encountered annual D_W, whilst the annual amount of calm conditions amount to 4.62 %.

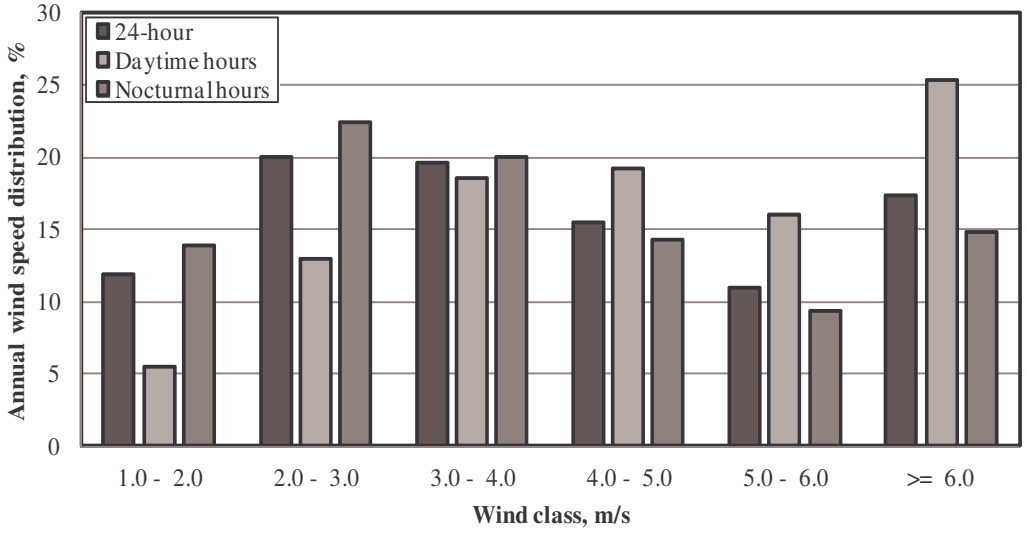

Figure 2-40: Annual reference height V_W-distribution at Majuba Power Station.

Figure 2-40 aids in examining the annual V_W distribution, which is not clear from the wind rose plot above. It depicts the annual daily, daytime and nocturnal hour distributions. Daytime hours are defined as 07h00 to 17h00 and nocturnal hours are defined as 18h00 to 06h00. The figure shows that V_W values between 2 and 4 m/s are most prevalent annually, followed by V_W values above 6 m/s. For V_W values below 4 m/s the daytime averages are lower than the equivalent nocturnal hours, but for V_W values above 4 m/s the daytime averages are higher. This entails that daytime hours are characterised by higher wind speeds on average and *vice versa* for nocturnal hours.

Throughout sections 2.8.1 to 2.8.5, the data and results are presented in terms of the four seasons (Summer, Autumn, Winter and Spring). This data is also presented in terms of daily as well as nocturnal hours to investigate the variation in b_W for these two periods. It is essential to understand the variations in the V_W and D_W for these periods in order to understand the b_W results. The average V_W values for the various periods discussed above are depicted in Table 2-7 below.

Table 2-7: Annual and seasonal average V_W-values at Majuba Power Station for daily, daytime and nocturnal hours.

Average wind speed, m/s	Annual	Summer	Autumn	Winter	Spring
24-hour day	3.74	4.1	3.61	3.6	4.38
Daytime	4.65	4.64	4.14	4.32	5.32
Nocturnal hours	3.29	3.55	3.07	2.88	3.41

It is found from the above results (Table 2-7) that Spring is characterised by the highest daily V_W values on average. The daytime hours during Spring largely contributes to the high daily average. Winter is characterised by the lowest average V_W but is closely followed by Autumn. These two seasons have very

similar average V_W-values during daytime and nocturnal hours. Daytime in Summer is characterised by V_W-values during daytime and nocturnal hours that are very similar to the overall annual daytime V_W.

The percentage calm conditions for the various seasons are depicted in Table 2-8. It is found that Autumn and Winter have very similar calm condition percentages. Winter is, however, characterised by the calmest conditions during a full day. Spring is characterised by the least amount of calm days, closely followed by Summer.

Table 2-8: Annual and seasonal calm conditions at Majuba Power Station for daily, daytime and nocturnal hours.

Average calms, %	Annual	Summer	Autumn	Winter	Spring
24-hour day	4.62	1.63	9.22	9.42	0.98
Daytime	2.5	0.54	5.44	5.52	0.32
Nocturnal hours	6.74	2.72	12.98	13.29	1.66

The variation in V_W and D_W during the four seasons for daytime and nocturnal hours is depicted in Figure 2-41 and Figure 2-42 respectively. The daytime variation shows that the prevailing D_W during Summer months is West-North-West, which is close to the D_W that is characterised by the highest V_W, which is North-West. The South-South-Westerly D_W is the least popular D_W during daytime hours in Summer.

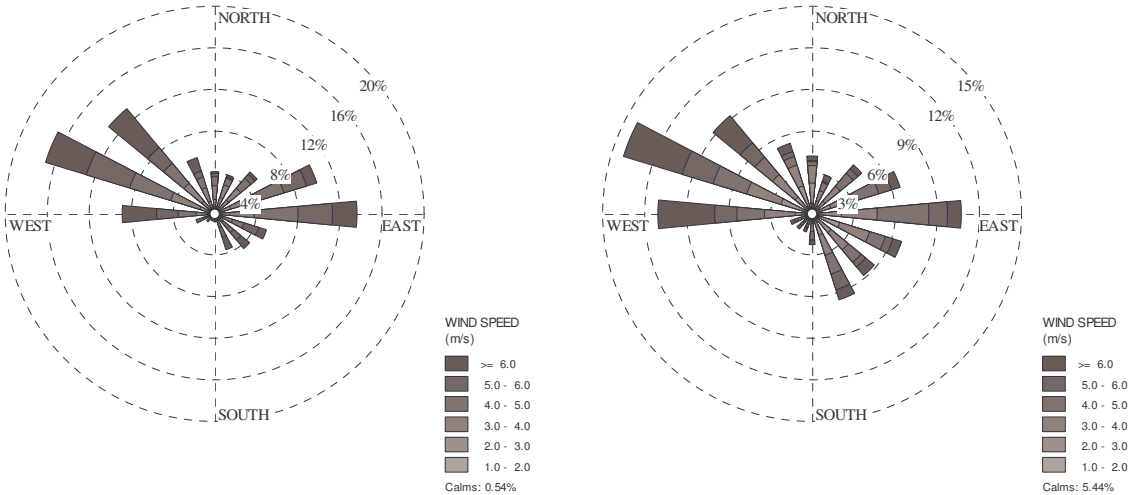

a) Summer **b) Autumn**

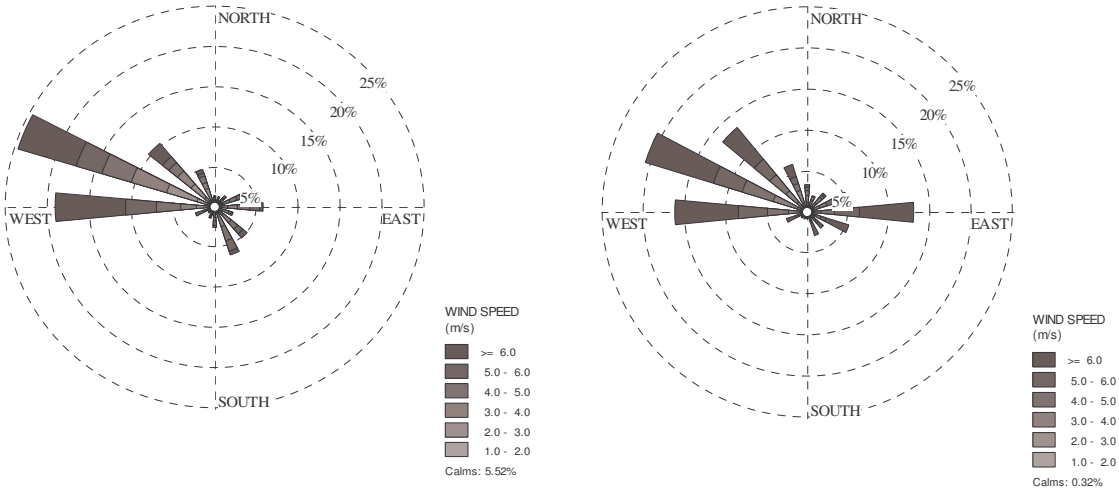

c) Winter **d) Spring**

Figure 2-41: Distribution of V_W and D_W during daytime hours at Majuba Power Station for the four seasons

The nocturnal variation during Summer, depicted in Figure 2-42 (a), indicates a dominant Easterly D_W that is also characterised by the largest amount of high V_W values. The least-preferred D_W during these periods is again South-South-West, as is the case with the annual results depicted in Figure 2-39. Figure 2-41 (a) and Figure 2-42 (a) indicate that the dominant D_W changes approximately 180° on average from daytime to nocturnal hours during Summer months at Majuba Power Station.

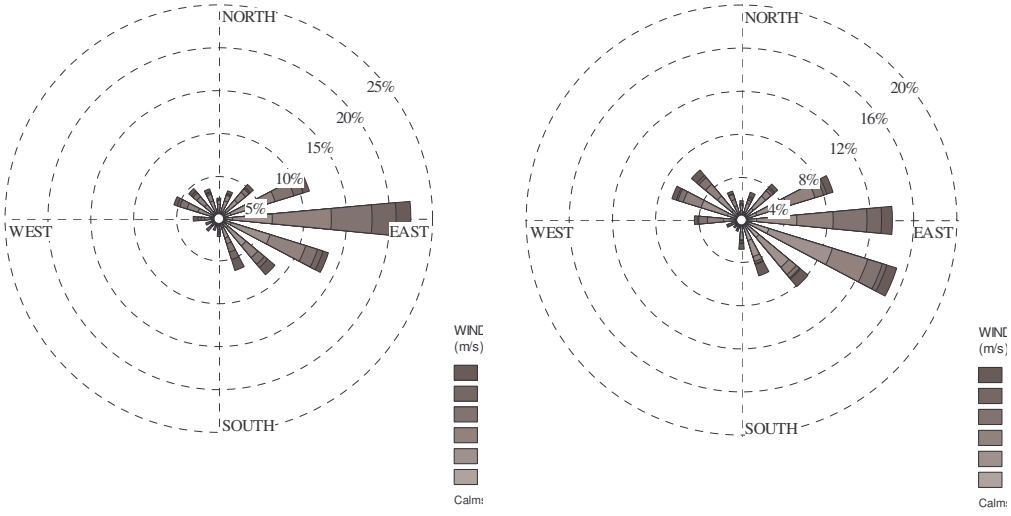

a) Summer **b) Autumn**

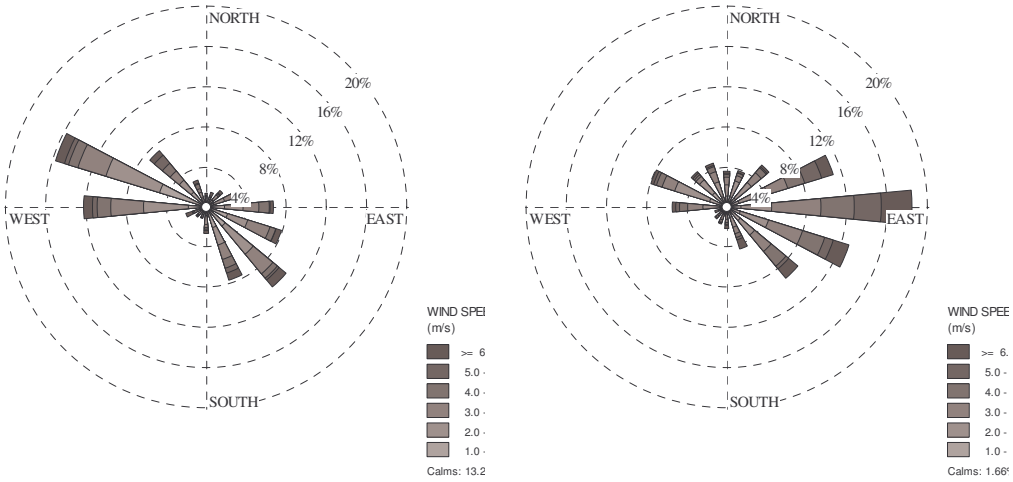

c) Winter **d) Spring**

Figure 2-42: Distribution of V_W and D_W for nocturnal hours at Majuba Power Station for the four seasons

The V_W-distribution for Summer at Majuba Power Station is depicted in Figure 2-43. This figure indicates very similar trends to the annual variation depicted in Figure 2-40. Summer months are, however, characterised by a smaller percentage of high V_W-values (above 6 m/s) during daytime compared to the annual average, and more V_W-values distributed between 4 and 6 m/s.

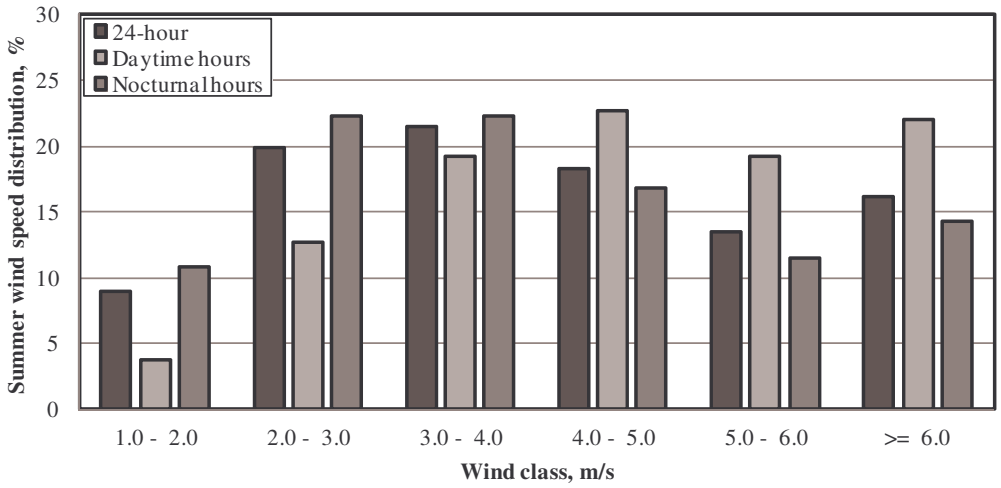

Figure 2-43: Reference height V_W-distribution during Summer at Majuba Power Station.

Figure 2-41 (b) and Figure 2-42 (b) represent the variation in V_W and D_W during Autumn. As is the case during daytime hours in Summer, Figure 2-41 (b) shows a dominant West-North-Westerly D_W during daytime hours in Autumn that is also characterised by the highest percentage of high V_W-values. It is, however, found

that a South-Easterly D_W is more prevalent during Autumn compared to the same times/periods in Summer.

The nocturnal variation in V_W and D_W during Autumn depicted in Figure 2-42 (b) indicates a dominant East-South-Easterly D_W, as is the case with Summer (Figure 2-42) (a), but is characterised by lower V_W-values on average and a higher percentage of calm conditions compared to similar times during Summer months (Table 2-7).

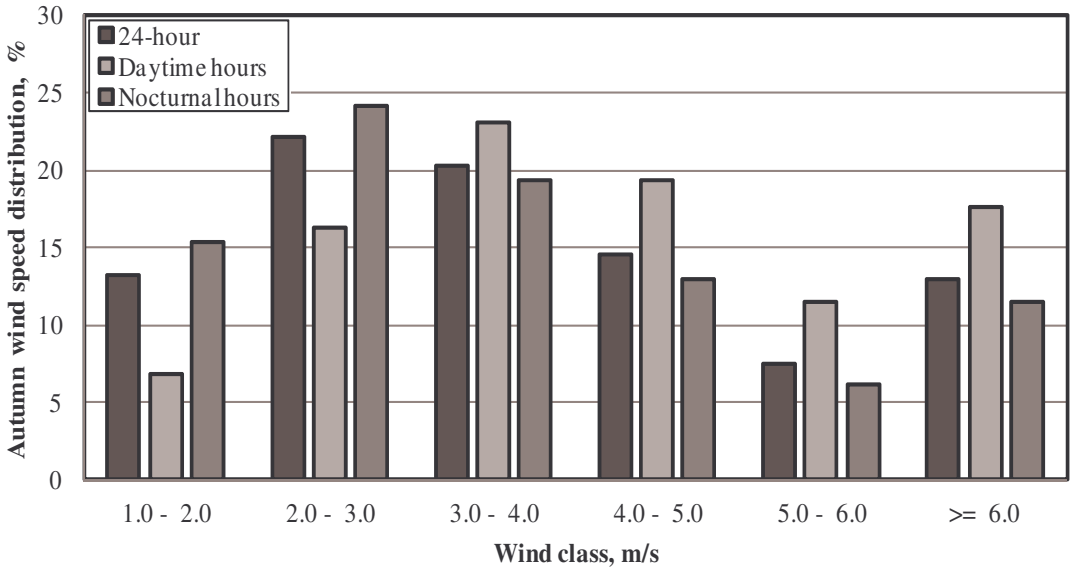

Figure 2-44: Reference height V_W-distribution during Autumn at Majuba Power Station.

Autumn is characterised by a lower percentage of high V_W-values than Summer, but follows a similar trend to the annual and Summer V_W-distributions (Figure 2-40 and Figure 2-43). In the latter, lower annual average V_W-values (below 3 m/s) are characterised by higher V_W-values during nocturnal hours compared to daytime hours, and *vice versa* for high annual average V_W-values.

Winter months are characterised by variations in V_W and D_W as depicted in Figure 2-41 (c) and Figure 2-42 (c) for daytime and nocturnal hours respectively. The daytime hours are frequented by a dominant West-North-Westerly D_W, which is also the direction that is typified by the highest V_W. Nocturnal hours during Winter show a dominant West-North-Westerly D_W in Figure 2-42 (c). This D_W is also characterised by the highest V_W values on average. Contrary to the results for Summer and Autumn, the dominant D_W during daytime and nocturnal hours in Winter remains in the same quadrant and does not shift 180°.

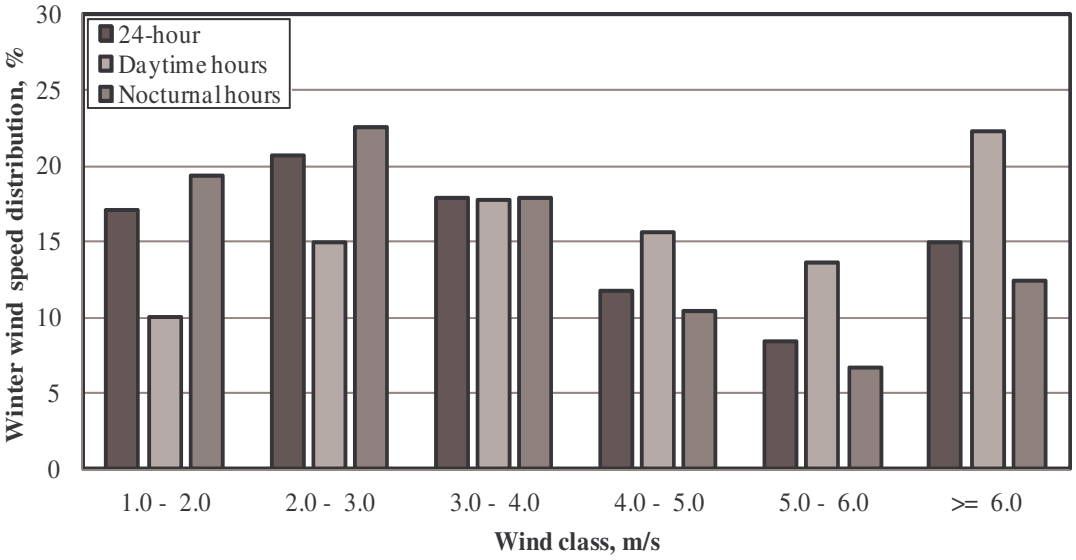

Figure 2-45: Reference height V_W-distribution during Winter at Majuba Power Station.

The V_W-distribution during Winter is depicted in Figure 2-45. The figure shows similar trends than the V_W-distribution figures for Summer and Autumn (Figure 2-43 and Figure 2-44). Winter is, however, characterised by a higher percentage of V_W-values between 1 to 2 m/s compared to Summer and Autumn, as well as a higher percentage of V_W-values above 6 m/s compared to Summer.

The variation in V_W and D_W for Spring at Majuba Power Station is depicted in Figure 2-41 (d) and Figure 2-42 (d).The daytime variation during Spring shows a dominant West-North-Westerly D_W that is also the D_W possessing the highest average V_W values. This period is characterised by very few calm conditions, amounting to 0.32 %, and is characterised by the least daytime calms throughout the year.

It is found that the dominant D_W is East during nocturnal hours, which is also the D_W that is characterised by the highest average V_W-values. The amount of calms during this period amounts to 1.66 %, which is the least amount of calms during nocturnal hours throughout the year. This indicates that Spring at Majuba Power Station is characterised by continuous winds and no extended periods of calm conditions.

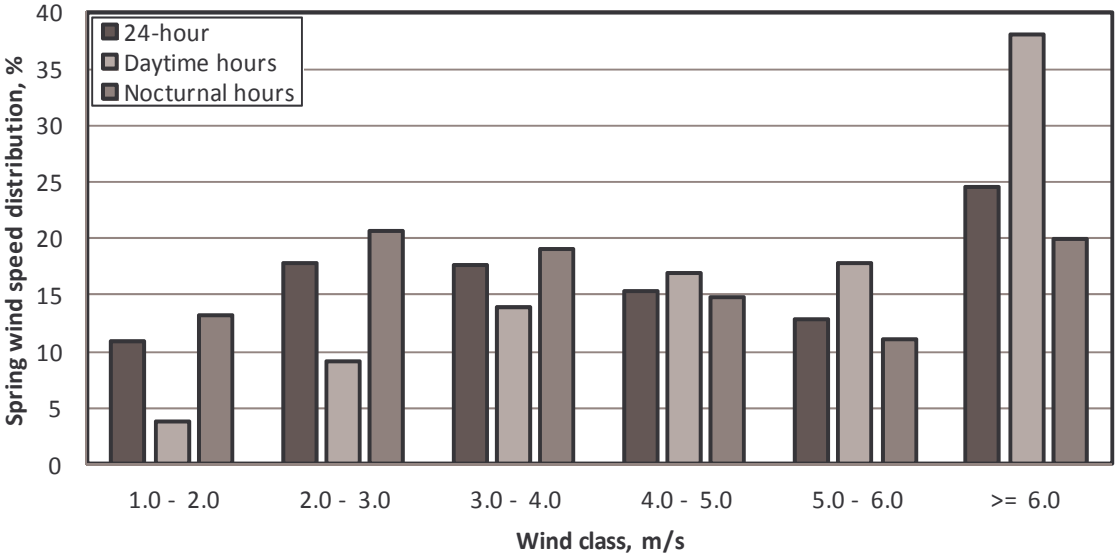

Figure 2-46: Reference height V_W-distribution during Spring at Majuba Power Station.

Spring's V_W-distribution, depicted in Figure 2-46, shows a similar trend than the other seasons, except that daytime hours are characterised by approximately 38 % V_W-values above 6 m/s. The seasonal results depicted Figure 2-40 and Figure 2-41 indicate that daytime hours are characterised by a dominant D_W in the North-West quadrant, whereas nocturnal hours are characterised by a dominant Easterly D_W, with the exception of Winter. These characteristics indicate that the two dominant D_W-values depicted in the annual variation in Figure 2-39 are associated with daytime and nocturnal hours respectively.

2.8.2. The effect of V_W on wind profiles

The V_W-values measured at different heights at Majuba Power Station's weather mast are used to determine and quantify its effect on b_W. The reference height V_W-values used for the analysis are divided into different intervals for which the wind profiles are determined. The data is gathered throughout the day and is therefore not limited to a specific time of the day. All data falling within a specific speed range are then averaged and scaled to provide a comparable average wind profile for the specific V_W-range.

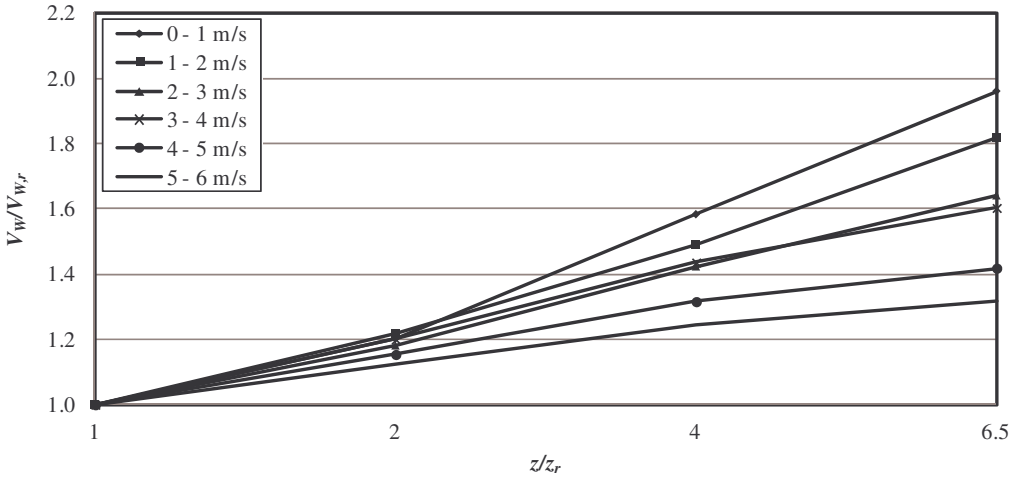

Figure 2-47: Wind profiles for V_W values up to 6 m/s at Majuba Power Station.

In Figure 2-47 the wind profiles for V_W values up to 6 m/s are depicted. The wind profiles are found to be much steeper at lower reference height V_W-values. As the reference height V_W increases, the wind profiles flatten out. The reason for this is that the effect of surface roughness on the wind profile is more pronounced at lower reference height V_W values, whereas it has a smaller influence when the reference height V_W increases.

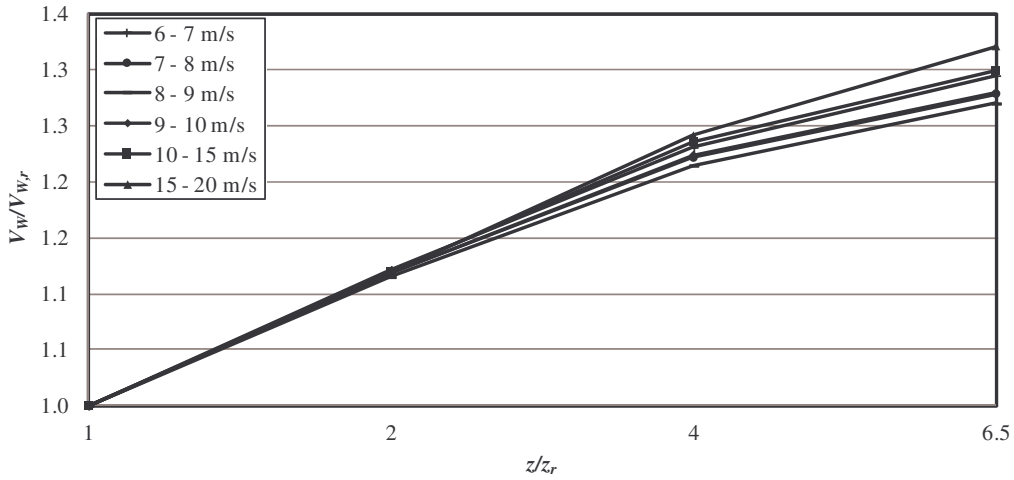

Figure 2-48: Wind profiles for V_W values from 6 m/s to 20 m/s at Majuba Power Station.

The results for V_W-values above 6 m/s are presented in Figure 2-48, which shows that the wind profiles are very similar across the range. It is again evident that the surface roughness has a smaller effect at these higher reference height V_W-values.

The measured results displayed in the two previous figures are approximated by means of equation (2-7) in order to obtain b_W. Solving this equation involves minimising the error between the measured and calculated V_W-values at different

heights, as explained in section 2.3.2 above. The optimisation strategy that is used is the Newton search method (Vanderplaats, 2007).

Table 2-9: Measured and calculated wind profiles with the accompanying deviation for different reference height V_W-ranges at Majuba Power Station.

Wind Speed	Measured $V_W/V_{W,r}$				Calculated $V_W/V_{W,r}$				Deviation			
(m/s)	$z/z_r = 1$	$z/z_r = 2$	$z/z_r = 4$	$z/z_r = 6.6$	$z/z_r = 1$	$z/z_r = 2$	$z/z_r = 4$	$z/z_r = 6.6$	$z/z_r = 1$	$z/z_r = 2$	$z/z_r = 4$	$z/z_r = 6.6$
0 - 1	1.00	1.20	1.58	1.96	1.00	1.28	1.65	1.96	0.00	-0.08	-0.06	0.00
1 - 2	1.00	1.22	1.49	1.82	1.00	1.25	1.56	1.82	0.00	-0.03	-0.07	0.00
2 - 3	1.00	1.18	1.42	1.64	1.00	1.20	1.44	1.64	0.00	-0.02	-0.02	0.00
3 - 4	1.00	1.20	1.44	1.60	1.00	1.19	1.42	1.60	0.00	0.01	0.02	0.00
4 - 5	1.00	1.15	1.32	1.42	1.00	1.14	1.30	1.42	0.00	0.02	0.02	0.00
5 - 6	1.00	1.12	1.24	1.32	1.00	1.11	1.23	1.32	0.00	0.02	0.01	0.00
6 - 7	1.00	1.12	1.23	1.30	1.00	1.11	1.23	1.32	0.00	0.01	0.00	-0.03
7 - 8	1.00	1.12	1.22	1.28	1.00	1.11	1.22	1.31	0.00	0.01	0.00	-0.03
8 - 9	1.00	1.12	1.21	1.27	1.00	1.10	1.21	1.30	0.00	0.01	0.00	-0.03
9 - 10	1.00	1.12	1.22	1.28	1.00	1.11	1.22	1.31	0.00	0.01	0.00	-0.03
10 - 15	1.00	1.12	1.24	1.30	1.00	1.11	1.23	1.32	0.00	0.01	0.01	-0.02
15 - 20	1.00	1.12	1.24	1.32	1.00	1.11	1.23	1.32	0.00	0.01	0.01	0.00

The results for the solved wind profiles are displayed in Table 2-9 with the measured wind profiles and the deviation between the measured and calculated values. The deviations between the measured and calculated values are found to be small throughout the range of reference height V_W-values, indicating that the optimised b_W is in fact correct.

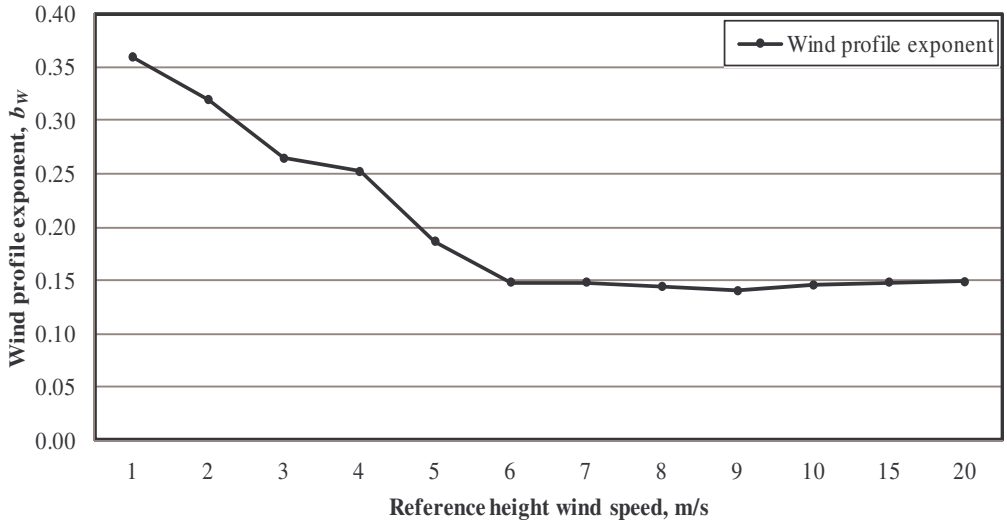

Figure 2-49: b_W-values for differing reference height V_W values at Majuba Power Station.

The b_W-values that correspond to the calculated wind profiles, depicted in Table 2-9 above, are plotted in Figure 2-49. This figure shows an initially high b_W, corresponding to the originally steep wind profile. The b_W-value decreases with increasing V_W values and flattens at 6 m/s. The b_W-value follows the 7th power law (section 2.2.3) for reference V_W-values higher than or equal to 6 m/s. Reference

height V_W-values lower than 6 m/s are characterised by an approximately linear increase in b_W up to a value close to 0.36 at 1 m/s V_W. b_W (at Majuba Power Station) can thus be characterised by means of a step function across the entire range of reference height V_W-values as follows:

$$\begin{aligned} b_W &= -0.041 \cdot V_W + 0.401 && V_W \leq 6 \ m/s \\ b_W &= 0.15 && V_W \geq 6 \ m/s \end{aligned} \qquad \textbf{(2-14)}$$

The trend of the annual average hourly b_W as a function of reference height V_W Majuba Power Station is depicted in Figure 2-50. Daytime b_W-values are found to be much more bunched for differing V_W-values. This is motivated by the higher average reference height V_W values during daytime hours and the relatively similar values in (Table 2-7). It is also found that b_W is rather erratic and much higher during nocturnal hours because of the lower average reference height V_W during nocturnal hours throughout the seasons (Table 2-7). Winter, which is characterised by the lowest annual average reference height V_W (Table 2-7) during nocturnal hours, has the highest nocturnal b_W. Summer and Spring, on the other hand, have higher annual average nocturnal reference height V_W-values with consequent lower nocturnal b_W-values.

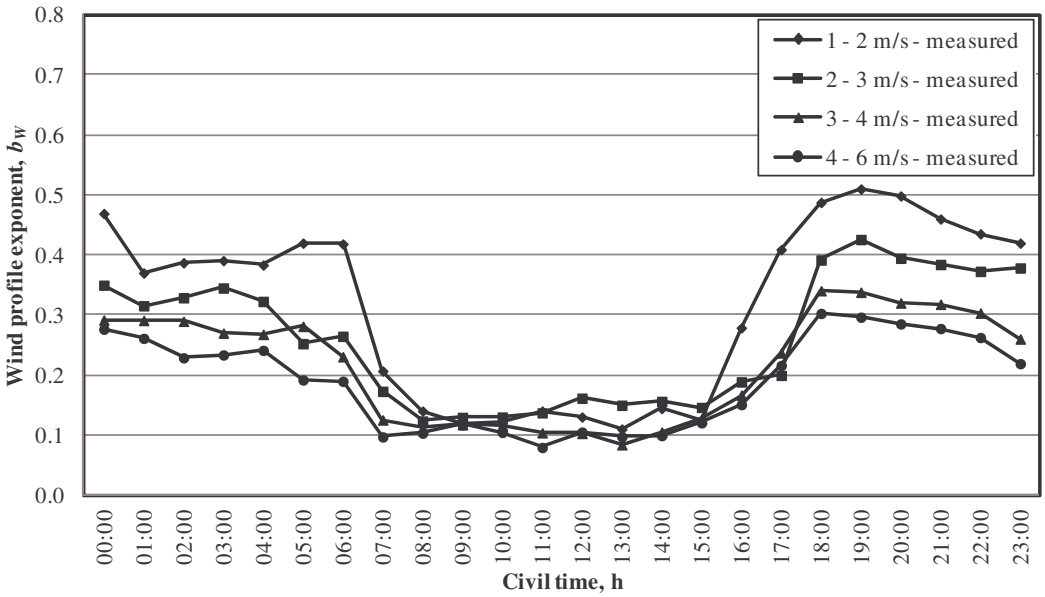

Figure 2-50: Variation in the hourly b_W for different reference height V_W-ranges at Majuba Power Station.

The daytime hour trends, from 07:00 to 15:00, are very stable and for this reason these trends are approximated by means of a single value. These values are provided in Table 2-10.

Table 2-10: Average b_W-values at Majuba Power Station for different reference height V_W values between 07:00 and 15:00.

Wind speed	07:00 to 15:00
1 - 2 m/s	0.14
2 - 3 m/s	0.15
3 - 4 m/s	0.11
4 - 6 m/s	0.10

2.8.3. The effect of D_W on wind profiles

The change in wind profiles for differing D_W values is plotted in Figure 2-51 and Figure 2-52.

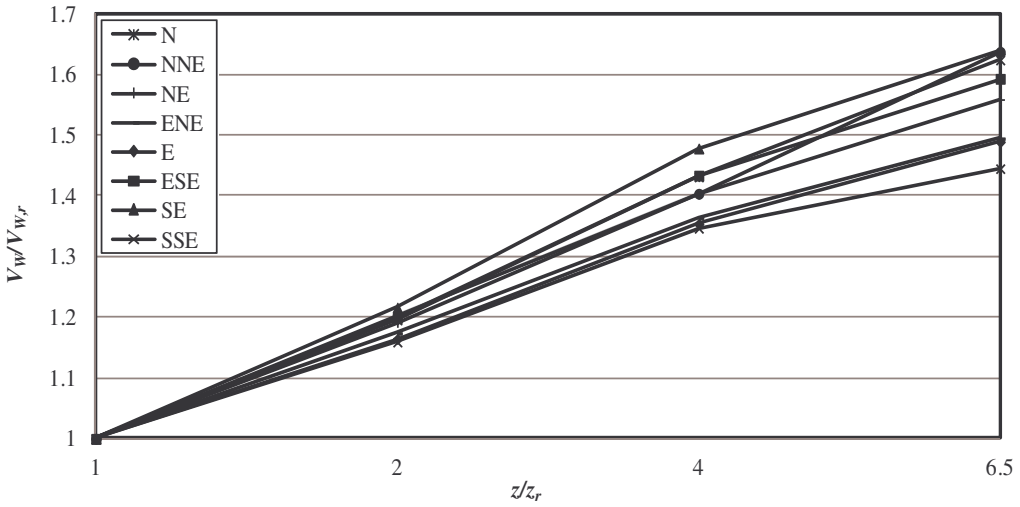

Figure 2-51: Wind profiles for different D_W-values, N – SSE, at Majuba Power Station.

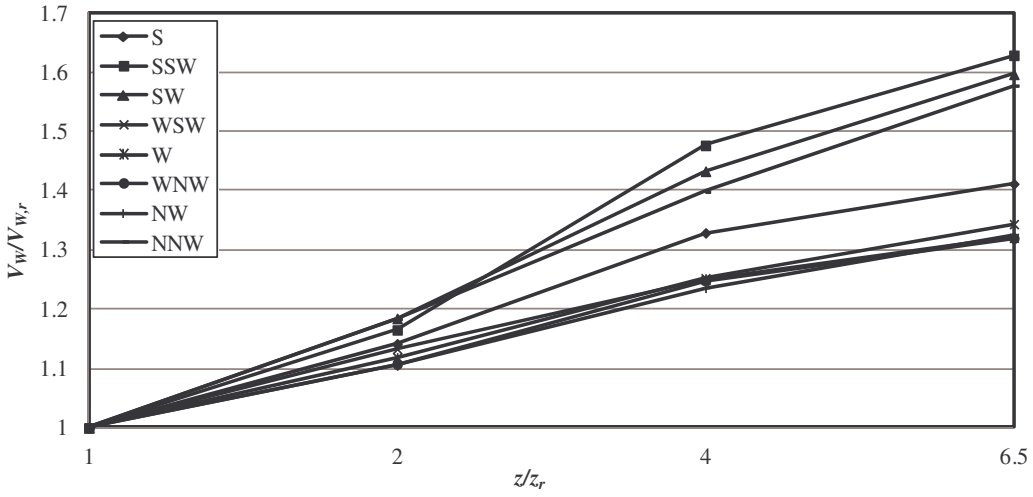

Figure 2-52: Wind profiles for different D_W-values, S – NNW, at Majuba Power Station.

Figure 2-51 depicts the profiles for D_W-values differing from a Northerly D_W to a South-South Easterly D_W, while Figure 2-52 depicts the profiles for the other D_W-values.

From the results displayed in these two figures it is found that the wind profiles do not change as dramatically with varying D_W-values – as is the case with the changes in V_W-values displayed in Figure 2-47 and Figure 2-48. It is also difficult to see any pattern in the change of the wind profiles with these two figures.

The measured results displayed in the above two figures are also approximated by means of equation (2-7). The results for the exponent are depicted in Figure 2-53. This figure depicts the b_W-values for differing D_W-values, the average exponent at Majuba Power Station as well as the 7th power law derived from literature (section 2.2.3). The higher average b_W-value indicates, as explained in the previous section, that the 7th power law is invalid as a single yearly average b_W-value for Majuba Power Station. The average yearly b_W-value at Majuba Power Station is 0.22.

The b_W-value varies without any visible pattern. It should be noted that although the variation in b_W-values are dependent on a number of parameters other than the D_W that are not integrated in this analysis, including the influence of the weather mast's structure, the effect of the D_W on b_W should still surface if the dependence exists.

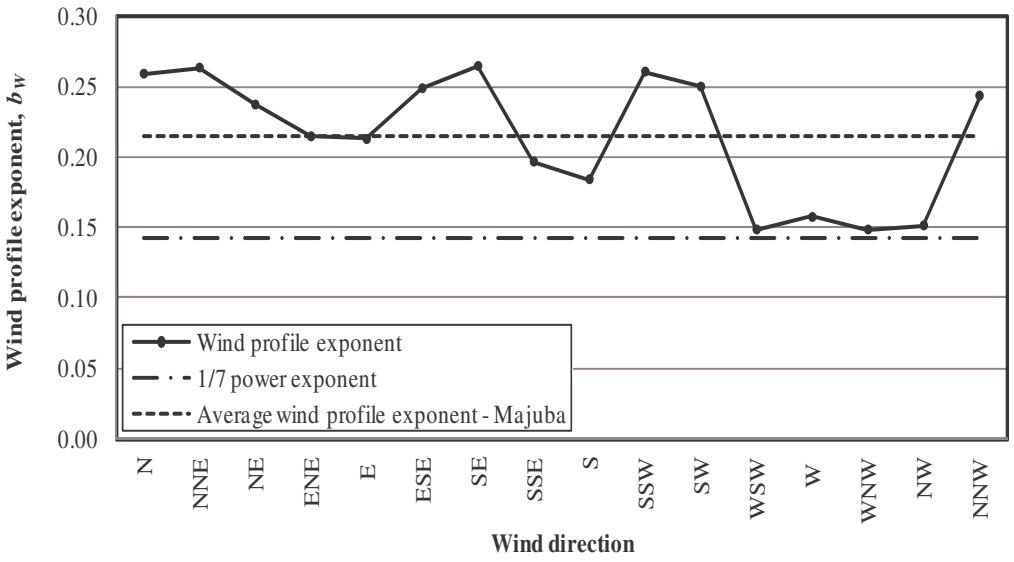

Figure 2-53: Annual average b_W for different D_W-values at Majuba Power Station.

As b_W cannot be approximated accurately mathematically, the effect of D_W-values on b_W are concluded/ assumed to be minimal.

2.8.4. Daily variations in b_W for the four seasons at Majuba Power Station

The daily variation in b_W for the four seasons is depicted in Figure 2-54. The hourly values are determined in a similar manner as explained in section 2.3.2, and are averaged for the four seasons. This figure shows that Winter at Majuba is characterised by larger b_W-values compared to the other three seasons across the 24-hour cycle. This is also motivated in Table 2-7; Winter is characterised by the lowest average V_W during daytime and nocturnal hours that relates to an increases in b_W as explained in section 2.5.1.

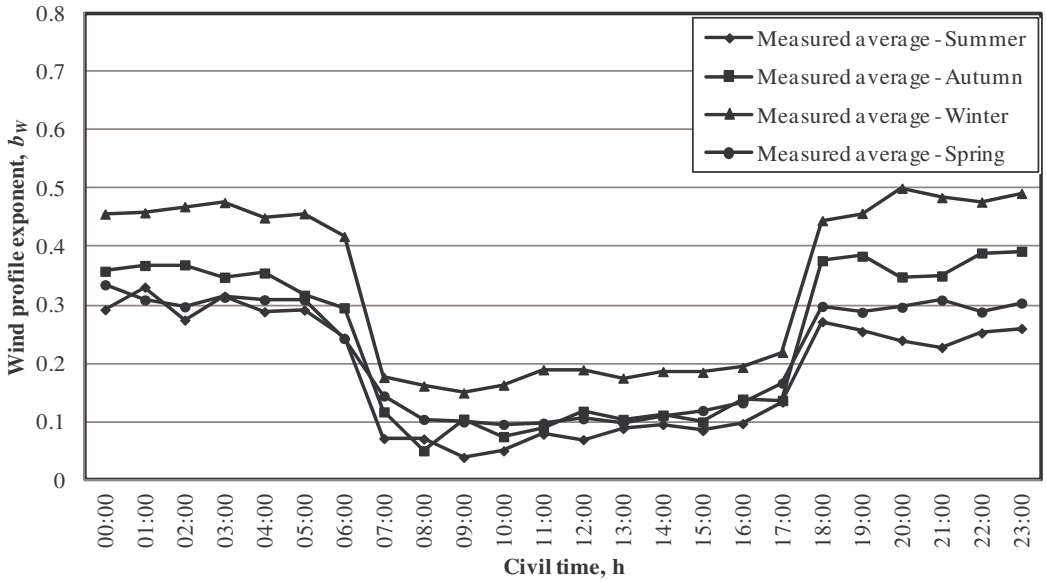

Figure 2-54: Measured hourly variation in b_W at Majuba Power Station for the four seasons.

Autumn is characterised by larger b_W-values during nocturnal hours than Summer and Spring, whereas Spring is typified by slightly higher b_W-values during night-time compared to the same times in Summer. The daytime b_W-values are relatively similar for Summer, Spring and Autumn, whereas Winter is characterised by slightly higher daytime b_W-values. The results depicted in Figure 2-54 correspond to the fact that Spring and Summer at Majuba Power Station are much windier seasons than Winter and Autumn, the calmer seasons. All of these results are motivated, in similar fashion to the Winter results discussed above, by means of the average seasonal V_W-values tabulated in Table 2-7 above. Figure 2-54 indicates that the b_W-values can be approximated in a similar way as the b_T-values in section 2.5 which is achieved by means of single average values for nocturnal and daytime hours.

These single average value approximations are depicted in Figure 2-55.

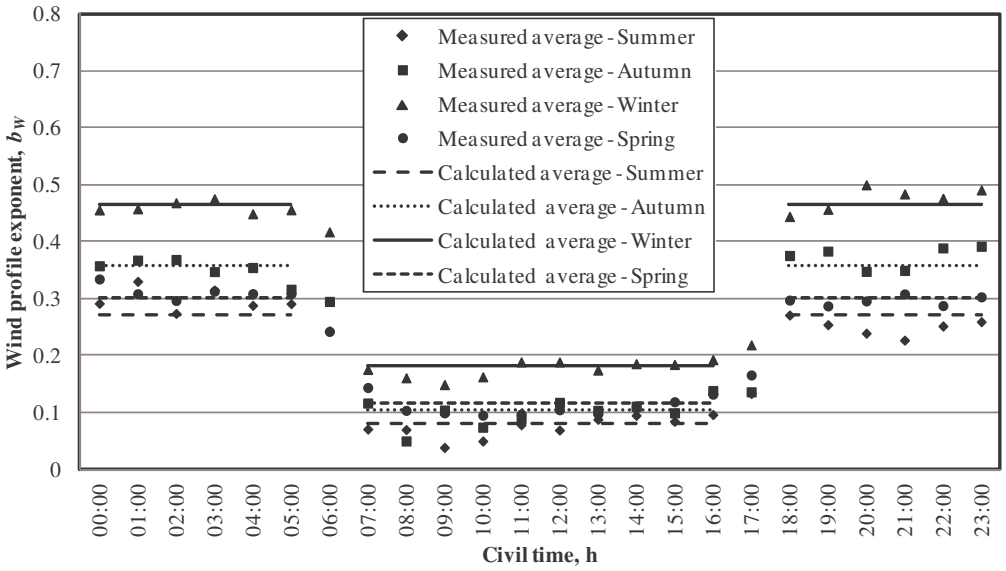

Figure 2-55: Measured hourly variation in b_W at Majuba Power Station for the four seasons with approximations.

The results depicted in Figure 2-55 are supplied in Table 2-11. This provides the reader with simple yet accurate approximations for b_W for any hour of the day throughout the four seasons. The transition periods are not of interest, as explained in section 2.5.1 above and further motivated in chapter 3 below.

Table 2-11: Approximated b_W-values for the periods 07:00 – 17:00 and 18:00 to 06:00 for the four seasons at Majuba Power Station.

Season	07:00 - 17:00	18:00 - 06:00
Summer	0.07991	0.27238
Autumn	0.10415	0.35764
Winter	0.18054	0.46421
Spring	0.11567	0.29977

2.8.5. Seasonal variation in the monthly average b_W

As is the case with the monthly variation in the average b_T (section 2.5.2), it can also be observed that the b_W-values follow similar trends. The monthly average b_W-values are, however, determined by averaging all the hourly b_W-values, and not only the value for a specific hour. The latter is the case with the monthly variation in b_T in section 2.5.2. The monthly variation in the average b_W is depicted in Figure 2-56. Winter months are found to be characterised by larger b_W-values because of the lower average reference height V_W during these months (Table 2-7). Summer and Spring are characterised by lower average b_W due to the higher average V_W-values during these months. The sinusoidal regression curve depicted in this figure predicts the monthly average b_W ($b_{W,ma}$) accurately on a yearly basis and is represented by the following equation:

$$b_{w,ma} = -5.9896\sin(0.16667\pi \cdot n_m + 1.4381) + 0.2376 \quad \textbf{(2-15)}$$

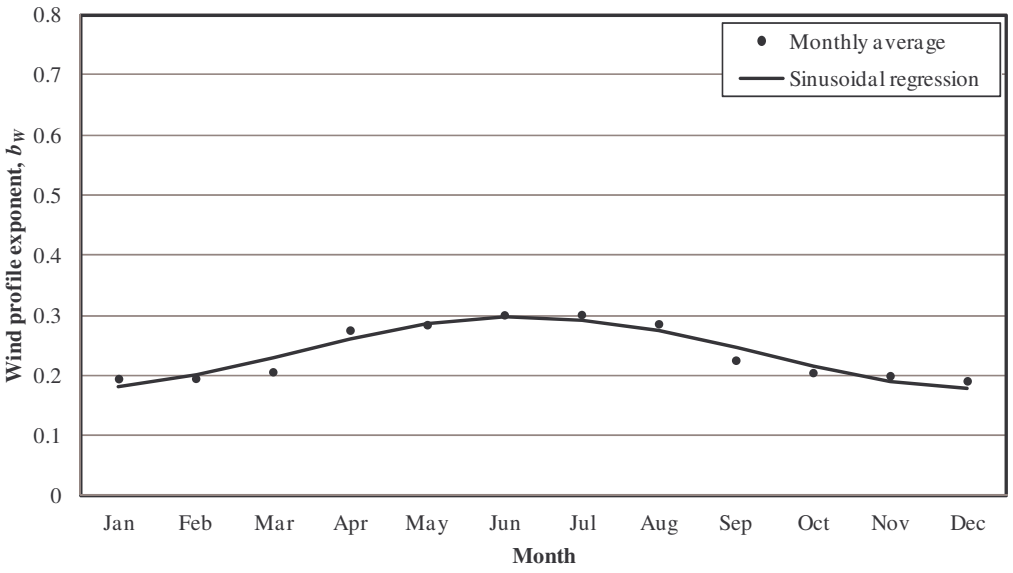

Figure 2-56: Calculated monthly variation in the average b_W for Majuba Power Station.

Equation (2-15) may be used to quickly and effectively calculate the average monthly b_W throughout the year.

2.9. CONCLUSION

The ambient conditions at Majuba Power Station are logged/ observed, evaluated and trended to satisfy the objectives outlined in section 1.2. The variation of individual parameters as functions of time provides the reader with adequate knowledge of the dynamics of these ambient parameters.

Using the temperature and temperature profile calculations discussed in section 2.5, it is possible to determine the average temperatures as well as the b_T for any time of day for the year. To calculate same, Figure 2-26 to Figure 2-31, equations (2-10) and (2-11), and the values provided in Table 2-6 are used. These values and equations are, however, limited to Majuba Power Station's specific geographical location.

Using the results discussed in section 2.6 it is possible to determine the average *RH* for any time of the day during the four seasons. It is also possible to determine the average monthly *RH* with the help of Figure 2-34. These results are used in section 4.3, where the influence of *RH* on NDWCTs is addressed. *RH*, however, fails to present a true reflection of the amount of water vapour in the air because of its dependence on T_a. On the other hand it provides a reasonable indication of when rain is expected. The variation in water vapour content in air is shown in Figure 2-37, which depicts the monthly variation in ω. This figure provides valuable information regarding the daily and nocturnal variations in the ω throughout the year, and is also used in section 4.3.

The V_W-results discussed in section 2.8 provide the reader with a thorough background of the annual variation and distribution of V_W and D_W at Majuba Power Station. It is concluded that the 7th power law, discussed in section 2.8.2, is not an accurate average annual b_W at Majuba Power Station. The average monthly b_W is higher than the assumed normal 7th power law b_W. With the use of Table 2-7 and equation (2-14) a more accurate seasonal average b_W can be calculated for nocturnal hours. The data in section 2.8.3 indicates that the effect of D_W-values on the b_W cannot be empirically calculated due to its erratic nature. The wind profile results depicted in section 2.8.4 and 2.8.5 indicate that it is possible to easily approximate the hourly and seasonal b_W-value.

The meteorological results in sections 2.4 to 2.8 correspond well to data presented in literature (Lander, 1991). These results provide the reader with simple methods of approximation for V_W, D_W, T_a, T_{awb}, b_W, b_T, RH, ω and p_a. The empirical correlations ensure that the reader can make informed decisions regarding the times at which NDWCT performance testing should be conducted. It is understandable that the results are local to Majuba Power Station. The techniques used to obtain the empirical equations and figures can, however, be used at other Eskom sites in order to gain similar knowledge of the ambient conditions at these sites.

CHAPTER 3
AMBIENT NDWCT DESIGN AND PERFORMANCE TEST CONDITIONS

3.1. INTRODUCTION

The effectiveness of coal-fired power plants, and in particular the cooling systems of power plants such as NDWCTs, is highly dependent on ambient conditions and the variation in ambient conditions (Kröger, 2004), as was mentioned chapter 1. The effectiveness of a NDWCT, portrayed in equation (3-1) below, is for instance dependent on changes in the temperature lapse rates as explained in section 2.1.

$$\varepsilon_{CT} = \left(T_{wi} - T_{wo}\right) \Big/ \left(T_{wi} - T_{awb}\right) \times 100\% \qquad \textbf{(3-1)}$$

Figure 3-1 depicts the measured relationship between Majuba Power Station's NDWCT effectiveness and LR_T.

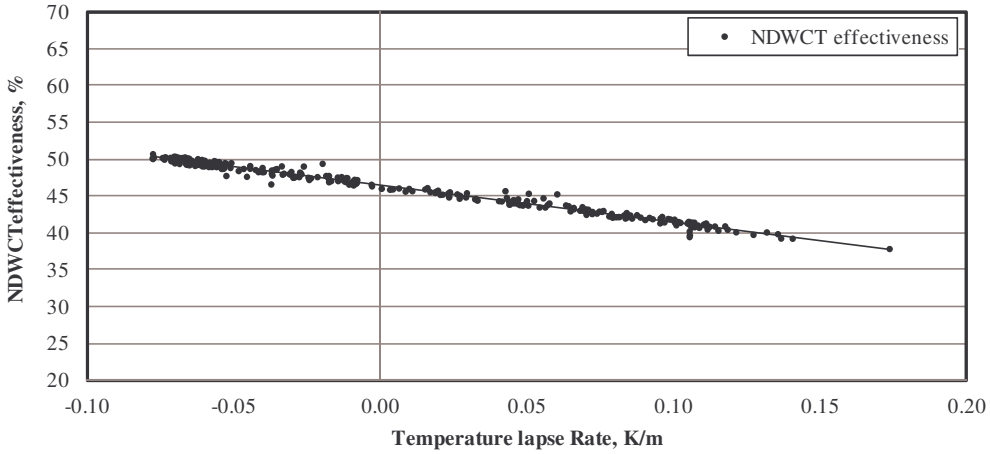

Figure 3-1: Majuba Power Station's NDWCT effectiveness vs. LR_T.

The effectiveness is higher when the lapse rate is negative, which related to mid-day. During periods when temperature inversions occur the effectiveness decreases, confirming Merkel (1925)'s contention that temperature inversions may be the cause of apparent inconsistencies in NDWCT performance predictions. During a temperature inversion the performance of the tower is measurably reduced due to the reduced driving potential and higher effective inlet air temperature (Kröger, 2004). Lauraine, Lemmens & Monjoie (1988) also mention that inversion periods should be avoided for NDWCT performance tests due to the accompanying reduction in plume dispersion. The linear trend indicates the general downward trend of the data as LR_T increases and becomes positive. This data compares well to data presented by Benton & Mirsky (1993). It should be noted that b_T can also be used as an indication of the LR_T and is in fact used throughout this study.

Other parameters that influence NDWCT effectiveness include V_W, D_W, T_a, b_W, p_a and RH. These influences are explained in more detail in section 5.5. T_{awb} can also

be used instead of T_a and RH due to the dependence of T_{awb} on these two parameters.

Taking the preceding discussion into account, a cooling system, accounting for more than 50% of the energy loss in power plants, need to operate effectively throughout its lifecycle and thus needs to be designed with the correct ambient design conditions.

In an attempt to satisfy the objectives set out in chapter 1, the researcher discusses the different standards that were considered, which is followed by a discussion of the original ambient design conditions for Majuba Power Station's NDWCTs. These original specifications are compared with the current design specification, followed by a discussion concerning a proposed alternative approach to determine NDWCT ambient design conditions. The segment is concluded by a section in which the researcher discusses the NDWCT performance test requirements at Majuba Power Station and the potential improvements and proposed amendments to the performance test procedures, codes and guidelines.

3.2. LITERATURE STUDY

In order to obtain valid performance or/ acceptance test ambient conditions, two NDWCT acceptance test codes were evaluated, namely the *British Standard for water cooling towers - Methods for performance testing* (BS4485 Part 2, 1988) – referred to as *BS* in this section, as well as the *Cooling Technology Institute Acceptance Test Code for Water Cooling Towers* (CTI ATC-105, 2000) – referred to as *CTI* in this section.

The conditions of equipment are similar for both standards and can be viewed in BS4485 Part 2 (1988) and CTI ATC-105 (2000). The conditions of atmosphere for both standards are compared below:

Wind speed (V_W):

- *CTI* states that the V_W should be within the contract specific limits. If not supplied though, the V_W should be below an average of 4.5 m/s over the test period and below 7 m/s over 1 minute gusts. The average is calculated between tower discharge height, between 45 m and 450 m from the NDWCT curb, and half of the NDWCT air inlet height, measured at least a quarter of the tower base diameter or twice air inlet height (whichever is the largest) from the NDWCT. The NDWCT discharge wind speed can, however, be visually noted by looking at the plume, which should fill the tower discharge completely and rise vertically. In this case V_W should only be measured (with an anemometer) and averaged at the bottom location.
- *BS* states that the V_W should be below an average of 5 m/s over the test period and below 7 m/s over 1 minute gusts. The V_W should be measured with an anemometer at 1.5 m to 2.0 m AGL at a windward distance from the NDWCT sufficient to eliminate the influence from the NDWCT structure.

Wet-bulb temperature (T_{awb}): Both standards specify the use of mechanically aspirated (*BS*: 3 – 6 m/s and *CTI*: 4.5 – 5.5 m/s) psychrometers with the temperature sensitive element shielded from ground radiation and with a wetted wick of 20 mm (*BS*) and 25 mm (*CTI*) respectively:

- *CTI* states that the T_{awb} shall be within ± 8.5 ^{o}C from the design T_{awb}, the Δ T_{awb} shall be less than 1^{o}C/hour for a single device and less than 1.5 ^{o}C/hr (on average) for more than 1 device during the test period. The air inlet T_{awb} instrumentation shall be located within 1.5 m from the NDWCT air intake and shall cover the inlet height of the NDWCT. The instrumentation shall have an accuracy of 0.05 ^{o}C. The number of measurement stations is dependent on the NDWCT air inlet area. For Majuba the air inlet area is approximately 5500 m^2, which relates to 16 individual stations according to Appendix G in CTI ATC-105 (2000).
- *BS* states that the T_{awb} shall be within ±5 ^{o}C from the design T_{awb} and shall be larger than 3 ^{o}C, the average Δ T_{awb} shall be less than 1 ^{o}C/hour during the test period. The nominal inlet T_{awb} (Arithmetic average of the measurements taken within 1.5 m of the NDWCT inlet and between 1.5 m and 2.0 m ABC on both sides of the NDWCT so as to substantially bracket the flow of air to the NDWCT) is likely to be identical to the far-field ambient T_{awb} (measured windward from the NDWCT and free from the influence of the tower) in the case of a NDWCT. In this case the T_{awb} shall be determined as the arithmetic average of measurements taken from 1.5 m to 2.0 m AGL to a point substantially bracketing the flow of air to the NDWCT. The location should be between 15 m and 100 m windward from the NDWCT or otherwise a mutually agreed location. The instrumentation shall have an accuracy of 0.05 ^{o}C. A minimum of 3 measurement stations are required around the circumference of the NDWCT.

Dry-bulb temperature (T_a): Both standards indicate that the T_a should be measured in a similar manner as stipulated for the T_{awb}.

T_a lapse rate:

- *BS* states that no atmospheric inversions are allowed during the acceptance test period. This should be verified by measuring T_a at 8 and 10 m AGL to verify a normal lapse rate.
- *CTI* states that the T_a measured near the top of the air inlet (10 m) should be at least 0.15 ^{o}C less than the T_a measured 1.5 m above grade level. This should be verified at 2 opposite locations on the circumference of the NDWCT.

Relative humidity (*RH*):

- *BS* states that the *RH* shall not fall below 40 % during an acceptance test
- *CTI* does not provide a minimum *RH* requirement

From the above comparison it is found that the two standards are rather similar in terms of the conditions of equipment and atmosphere required for a successful NDWCT performance or/ acceptance test.

The *CTI* requirements for measuring T_a and T_{awb} are, however, more thorough with 16 measurement stations required for a successful test to be conducted at Majuba. A statement is made in *BS* that the far-field T_{awb} and nominal air inlet T_{awb} is likely to be identical. This statement is evaluated in section 3.5.

Additional to the two standards discussed above, the Engineering and Construction contract for the NDWCTs and associated systems at Majuba power station was also studied and is referenced throughout the following sections in this chapter.

3.3. MAJUBA POWER STATION's NDWCT AMBIENT DESIGN CONDITIONS

Majuba Power Station's NDWCTs were designed using T_a measured at Nooitgedacht weather station as the main design variable. The annual T_a-distribution used during the design phase is depicted in Figure 3-2. The most common annual T_a during the design phase was 14°C.

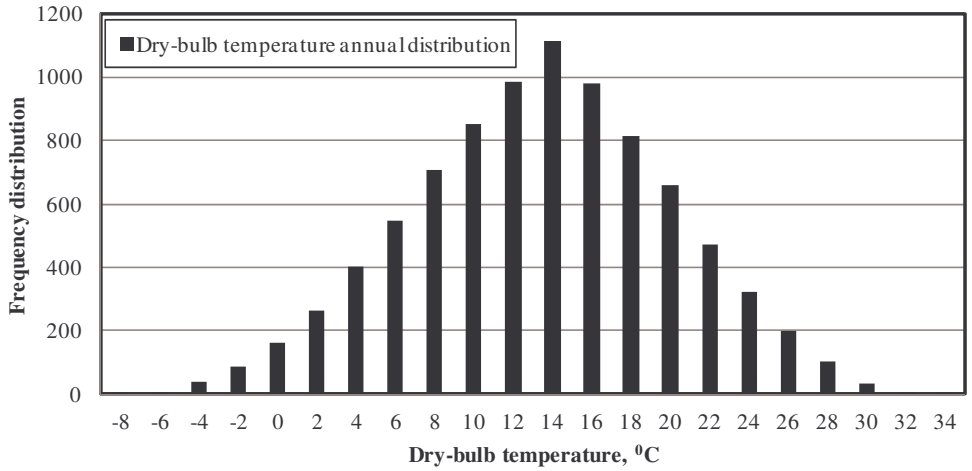

Figure 3-2: Majuba Power Station's NDWCT design phase annual T_a-distribution.

The T_a-distribution depicted above was used to determine the annual average design parameters for the NDWCT at Majuba Power Station. The weighted average T_a was used to calculate the annual average p_c, cooling system water consumption, P_{st} and the rate of heat rejection.

The Engineering and Construction contract for Majuba's NDWCTs indicate that the average T_{awb}, during the periods when T_a is 14°C, is 10.6°C. The guaranteed average p_c is 5.7 kPa, while the guaranteed condenser CW inlet and outlet temperatures (T_{cwi} and T_{cwo}) are at 21.70°C and 33.39°C respectively during the same period.

By utilising logged data gathered over the period August 2009 to July 2010 from the weather mast located near Majuba Power Station (section 2.3), the T_a-distribution is determined and is depicted in Figure 3-3. The data in is figure correlates well to the design phase results depicted in Figure 3-2. A T_a between 14°C and 15°C is found to be dominant, as is the case in Figure 3-2.

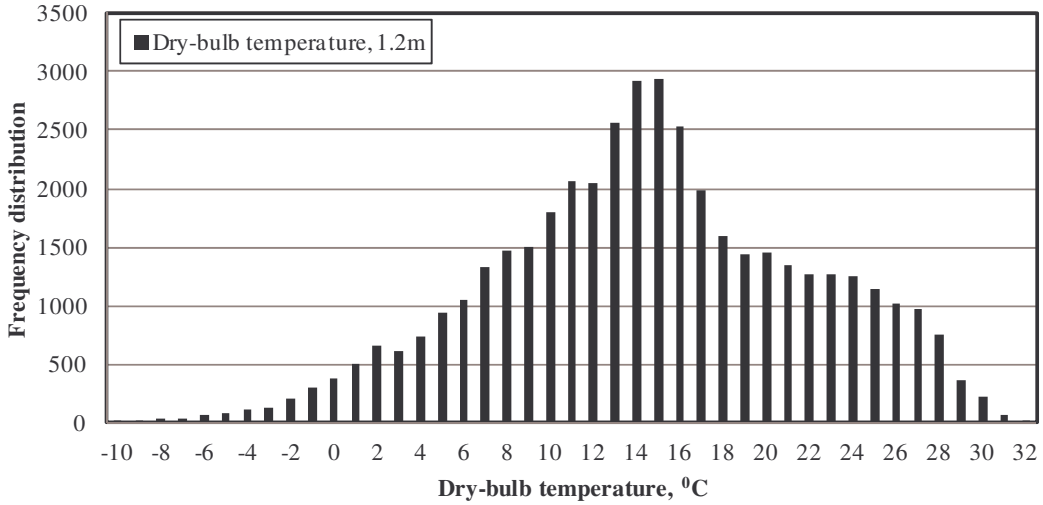

Figure 3-3: Majuba Power Station's annual T_a-distribution from 2009 to 2010.

Using the T_a-distribution depicted above, the current averages for the design ambient parameters are are depicted, together with the original design specifications, in Table 3-1.

Table 3-1: Majuba Power Station's original and current ambient design specifications.

Ambient design parameter	Symbol	Original design value	Current results	Units
Dry-bulb temperature	T_a	14.0	14.5	^0C
Wet-bulb temperature	T_{awb}	11.6	12.9	^0C
Relative humidity	RH	68.34	84.40	%
Atmospheric pressure	p_a	83.492	83.291	kPa
Dry adiabatic lapse rate	$DALR$	-0.00975	-0.00229	K/m
Wind velocity (10 m)	V_W	6.0	3.74	m/s
Wind direction at (10 m)	D_W	E	E	#

The current and original T_a and p_a correspond well according to Table 3-1 above. The rest of the parameters, however, fail to correlate to the original specifications. This can be due to seasonality as well as the ambient characteristics of the period used for the analysis. This variation between the original and current design specifications is thus not greatly problematic, whilst the process of determining the specific design values by only using the annual T_a-distribution is, however, a cause for concern. The latter is evaluated in the following section.

The current DALR is much lower than the original value. The reason for this is that the original LR_T was not determined, but rather taken as the DALR stated in section 2.2.2 by Kröger (2004). The DALR is specific to conditions where air is moving adiabatically up-and down in the atmospheric pressure field. The assumption that was made for this DALR is not accurate as it is found that the current DALR is less negative compared to the originally value. The current measured DALR is averaged for the entire year using only the values corresponding to 12:00 in order to obtain a realistic DALR comparison.

The annual T_{awb}-distribution is depicted in Figure 3-4. The distribution indicates that a T_{awb} of 14°C was the most prominent during 2009 to 2010.

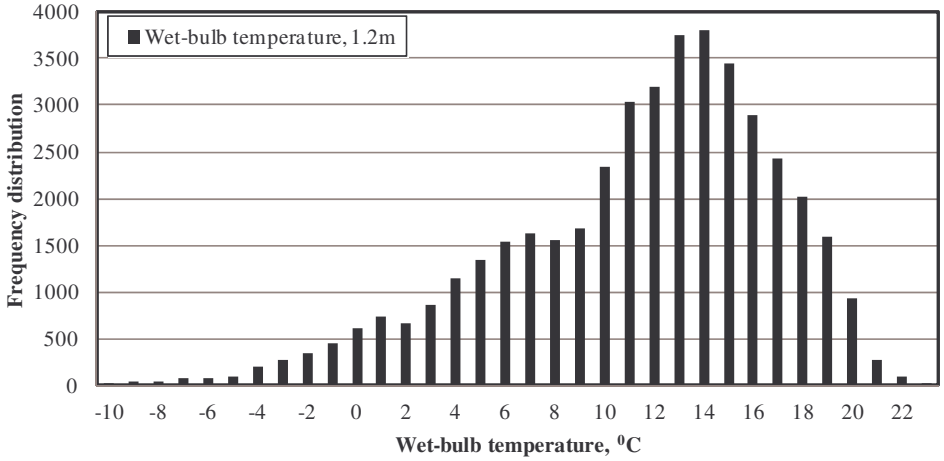

Figure 3-4: Majuba Power Station's annual T_{awb}-distribution from 2009 to 2010.

The average T_{awb} during the periods when a T_a of 14°C is prominent, is 12.91°C (Table 3-1). It is thus still found that the incorrect average T_{awb} is used when only considering the weighted average T_a-distribution.

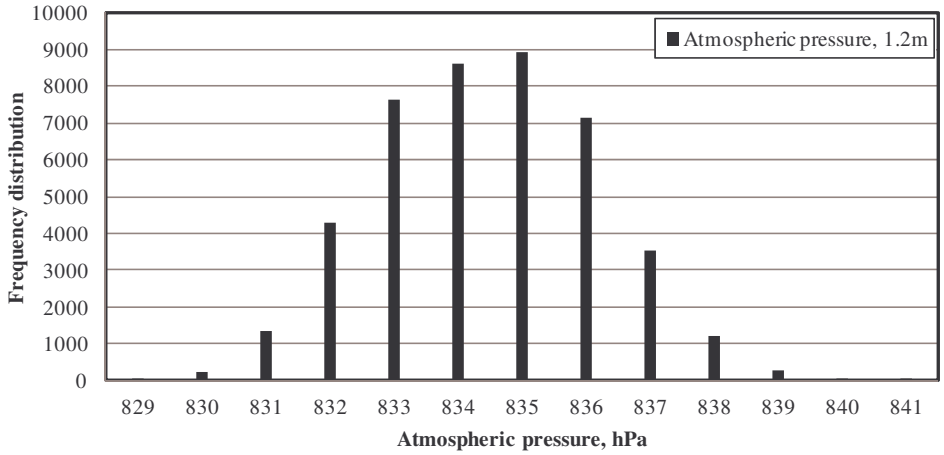

Figure 3-5: Majuba Power Station's annual p_a distribution from 2009 to 2010

The annual p_a is depicted in Figure 3-5. A p_a of between 834 hPa and 835 hPa was found to be most common during this period. The average p_a during periods when the most common T_a (Figure 3-3) is prevalent is, however, 833 hPa (Table 3-1). This again suggests that the incorrect average p_a is used when only considering the weighted average T_a-distributions as discussed above.

The same scenario is evident with the annual *RH*-distribution depicted in Figure 3-6: The most common *RH* is above 95%, but the average *RH* relating to the most common T_a is 84% (Table 3-1).

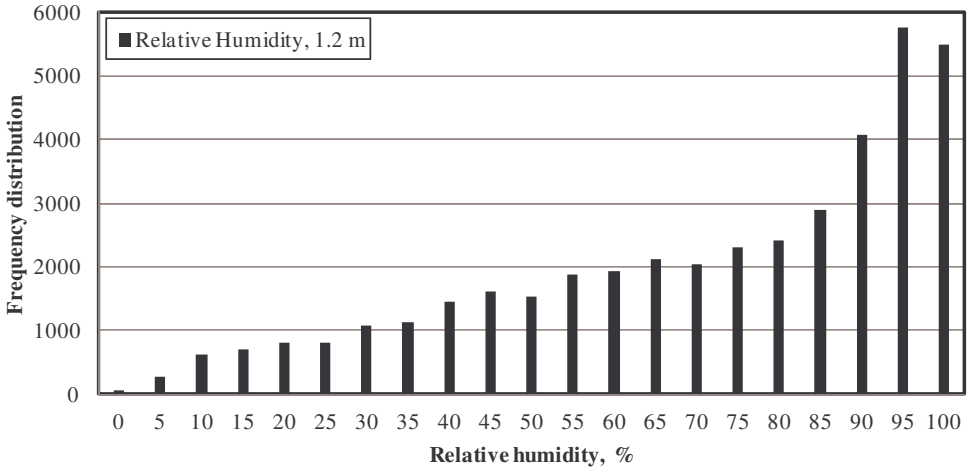

Figure 3-6: Majuba Power Station's annual *RH* distribution from 2009 to 2010

It is known that the T_{awb} is dependent on the T_a, *RH* as well as p_a. The *RH* as well as the p_a-averages was incorrect, which led to the incorrect T_{awb}-averages being used/ calculated. These results show that erroneous design specifications can occur when only considering the weighted average distribution of one independent variable and using this distribution in determining the design values for the other independent variables.

During the approach discussed above, where the T_a–distribution is used to determine the other design specifications, an assumption is made that the NDWCTs have a specific heat rejection load that remains relatively constant throughout the year. In other words the power station is designed for base-loading conditions throughout its lifetime and not for load-following- or two-shifting conditions. Majuba Power Station was initially designed to be a continuous base-loading station but due to the high cost of fuel and the load demand, load-following and two-shifting running regimes were later implemented and are still being used today (as at 2010). The assumption that Majuba would be a base-loading station throughout its lifetime thus leads to an inaccurate determination of ambient design conditions.

A different approach for determining NDWCT ambient design conditions including different running regimes is discussed in section 3.4.

3.4. A NEW APPROACH IN DETERMINING NDWCT AMBIENT DESIGN CONDITIONS

NDWCTs are driven by T_{awb}. This temperature is a function of T_a, RH and p_a. The use of T_a distributions only for the design of NDWCTs is less accurate as it fails to consider the effect and interdependence of RH and p_a to T_{awb}. Future NDWCT should thus be designed with the average annual T_{awb} distribution in mind and not the average annual T_a, as discussed in section 3.2. This, together with the distributions for V_W, D_W and the other parameters discussed in section 3.2, will lead to more accurate design conditions that will inherently lead to the optimal effectiveness of NDWCTs.

The power station's daily variation in net revenue should also be considered when determining the design T_{awb}-distribution. Majuba Power Station currently charges a fixed rate per MW P_{st} throughout the day. Consequently the running regime (average daily variation in P_{st}) can be used as a measure of net revenue. Including the running regime does not influence the general technique for determining the ambient design conditions discussed in section 3.2, but it does influence the results obtained when using this technique.

It is suggested that the annual distribution of T_{awb} be used for the design of base-load power stations. The design specifications should furthermore be set up using a similar method as explained in section 3.2. This approach is possible as the NDWCT will essentially experience a constant heat load that is only influenced by the performance of the NDWCT, and thus the variability in ambient conditions, and not due to heat-load cycle variability that occurs during load-following and two-shifting running regimes.

The ambient design conditions of stations that are characterised by load-following or two-shifting running regimes need to be determined by manipulating the results obtained from employing the general technique discussed in section 3.2 and in the current section. This entails that the T_{awb}-distribution be manipulated as is discussed in the following paragraph:

The annual average P_{st} and Maximum Continuous Rating (% MCR) as a function of time for Majuba Power Station's units' four-to-six (wet-cooled units) are depicted in Figure 3-7. This figure portrays the load-following regime that Majuba applies. The two-shifting is not accurately represented as each unit is not two-shifted on a daily basis and the average of the 3 units will thus be higher than 0. The effect of two-shifting is, however, evident during nocturnal hours, when the average P_{st} is less. This figure indicates that the periods from 06:00 to 11:00, 12:00 to 17:00 and 18:00 to 23:00 have approximately similar load averages (3211 MWh or 25.58 %, 3455 MWh or 27.53 % and 3441 MWh or 27.42 %) while the period from 00:00 to 05:00 is characterised by a lower load average of 2440 MWh or 19.46 %.

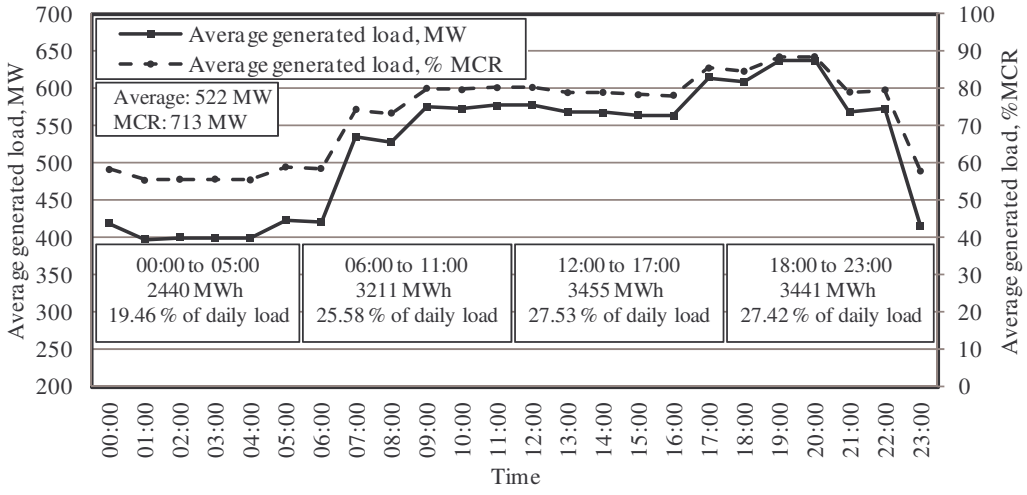

Figure 3-7: Average P_{st} vs. Time on U4 to U6 at Majuba Power Station.

The average daily load figure, displayed above, needs to be incorporated in the T_{awb}-distribution to ensure that the running regime forms part of the ambient design condition-determination process. This is achieved by obtaining the T_{awb}-distributions for the four periods displayed in Figure 3-7 and multiplying these entire distributions by the average percentage (%) of the daily load and adding the resultant distributions to obtain an overall distribution.

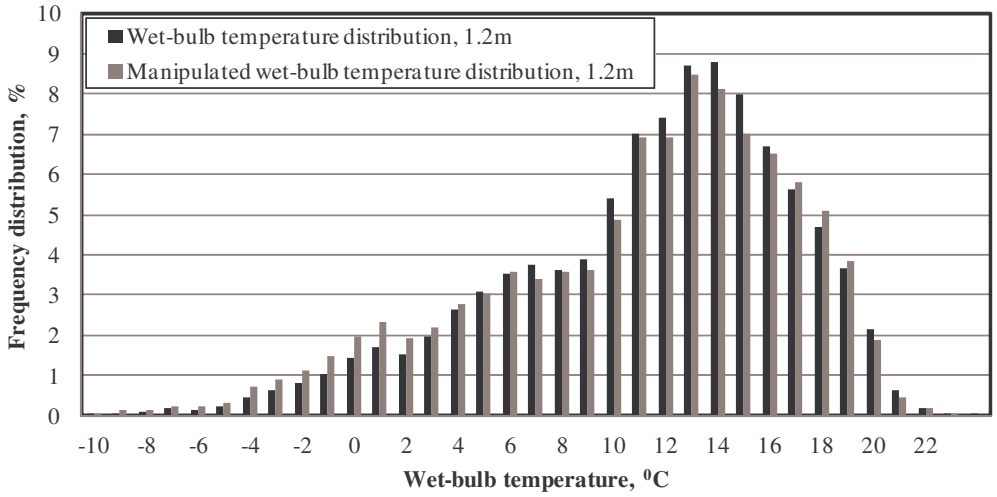

Figure 3-8: Manipulated and original T_{awb}-distribution at Majuba Power Station from August 2009 to July 2010.

The manipulated T_{awb}-distribution at Majuba Power Station for the period from August 2009 to July 2010 is plotted in Figure 3-8. This figure indicates that the manipulated distribution is very similar to the original distribution, which is also plotted in Figure 3-4. Figure 3-8 does, however, indicate that the design T_{awb} is actually 13 °C and not 14 °C, as depicted in Figure 3-4. This is a relatively small difference, but the difference is still evident and can be larger at other plants and

locations, or for other parameters. This finding motivates the assertion that this method should be employed when determining ambient design conditions.

In conclusion it is submitted that the determination of ambient design conditions, keeping the operating regime in mind, is of vital importance. As discussed respectively in the first and latter part of section 3.4, base-load station ambient design conditions should be determined without including the load-regimes while load-following and two-shifting station ambient design conditions should be determined by including the load regimes, or the daily variation in net revenue if the price per MW P_{st} varies throughout the day. The use of T_{awb} is highlighted above the use of T_a-values as the main design variable as T_{awb}-values form the cooling limits for NDWCTs. These small modifications to the determination process may increase the initial capital expenditure, but will also increase the overall effectiveness of the NDWCT - invariably reducing the lifecycle cost of the cooling system.

3.5. NDWCT PERFORMANCE TEST REQUIREMENTS

In the *British Standard* (BS4485 Part 2, 1988), the conditions of atmosphere required to obtain valid performance test results are provided and are discussed in section 3.2 together with the requirements stipulated in CTI ATC-105 (2000). As noted in this section, the two standards have similar criteria barring with a few differences. The BS 4485 was used during the original performance tests of Majuba Power Station's NDWCTs and is referenced in the below discussion.

In order to meet the requirements set out in these codes and to complete a successful NDWCT performance test, a day and time with characteristics that resemble the original design specifications should therefore be chosen. It is also important to choose the time of day so that atmospheric conditions, including LR_T and wind lapse rate (LR_W), are stable and so that no inversions will occur.

These requirements naturally motivate why the transition periods from nocturnal hours to sunrise and sunset to nocturnal hours, for all of the results and figures in this document, will not be used during performance testing and are thus not of interest to the reader. For this reason these periods are not discussed in detail. Daytime hours should be used to avoid inversions, as well as to ensure safety and accuracy as listed above. The graphs for T_a (Figure 2-29), V_W (Figure 2-54) and RH (Figure 2-33) indicate that 12:00 to 14:00 are characterised by the most stable conditions throughout the year. This time period should therefore be used when conducting performance tests.

Considering the seasonal mid-day (12:00) T_{awb}-variation depicted in Figure 2-28, it is found that the average T_{awb} is 13.8 ^{o}C and the minimum and maximum T_{awb}-values are 8.5 ^{o}C and 18.25 ^{o}C respectively. Figure 3-8 also indicates that a T_{awb} between 13 ^{o}C and 14 ^{o}C is the most prevalent throughout the year. Considering that the design should be conducted with T_{awb} within ± 5 K of the design it may be argued, with the use of Figure 2-28, that the NDWCT performance tests could be conducted during any time of the year. Figure 2-26, however, indicates that Summer months are characterised by the least intense LR_T-values during mid-day.

This will increase the overall NDWCT air-inlet $T_{a,}$ which will decrease the effectiveness of the NDWCT. Conducting performance tests during this time will thus ensure that the NDWCTs will perform equally or better throughout the year considering the LR_T-values. This motivates that Summer months should be preferred with regards to T_{awb} when conducting NDWCT performance tests.

Figure 3-6 indicates that the most prevalent *RH* throughout the year is approximately 95%. Using Figure 2-34 it is found that these high *RH* values are encountered during Summer, which again motivates that Summer should be preferred when conducting NDWCT performance tests. This will also ensure that the specifications listed above ($RH > 40\%$) should be met.

In order to satisfy the wind characteristics listed above it is necessary to ensure that the V_W does not exceed 5 m/s and that average gusts should not exceed 7 m/s over 1 minute. Although it is difficult to pinpoint a day in a season that will have the correct wind conditions to conduct NDWCT performance tests, it is noted in Table 2-7 that the average V_W during Summer (4.64 m/s) is very close to the yearly average (4.65 m/s). This together with the knowledge that Spring is the windy season at Majuba (motivated by Figure 2-46),and that Summer is characterised by a large percentage of V_W-values between 3 and 5 m/s (Figure 2-43), it is proposed that Summer is also preferable for NDWCT performance tests at Majuba Power Station with reference to wind.

Although it is imperative to understand when to conduct performance tests, it is also necessary to take note of where the ambient parameters used during the tests should be measured. During the design of the NDWCT and the initial performance tests, the T_{awb} should for instance be measured at the NDWCT inlet and it is assumed that this T_{awb} should be identical to the far-field T_{awb} measurement, as stated in BS 4485 part 2 (1988). During normal operation, the NDWCT inlet T_{awb} measurement is not always available. Most sites have a weather mast that is located away from the NDWCT inlet (Section 2.3), and during normal operation engineers have to rely on far-field measurements as an indication of the NDWCT air-inlet T_{awb}. With the next test, discussed in section 3.5.1 below, the researcher aims to evaluate the difference between the T_{awb} measured at the weather mast and the NDWCT inlet at Majuba Power Station. The relevant conclusions are provided in order to evaluate the statement that the NDWCT inlet T_{awb} should be identical to the far-field T_{awb}.

3.5.1. T_{awb} comparison between far-field and NDWCT inlet measurements

In order to complete this test, data loggers (discussed in section 2.3) were installed on Majuba Power Stations weather mast at 6 different heights from 1.2 m to 40 m (discussed in section 2.3) and at the air inlet of NDWCT 6 at 1.2 m, 5 m, 7.5 m and 9 m respectively. The geographical locations are depicted in Figure 2-8 and it should be noted that the data loggers were only installed at 1 peripheral location on NDWCT 6 due to an insufficient amount of loggers to install at 3 locations as per BS 4485 (1988). The site-specific locations are depicted in Figure 3-9 below.

The photographs in the figure below show the shielded data loggers. Shields were incorporated in order to eliminate the influence of *SR* and to reduce the amount of drift spray coming in contact with the data logger. The flora during the Winter period (time and duration explained in section 2.3.2) is depicted in Figure 3-9 (d). This picture indicates that the flora is very similar to the Winter flora noted in Figure 2-16 in section 2.4.

a) NDWCT inlet data logger installation on wind-wall

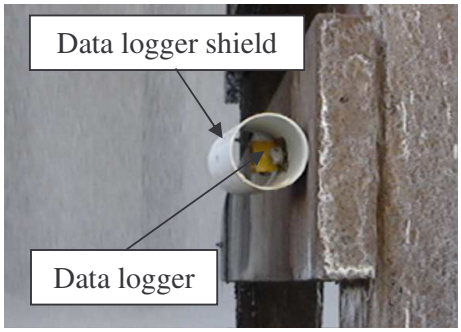

b) NDWCT Inlet data logger and shield

c) Weather mast data logger installation

d) Weather mast data logger and shield

Figure 3-9: Photographs depicting the data logger installation on Majuba Power Station's weather mast and NDWCT inlet.

Figure 3-10 depicts T_{awb}-values calculated and averaged over two weeks in June 2011 at Majuba Power Station's weather mast and NDWCT inlet respectively. The figure indicates that the weather mast temperature profiles correspond well to the data presented in section 2.5. The T_{awb} calculated (A.1.5) at the NDWCT inlet fails to correspond well to the equivalent height's T_{awb} calculated at the weather mast. T_{awb} values measured at the NDWCT inlet are measured to be higher than the T_{awb} measured at 40 m AGL at the weather mast during nocturnal hours, when temperature inversions occur. During daytime periods, especially between 12:00 and 14:00 (the period that is of interest, as motivated in section 3.5), it is found that the T_{awb} measured at the NDWCT inlet correspond to a T_{awb} between 1.2 m and 40 m on the weather mast.

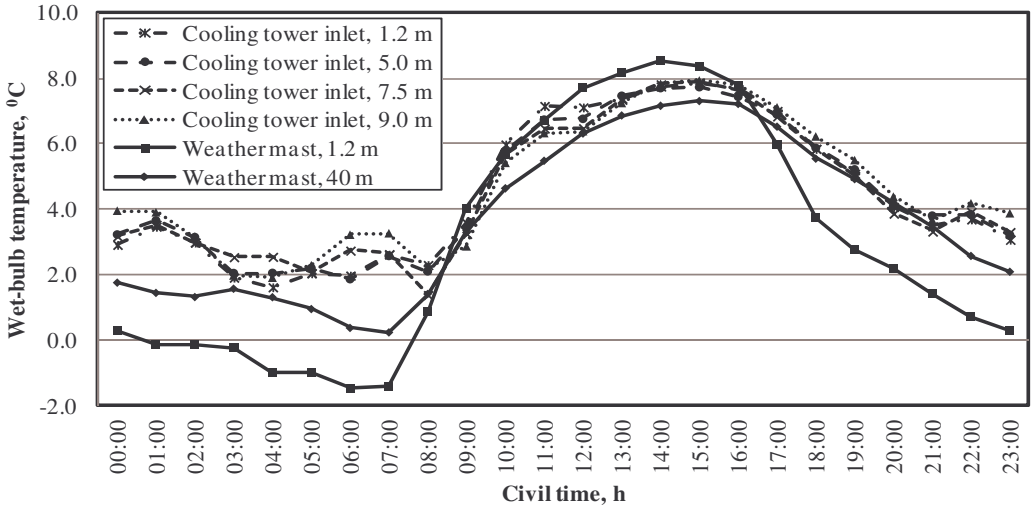

Figure 3-10: Average hourly T_{awb} measured at Majuba Power Station's weather mast and at the NDWCT inlet in June 2011.

Using the knowledge gained in chapter 2 regarding the LR_T, it is possible to calculate what height on the weather mast corresponds to the T_{awb} at the NDWCT inlet. The T_{awb} profiles are depicted below in Figure 3-11.

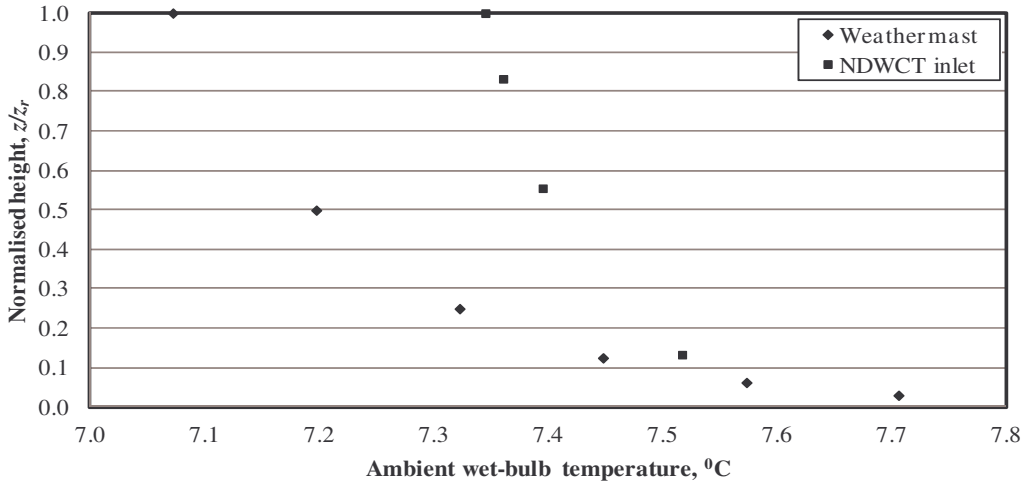

Figure 3-11: Tawb-profiles calculated at the NDWCT inlet and the weather mast at Majuba Power Station between 12:00 and 14:00 in June 2011

Taking note that z_r = 40 m for the weather mast and 9 m for the NDWCT inlet, this figure indicates that the T_{awb} values measured at the NDWCT inlet compares to T_{awb} values measured between 1.2 m and 10 m on the weather mast. The T_{awb} values are tabulated below.

Table 3-2: T_{awb} measured at different heights at the weather mast and NDWCT inlet at Majuba Power Station between 12:00 and 14:00 in June 2011

Weather Mast		NDWCT inlet	
z	T_{awb}	z	T_{awb}
1.2	7.71	1.2	7.51
2.5	7.57	5	7.4
5	7.45	7.5	7.36
10	7.32	9	7.34
20	7.2		
40	7.07		

From the results depicted above it is found that the T_{awb} values measured at the NDWCT inlet do not correspond to the equivalent T_{awb} at the weather mast, taking into account that the airflow near the top of the NDWCT air inlet is much higher compared to at the base, which is used to weight the higher T_{awb} values more heavily. It is furthermore established that the average NDWCT inlet T_{awb} compares to a T_{awb} measured between 5 and 10 m on the weather mast at a time between 12:00 and 14:00. This contention is further motivated by ω values measured at the two locations that also indicate that the NDWCT inlet ω correspond to a ω measured between 1.2 m and 10 m on the weather mast. This is depicted in Figure 3-12.

The statement made in BS 4485 (1988) that the far-field and NDWCT-inlet T_{awb} values should be identical is thus proven inaccurate when using a reference height of 1.2 m AGL (Louth, 1996). Using the BS 4485 (1988) temperature reference height of 1.5 m to 2.0 m ABC will, however, provide more accurate results, but due to the results depicted in the above figure it is consequently recommended that a far-field T_{awb} measured at a height of 10 m be used during NDWCT-design stages as the NDWCT reference height temperature. It should, however, be noted that the industry-standard temperature reference height (Louth, 1996) should still be used during b_T calculations.

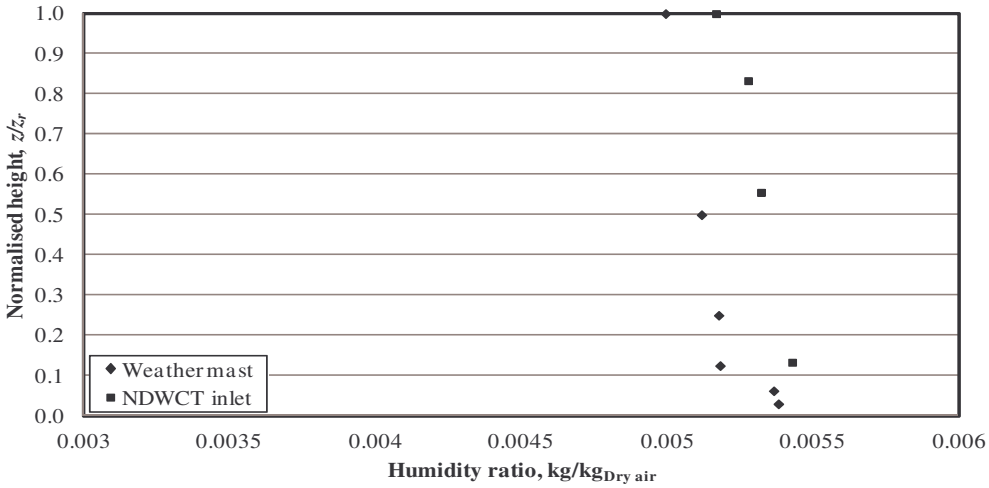

Figure 3-12: ω-profiles calculated at the NDWCT inlet and the weather mast at Majuba Power Station between 12:00 and 14:00 in June 2011.

3.6. CONCLUSION

The original NDWCT-design conditions for Majuba Power Station are discussed and evaluated in section 3.2. These conditions, although relatively accurate, fail to correspond well in some instances to the current (as at 2009 to 2010) design conditions, which were determined using the same method used for determining the original values.

In section 3.4 the researcher proposes an improved technique to determine ambient design conditions and furthermore focuses on the use of T_{awb} as the main design variable as well as the specific turbine load regimes in order to obtain more accurate and representative NDWCT-design conditions. This method indicates that the design parameters do differ from the original when this technique is implemented. Although relatively small, this difference can have a major impact on the overall life-cycle cost of the wet-cooling system and thus the power station.

A number of aspects regarding the performance test conditions are discussed in section 3.5. Daytime hours (12:00 to 14:00) are prevalent when conducting performance tests on NDWCTs. It is furthermore found and suggested that Summer months are the most advantageous for Majuba Power Station when conducting these tests. The researcher also indicates in this section that the T_{awb} values measured at the NDWCT- inlet and the weather mast do not correspond accurately to within 0.1 K. The temperatures measured at the NDWCT-inlet correspond to T_{awb} values measured between 5 m and 10 m on the weather mast at Majuba. It is recommended to use a height of 10 m on the weather mast to determine NDWCT-design conditions.

CHAPTER 4
WATER-STEAM CYCLE η_{th} AND p_c FUNCTIONAL DEPENDENCE

4.1. INTRODUCTION

Majuba Power Station's water-steam cycle is based on the Rankine concept with superheat, reheat and regeneration, and is depicted in Figure 4-1 below:

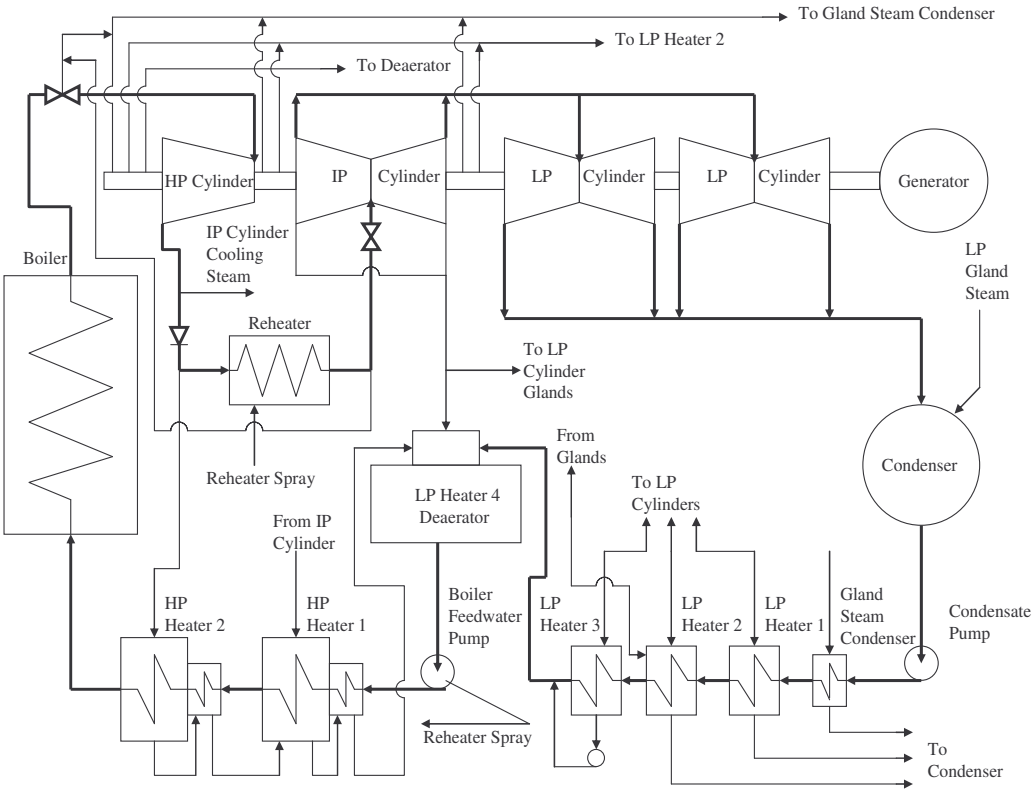

Figure 4-1: Diagram of Majuba Power Station's water-steam cycle.

Using the realised Carnot cycle, the η_{th} of a water-steam cycle is determined as follows (Çengel, 2003) where Q_{in} refers to the total heat input into the boiler, W_{net} to the net work output from the turbine and P_{aux} to the auxiliary power consumed by the specific unit:

$$\eta_{th} = 1 - \sqrt{\frac{T_L}{T_H}} = W_{net} / Q_{in} = f\left(W_{net}, Q_{in}\right) \qquad \textbf{(4-1)}$$

where

$$W_{net} = P_{st} - P_{aux} = f(P_{st}, P_{aux}) \quad \textbf{(4-2)}$$

The cycle's η_{th} may be improved by either increasing the average temperature at which heat is transferred to the working fluid in the boiler (T_H), or by decreasing the average temperature at which heat is rejected from the working fluid in the condenser (T_L).

Çengel (2003) evaluates numerous methods to increase the thermal cycle efficiency. For the purpose of this discussion the reduction of T_L (which, for illustration purposes, may be assumed to be the condenser saturation temperature (T_{sat})), and thus the reduction of p_c, form the basis for the study. This is due to its direct relationship to NDWCT-effectiveness. This is also motivated in chapter 1, where it is stated that one of the main objectives of this study is to quantify the possible financial implications that a reduced heat rejection load caused by a reduced p_c may have.

Due to Majuba Power Station's two-shifting running regime, the evaluation of the water-steam cycle η_{th} is more complicated. Two different boiler operating modes exist, whereof the first is known as the 'fixed pressure mode'; the main steam pressure (p_{HP}) is regulated by means of throttling through the governing valves upstream of the high-pressure (HP) and intermediate-pressure (IP) turbines. This regime is used during steady state conditions, normally above 90 % MCR, but may be manipulated by the operator during abnormal situations to between 80 % and 100 % MCR depending on his throttling set-point.

The second mode, namely the 'sliding pressure mode', is where no throttling takes place at the turbine and the pressure as result slides. This regime is used between boiler main-steam pressures of 8.2Mpa and 17.3Mpa (transient conditions such as start-ups and shut-downs).

For the purpose of this investigation the focus is on full load steady-state conditions, and thus the fixed pressure control boiler operating mode. The amount of throttling that takes place during steady-state conditions is minimal and regarded to be relatively constant at full-load. The chapter includes a discussion regarding the determination of the water-steam cycle η_{th} by means of historical plant data. This is followed by a similar discussion regarding p_c.

4.2. WATER-STEAM CYCLE η_{th}

As described in equation (4-1), the water-steam cycle η_{th} is a function of both Q_{in} and W_{net}. It is thus required that both of these parameters be determined accurately. Q_{in} can be determined with a few different methods: The first and most obvious method is to use the coal lower heating value (LHV) and the mass flow rate (m_{coal}).

$$Q_{in} = LHV \cdot m_{coal} \quad \textbf{(4-3)}$$

The dry-basis coal calorific value (CV), also known as the upper heating value (UHV) or the higher heating value (HHV), is measured once a day by sampling the pulverised fuel (PF) from the mill feeders. The LHV is determined by subtracting the heat required to remove the moisture from the coal ($q_{moisture}$) from the UHV, as depicted in equation (4-4).

$$LHV = UHV - q_{moisture} \quad \textbf{(4-4)}$$

where $q_{moisture}$ can be calculated as follows:

$$q_{moisture} = i_{fgw} \cdot \%_{moisture} \quad \textbf{(4-5)}$$

The m_{coal}-value is calculated by measuring the primary air (PA) flow. The boiler master controller assumes a one: one mass ratio between PA (measured by an aerofoil) and PF. This assumption is verified every 6 months by means of PF sampling. Both the LHV and m_{coal} are found to be difficult to measure and calculate and are not measured continuously. It therefore poses a risk to the integrity of the data during evaluation.

Another approach in determining Q_{in} is to use the heat added to the working fluid in the boiler ($Q_{in,steam}$) together with the boiler efficiency (η_{Boiler}). This is explained below.

$$Q_{in} = Q_{in,steam} / \eta_{Boiler} = f\left(Q_{in,steam}, \eta_{Boiler}\right) \quad \textbf{(4-6)}$$

where

$$Q_{in,steam} = m_{HP} \cdot \left(h_{o,HP} - h_{i,HP}\right) + m_{CRH} \cdot \left(h_{o,CRH} - h_{i,CRH}\right) \quad \textbf{(4-7)}$$

The m_{HP}-value, together with the boiler inlet- and outlet temperature and pressure and the re-heater inlet and outlet temperature and pressure, are measured continuously. From these temperatures and pressures the enthalpies $h_{i,HP}$, $h_{o,HP}$, $h_{i,CRH}$ and $h_{o,CRH}$ are calculated. The cold re-heat (CRH) flow rate (m_{CRH}) is, however, not measured at Majuba Power Station.

According to the partial load- and full load heat balance diagrams for Majuba Power Station it is, however, possible to calculate the flow through the re-heater. The percentage of the m_{HP} that passes through the re-heater for different loads is depicted below in Figure 4-2. It is found that, at higher loads, less of the m_{HP} passes through the re-heater as m_{CRH}, and *vice versa*.

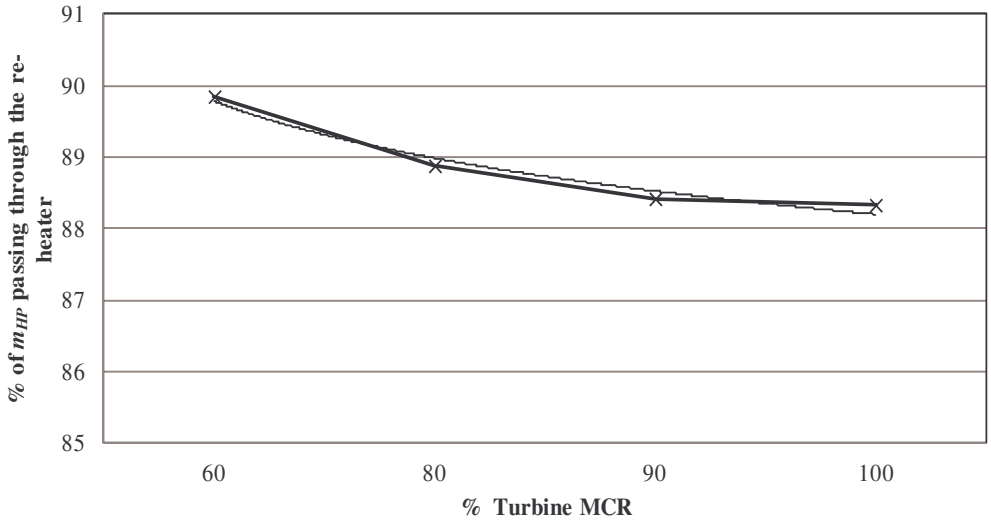

Figure 4-2: Percentage of m_{HP} passing through the re-heater (m_{CRH}) vs. % MCR at Majuba Power Station.

The equation describing this relation, provided below, is used to calculate m_{CRH}:

$$m_{CRH} = 103.8 \cdot m_{HP}^{-0.035} \quad \textbf{(4-8)}$$

For the purpose of this study, where the focus is on reducing T_L and thus p_c, the original equipment manufacturer (OEM)-specified 97 % MCR boiler efficiency of 94.40 % is used and assumed to stay unchanged at steady-state loads above 90 % MCR (η_{Boiler} is 94.62 % at 60 % MCR and 94.24 % at 100 % MCR). As a result all the parameters are either measureable or constant and it is thus straightforward to determine Q_{in}.

Another, and most probably the easiest way to determine Q_{in}, is to use the relationship between Q_{in} and m_{HP} as depicted in Figure 4-3 below. This relationship is drawn with reference to the thermal heat balance diagrams for Majuba Power Station. The relationship is found to be very linear. Using the linear trend equation in the figure, together with the 100 % MCR $Q_{in,steam}$ of 1311 MW, it is possible to calculate the partial load $Q_{in,steam}$. Using the constant η_{Boiler} discussed above it is possible to determine Q_{in} using equation (4-6). Equation (4-9) below is a correlation of the data calculated with equation (4-6).

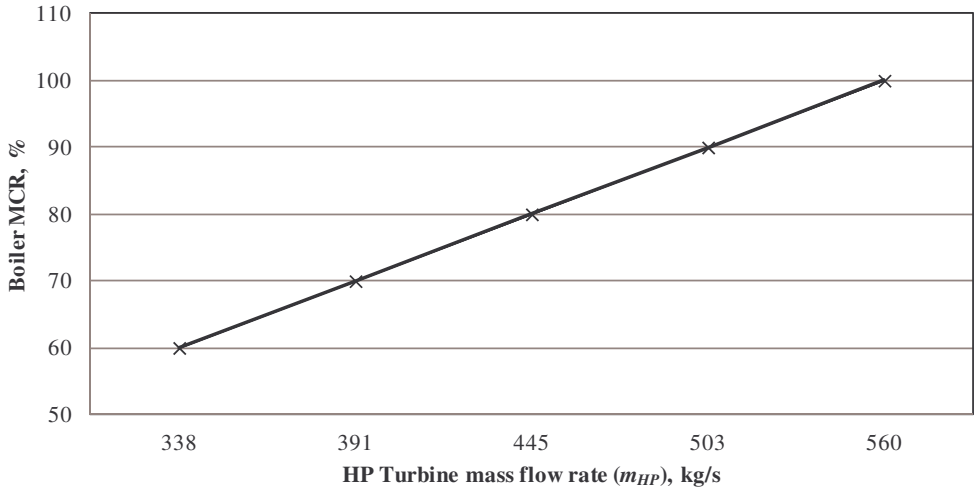

Figure 4-3: Relationship between m_{HP} and the *% MCR* of the boiler at Majuba Power Station.

Using the regression in Figure 4-3 as well as the η_{Boiler} explained above, Q_{in} is determined as follows:

$$Q_{in} = (0.18015 \cdot (m_{HP} - 338) + 60) \cdot 1311 / \eta_{Boiler} \quad \textbf{(4-9)}$$

Referring to equation (4-2), P_{st} is measured by means of voltage-transformers and current transformers on the low-voltage side of the generator transformer. At steady-state conditions the P_{aux}-value consumed by the unit is relatively constant. This parameter is thus omitted from the η_{th} analysis and it is assumed that W_{net} equals $P_{st,}$ which is the gross power (W_{gross}).

The OEM provides an empirical relationship between P_{st} and p_c, also assuming that W_{gross} equals P_{st}, which is manipulated to represent the relationship between the water-steam cycle η_{th} and p_c by dividing it with $Q_{in,100\%}$. This equation is based on a steady boiler load of 100% MCR. From the above and equation (4-1), η_{th} is found to be primarily dependent on p_c and Q_{in}:

$$\eta_{th} = f(Q_{in}, p_c) \quad \textbf{(4-10)}$$

In order to obtain a representative relationship between the water-steam cycle η_{th} and the parameters stated above from historical plant data, a regression must be performed. It is intuitive that the relationship is not linear, but by implementing various mathematical manipulations it is possible to obtain a linear relationship in order to perform a regression. The relationship between the water-steam cycle η_{th} and the parameters in equation (4-10) is stated below, where a_1 – a_3 are the parameters to be optimised with the regression.

$$\eta_{th} = a_1 \cdot Q_{in}^{\ a_2} \cdot p_c^{\ a_3} \quad \textbf{(4-11)}$$

With the use of the natural logarithm (*ln*), the equation can be manipulated to provide the following linear relationship:

$$\ln(\eta_{th}) = \ln(a_1 \cdot Q_{in}^{\ a_2} \cdot p_c^{\ a_3}) \\ = \ln(a_1) + a_2 \cdot \ln(Q_{in}) + a_3 \cdot \ln(p_c) \quad \textbf{(4-12)}$$

Solving for the variables (a_1 – a_3) in equation (4-12) above (with the use of historical plant data and equation (4-11)), yields the following relationship between the water-steam cycle η_{th} the parameters in equation Figure 4-9:

$$\eta_{th} = 7362.915 \cdot Q_{in}^{\ -0.68349} \cdot p_c^{\ -0.01944} \quad \textbf{(4-13)}$$

Using equation (4-13), the relationship between the water-steam cycle η_{th} and the p_c, with a constant Q_{in}, is predicted in Figure 4-4 below. The OEM-specification, is also presented.

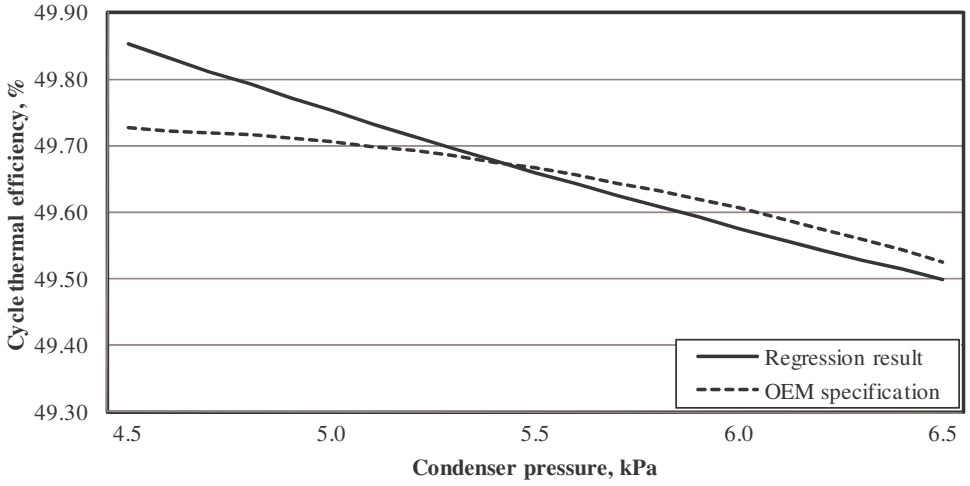

Figure 4-4: Water-steam cycle η_{th} vs. p_c at Majuba Power Station – OEM-specification and regression result.

Efficiency is found to decrease with increasing p_c, a finding that is intuitive. The regression results also relate well to the OEM-specification within the range specified in the figure. It should be noted that the OEM-specification has a more concave shape compared to the regression result, which has a more convex shape. This is attributed to the η_{th} that is not only dependent on the two parameters stated above, but also on a number of other parameters with smaller effects that are omitted for the sake of simplicity. One such parameter is the amount of auxiliary steam self-supplied by the unit and the amount of auxiliary steam drawn from the auxiliary steam range.

The relationship between η_{th} and p_c is, however, determined, and compares well to the original OEM-specification in the region of interest with the use of the minimum amount of historical plant data.

4.3. CONDENSER SATURATION PRESSURE

In the previous section the relationship between η_{th} and p_c was determined. The objective in this section is to find the relationship between the p_c and its independent variables. The p_c is a function of T_{cwi} and thus the NDWCT effectiveness, which is a function of both ambient conditions (including T_{awb}, p_a, b_T, V_W, D_W and b_W) as well as unit-specific conditions that include P_{st} and m_{cw}. This functional dependence is illustrated by equation (4-14).

$$p_c = f\left(m_{cw}, P_{st}, T_{cwi}\right) \tag{4-14}$$

where

$$T_{cwi} = f\left(m_{cw}, T_{awb}, p_a, b_T, V_W, D_W, b_W\right) \tag{4-15}$$

thus

$$p_c = f\left(m_{cw}, P_{st}, T_{awb}, p_a, b_T, V_W, D_W, b_W\right) \tag{4-16}$$

The effect of the D_W on the efficiency is minimal, which leads to the parameters being omitted in order to simplify the process. Another reason for the exclusion of this parameter is explained in section 4.4.

As explained in section 4.2 above (equations (4-11) to (4-13)), a regression is employed to obtain the relationship between p_c and the independent parameters displayed above:

$$p_c = 1.020278 \cdot T_{awb}^{\,0.348387} \cdot p_a^{\,-0.45922} \cdot b_T^{\,0.009761} \cdot V_W^{\,0.067076} \cdot b_W^{\,0.070128} \cdot m_{cw}^{\,-0.04107} \cdot P_{st}^{\,v0.649964} \tag{4-17}$$

With the use of the above equation it is possible to depict the dependence between pc and the individual parameters visually by using design specifications and varying each parameter individually. The dependence between pc and Tawb is depicted below in Figure 4-5:

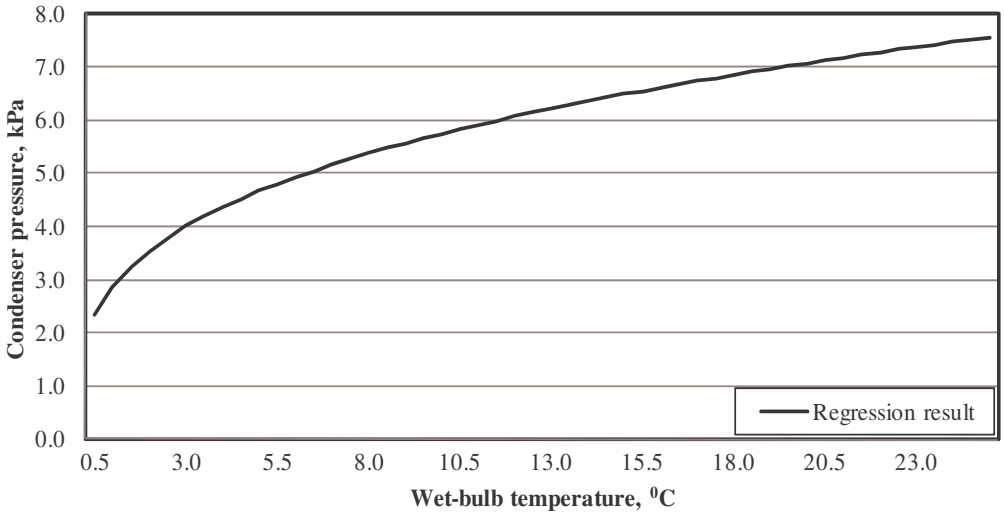

Figure 4-5: p_c vs. reference height T_{awb} at Majuba Power Station.

It is noted from the above figure that p_c is strongly dependent on T_{awb}; an observation that h is intuitive as this T_{awb} is the physical cooling limit for NDWCTs. As T_{awb} increases, the NDWCT driving force decreases; simultaneously increasing T_{cwo}.

The calculated relationship between b_T and p_c is depicted in Figure 4-6. Note the different scale used in this figure. It is found that p_c naturally increases when b_T increases. From literature it is expected that the dependence is more pronounced (Figure 3-1). Due to the positive b_T that relates to nocturnal hours mostly, when P_{st} is less due to the two-shifting and load-following running regimes which decreases p_c, the effect is more subdued.

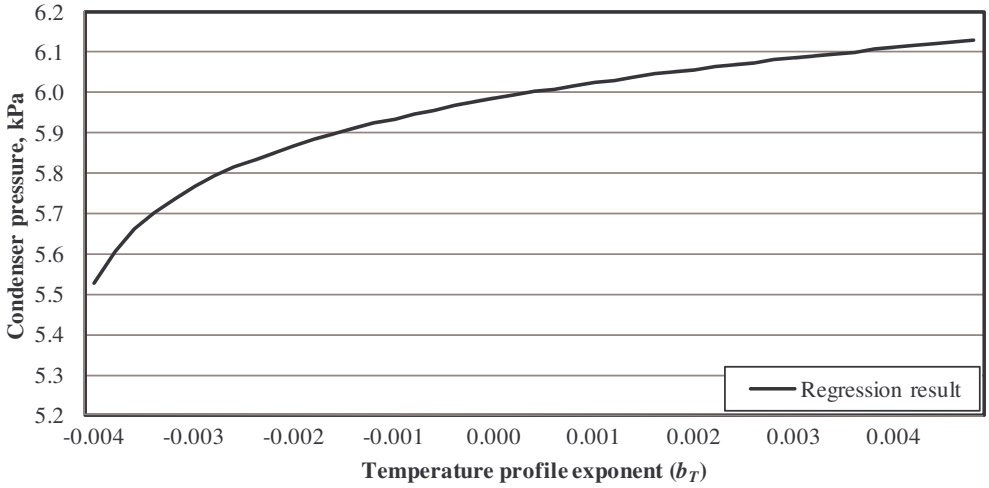

Figure 4-6: p_c vs. b_T at Majuba Power Station.

The effect of V_W on p_c is depicted in Figure 4-7 below. It is found that p_c, and thus the NDWCT effectiveness, is highly dependent on the reference height V_W. This effect is important and not well documented for all the NDWCTs in the Eskom fleet.

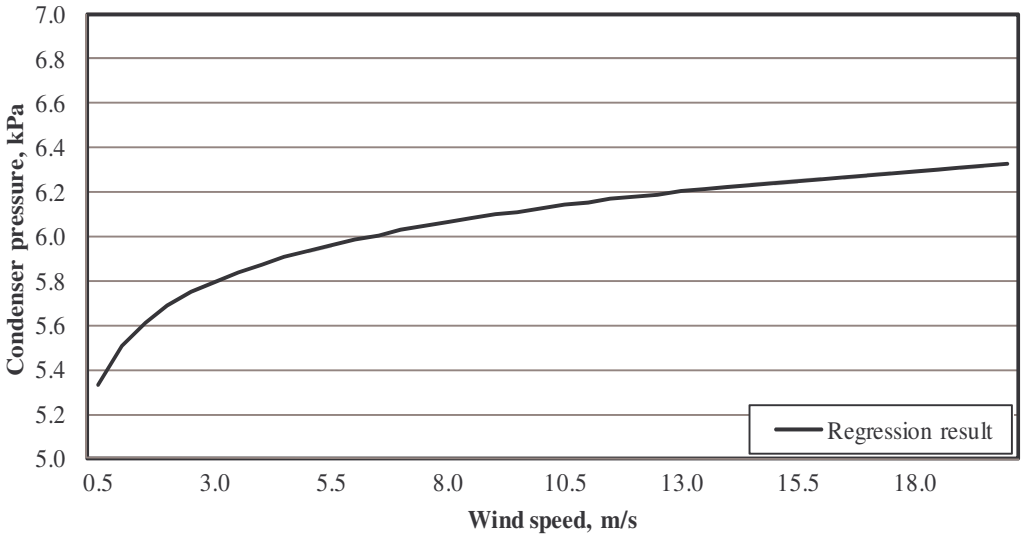

Figure 4-7: p_c vs. reference height V_W at Majuba Power Station.

Bourillot *et al.* (1980) mention that low reference height V_W-values are detrimental to the performance of NDWCTs as it destroys the well-proportioned and axisymmetric air field at the NDWCT inlet. This leads to an increase in p_c. As V_W increases, the turbulence in the NDWCT increases, which enhances the heat- and mass transfer performance and increases the NDWCT performance. This conversely leads to a reduction in p_c. This double effect is impossible to determine with the power function used in equation (4-17), but the p_c is found to flatten out at higher V_W-values, which indicates that this double effect may be present.

The effect of m_{cw} on p_c is depicted in Figure 4-8. The relationship depicts that the p_c decreases with increasing m_{cw}, which is intuitive as the ΔT across the condenser decreases as m_{cw} is increased. This is explained in more detail in chapter 6.

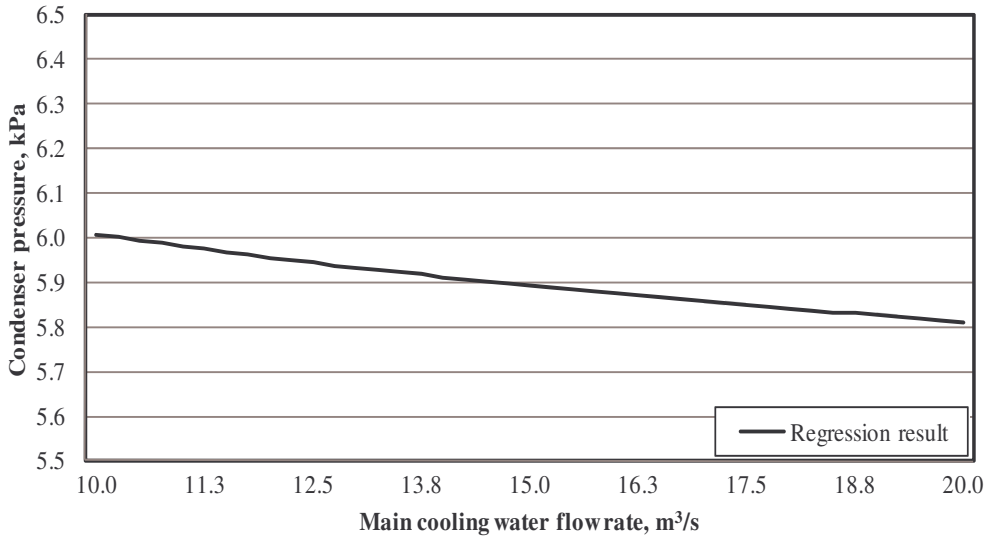

Figure 4-8: p_c vs. m_{cw} at Majuba Power Station

The effect of P_{st} on condenser back-pressure is depicted in Figure 4-9 below.

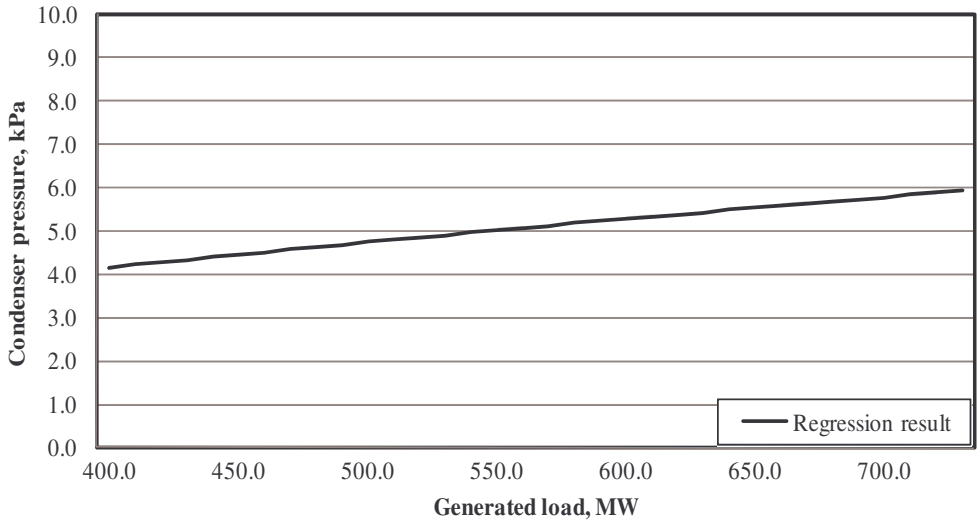

Figure 4-9: p_c vs. P_{st} at Majuba Power Station.

The figure indicates that p_c increases with an increase in P_{st}. This finding seems natural, as the amount of steam entering the condenser increases, which increases the heat load on the condenser and therefore also increases p_c.

The calculated relationship between p_c and the relevant independent parameters indicates that it is possible, with the use of the minimum amount of historical plant data, to determine the effect of independent parameters on p_c by means of a regression quickly and effectively.

4.4. CONCLUSION

Throughout this chapter the objectives set out in chapter 1 are met. These include the ability to quickly and effectively determine the functional dependence between the water-steam cycle η_{th} and the parameters that affect it, such as p_c; as well as to determine the p_c functional dependence by utilising a parametric study. These objectives are achieved by using historical plant data with a regression. The p_c results depicted throughout the chapter are accurate to within 0.1 kPa on average.

The historical plant data included all the variables that have the greatest influence on η_{th}, according to literature and the specific plant knowledge. The b_W was omitted from the dataset due to the fact that the reference height V_W was included and the functional dependence between the reference height V_W and b_W is discussed in section 2.8.2. The D_W was also omitted as the effect of the D_W could not be accurately calculated by means of the power-law equations that were implemented. It should, however, be noted that the effect of D_W on p_c will be extremely small if calculated, as depicted below in Figure 4-10, where it is found that the linear trend-line is basically constant.

In section 4.3 it was noted that the double effect of V_W on p_c, found in literature, cannot be accurately portrayed with the use of the power law equations and the corresponding multi-linear regression. It should, however, be noted that this effect is not of great interest as the higher V_W-values, where this double effect is found, is much higher than the NDWCT design specification for V_W. These high V_W values only occur for a very small period of time annually as discussed in section 2.8.

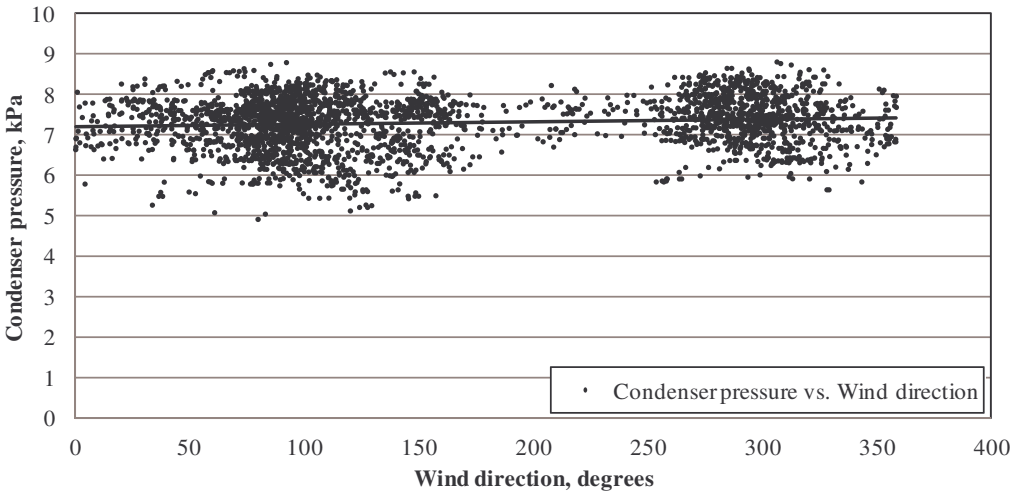

Figure 4-10: p_c vs. D_W at Majuba Power Station.

The plant-specific parameters that are required to effectively calculate the functional dependencies and to ultimately monitor the condition of the plant, explained in this chapter, are summarised in Table 4-1:

Table 4-1: η_{th} and p_c functional dependence - required parameters.

Description	Symbol	Measurement technique	Cost
Generated load	P_{st}	Current transformer (ISTAT 200)	R 10,000.00
Boiler inlet enthalpy	h_i	Calculated	R 0.00
Boiler outlet enthalpy	h_o	Calculated	R 0.00
HP steam massflow rate	m_{HP}	Pressure drop over an oriface plate	R 8,500.00
Boiler efficiency	η_{boiler}	OEM specification	R 0.00
Condenser pressure	p_c	Pressure transducer	R 8,500.00
Cooling water mass flow rate	m_{cw}	Pressure drop over an oriface plate	R 10,000.00
Wet-bulb temperature	T_{awb}	Thermistor	R 5,500.00
Atmospheric pressure	p_a	Pressure transducer	R 7,500.00
Temperature profile exponent	b_T	Calculated as explained in chapter 2	R 0.00
Reference height wind speed	V_W	Anemometer	R 15,000.00
Reference height wind direcion	D_W	Anemometer	R 15,000.00

It should be noted that some of the parameters that are provided in Table 4-1 are only used due to the unavailability of online measurement instrumentation for the preferred variables. An example of this is given early in chapter 4 where the total boiler heat-input is not determined by using the coal parameters, but rather by using $Q_{in,steam}$ and η_{boiler}, or by using the relationship between m_{HP} and the boiler load.

In conclusion it may be noted that this technique can be used at other sites in order to quickly and effectively determine the functional dependencies between the power plant efficiency and its independent variables in order to accurately determine the lifecycle cost impact of improvements made to NDWCT design as well as during NDWCT retrofits.

CHAPTER 5
MODELLING MAJUBA POWER STATION'S NDWCTs

5.1. INTRODUCTION

The performance of NDWCTs is dependent on various parameters. These parameters include geometry, meteorological conditions (Ding, 1992), NDWCT internals such as packing, sprayers, structures and drift eliminators, T_{cwo} and m_{cw}. Predicting the effectiveness of NDWCTs is usually accomplished by means of modelling the mathematical relationships between the effectiveness and the dependent parameters.

The 1-dimensional (1-D) NDWCT model that is discussed in section 5.2 is an example of such a model. This model has been used extensively by Kröger (1998) for NDWCT effectiveness calculations. Some of the mathematical relationships implemented in this model are, however, empirical and thus not completely representative. In addition the influence of independent variables on the NDWCT effectiveness, including as V_W and D_W, is continuously under investigation. This entails that certain influential relationships are not part of the mathematical model and are still investigated to gain a better understanding of the dynamics involved.

In the light of these mathematical prediction models' limitations, a need exists for the development of NDWCT models that can accurately predict the effectiveness of NDWCTs in order to improve already accurate mathematical models such as the 1-D model in specific areas. This includes all relationships between effectiveness and the various independent parameters.

Artificial Neural Networks (ANN) present an attractive method of determining relationships between data. These networks do not find any mathematical relationship between data, but rather examine the N-dimensional space created by the data (each variable represents one dimension). It locates the optimum point in this N-dimensional space representing the best prediction parameters for the network model. A trained ANN can be used to approximate the mathematical correlations between data and to evaluate the influence of individual parameters on NDWCT effectiveness. Appendix C provides more information regarding the theoretical fundamentals of ANNs.

The researcher aims to discuss and compare the 1-D mathematical- and ANN model that was created for Majuba Power Station's NDWCTs. The theory behind the 1-D mathematical model is discussed in Section 5.2. This section references to the 1-D model sample calculations presented in appendix B, which provides the reader with information and results for the model under design conditions and under improved conditions (discussed in section 6.5).

In section 5.4 the ANN is discussed. This discussion includes the model architecture, the dataset manipulations and the results obtained for the training and testing phases. Both the 1-D and ANN model are compared in section 5.5, which provides an independent variable sensitivity analysis using the trained ANN as well as the 1-D model. It should be noted that this ANN is set up in a similar

manner to the conventional 1-D mathematical model. This is, however, not necessarily the optimum way to set up an ANN, but it provides an effective comparison between the two different models.

The section is concluded with a discussion of the advantages and disadvantages of an ANN as a NDWCT efficacy prediction tool; and the use of an ANN to improve the existing 1-D mathematical model that overestimates the effectiveness of the NDWCT at Majuba Power Station consistently. Some of the reasons for this overestimation are discussed in section 5.5. A more effective way to set up an ANN is also discussed, and lastly the parameters required setting up an effective NDWCT-ANN are discussed. The main section objectives are summarised in section 1.2.

5.2. NDWCT ANN LITERATURE STUDY

The use of ANNs in predicting the performance on NDWCTs has been studied by Hozos, Ertune & Bulgurcu (2007). The research shows that ANNs can be used to accurately predict the performance of NDWCTs once sufficiently trained. The effect of independent parameters on the overall performance of the NDWCT can also be evaluated accurately and can be used to improve more conventional mathematical models.

The performance prediction of NDWCTs using ANN under cross-wind conditions has been studied by Gao, Sun, Zhou, Shi, Zhao & Wang (2008) with good results. Most of these studies were, however, conducted in a controlled environment and not in a real life scenario such as at Majuba Power Station's NDWCTs.

Kůrková, Steele, Neruda & Kárný (2001) also conducted experiments on a pilot cooling tower in combination with a representative mathematical model to estimate volumetric heat transfer coefficients for different operating conditions. The functional dependence between the coefficients and the model inputs were modelled by means of an ANN and non-linear regression with the ANN yielding more accurate results. They also propose a hybrid concept of incorporating the ANN into the mathematical model in order to improve the accuracy of the model.

5.3. MAJUBA POWER STATION's 1-D MATHEMATICAL NDWCT MODEL

5.3.1. Introduction

In an attempt to determine the performance characteristics of Majuba Power Stations' NDWCTs, a number of different models have been developed. These include one-, two- and three-dimensional models. All of these models, however, use simplifying assumptions and make use of empirical and experimental data to reduce the complexity thereof. The results obtained with the "multi-dimensional" numerical codes are thus not necessarily always better than those obtained by the application of extended 1-D point models, which can potentially produce results of a relatively high degree of accuracy (Kröger, 1998). The use of 1-D models is, however, restricted to cases where the NDWCT's fill is uniform throughout,

entailing that the flow through the tower is essentially uniform. This is indeed the case at Majuba Power Station and it serves as motivation for using a 1-D method of analysis in modelling the NDWCTs at Majuba Power Station.

The 1-D NDWCT model explained in this section is programmed to determine the heat rejection rate and water evaporation loss of a NDWCT under specific ambient- and inlet conditions. The Merkel method for heat- and mass transfer in the fill is employed for the determination of these transfer parameters. This method includes an improved energy equation that determines the heat rejection rate of the cooling tower and incorporates the energy associated with water evaporation.

A discussion of the theory used to create the 1-D model is presented in this section, and includes sections regarding the conservation of energy, mass and momentum. The optimisation strategy is also discussed, followed by evaluations of the Majuba Power Station-specific 1-D model alterations and the Majuba NDWCT 1-D model sample calculations.

The main NDWCT dimensions and -areas that are used in the model are depicted in Figure 5-1:

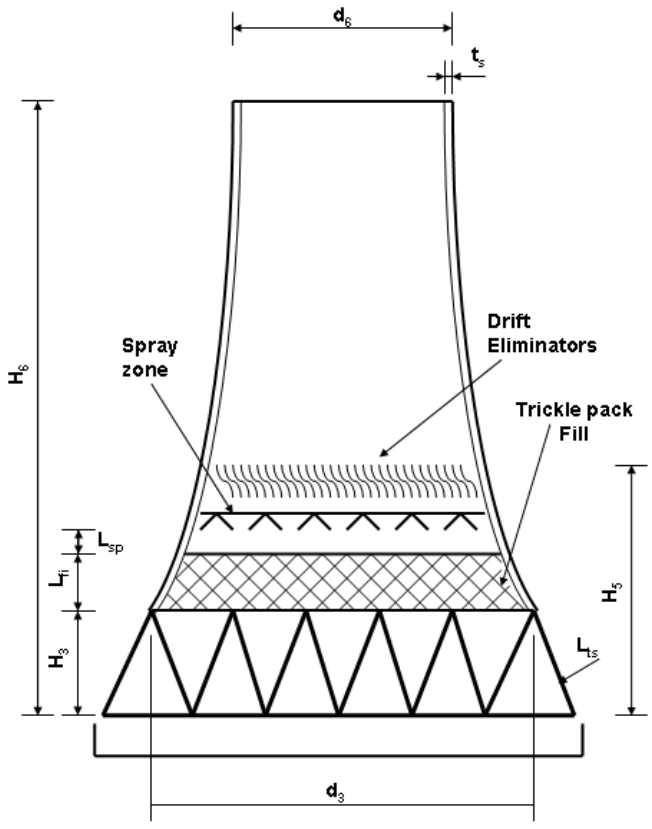

Figure 5-1: Majuba Power Station's NDWCT dimensions.

5.3.2. Merkel method of analysis with an improved energy equation

Conservation of energy and mass

Throughout the 1-D model the Merkel method for heat- and mass transfer in the fill is used. Merkel makes a number of critical assumptions that eases the calculations in the model. One of these assumptions is that the state of the air exiting the fill region is saturated. Throughout the derivation of his dimensionless governing equations for heat- and mass transfer in a counter flow NDWCT, equations (5-1) and (5-2), he makes two more critical assumptions, namely:

- The Lewis factor is equal to unity; and
- The reduction in water flow rate due to evaporation is neglected.

With these assumptions Merkel derived his governing equations for heat- and mass transfer

$$\frac{di_{ma}}{dz} = \frac{h_d a_{fi} A_{fr}}{m_a}\left(i_{masw} - i_{ma}\right) \tag{5-1}$$

and

$$\frac{dT_w}{dz} = \frac{m_a}{m_w}\frac{1}{c_{pw}}\frac{di_{ma}}{dz} \tag{5-2}$$

It is not possible to calculate the state of the air leaving the fill with equations (5-1) and (5-2) alone as at least two properties are required to make this calculation. As stated, Merkel makes the assumption that the air leaving the fill is saturated; enabling him to determine the temperature and density of the air and the draft accordingly.

Merkel then combines equations (5-1) and (5-2) to form the so-called "Merkel's equation" and the dimensionless coefficient of performance ($h_d a_{fi} L_{fi}/G_w$) is known as the "Merkel number". This is represented by equation (5-3):

$$\begin{aligned} Me &= \frac{h_d A}{m_w} = \frac{h_d a_{fi} A_{fr} L_{fi}}{m_w} = \frac{h_d a_{fi} L_{fi}}{G_w} = \int_{T_{wo}}^{T_{wi}} \frac{c_{pw}\, dT_w}{\left(i_{masw} - i_{ma}\right)} \\ &\approx \frac{c_{pwm}\left(T_{wi} - T_{wo}\right)}{4}\left(\frac{1}{\Delta i_{(1)}} + \frac{1}{\Delta i_{(2)}} + \frac{1}{\Delta i_{(3)}} + \frac{1}{\Delta i_{(4)}}\right) \end{aligned} \tag{5-3}$$

The integral in equation (5-3) needs to be solved numerically. Many different numerical techniques are discussed by Kloppers & Kröger (2005b) but they found that the Chebyshev technique yields very accurate results compared to other techniques. When one applies the Chebyshev numerical integration method to the Merkel equation, the approximation displayed above is yielded. In this

approximation the enthalpy differentials are dependent on the following intermediate temperatures:

$$\begin{aligned} T_{w(1)} &= T_{wo} + 0.1(T_{wi} - T_{wo}) \\ T_{w(2)} &= T_{wo} + 0.4(T_{wi} - T_{wo}) \\ T_{w(3)} &= T_{wo} + 0.6(T_{wi} - T_{wo}) \\ T_{w(4)} &= T_{wo} + 0.9(T_{wi} - T_{wo}) \end{aligned} \tag{5-4}$$

For the calculation of i_{ma} equation (5-2) may be manipulated to give the following:

$$\begin{aligned} m_a \, di_{ma} &= m_w \, c_{pwm} \, dT_w \\ di_{ma} &= \frac{m_w \, c_{pwm} \, dT_w}{m_a} \end{aligned} \tag{5-5}$$

The Merkel equation (5-3) can now be applied to the NDWCT to determine the transfer coefficients. The reader is, however, reminded that the NDWCT's heat- and mass transfer area is divided into three distinct areas, namely the spray zone (*sp*), the fill zone (*fi*) and the rain zone (*rz*). The Merkel equation thus needs to be applied to all three sections in order to obtain the overall transfer coefficients. Equation (5-3) is manipulated to incorporate all three sections as follows:

$$\begin{aligned} &Me_{sp} + Me_{fi} + Me_{rz} \\ &= \frac{h_{sp} \, a_{sp} \, A_{sp} \, L_{sp}}{m_w} + \frac{h_d \, a_{fi} \, A_{fr} \, L_{fi}}{m_w} + \frac{h_{drz} \, a_{rzi} \, A_{fr} \, L_{rz}}{m_w} \\ &= \int_{T_{wo}}^{T_{wi}} \frac{c_{pw} \, dT_w}{(i_{masw} - i_{ma})} \end{aligned} \tag{5-6}$$

With equation (5-6) it is possible to calculate T_{cwo}. Once T_{cwo} is known, it is possible to calculate the rate of heat rejection by the NDWCT. As discussed earlier, an improved energy equation is used to determine the heat rejection rate, given by:

$$\begin{aligned} Q_w &= m_w \, c_{pwi} (T_{wi} - 273.15) \\ &- [m_w - m_a (w_5 - w_1)] c_{pwo} (T_{wo} - 273.15) \end{aligned} \tag{5-7}$$

This heat rejection rate must be similar to the heat rejection rate of the air for the model to be convergent. This heat rejection rate is simply given by:

$$Q_a = m_a (i_{ma5} - i_{ma1}) \tag{5-8}$$

Once these two heat rejection rate values are equal to an acceptable degree of accuracy agreeable amount of accuracy, the heat balance is satisfactory and it is then imperative that a momentum balance be verified.

Conservation of momentum

The momentum equilibrium can be found where the pressure differential at the mean fill height between the inside and outside of the NDWCT equals the summation of the pressure drops across all the flow restrictions. This equation is defined by Kröger (1998) as the "draught equation" and is given by:

$$\begin{aligned}&(p_{a1}-p_{a7})-(p_{a1}-p_{a34})-(p_{a34}-p_{a6})-(p_{a6}-p_{a7})=\\&\left(\begin{array}{l}K_{tsfi}+K_{ctfi}+K_{rzfi}+K_{fsfi}+K_{ctcfi}+\\K_{fi}+K_{ctefi}+K_{spfi}+K_{wdfi}+K_{defi}\end{array}\right)\times\\&\frac{\left(\frac{m_{av15}}{A_{fr}}\right)^2}{2\rho_{av15}}+\alpha_{e6}\frac{\left(\frac{m_{av6}}{A_{fr}}\right)^2}{2\rho_{av6}}\end{aligned} \qquad \textbf{(5-9)}$$

These pressure drops on the left-hand side of equation (5-9) are given by Kröger (1998) as:-

$$(p_{a1}-p_{a7})=p_{a1}\left[1-\left(1+DALR\frac{H_6}{T_{a1}}\right)^{3.5(1+w_1)\left(1-\frac{w_1}{w_1+0.62198}\right)}\right] \qquad \textbf{(5-10)}$$

$$(p_{a1}-p_{a34})=p_{a1}\left[1-\left(1+DALR\frac{H_3+L_{fi}/2}{T_{a1}}\right)^{3.5(1+w_1)\left(1-\frac{w_1}{w_1+0.62198}\right)}\right] \qquad \textbf{(5-11)}$$

$$(p_{a34}-p_{a6})=p_{a5}\left[1-\left(1+\xi_{Ta5}\frac{H_6-H_3-0.5L_{fi}}{T_{a5}}\right)^{\frac{-0.021233(1+w_5)}{\xi_{Ta5}(w_5+0.62198)}}\right] \qquad \textbf{(5-12)}$$

$$(p_{a6}-p_{a7})=\left(0.02Fr_D^{-1.5}-\frac{0.14}{Fr_D}\right)\frac{\left(\frac{m_{av5}}{A_6}\right)^2}{\rho_{av6}} \qquad \textbf{(5-13)}$$

With equations (5-10) through (5-13) it is possible to solve the draught equation (5-9). This equation is solved by equating the left- and right-hand sides and iterating until these sides have converged. This is the same process that is

followed with the conservation of energy and mass discussed in the previous section. It is clear that this iterative solution is rather complicated, and for this reason the optimisation strategy followed to find the solution is explained in the following section.

5.3.3. Optimisation strategy

As explained in the previous section, the 1-D model is solved once the conservation of energy and momentum have individually converged. To find this solution a number of variables are continuously changed until the optimum solution is reached. A downward simplex algorithm optimiser is used for this analysis. The reason for this choice is that this optimiser is easy to implement as it only needs an objective function and an initial guess for the design variables used in the optimisation. No constraints are necessary for the optimisation. The design variables that are used in the optimiser are the following:

- Mean air vapour mass flow rate through the fill, m_{av15}
- Static pressure after the drift eliminators, p_{a5}
- Air temperature after the drift eliminators, T_{a5}
- Water-outlet temperature, T_{cwo}
- Static pressure at the tower outlet, p_{a6}

These design variables are used to optimise the objective function that is only a minimum function between iterations and is given by:

$$f_{min} = \left|\left[\left(Q_w - Q_a\right) \div Q_w\right]\right| + \left|\left[\left(Draught_{lhs} - Draught_{rhs}\right) \div Draught_{lhs}\right]\right| + \left|\left[\left(p_5 - p_{5new}\right) \div p_5\right]\right| + \left|\left[\left(p_6 - p_{6new}\right) \div p_6\right]\right| + \left|\left[\left(Metot - Meint\right) \div Metot\right]\right| \quad \textbf{(5-14)}$$

where

$Draught_{lhs}$, $Draught_{rhs}$ = Left- and right-hand side of equation (5-9), Pa

Q_a = Heat rejection rate of air, equation (5-8)

Q_w = Heat rejection rate, equation (5-7)

Me_{int} = Merkel number, right-hand side of equation (5-6)

Me_{tot} = Merkel number, left-hand side of equation (5-6)

$$p_{a5} = p_{a1}\left[1 + \frac{DALR\left(H_3 + L_{fi}/2\right)}{T_{a1}}\right]^{\left(3.5(1+w_1)\left(1 - \frac{w_1}{w_1 + 0.62198}\right)\right)} - \left(K_{tsfi} + K_{ctfi} + K_{rzfi} + K_{fsfi} + K_{fi} + K_{ctefi} + K_{spfi} + K_{wdfi} + K_{defi}\right)\frac{\left(\frac{m_{av15}}{A_{fr}}\right)^2}{2\rho_{av15}} \quad \textbf{(5-15)}$$

$$p_{a6} = p_{a7}\left(0.02\,Fr_D^{-1.5} - \frac{0.14}{Fr_D}\right)\frac{\left(\frac{m_{av5}}{A_6}\right)^2}{\rho_{av6}} \quad \textbf{(5-16)}$$

The initial conjecture for the design variables is determined as follows:

- The initial value for m_{av15} is chosen to be 3.5 times the value of the frontal area of the fill (A_{fr}). The reason for this decision is that the maximum air-charge through the NDWCT that can be expected is about 3.5 times the value of A_{fr}, with the normal value normally in the region of 1.5 to 2 times that of A_{fr}.
- The initial value for p_{a5} is determined by the following equation:

$$p_{a5} = p_{a1} - \rho \cdot g \cdot H_5 \quad \textbf{(5-17)}$$

- The initial guess for p_{a6} is determined in the same manner as for p_{a5} with H_6.
- The value for T_{a5} is initially calculated according to the DALR using T_{a1} at 1 m AGL. as well as the height to the top of the drift eliminators, h_5.
- The T_{cwo}, is initially chosen to be equal to the T_{awb} at ground level; T_{awb1}.

5.3.4. 1-D Model alterations

For the entire design of Majuba Power Station's 1-D mathematical model, a sample calculation provided by Kröger (1998) was used. During the initial testing of Majuba Power Station's NDWCT 1-D model, which included comparing the 1-D model results to performance test guarantees, the model provided accurate results. It was, however, noted that the model provided erroneous results once the optimised m_{av15} was lower than approximately 8000 kg/s. The reason for this is due to the rain zone correction coefficient (C_{RZ}).

This empirical coefficient (Kröger, 1998) is used as a correction factor in order to obtain the correct inlet-loss coefficient in the presence of a rain zone, as explained in appendix B and Kröger (1998). The empirical relationship between C_{RZ} and m_{av15}, however, illustrates that C_{RZ} becomes negative at lower m_{av15} values. This is portrayed by Figure 5-2.

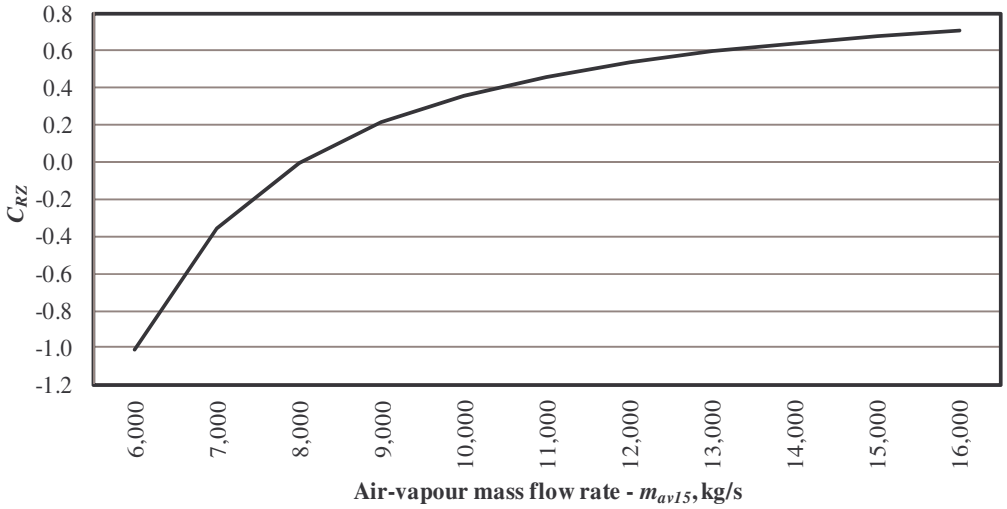

Figure 5-2: Empirical relationship between C_{RZ} and m_{av15}

Due to the fact that the re-evaluation of this empirical relationship was not part of the initial scope of research, it was decided to eliminate the potential errors by setting C_{RZ} equal to 1. The consequence of this change is discussed in section 5.5.

5.3.5. 1-D model results

The sample calculations of the 1-D NDWCT model are presented in appendix B. The first sample calculation provides a step-by-step answer sheet that readers may use to verify the model's accuracy using design specifications. The second sample calculation provides the answers for an improved 1-D model. The proposed improvements are discussed in section 6.5 below.

5.4. MAJUBA POWER STATION's ANN NDWCT MODEL

In this section the researcher discusses the NDWCT-ANN dataset description as well as the program architecture and the ANN training and testing phase results. The ANN theory is provided in appendix C.

5.4.1. ANN dataset description

In order to set up an ANN the correct data should be used. As explained in section 2.1, NDWCTs are dependent on a number of parameters. All of these parameters form part of the ANN dataset as inputs in order to train an accurate ANN. NDWCT effectiveness is determined by evaluating the cooling water temperature range ($T_{cwi} - T_{cwo}$). Due to the fact that the 1-D mathematical model, discussed in section 5.2, predicts T_{cwo} using T_{cwi} and the other relevant independent variables as inputs, it was, however, decided to set up this ANN to predict T_{cwo} instead of the cooling range to aid in the comparison of the two models. The T_{cwo} thus forms the output of the ANN. The inputs and outputs used to train the ANN for Majuba Power Station's NDWCTs are depicted in Table 5-1 below.

Table 5-1: Majuba Power Station's NDWCT-ANN dataset configuration.

Variables	I/O	Symbol	Units	Sub-sets				
				1	2	3	4	5
Average wind speed	I	V_W	m/s	0.30	0.31	0.32	0.34	0.31
Average wind direction	I	D_W	0	0.91	0.90	0.94	0.89	0.90
Average dry-bulb temperature	I	T_a	^{0}C	0.41	0.41	0.42	0.42	0.43
Average wet-bulb temperature	I	T_{awb}	^{0}C	0.45	0.46	0.44	0.47	0.50
Atmospheric pressure	I	p_a	hPa	0.25	0.26	0.24	0.30	0.32
Relative Humidity	I	RH	%	0.54	0.56	0.56	0.55	0.54
Rainfall	I	RF	mm	0.00	0.00	0.00	0.00	0.00
Cooling tower inlet flow rate	I	m_{cw}	m^3/s	0.88	0.95	0.96	0.97	0.89
Cooling tower inlet CW temperature	I	T_{cwi}	^{0}C	0.85	0.86	0.85	0.84	0.83
Average generator MW	I	P_{st}	MW	0.92	0.93	0.89	0.86	0.92
Cooling tower pond temperature	O	T_{cwo}	^{0}C	0.55	0.52	0.54	0.55	0.56

The average P_{st} is notably part of the dataset as the wet cooling system at Majuba Power Station is common to three units. Majuba Power Station is a two-shifting and load-following station, which means that some of these three units can be off-load at any time and the load varies throughout the day depending on the demand. The average P_{st} indicates whether some of these units are off-load, and if that is the case, what the effect of that is on the NDWCT effectiveness.

The data that is used in this discussion were collected over a period of 1 month from 18 August 2009 to 22 September 2009. The entire dataset consists of 4750 sub-sets; which are datasets within the main dataset that represent average parameter data for a specific time. The data is averaged every 10 minutes on the same basis as discussed in section 2.3.2. The reason for averaging the data is to minimise the size of the dataset because ANN functional evaluations (epochs) are expensive in a computational level especially if a large number of input parameters are present.

The dataset is also scaled in accordance with a process explained in equation (5-18):

$$z = (x - x_{\min})/(x_{\max} - x_{\min}) \tag{5-18}$$

The dataset explained above is split into two separate datasets representing the datasets to be used during the training and testing phases of the ANN. During the training phase the data is used to train the ANN, and during the testing phase the performance of the ANN is evaluated by means of the testing dataset. The ratio of the split is respectively 80% and 20% for the training- and testing datasets.

5.4.2. ANN model programme architecture

A three layer back-propagation (BP) network is employed for Majuba Power Station's NDWCT-ANN model, which is established using the freeware package, Scilab's, Artificial Neural Network Toolbox. One hidden layer is used and is sufficient to train an N-dimensional network. The input layer consists of 10 nodes that are described in Table 5-1 above. The output layer consists of 1 node that is

the NDWCT T_{cwo} explained in Table 5-1. The hidden layer consists of 4 nodes that are determined by means of equation (5-19) below, as presented by Gao *et al.* (2008):

$$Layers_{\ Hidden} = ceil\left(\sqrt{Input_{\ layersize} \times Output_{\ layersize}}\right) \quad \textbf{(5-19)}$$

As stated in appendix C, section C.5, the network is trained by manipulating the relevant weights and thresholds of the individual neurons for the second and third layer. The first layer represents the inputs, which are not manipulated during the training process. The minimum and maximum for the weights is defined as -1 and +1 respectively, while the threshold is defined as 0. This makes the network extremely sensitive. It also ensures that the ANN model is trained by only manipulating the weights of the individual neurons, which makes the training process less computationally expensive.

The number of functional evaluations is limited to 100 000 epochs, while the finite difference convergence criteria is defined as 1, which entails that the training phase will be halted once the network is trained to predict the output to within a scaled cumulative error of 1. This finite difference is determined by means of the cumulative sum-of-squares error (mean square error (MSE)) between the actual network targets "*t*" and the trained network outputs "*y*". This is explained by equation (5-20) below.

$$MSE = \frac{1}{N}\sum_{i=1}^{N}\left(t_i - y_i\right)^2 \quad \textbf{(5-20)}$$

where

N = number of datasets

t_i = target outputs

y_i = trained outputs

A correlation coefficient (R), which is a measure of how well the variation in the trained outputs is explained by the experimental values, is also used to assess the overall agreement between the trained- and target outputs. A value for R close to +1 indicates a strong agreement of trained- and target values, while a value close to -1 indicate a strong disagreement between these two parameters. The correlation coefficient is explained in equation (5-21) below.

$$R = \frac{\mathrm{cov}(t, y)}{\sqrt{\mathrm{cov}(t,t)\cdot\mathrm{cov}(y,y)}} \quad \textbf{(5-21)}$$

where

$$\text{cov}(t, y) = E\left[(t - \mu_t)(y - \mu_y)\right] \quad \textbf{(5-22)}$$

$$\text{cov}(t, t) = E\left[(t - \mu_t)^2\right] \quad \textbf{(5-23)}$$

$$\text{cov}(y, y) = E\left[(y - \mu_y)^2\right] \quad \textbf{(5-24)}$$

cov = Covariance
μ_t = Mean value of the target values
μ_y = Mean value of the trained values
E = Expected value

The MSE is determined for the training- and testing phases and then compared. These two errors need to be similar for the network to be accurate in predicting outputs. This accuracy will be reflected by the value of *R*.

The ANN is trained with the Conjugate Gradient optimisation algorithm, employing a logistic activation function for the individual neurons (section C.5). This is the default neuronal activation function.

5.4.3. Majuba Power Station's NDWCT-ANN results

The correlation analysis for the training- and testing phases are evaluated below. This is followed by a discussion regarding the capabilities of the trained ANN in predicting the performance of Majuba Power Station's NDWCTs with respect to various independent variables.

Training results

The ANN training phase is governed by the amount of functional evaluations as well as the finite difference (MSE) as explained in section 5.4.2 above.

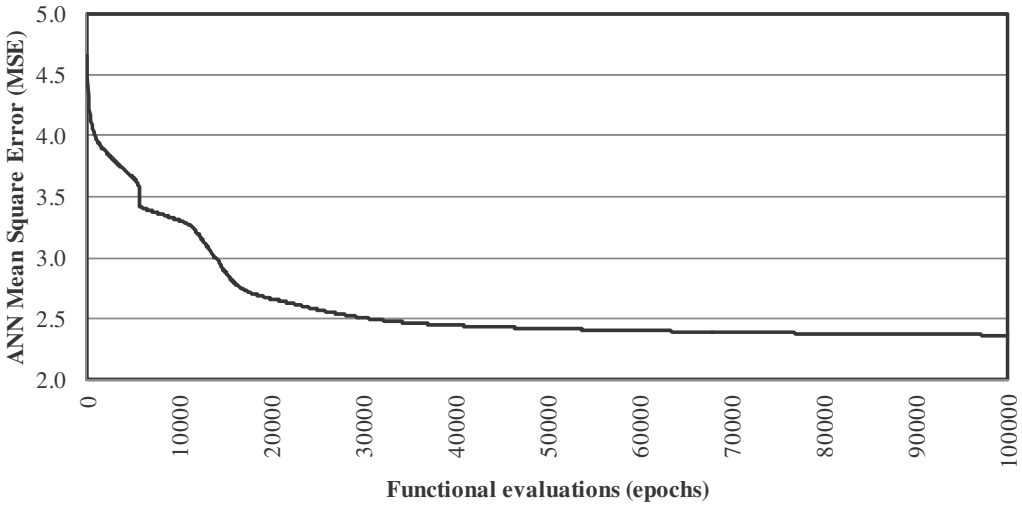

Figure 5-3: Majuba Power Station's NDWCT-ANN training phase Mean Square Error (MSE)

The network training phase MSE is depicted in Figure 5-3. The MSE is still higher than 1.0 after the 100 000 epochs. This entails that the network training was stopped by the amount of epochs and not by the finite difference MSE. From the figure above it is clear that the change in error is extremely small from 50 000 epochs to 100 000 epochs. When extrapolating the error it is found that about 250 000 epochs will be required to provide a nearly converged solution. These epochs are, however, computationally expensive and the training process is therefore fixed at 100 000 epochs.

The correlation curve for T_{cwo} during the ANN training phase is depicted in Figure 5-4 below. This figure contains a 45° dotted line ($A=T$) which represents the line on which the actual values are equal to the trained values.

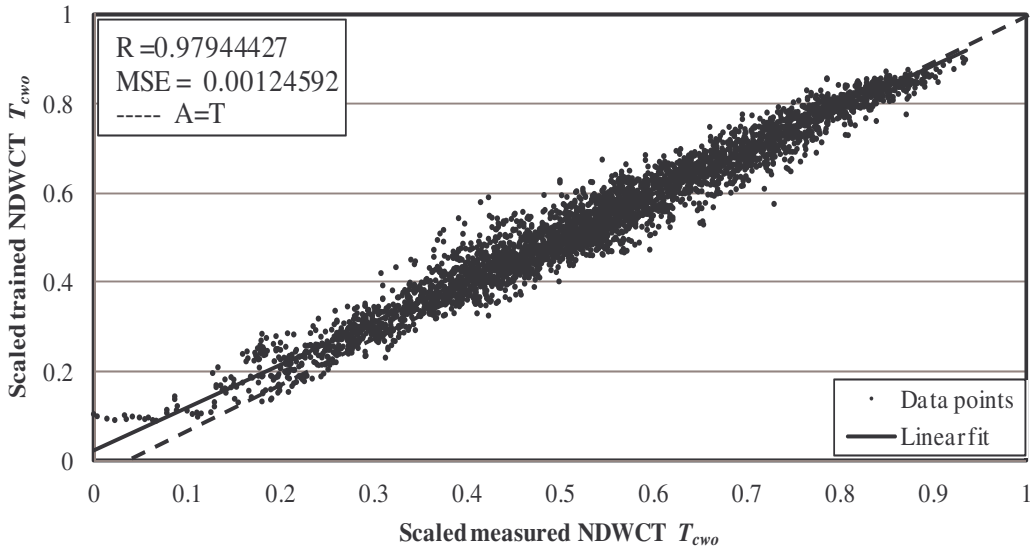

Figure 5-4: Scaled trained NDWCT T_{cwo} vs. measured T_{cwo}

Figure 5-4 illustrates that the ANN predicts the actual NDWCT pond temperature quite accurately, with a final MSE of 0.00124592. The corresponding correlation coefficient, R, is 0.97944427. This confirms the prediction accuracy. The linear fit through the data depicted in Figure 5-4 indicates that the trained network results are extremely close to the 45° line ($A=T$), which further motivates the accuracy of the trained results.

The area in Figure 5-4 which indicates the largest error is between 0.3 and 0.7 on the x-axis. This is the area in which the NDWCT mostly operates and therefore it is also the area that represents the most data. It is furthermore the area that will receive the most training. It is thus natural that this area will have some outliers because of system transients, measurement equipment errors and training errors. There is, however, room for improvement considering the accuracy of the above results, which is essentially dependent on the number of epochs used in the training phase.

Testing results

The correlation curve for the NDWCT T_{cwo} during the ANN testing phase is depicted in Figure 5-5 below. These results are obtained from using the trained ANN and testing it with a new set of data, as explained in section 5.4.1. The figure also contains a 45 ^{o} dotted line ($A=T$) that represents the line on which the actual values are equal to the trained values.

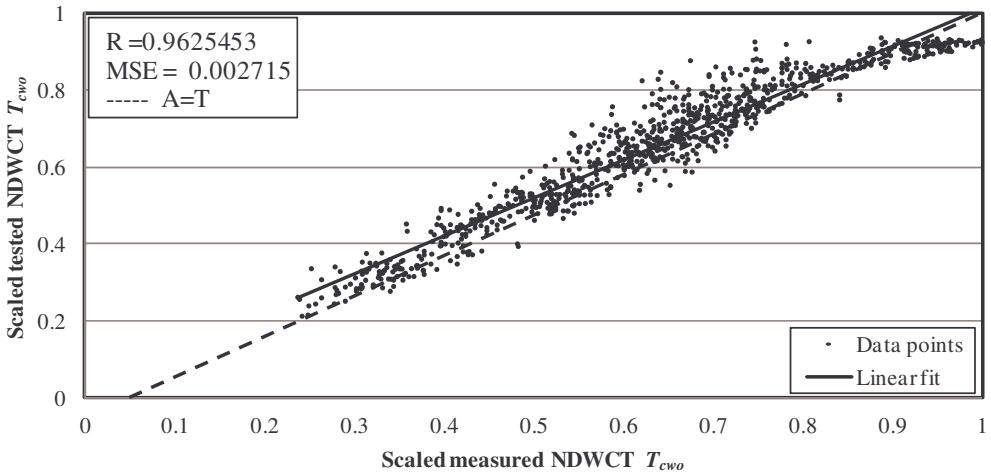

Figure 5-5: Scaled tested NDWCT T_{cwo} vs. measured T_{cwo}

From Figure 5-5 above the MSE is 0.002715 and R of 0.9625453. These parameters confirm the agreement between the measured and tested cooling water temperature, as is the case with the training results depicted in Figure 5-4. It should be noted that the MSE and correlation coefficient, R, is respectively higher and lower compared to the training phase results. The reason for this is explained below.

The section in Figure 5-5 that depicts the largest deviation is from 0.5 to 0.8 on the x-axis. This shows that the NDWCTs at Majuba Power Station were operating at a higher temperature for the testing phase dataset. This section has not received as much training as the section discussed previously during the training phase. This is the main reason why this section shows larger errors during the testing phase compared to the training phase. It is submitted that if a full year's worth of data was used, the testing phase results should be slightly more accurate.

The overall comparison is, however, relatively accurate, as shown by R and the linear fit in Figure 5-5, which indicates that the tested results are very close to the 45 ^{o} dotted line ($A=T$) on average.

Discrepancies between training and testing results

In the previous two sections it is shown that the ANN testing phase results show a larger scatter compared to the ANN training phase results. The reason for this discrepancy is the fact that the testing phase utilises datasets that are different, in terms of values and combinations of values, to those used in the training phase.

Put differently the training dataset does not necessarily include the entire range for specific parameters or all the different combinations between the different parameters that are used in the testing phase. The ranges are highlighted in Table 5-2, which depicts the minimum and maximum values for the specific parameters used in the training and testing phases.

Table 5-2: ANN dataset minimum and maximum values.

Paramter	Units	Training dataset		Testing dataset	
		Min	Max	Min	Max
Wind speed	m/s	1.0	18.1	1.3	10.8
Wind direction	0	4	357	13	351
Ambient dry-bulb temperature	^{0}C	-4.4	28.9	3.0	28.9
Ambient wet-bulb temperature	^{0}C	-4.9	21.0	-4.9	21.0
Atmospheric pressure	hPa	830.0	838.0	831.0	836.0
Relative humidity	%	2.06	97.80	3.92	97.70
Rainfall	mm	0.00	1.00	0.00	0.00
CT mass flow rate	m^3/s	8.67	19.73	11.03	20.24
CT inlet CW temperature	^{0}C	16.83	38.67	16.83	40.83
Average generator MW	MW	150.27	709.40	150.00	714.00

The minimum and/ or maximum values for m_{cw}, T_{cwi} as well as P_{st} of the testing phase, is outside the minimum or maximum boundaries set in the training phase. This means that the ANN has not yet recognised these extremes of the specific parameters and the network will therefore invariably produce erroneous results.

The different combinations of values used during the testing phase have the same effect. The ANN was not yet been trained to recognise the specific combinations of values and thus produces slightly erroneous results.

More training will invariably improve the testing phase results. For the purpose of this investigation, the results depicted in the previous two sections are, however, adequate.

5.5. ANN- AND 1-D MODEL RESULTS COMPARISON

In this section the researcher compares the 1-D mathematical model and the ANN model with measured values. For the purpose of this discussion the NDWCT temperature approach is used as a measure of the NDWCT effectiveness. The temperature approach is the difference between T_{cwo} and T_{awb} measured at a reference height of 1.2 m.

The sensitivity of the NDWCT effectiveness to the change in independent parameters such as V_W, D_W, T_a, LRT LR_T, p_a and RH is used to compare the models. It should be noted that the purpose of this discussion is not to determine the sensitivity by means of regression, but only to show the comparison between the measured- and ANN results.

The following results are averaged for a specific x-axis value. This means that, for instance, all the results that have a reference height V_W of between 4.5 m/s and 5.5

m/s are averaged to represent one value for a reference height V_W of 5 m/s. This decreases the scatter in the data and depicts the trends clearly. Both models are thus evaluated with the same data throughout. The predicted values are the ANN results, whereas the calculated values are the 1-D model results.

Figure 5-6 below depicts the sensitivity of the temperature approach to LR_T. The measured approach indicates that the temperature approach has a natural and generally upward trend for an increasing LR_T. The higher temperature approach at a LR_T of -0.015 k/m is caused by a higher average T_a associated with this lapse rate. This invariably decreases the temperature driving force as explained above. As LR_T increases, which relates to more intense temperature inversions, the measured approach increases as expected.

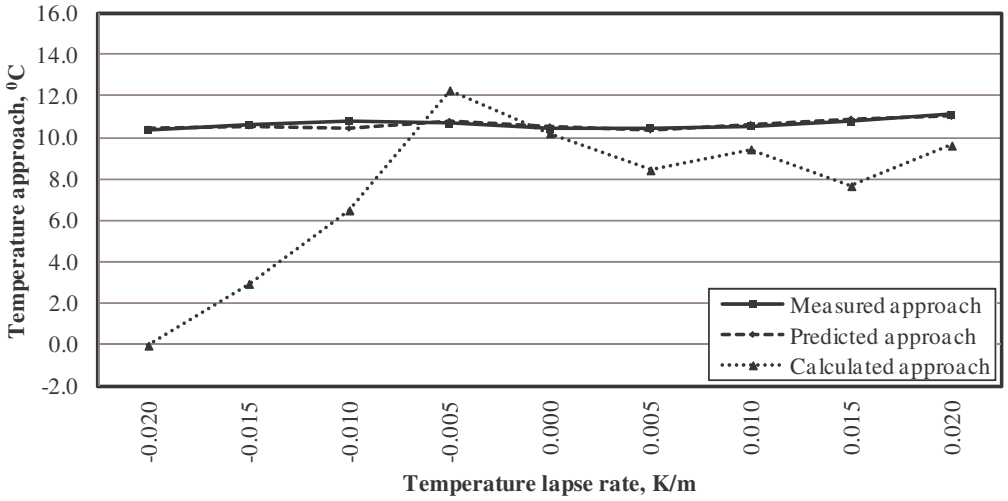

Figure 5-6: Sensitivity of Majuba Power Station's NDWCT temperature approach to the average LR_T.

The predicted approach is found to be very similar to the measured approach throughout the range of LR_T values. This indicates that the ANN is trained sufficiently to predict the effect of this independent parameter adequately. The deviation observed at a lapse rate of -0.010 is caused by insufficient training at this specific lapse rate. This can, however, be rectified by increasing the ANN training to include more datasets within this LR_T range.

The calculated approach in Figure 5-6 presents a problem. The 1-D mathematical model's optimisation algorithm (discussed in section 5.3.2) struggles to find the optimum solution once the LR_T is varied. The exact reason for this was not apparent during this study.

In order to compare the results from the two models it was decided to keep the LR_T constant at -0.00975 K/m, which is the lapse rate used by Kröger when the model was designed (Kröger, 1998). This entails that the 1-D model will over-predict the effectiveness of the NDWCT if the LR_T is higher than -0.00975 K/m, which is more than 90% of the time annually. This over-prediction is caused by

the increased NDWCT inlet T_a. The following figures will thus show an offset that can be attributed to the fixed LR_T.

The sensitivity of the temperature approach with respect to the V_W is depicted in Figure 5-7 below. It is found that the measured temperature approach increases with increasing reference height V_W up to approximately 10 m/s. An increase in temperature approach relates to a decrease in NDWCT effectiveness and *vice versa*. The temperature approach thereafter remains stable up to approximately 13 m/s, after which it decreases with increasing reference height V_W. This relates well to data presented by Bourillot *et al.* (1980) wherein he argues that low reference height V_W is detrimental to the performance of NDWCTs as it destroys the well-proportioned and axisymmetric air field at the tower inlet. As the reference height V_W increases, the turbulence in the tower increases, which enhances the heat- and mass transfer performance and increases the NDWCT performance.

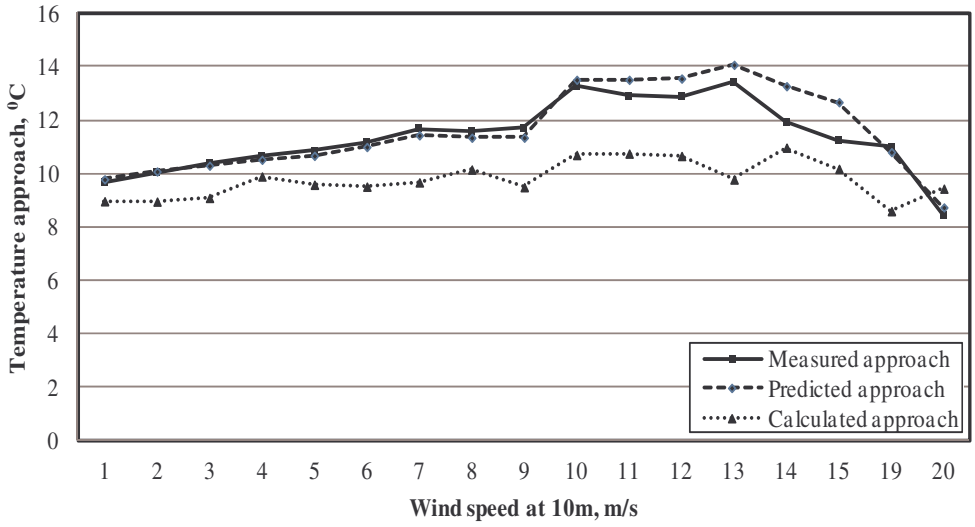

Figure 5-7: Measured and calculated sensitivity of Majuba Power Station's NDWCT temperature approach to the average reference height V_W.

In Figure 5-7 it is found that the measured and predicted temperature approach profiles are very similar throughout. At higher reference height V_W values the ANN over-predicts the temperature approach and thus underestimates the NDWCT effectiveness. This can be attributed to the amount of training that the ANN had in these high reference height V_W ranges. Overall the ANN predicts the temperature approach with reference to V_W accurately.

The calculated results depicted in Figure 5-7 do not compare well to the measured results. This is partly due to the fact that the 1-D mathematical does not include an empirical relationship between the NDWCT effectiveness and reference height V_W, and partly due to the fact that the LR_T is fixed at –0.00975 K/m. The fixed lapse rate relates to the offset in Figure 5-7 and the missing empirical relationship relates to the fact that the temperature approach remains essentially constant throughout, barring a few dips and spikes in the data. These variations are mainly

caused by measurement inaccuracies and the generally dynamic behaviour of the NDWCTs.

The dynamic behaviour can be explained as follows: A higher V_W causes an increase in measured temperature approach and thus an increase in overall NDWCT T_{cwo}. This higher T_{cwo} increases the NDWCT T_{cwi}, which decreases the overall effectiveness of the NDWCT. The datasets used to determine the calculated approach includes the results of this dynamic behaviour (the increased average T_{cwo}), and the calculated results will therefore show signs of similar behaviour to the measured approach even if no empirical relationship exists between the effectiveness and the reference height V_W.

The sensitivity of the temperature approach to the reference height D_W is depicted in Figure 5-8 below.

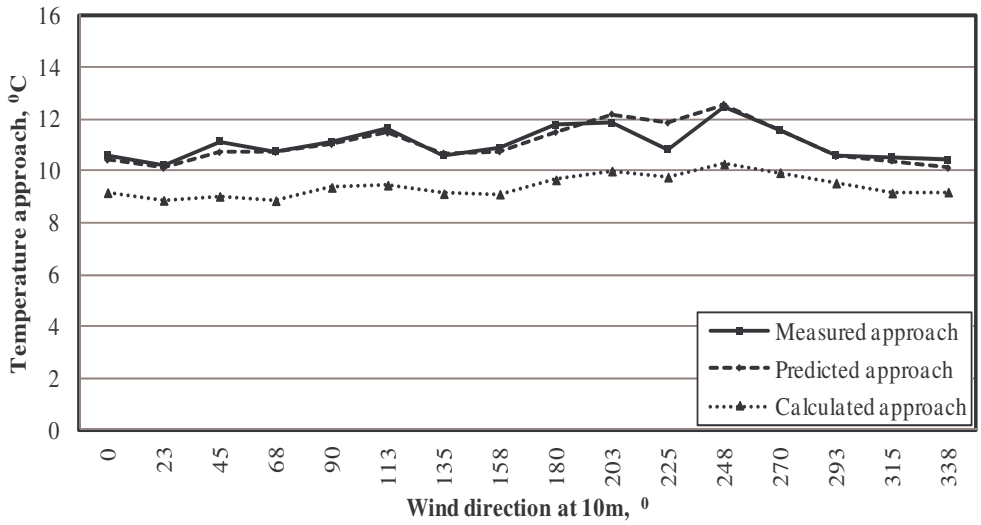

Figure 5-8: Sensitivity of Majuba Power Station's NDWCT temperature approach to the average reference height D_W

It is found that the measured temperature approach is not as sensitive to the D_W as it is to V_W. Figure 5-8 does, however, show an increase in temperature approach for D_W values between 90 and 115 degrees and between 180 and 250 degrees. The reasons for this are explained with the help of the wind roses (Figure 2-39 to Figure 2-46) presented in section 2.8. The average yearly V_W is higher when a D_W of between 70 and 115 degrees is present, and therefore an increase in the temperature approach will be present. The higher temperature approaches between 160 and 250 degrees are also caused by higher average V_W values, which are not easily recognisable in Figure 2-39 due to the small frequency associated with these D_W values.

The predicted temperature approach is close to the measured approach in Figure 5-8. This shows that the ANN can accurately predict the temperature approach for an average specific D_W. The calculated approach does not, however, predict the measured approach accurately, partly because of the fixed LR_T and partly because

of the fact that the D_W does not for part of the 1-D model calculations. The reason for the gradual variation between 160 and 300 degrees is the overall dynamic behaviour of the NDWCTs. The 1-D model thus struggles to predict the effectiveness of the NDWCTs at Majuba Power Station accurately for varying D_W values.

The sensitivity of the temperature approach to the reference height T_a is depicted in Figure 5-9 below. It is found that the measured approach is higher for lower temperatures (below 13°C). These temperature are, however, mostly prevalent during periods when temperature inversion prevail, which is the reason for the higher approach.

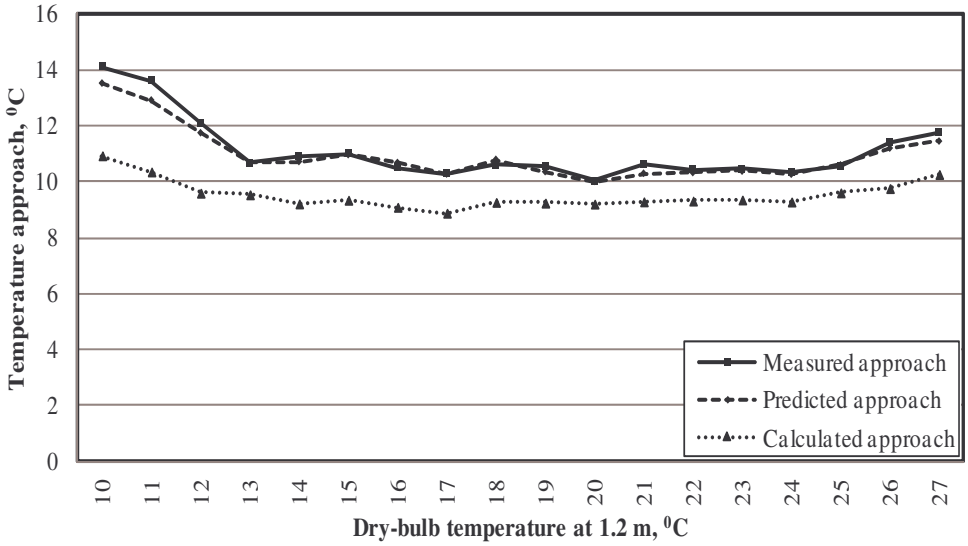

Figure 5-9: Sensitivity of Majuba Power Station's NDWCT temperature approach to the average reference height T_a

The measured temperature approach remains relatively constant throughout the temperature range (from 13 °C to 24 °C), after which it increases again because of the lower temperature driving force at higher ambient temperatures. It is found that the ANN can accurately predict the average temperature approach for a specific reference height T_a. The calculated results depicted in Figure 5-9 over-predict the effectiveness of the NDWCT throughout due to reasons discussed earlier in this section. This offset, however, remains relatively constant throughout the range of T_a values, which indicates that the 1-D mathematical model can predict the effectiveness of the NDWCTs throughout the temperature range once a representative LR_T can be used in the calculations.

The effect of p_a on the NDWCT temperature approach is depicted in Figure 5-10 below.

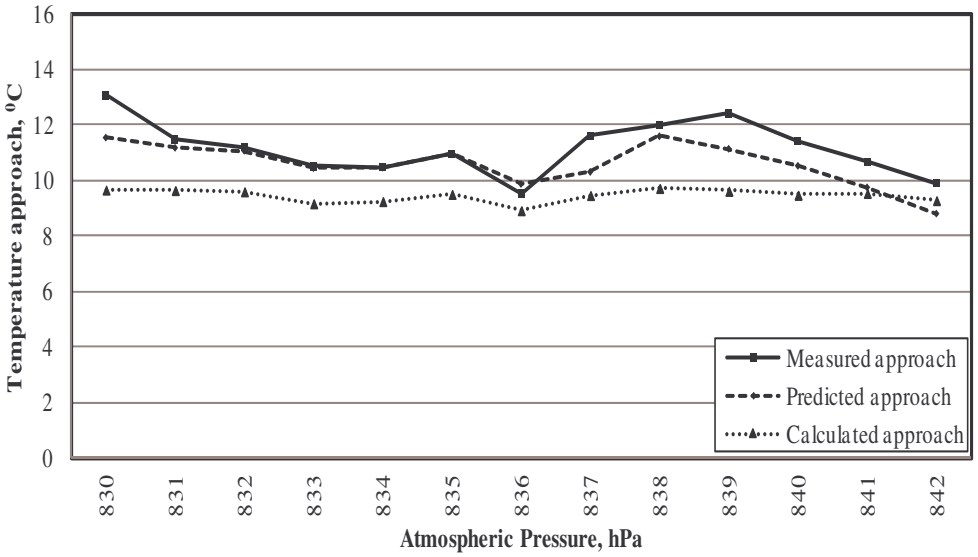

Figure 5-10: Sensitivity of Majuba Power Station's NDWCT temperature approach to the average reference height p_a

Figure 5-10 depicts the general downward trend of the temperature approach with increasing p_a. The higher pressure causes a higher pressure differential between the inside and outside of the NDWCT, increasing the flow through the NDWCT. The increase in temperature approach at 836 hPa to 839 hPa is caused by the fact that this data was collected during primarily nocturnal hour periods that are characterised by temperature inversions and increases the temperature approach as explained earlier.

Overall the ANN accurately predicts the effectiveness of the NDWCT except at higher p_a values. The reason for this is related to training during these periods. The amount of time annually when the p_a is so high is minimal, which minimises the amount of training and testing datasets available during these periods (and) that leads to the overestimated NDWCT effectiveness.

It is again seen that the calculated approach constantly underestimates the temperature approach due to reasons explained earlier. The calculated values furthermore do not vary significantly (as much as the measured values) with a change in p_a.

In Figure 5-11 below the sensitivity of the temperature approach to *RH* is depicted. The measured approach is relatively constant throughout the range of the average *RH*, except at lower values that are prevalent during midday when ambient temperatures are high, which decreases the effectiveness of a NDWCT.

The ANN is capable of accurately predicting the temperature approach for a specific *RH* as depicted in Figure 5-11. It is again found that an offset exists between the calculated and measured temperature approaches due to the reasons discussed earlier in this section.

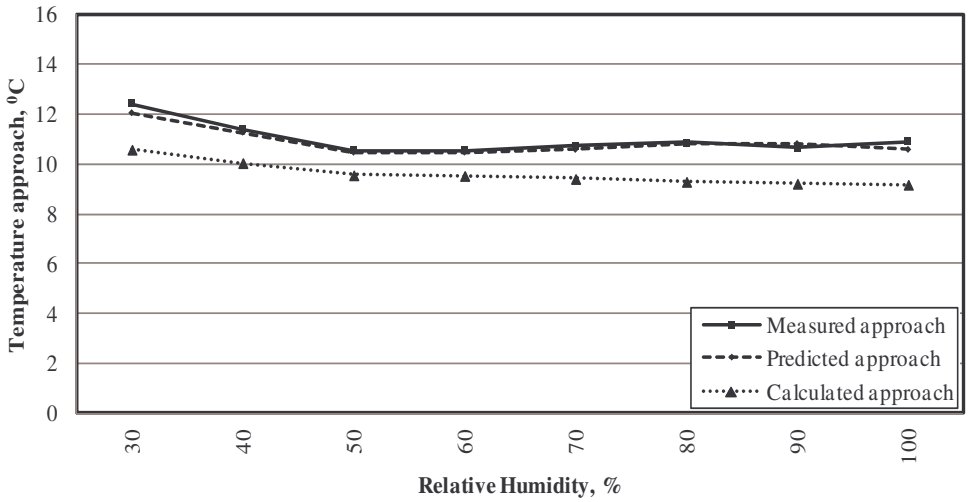

Figure 5-11: Sensitivity of Majuba Power Station's NDWCT temperature approach to the average reference height *RH*

It is interesting to note that the calculated approach decreases slightly from 50 % *RH* onwards to 100 % *RH*, which is not the case for the measured values. This can again be attributed to the fact that the LR_T is kept constant throughout. The reason for this is that the higher *RH* values occur during nocturnal hours when temperature inversions occur, which decreases the overall effectiveness of the NDWCT. The fixed LR_T does thus not only account for the offset between the measured and calculated values in Figure 5-11, but it also contributes to the distorted calculated temperature approach at higher *RH* values.

5.6. CONCLUSION

The ANN and 1-D models created for Majuba Power Station are discussed and evaluated in this chapter. The initial results for the training and testing phases of the ANN model show that, with sufficient training, an ANN can accurately predict the performance of the NDWCTs at Majuba. The 1-D model's accuracy using design conditions can be verified in appendix B.

The effect of the different independent variables on the temperature approach of the NDWCT is also evaluated by means of the trained network and the 1-D mathematical model. Throughout this section it is found that the 1-D model constantly underestimates the temperature approach and thus overestimates the NDWCT effectiveness. The reasons for this is the inability of the 1-D model to predict the NDWCT effectiveness accurately for varying LR_T-values as well as C_{RZ}, that was fixed to equal 1. It is also found that the 1-D model should be improved to properly predict the effect of V_W and D_W on NDWCT effectiveness.

The ANN model enables the user to evaluate other NDWCT efficiency calculation models, including the mathematical 1-D model, in order to improve and optimise these models. The optimisation will involve including the effect of new independent variables on the output and evaluating the current mathematical logic

employed in the models. As the ANN is developed for a specific location it is also possible to evaluate the effect of site-specific parameters such as obstructions and develop more site-specific 1-D mathematical models.

A number of improvements are possible regarding the accuracy of the ANN. These include increasing the number of epochs used in the training phase. This approach is, however, not recommended as these epochs are computationally expensive, and become even more so when the number of variables increase.

Another way of increasing the accuracy is to scrutinise the dataset used for training and testing phases. This involves minimising the ranges of the variables in order to minimise the number of possible values that a specific variable can be assigned. This is possible because all measurement devices have some degree of uncertainty as well as some degree of drift. An example of this is m_{cw} at Majuba Power Station, which remains essentially constant during steady load conditions. This measurement, however, fluctuates between 14 m^3/s and 22 m^3/s instead of showing a continuous reading of 17.8m^3/s, which is the correct flow rate according to the pump performance curves. The measurement device used for the flow measurement is therefore not very accurate. The dataset should in future be modified in order to remove this big range of mass flow rate values. This will inherently decrease the convergence time for the neural network.

As discussed in section 2.3, T_{awb} is dependent on p_a, RH and T_a. It is thus not required to have all these parameters as an ANN input as is the case above because of their dependence on other independent parameters. The improvements discussed above are essential in creating an accurate and effective ANN.

As is emphasized earlier in this section, it is essential to use the correct data when setting up an ANN. It is also vital to ensure that the correct network inputs and output parameters are used. In the case of Majuba Power Station's NDWCT-ANN, the output was chosen to be the T_{cwo} in order to ensure similarity between the 1-D mathematical model and the ANN to be able to compare and improve the two models. A more effective way to set up the ANN is, however, to include the T_{cwi} as an output, and convert the ANN output to the NDWCT cooling range. This will ensure that more accurate results are obtained in the sense that less errors can occur when specifying the inputs. The T_{cwi} is dependent on the average load, p_c and T_a amongst others, which entails that it should be specified correctly when used as an input to the ANN model.

It is generally and finally concluded that ANNs are powerful prediction tools and may be utilised to evaluate and understand current, more fundamental tools such as the 1-D mathematical model which can ultimately be used as a NDWCT performance/ condition monitoring tool. The use of the ANN networks are limited by the fact that extrapolation of the effect of independent variables on the output is still currently under investigation. This is, however, not impossible and should be evaluated in future studies in order to further motivate the use of ANN as a prediction tool of choice when other, more fundamental, prediction tools (such as the 1-D model), are unavailable.

CHAPTER 6
FINANCIAL IMPACT OF REDUCING p_c

6.1. INTRODUCTION

Power plants' efficiency is strongly affected by the thermal performance of the cooling system, which is generally optimised by means of a lifecycle cost analysis.

During the long lifecycle of a power plant design modifications may be required due to changes in fuel costs, different load requirements, new legislation, and technological advances. These can result in improved performance in order to be more economical and to reduce the possibly negative environmental impact of the plant.

Considering the abovementioned criteria a financial study has been completed, indicating the advantages that a reduction in p_c will have on the overall cycle efficiency (η) at Majuba Power Station. The main section objectives are highlighted in section 1.2.

The section includes a discussion regarding how p_c is raised and maintained in a condenser, after which the process of minimising the low-pressure (LP) turbine saturation temperature (T_{sat}), and thus p_c, is explained. The financial impact analysis follows and the section is then concluded.

6.2. THE IMPORTANCE OF CONDENSER VACUUM

The thermal efficiency of the power cycle is highly dependent on p_c and therefore T_{sat} (Çengel, 2003).

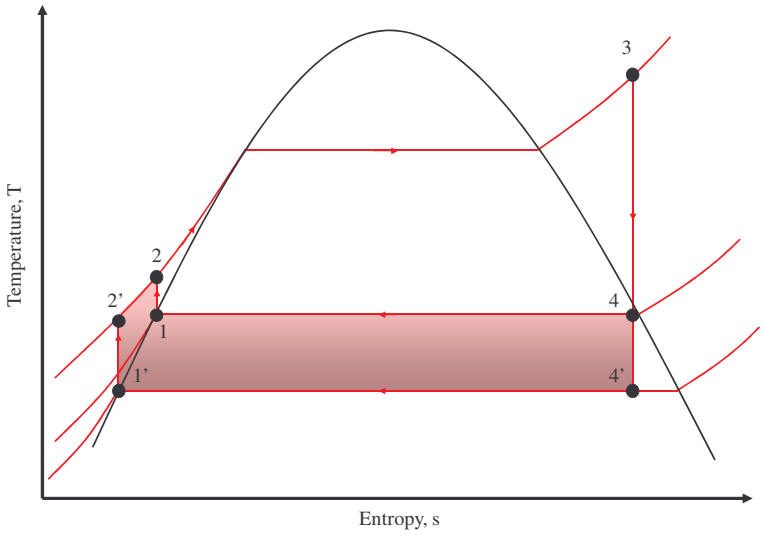

Figure 6-1: Rankine cycle explaining the improved thermal cycle work output with an improved p_c

This is explained with the help of Figure 6-1, depicting a simple Rankine cycle on a *T-s* diagram. For explanation purposes the turbine inlet conditions are kept unchanged and an ideal Rankine cycle is used. The area under a *T-s* diagram, for a given thermodynamic process, represents heat. From the first law of thermodynamics, the net heat-input into a thermodynamic cycle is equal to the net work output of the cycle. A lower condenser T_{sat} and therefore p_c increases the net heat-input and thus the net work output of the thermodynamic cycle. This increased net heat-input is represented in Figure 6-1 by the shaded area within the saturation line between 1, 4, 4' and 1'. The heat-input requirements also increase (represented by the area between 2', 2, 1 and 1'), but this is minimal compared with the net work output gained.

6.3. RAISING AND MAINTAINING p_c IN A CONDENSER

The main function of the condenser is to remove the latent heat from the wet-steam exiting the turbine and to thereby condense the steam in order to pump it back to the boiler. Condensing the steam at a specific temperature and pressure is important in order to create a vacuum after the LP turbine last-stage blades. This is achieved by condensing the incoming steam at a rate that is faster that the rate at which the steam enters the condenser. This rate of condensation is known as the heat rejection rate (HRR). The cooling water flowing through the condenser tubes is the main heat transfer medium and the HRR is mainly a function of the condenser T_{cwi} as well as m_{cw}.

6.4. MINIMISING CONDENSER T_{sat}

An elementary thermodynamic design of a condenser is explained and used in this section. The temperature profiles in a condenser will be used to discuss the process of minimising T_{sat} and p_c. Note that the following discussion is based on a constant P_{st}, m_{cw} and therefore a constant HRR. This will ensure that the condenser's log mean temperature difference (LMTD) (ΔT) will remain constant. The reasons for this are explained below. The temperature profiles for a single pass condenser (installed at Majuba Power Station) are depicted in Figure 6-2.

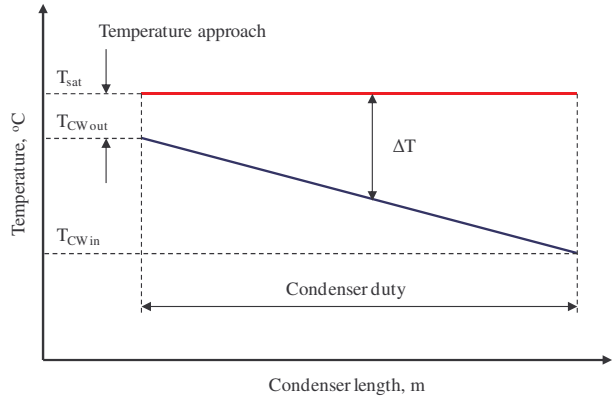

Figure 6-2: T_{sat} and T_{cw}-profiles in a condenser as a function of the condenser length

The condenser T_{sat} can be reduced by:

- Increasing m_{cw};
- Increasing the surface area of the condenser and the cooling towers; and/ or
- Increasing the heat transfer coefficient and Merkel number of the condenser and NDWCT respectively.

Increasing m_{cw} and the surface areas of the condenser and cooling tower involves physical changes to the plant that poses huge financial implications. For this reason these methods are not considered as viable options. Improving both the heat transfer coefficient and Merkel number of the condenser and NDWCT thus form the basis of the following discussion.

In order to improve p_c it is required to reduce the condenser T_{cwi}. When this T_{cwi} is reduced by a specific amount, the condenser T_{sat} will also be reduced by the same amount. This is explained visually in Figure 6-3.

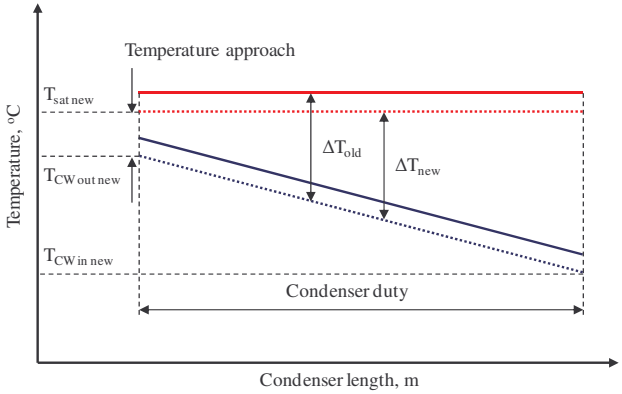

Figure 6-3: Improved T_{sat} profile as a function of the improved condenser T_{cwi}

Figure 6-3 depicts the lowered cooling water temperature profile and the corresponding lowered T_{sat} profile. The old- and new LMTD (ΔT) are equal due to the basis explained earlier which states that P_{st} and m_{cw} are constant and therefore HRR is also constant.

In achieving a lower condenser T_{cwi}, the NDWCT effectiveness needs to be improved. In section 6.5 the researcher discusses the proposed improvements to the NDWCTs at Majuba Power Station that will ensure that a decreased condenser T_{cwi}, and therefore an improved T_{sat} and p_c, are achieved. This section is followed by a section wherein the financial impact of these improvements is evaluated.

6.5. PROPOSED IMPROVEMENTS TO THE NDWCTs AT MAJUBA POWER STATION

The NDWCTs at Majuba Power Station are the most recent additions to Eskom's NDWCT fleet. These towers were designed to perform optimally in the sense that the NDWCTs and the condensers were designed in conjunction with another. This

was not the case for the other, older, Eskom stations. There is, however, still room for improvement in some areas of the NDWCTs at Majuba Power Station.

One of the areas that has been researched extensively by Terblanche, Reuter & Kröger (2008) is the rain zone of the NDWCTs. The mean NDWCT d_d at Majuba Power Station is 0.0052 m. A decrease in the size of d_d will increase the rz Merkel number NDWCT and thus the heat transfer rate of the NDWCT because of the increased heat transfer area. Studies show that the d_d of a trickle-pack fill (installed at Majuba Power Station) can be reduced from 0.0052 m to 0.0029 m by means of a modification to the trickle-packing.

The increase in NDWCT effectiveness due to a smaller d_d is measured in terms of the decrease in T_{cwo} Using the 1-D mathematical model developed for Majuba Power Station's NDWCTs, explained in 5.2 a 0.45 K decrease in T_{cwo} is calculated to be possible when the d_d is decreased from 0.0052 m to 0.0029 m. The sample calculations for these two models are shown in appendix B.

As explained in section 6.4 the condenser T_{sat} will decrease by an amount similar to the amount that T_{cwo} decreases. This decrease in T_{sat} (from a design value of 35.23 ^{o}C to 34.78 ^{o}C) relates to a decrease in p_c of 0.15 kPa from 5.7 kPa (design) to 5.55 kPa according to equation (A-11) in appendix A.

It should be noted that the proposed NDWCT improvement discussed above is one of many proposed by Reuter, Terblanche & Kröger (2008). This measure is, however, the only efficiency improvement exploited for Majuba Power Station's NDWCTs. The reason for only exploring this single measure is explained in section 6.7 below.

The validity of the proposed improvement (section 6.5) needs to be evaluated by means of a financial study, which is evaluated in section 6.6.

6.6. FINANCIAL IMPACT ANALYSIS

Due to Majuba Power Station being a two-shifting power station, the effect of improving η by means of increasing the effectiveness of the NDWCTs is generally defined in a two-fold manner. This includes a combination of a reduction in fuel consumption and thus fuel cost during load-following periods, and an increase in P_{st} and thus revenue during full-load periods.

On average, Majuba Power Station runs at full load, which is defined as loads higher than 95 % MCR, 31 % of the time annually (Table 6-1). This entails that one may expect revenue savings during this period and operational expenditure (fuel cost) savings during 69 % of the time when Majuba Power Station is in a load-following/ two-shifting mode at an average annual P_{st} of 458 MW per unit (Table 6-1).

In order to quantify the revenue savings financially the improvement in p_c discussed in section 6.5 must be related to an increase in P_{st}. This is accomplished with the help of equation (4-13), which is the calculated relationship between P_{st} and p_c.

The improved p_c discussed above relates to a P_{st} increase (ΔP_{st}) of 0.180 MW per unit, which equates to 0.54 MW for units 4 to 6 at Majuba Power Station. The financial implication of this revenue saving (S_R) is explained with the help of equation (6-1) and Table 6-1 below:

$$S_R = \Delta P_{st} \cdot 24 \cdot 365 \cdot T_{full-load\%} \cdot R_{E-2011} \quad \textbf{(6-1)}$$

Table 6-1: Majuba Power Station's NDWCT improvement - financial impact analysis parameters.

Parameter	Symbol	Unit	Value	Comment
Cost of coal	R_{Coal}	R/ton	313.42	Actual for Oct 2010
Average CV of coal	CV_{Coal}	MJ/kg	20.0	Majuba average Oct 2009 - Sep 2010
Price of electricity 2011	R_{E-2011}	R/kWh	0.52	Official price for 2011/2012
Inflation	*Inf*	%	5.5	Average of the last 3 years
Tax rate	*Tax*	%	28	Nominal tax rate
% of time on full load	$T_{full-load\ \%}$	%	31	Average Oct 2009 - Sep 2010
Average net load of Majuba	$P_{net-average}$	MW	2748	Average net load, Oct 2009 - Sep 2010
Average max load of Majuba	$P_{max-average}$	MW	3801	Average net load, Oct 2009 - Sep 2010
Net heat rate	*HR*	MJ/kWh	10.8	Average net heat rate, Oct 2009 - Sep 2010

During the periods when the unit is not running at full load, the savings due to the cycle's efficiency improvement is reflected through a reduction in operational expenditure (S_o) in the form of fuel (coal) cost. This reduction is described with the help of Table 6-1, equation (6-2) and equation:

$$\Delta Coal = P_{net-average} \cdot 24 \cdot 365 \cdot HR / CV_{Coal} - \left(P_{net-average} + \Delta P_T \cdot T_{full-load\%}\right) \cdot 24 \cdot 365 \cdot [HR / \left(1 + \Delta P_T / P_{max-average}\right)] / CV_{Coal} \quad \textbf{(6-2)}$$

and the corresponding operational expenditure savings respectively (S_O):

$$S_O = \Delta Coal \cdot R_{Coal} \quad \textbf{(6-3)}$$

Using the above equations (equations (6-1) to (6-3)) it is possible to calculate the total financial year savings (S_R + S_O) displayed in Table 6-2. These savings are extrapolated by using the nominal inflation rate of 5.5 % displayed in Table 6-1 above in order to obtain representative values for future financial years. It should be noted that these values are calculated with an estimated commissioning date of 29 February 2012, which is the end of financial year in 2012.

Table 6-2: Calculated (using equation (4-13)) total benefits after implementation of proposed modifications to Majuba Power Stations' NDWCTs.

Benefits	Symbol	Units	2013	2014	2015	2016
Potential increased electrical output at full load	ΔP_{st}	*MW*	0.7	0.7	0.7	0.7
Potential revenue savings	S_R	*ZARm p.a.*	0.994	1.242	1.548	1.633
Potential reduced coal consumption	$\Delta Coal$	*Tons p.a.*	1376.0	1376.0	1376.0	1376.0
Potential operational expenditure savings	S_O	*ZARm p.a.*	0.431	0.455	0.480	0.506
Total benefits	$S_R + S_O$	*ZARm p.a.*	1.425	1.697	2.028	2.140

The results portrayed by Table 6-2 illustrate that the proposed improvements to the NDWCTs, discussed in section 6.5, will result in an overall saving of R1.576M for the first year after commissioning, which is financial year 2013. The total savings escalate thereafter due to inflation, as explained. These results compare relatively well to the results obtained from implementing the OEM-specified equation for P_{st} as a function of p_c:

Table 6-3: Calculated total benefits after implementation of proposed modifications to Majuba Power Stations' NDWCTs

Benefits	Symbol	Units	2013	2014	2015	2016
Potential increased electrical output at full load	ΔP_{st}	*MW*	0.7	0.7	0.7	0.7
Potential revenue savings	S_R	*ZARm p.a.*	1.548	1.633	1.723	1.818
Potential reduced coal consumption	$\Delta Coal$	*Tons p.a.*	1376.0	1376.0	1376.0	1376.0
Potential operational expenditure savings	S_O	*ZARm p.a.*	0.506	0.534	0.564	0.595
Total benefits	$S_R + S_O$	*ZARm p.a.*	2.055	2.168	2.287	2.413

The savings presented in Table 6-3 are higher than the calculated savings in Table 6-2. It should be noted that the savings in Table 6-3 are, however, based on new turbines with the best possible efficiency, which is not the case for turbines that have been in service for a number of years. It is thus safe to conclude that the savings presented in Table 6-2 are accurate.

In order to be able to validate the implementation potential it is required to relate the initial capital expenditure to the savings explained above. The ratio that represents this is the payback period. Due to the fact that the implementation cost was unavailable, it is best to use a respective payback period and to work retrospectively to find out what the implementation is allowed to cost in order for it to be a viable option.

Using a healthy payback period of 5 years it is possible to calculate the implementation cost limit (C_{IL}) as follows:

$$C_{IL} = IRR \cdot (S_R + S_O) \tag{6-4}$$

The above equation makes it is possible to calculate that the proposed improvements discussed in section 6.5 needs to cost less than R7.882M during 2013 to implement and commission across all three NDWCTs in order to make it a viable potential improvement measure. The implementation cost limits are tabulated below for financial years 2013 to 2016. The values are based on the yearly savings tabulated in Table 6-2.

Table 6-4: Calculated cost of implementation limit for the proposed modifications to Majuba Power Station's NDWCTs

Benefits	Symbol	Units	2013	2014	2015	2016
Total benefits	$S_R + S_O$	*ZARm p.a.*	1.425	1.697	2.028	2.140
Total allowable implementation cost	C_{IL}	*ZARm p.a.*	7.126	8.487	10.141	10.699

Considering that Majuba Power Station is designed to reach its end of life (EOL) in 2061, it is calculated, using the inflation rate depicted in Table 6-2, that the

overall saving resulting from the implementation and commissioning of this single measure explained in section 6.5 amounts to R366.4M.

6.7. CONCLUSION

In this chapter the researcher discusses the dependence of P_{st} on p_c, using the definitions of Rankine cycle thermal efficiency, the corresponding *T-s* diagrams as well as an explanation of the effect of reduced p_c on the thermal efficiency. As is stated in section 6.4, one way to effectively reduce p_c is to reduce the NDWCT T_{cwo} or condenser T_{cwi}.

The effect of only one modification to the NDWCTs at Majuba Power Station - which includes the best-designed and -performing NDWCT cooling systems in the Eskom fleet (2011) - is discussed in section 6.5. The financial impact of this single measure is evaluated in section 6.6, where it is explained that Eskom can benefit to the amount of R366.4M over the life-cycle of Majuba Power Station if this single measure is adopted and implemented.

As stated in the section 2.1, Eskom's fleet of NDWCTs consists of a number of NDWCTs that need to be repacked during their lifetime. These NDWCTs are, however, not designed as optimally as the towers at Majuba Power Station, which inherently means that these NDWCTs will benefit more from similar improvements to those implemented at Majuba. These factors motivate that Eskom needs to investigate the improvement potentials and financial impact thereof of each tower in its fleet individually, in a similar fashion as discussed in this section.

CHAPTER 7
CONCLUSIONS AND RECOMMENDATIONS

The ambient conditions measured, evaluated and trended in chapter 2 are specific to Majuba Power Station. These conditions should be evaluated in a similar manner at other plants and locations to ensure that all ambient conditions are evaluated and accounted for when designing or testing the performance of NDWCTs. The correlations determined for T_a, T_{awb}, b_T, RH, b_W, V_W, D_W and p_a provide simple tools to evaluate the effect of different ambient conditions on NDWCT effectiveness. With the knowledge gained from evaluating the ambient conditions it is possible to determine the DALR, which was chosen with reference to literature during the design phase at Majuba (as discussed in section 2.5). The same accounts for the 7th power law, which is not valid at Majuba as motivated in section 2.8.

The use of T_{awb} as the principle NDWCT design variable is recommended above that of T_a, which was used during the original design of Majuba Power Station's NDWCTs. It is also proposed that the variation in daily net revenue, or load regimes for daily fixed rates per MW P_{st}) be used during the evaluation of the ambient design conditions in order to ensure that the correct design conditions are obtained. The time period between 12:00 to 14:00 is recommended for NDWCT performance tests at Majuba Power Station. Summer months are furthermore also preferred, as explained in chapter 3. The industry-standard temperature reference height of 1.2 m AGL (Louth, 1996) should be used during the evaluation of b_T, but a far-field T_{awb} measured at 10 m AGL should be used as a representative NDWCT-inlet T_{awb} during the design and performance testing of NDWCTs if NDWCT-inlet measurements are unavailable, as explained in section 3.5.

For lifecycle cost analysis purposes the parameters that are required to effectively determine the functional dependence of Majuba Power Station's effectiveness are discussed in section 4.4. It should be noted that different methods are available to determine Q_{in} to the boiler. During this study $Q_{in,steam}$, together with the η_{boiler}, was used as an indication of Q_{in}. Due to the unavailability of certain measurement equipment it is recommended that the different methods, as discussed in section 4.2, be evaluated and used at and for specific sites.

The 1-D mathematical model and the ANN predict the NDWCT effectiveness accurately using design conditions. The ANN is a powerful tool and can be used to evaluate the effectiveness/ monitor the condition of NDWCTs once trained sufficiently. It is, however, recommended that care should be taken when setting up an ANN. The proper dataset should be used and the correct input and output variables should be defined in order for the ANN model to work correctly.

Finally, it is recommended that South Africa's power utility, Eskom, evaluate the potential improvements at the other power stations that have NDWCTs in order to check the viability of NDWCT improvements. This is motivated by the fact that Eskom can save approximately R366.4 M over the lifecycle of Majuba Power Station by simply implementing a small modification to reduce the rain zone drop size of the NDWCTs, as discussed in chapter 6.

APPENDIX A
THERMO-PHYSICAL PROPERTIES

A.1 INTRODUCTION

In this appendix the researcher describes the thermo-physical properties of dry air, saturated water vapour, a mixture of air and water vapour and saturated liquid water, as summarised by Kröger (1998). The method used in calculating T_{awb} is also explained (Allen *et al.*, 1990).

A.1.1 Thermo-physical properties of dry air from 220 K to 380 K at standard atmospheric pressure (101325 N/m^2)

Density:

$$\rho_a = p_a / (287.08T), kg/m^3 \qquad \textbf{(A-1)}$$

Specific heat:

$$c_{pa} = 1.045356\times10^{3} - 3.16178310^{-1}\times T + 7.08381410^{-4}\times T^2 - 2.705209\times T^{-7}T^3, J/kgK \qquad \textbf{(A-2)}$$

Dynamic viscosity:

$$\mu_a = 2.287973\times10^{-6} + 6.259793\times10^{-8}T - 3.131956\times10^{-11}T^2 + 8.15038\times T^{-15}T^3, kg/sm \qquad \textbf{(A-3)}$$

Thermal conductivity:

$$k_a = -4.937787\times10^{-4} + 1.01808710^{-4}\times T - 4.627937\times10^{-8}T^2 + 1.250603\times10^{-11}T^3, W/mK \qquad \textbf{(A-4)}$$

A.1.2 Thermo-physical properties of saturated water vapour from 273.15 K to 380 K

Vapour pressure:

$$p_v = 10^{z}, N/m^2 \qquad \textbf{(A-5)}$$

where

$$z = 10.79586(1 - 273.16/T) + 5.02808\log_{10}(273.16/T)$$
$$+ 1.50474\times10^{-4}[1 - 10^{-8.29692\{(T/273.16)-1\}}] \quad \textbf{(A-6)}$$
$$+ 4.2873\times10^{-4}[10^{4.76955(1-273.16/T)} - 1] + 2.786118312$$

Specific heat:

$$c_{pv} = 1.3605\times10^{3} + 2.31334T - 2.46784\times10^{-10}T^{5}$$
$$+ 5.91332\times T^{-13}T^{6}, J/kgK \quad \textbf{(A-7)}$$

Dynamic viscosity:

$$\mu_{v} = 2.562435\times10^{-6} + 1.816683\times10^{-8}T + 2.579066\times10^{-11}T^{2}$$
$$- 1.067299\times T^{-14}T^{3}, kg/ms \quad \textbf{(A-8)}$$

Thermal conductivity:

$$k_{v} = 1.3046\times10^{-2} - 3.756191\times10^{-5}T + 2.217964\times10^{-7}T^{2}$$
$$- 1.111562\times10^{-10}T^{3}, W/mK \quad \textbf{(A-9)}$$

Vapour density:

$$\rho_{v} = -4.062329056 + 0.10277044T - 9.76300388\times10^{-4}T^{2}$$
$$+ 4.475240795\times10^{-6}T^{3} - 1.004596894\times10^{-8}T^{4} \quad \textbf{(A-10)}$$
$$+ 8.9154895\times10^{-12}T^{5}, W/mK$$

Temperature:

$$T = 164.630366 + 1.832295\times10^{-3}p_{v} + 4.27215\times10^{-10}p_{v}^{2}$$
$$+ 3.738954\times10^{3}p_{v}^{-1} - 7.01204\times10^{5}p_{v}^{-2} \quad \textbf{(A-11)}$$
$$+ 16.161488\ln p_{v} - 1.437169\times10^{-4}p_{v}\ln p_{v}, K$$

A.1.3 Thermo-physical properties of a mixture of air and water vapour

Density:

$$\rho_{av} = (1+w)[1 - w/(w+0.62198)]p_{abs}/(287.08T), kgair - vapor/m^{3} \quad \textbf{(A-12)}$$

Specific heat:

$$c_{pav} = (c_{pa} + wc_{pv})/(1+w), J/Kkg \cdot air - vapor \quad \textbf{(A-13)}$$

Or the specific heat of the air-vapour mixture per unit mass of dry air

$$c_{pma} = (c_{pa} + wc_{pv}), J/Kkg \cdot dry - air \quad \textbf{(A-14)}$$

Dynamic viscosity:

$$\mu_{av} = (X_a \mu_a M_a^{0.5} + X_v \mu_v M_v^{0.5})/(X_a M_a^{0.5} + X_v M_v^{0.5}), kg/ms \quad \textbf{(A-15)}$$

where

$$\begin{aligned} M_a &= 28.97 kg/mole \\ M_V &= 18.016 kg/mole \\ X_a &= 1/(1+1.608w) \\ X_v &= w/(w+0.622) \end{aligned} \quad \textbf{(A-16)}$$

Thermal conductivity:

$$k_{av} = (X_a k_a M_a^{0.33} + X_v k_v M_v^{0.33})/(X_a M_a^{0.33} + X_v M_v^{0.33}), W/mK \quad \textbf{(A-17)}$$

Humidity ratio:

$$w = \left(\frac{2501.6 - 2.3263(T_{awb} - 273.15)}{2501.6 + 1.8577(T_a - 273.15) - 4.184(T_{awb} - 273.15)}\right)\left(\frac{0.62509 p_{vwb}}{p_{abs} - 1.005 p_{vwb}}\right) - \left(\frac{1.00416(T_a - T_{awb})}{2501.6 + 1.8577(T_a - 273.15) - 4.184(T_{awb} - 273.15)}\right), kg/kg \cdot dry \cdot air \quad \textbf{(A-18)}$$

Enthalpy:

$$i_{av} = [c_{pa}(T_a - 273.15) + w\{i_{fgwo} + c_{pv}(T_a - 273.15)\}]/(1+w), J/kg \cdot air - vapour \quad \textbf{(A-19)}$$

Or the enthalpy of the air-vapour mixture per unit mass of dry air

$$i_{ma} = c_{pa}(T - 273.15) + w\{i_{fgwo} + c_{pv}(T - 273.15)\}, J/kg \cdot dry - vapour \quad \textbf{(A-20)}$$

where the specific heats are evaluated at *(T + 273.15)/2* and the latent heat i_{fgwo}, is evaluated at *273.15 K* according to equation (A-25).

A.1.4 Thermo-physical properties of saturated liquid water from 273.15 K to 380 K

Density:

$$\rho_w = (1.49343\times10^{-3} - 3.7164\times10^{-6}T + 7.09782\times10^{-9}T^2 - 1.90321\times10^{-20}T^6)^{-1}, kg/m^3 \quad \textbf{(A-21)}$$

Specific heat:

$$c_{pw} = 8.15599\times10^{3} - 2.80627\times10T + 5.11283\times10^{-2}T^2 - 2.17582\times10^{-13}T^6, J/kgK \quad \textbf{(A-22)}$$

Dynamic viscosity:

$$\mu_w = 2.414\times10^{-5}\times10^{247.8/(T-140)}, kg/ms \quad \textbf{(A-23)}$$

Thermal conductivity:

$$k_w = -6.14255\times10^{-1} + 6.9962\times10^{-3}T - 1.01075\times10^{-5}T^2 + 4.74737\times10^{-12}T^4, W/mK \quad \textbf{(A-24)}$$

Latent heat of vaporisation:

$$i_{fgw} = 3.4831814\times10^{6} - 5.8627703\times10^{3}T + 12.139568T^2 - 1.40290431\times10^{-2}T^3, J/kg \quad \textbf{(A-25)}$$

Critical pressure:

$$p_{wc} = 22.09\times10^{6}, N/m^2 \quad \textbf{(A-26)}$$

Surface tension:

$$\sigma_w = 5.148103\times10^{-2} + 3.998714\times10^{-4}T - 1.4721869\times10^{-6}T^2 + 1.21405335\times10^{-9}T^3, N/m \quad \textbf{(A-27)}$$

A.1.5 Wet-bulb temperature

To calculate T_{awb} the method defined by Allen *et al*. (1990) is used. This method determines the T_{awb} using T_a, p_a and RH. The steps used to calculate T_{awb} are outlined below:

Step 1:

Compute the water vapour pressure of the air using the RH and T_a:

Saturated water vapour pressure:

$$p_v(T_a) = 0.611e^{[17.27T_a/(T_a+237.3)]} \quad \textbf{(A-28)}$$

Water vapour pressure:

$$p_{av} = p_v \times (RH/100) \quad \textbf{(A-29)}$$

Step 2:

Calculate the dew-point temperature (T_{dp}) using p_{av}:

$$T_{dp} = (116.9 + 237.3\times\ln(p_{av}))/(16.78 - \ln(p_{av})) \quad \textbf{(A-30)}$$

Step 3:

Calculate the T_{awb} with T_a, T_{dp}, p_{av} and p_a as follows:

$$T_{awb} = ((\chi\times T_a) + (\delta\times T_{dp}))/(\chi+\delta) \quad \textbf{(A-31)}$$

where

$$\chi = 0.00066\cdot p_a \quad \textbf{(A-32)}$$

$$\delta = 4098\times p_{av}/(T_{dp+237.3})^2 \quad \textbf{(A-33)}$$

APPENDIX B
SAMPLE CALCULATIONS FOR MAJUBA POWER STATION's NDWCT 1-D MODEL

In this appendix the mean values are determined as follows:

$$X_{mean} = (X_a + X_b)/2 \qquad \textbf{(B-1)}$$

Errors are determined in the following manner:

$$X_{mean} = 100 \times abs(X_a + X_b)/X_a \qquad \textbf{(B-2)}$$

The equations that are used throughout this appendix are referenced to Kröger (1998).

B.1 DESIGN CONDITIONS

This sample calculation provides the results for the 1-D model when Majuba Power Station's design conditions are used.

NDWCT design data

Dimensions			
Tower height	H_6	153.0	m
Tower inlet height	H_3	9.5	m
Tower inlet diameter	d_3	87.532	m
Shell base cross-sectional area	A_3	6017.604	m^2
Tower outlet diameter	d_6	54.000	m
Tower outlet cross-sectional area	A_6	2290.221	m^2
Fill height	L_{fi}	1.800	m
Spray zone height	L_{sp}	1.500	m
Inlet rounding	r_i	0.000	m
Number of tower supports	n_{ts}	64.000	#
Length of tower supports	L_{ts}	9.618	m
Diameter of tower supports	d_{ts}	0.700	m
Drag coefficient of tower supports (round)	C_{Dts}	1.100	#
Shell thickness (inlet)	t_s	0.920	m
Ambient conditions			
Atmospheric pressure at ground level	p_{a1}	83492.000	Pa
Air temperature at ground level	T_{a1}	287.150 14.000	K °C
Wet-bulb temperature at ground level	T_{awb1}	283.750 10.600	K °C
Ambient Temperature gradient from ground	*DALR*	-0.00975	K/m
Operating conditions			
Inlet water temperature	T_{wi}	306.540 33.390	K °C
Water mass flow rate	m_w	17800.000	kg/s

Performance characteristics

The NDWCT is fitted with a trickle pack fill for which the performance characteristics are:

Effective frontal area of the fill	A_{fr}	5897.000	m^2
Mean drop diameter in the rain zone	d_d	0.0052	m
Fill support system and contraction loss coefficient based on Afr	K_{fs}	0.500	#
Water distribution loss coefficient	K_{wd}	0.500	#
Kinetic energy coefficient at tower outlet	α_{e6}	1.010	#
Constants			
Pi constant	π	3.14159	rad
Gravitation constant	g	9.80	m/s^2
Vapour gas constant	R_v	461.52	J/kg.K
Air gas constant	R_a	287.08	J/kg.K
Air molecular weight	M_a	28.970	kg/mole
Vapour molecular weight	M_v	18.016	kg/mole
Latent heat of vaporization at 273.15 K	i_{fgwo}	2501598	J/kg
NDWCT solution			
Air-vapour mass flow rate through the fill	m_{av15}	11325.28	kg/s
Air pressure after the drift eliminators	p_{a5}	83302	Pa
Air temperatures after the drift eliminators	T_{a5}	302.980	K
Air pressure at the tower outlet	p_{a6}	81986.9	Pa
Mean re-cooled water-outlet temperature	T_{wo}	294.867 21.717	K °C

Thermo-physical properties:

The thermo-physical properties of the air at (1), employing the equations given in A.1.1, are as follows:

Specified air-inlet dry-bulb temperature	T_{a1}	287.15	K
Specified air-inlet wet-bulb temperature	T_{awb1}	283.75	K
Humidity ratio (equation (A-17))	w_1	0.008312277	*kg/kg d.a.*
Humidity ratio of saturated air at Two (equation (A-17)	w_{s1}	0.020072665	*kg/kg d.a.*
Density (equation (A-12))	ρ_{av1}	1.00777	kg/m^3
Dynamic viscosity (equation (A-3))	μ_{av1}	1.7788E-05	Pa.s
Enthalpy (equation (A-20))	i_{ma1}	35101.41383	J/kg
Specific heat (equation (A-2))	c_{pa1}	1006.6	J/kg.K
Specific heat (equation (A-6))	c_{pv1}	1874.5	J/kg.K

If the air is assumed to be saturated immediately after the drift eliminator, the wet-bulb temperature at (5) will be equal to the given dry-bulb temperature at this elevation, therefore

Wet-bulb temperature	T_{awb5}	302.980	K

The corresponding thermo-physical properties at (5) can be determined using the equations given in Appendix A.

Vapour pressure (equation (A-5))	p_{v5}	4201.77	Pa

Humidity ratio (equation (A-16))	w_5	0.033213444	kg/kg d.a.
Density (equation (A-12))	ρ_{av5}	0.939359297	kg/m^3
Dynamic viscosity (equation (A-14))	μ_{av5}	1.82991E-05	Pa.s
Enthalpy (equation (A-20))	i_{ma5}	114973.047	J/kg
Specific heat (equation (A-2))	c_{pa5}	1007.1	J/kg.K
Specific heat (equation (A-6))	c_{pv5}	1888.8	J/kg.K
The mean pressure of the air-vapour in the fill (equation (B-1))	p_{a15}	83396.9	Pa
The approximate harmonic mean density of the air-vapour in the fill (equation (B-1))	ρ_{av15}	0.972364	kg/m^3
The mean air temperature (equation (B-1))	T_{a15}	295.065 21.916	K °C

The thermo-physical properties of water at the inlet temperature T_{wi} are as follows:

Specific heat (equation (A-22))	c_{pwi}	4177.490	J/kg.K

The thermo-physical properties of water at the outlet temperature T_{wo} include:

Density (equation (A-21))	ρ_{wo}	997.797	kg/m^3
Specific heat (equation (A-22))	c_{pwo}	4183.641	J/kg.K
Surface tension (equation (A-27))	σ_{wo}	0.072514	N/m
The mean water temperature (equation (B-1))	T_{wm}	300.689 27.539	K °C
Specific heat at T_{wm} (equation (A-22))	c_{pwm}	4179.7	J/kg.K

Flow rates:

The dry air mass flow rate can be determined from the following relation:

$$m_a = \frac{2 \cdot m_{av15}}{2 + w_1 + w_5}$$ m_a 11094.9 kg/s

The respective flow rates upstream and downstream of the fill are thus

Upstream:	$m_{av1} = m_a \cdot (1 + w_1)$	m_{av1}	11187.1	kg/s
Downstream:	$m_{av5} = m_a \cdot (1 + w_5)$	m_{av5}	11463.4	kg/s

The corresponding mass velocities are: $G_{av15} = \frac{m_{av15}}{A_{fr}}$ G_{av15} 1.921 kg/m^2.s

$$G_a = \frac{m_a}{A_{fr}}$$ G_a 1.88145 kg/m^2.s

$$G_{av1} = \frac{m_{av1}}{A_{fr}}$$ G_{av1} 1.89709 kg/m^2.s

$$G_{av5} = \frac{m_{av5}}{A_{fr}}$$ G_{av5} 1.94394 kg/m^2.s

$$G_w = \frac{m_w}{A_{fr}}$$ G_w 3.01848 kg/m^2.s

Transfer coefficients or Merkel numbers:

The transfer coefficient of the rain zone of this particular tower is approximated. The α-coefficients appearing in this equation for the rain zone transfer coefficient and the pressure drop, required later on, are as follows:

$$a_\mu = 3.061 \cdot 10^{-9} \cdot \left(\frac{\rho_{wo}^{\ 4} \cdot g^{9}}{\sigma_{wo}} \right)^{0.25}$$ α_μ 1.000135 #

$$a_\rho = \frac{998}{\rho_{wo}}$$ α_ρ 1.000202 #

$$a_\mu = 73.298 \cdot \left(\frac{\sigma_{wo}^{\ 3} \cdot g^{5}}{\rho_{wo}^{\ 3}} \right)^{0.25}$$ α_v 1.000367 #

$$a_\mu = 36.122 \cdot \left(\frac{\sigma_{wo} \cdot g}{\rho_{wo}} \right)^{0.25}$$ α_L 1.000103 #

It can be seen that the values of these values are close to unity.

The diffusion coefficient at air-inlet conditions is:

$$D_1 = \frac{0.04357 \cdot T_{a1}^{\ 1.5} \cdot \left(\frac{1}{28.97} + \frac{1}{18.016} \right)^{0.5}}{p_{a1} \cdot \left(29.9^{0.333} + 18.8^{0.333} \right)^2}$$ D_1 2.29903E-05 m^2/s

The Schmidt number is: $Sc_1 = \frac{\mu_{av1}}{\rho_{av1} \cdot D_1}$ Sc_1 0.767740 #

The air-vapour velocity before the fill: $v_{av3} = \frac{m_{av1}}{\rho_{av1} \cdot A_{fr}}$ v_{av3} 1.88245 m/s

With these values find:

$$A_{rz1} = 12 \cdot \left(\frac{D_1}{v_{av3} \times d_d} \right) \cdot \left(\frac{H_3}{d_d} \right) \cdot \left(\frac{p_{a1}}{\rho_{wo} \cdot R_v \cdot T_{a1}} \right) \cdot Sc_1^{\ 0.33} \cdot \left(\frac{\ln\left(\frac{w_{s1} + 0.622}{w_1 + 0.622} \right)}{w_{s1} - w_1} \right)$$ A_{rz1} 0.046834 #

$$A_{rz2} = 0.90757 \cdot a\rho \cdot \rho_{av1} - 30341.04 \cdot a_\mu \cdot \mu_{av1} - 0.37564$$ A_{rz2} -0.00060 #

$$A_{rz3} = 0.55 + 41.7215 \cdot \left(a_L \cdot d_d \right)^{0.80043}$$ A_{rz3} 1.169750 #

$$A_{rz4} = \left(3.11 \cdot e^{0.15 \cdot a_v \cdot v_{av3}} - 3.13 \right) \cdot \left[3.741 \cdot \left(a_L \cdot H_3 \right)^{-1.23456} + 0.713 \right]$$ A_{rz4} 0.940594 #

$$A_{rz5} = e^{5.3759 \cdot e^{-0.2092 \cdot a_L \cdot H_3} \cdot \ln\left(0.3719 \cdot e^{0.0019055 \cdot a_L \cdot d_3} + 0.55 \right)}$$ A_{rz5} 0.992189 #

The substitution of the above equations into the following equation yields the transfer coefficient applicable to the rain zone, the rain zone Merkel number is:

$$Me_{rz} = A_{rz1} \cdot \left(A_{rz2} + 4.04016 A_{rz3} \cdot A_{rz4} \cdot A_{rz5} \right)$$ Me_{rz} 0.206534 #

The transfer coefficient applicable to the fill, the fill Merkel number is:

$$Me_{fi} = 0.25575 \cdot L_{fi} \cdot G_w^{-0.094} \cdot G_a^{0.6023}$$ Me_{fi} 1.267680 #

The transfer coefficient applicable to the spray zone, the spray zone Merkel number is:

$$Me_{sp} = 0.2 \cdot L_{sp} \cdot \left(\frac{G_a}{G_w}\right)^{0.5}$$ Me_{sp} 0.236849 #

The overall transfer coefficient is the sum of the transfer coefficients of the rain, fill and spray zones respectively.

$$Me_{CT} = Me_{rz} + Me_{fi} + Me_{sp}$$ Me_{CT} 1.712333 #

If the four point form of the Chebyshev integral is applied to this relation, the integral on the right-hand side can be determined as follows:

The enthalpy differentials are dependent on the following intermediate temperatures:

$$T_{wa} = T_{wo} + 0.1 \cdot (T_{wi} - T_{wo})$$ T_{wa} 296.031 K

$$T_{wb} = T_{wo} + 0.4 \cdot (T_{wi} - T_{wo})$$ T_{wb} 299.524 K

$$T_{wc} = T_{wo} + 0.6 \cdot (T_{wi} - T_{wo})$$ T_{wc} 301.853 K

$$T_{wd} = T_{wo} + 0.9 \cdot (T_{wi} - T_{wo})$$ T_{wd} 305.346 K

The humidity ratios of saturated air at the intermediate water temperatures are (equation (A-18)):

$$w_{sa} = f(T_{wa}, p_{a15}, p_v(T_{wa}))$$ w_{sa} *0.021622* kg/kg d.a.

$$w_{sb} = f(T_{wb}, p_{a15}, p_v(T_{wb}))$$ w_{sb} *0.02686* kg/kg d.a.

$$w_{sc} = f(T_{wc}, p_{a15}, p_v(T_{wc}))$$ w_{sc} *0.03097* kg/kg d.a.

$$w_{sd} = f(T_{wd}, p_{a15}, p_v(T_{wd}))$$ w_{sd} *0.03824* kg/kg d.a.

From these intermediate temperatures and humidity ratios the enthalpies of saturated air at the intermediate water temperatures are determined as follows (equation (A-19) :

i_{maswa} 78045.7 J/kg

i_{maswb} 95056.2 J/kg

i_{maswc} 108038 J/kg

i_{maswd} 130389 J/kg

The intermediate air enthalpies are also calculated using these values.

$$i_{maa} = \frac{m_w \cdot c_{pwm} \cdot (T_{wa} - T_{wo})}{m_a} + i_{ma1}$$ i_{maa} 42908.87 J/kg

$$i_{mab} = \frac{m_w \cdot c_{pwm} \cdot (T_{wb} - T_{wo})}{m_a} + i_{ma1}$$ i_{mab} 66331.26 J/kg

$$i_{mac} = \frac{m_w \cdot c_{pwm} \cdot (T_{wc} - T_{wo})}{m_a} + i_{ma1}$$ i_{mac} 81946.18 J/kg

$$i_{mad} = \frac{m_w \cdot c_{pwm} \cdot (T_{wd} - T_{wo})}{m_a} + i_{ma1}$$ i_{mad} 10536.86 J/kg

Find the difference in enthalpies:

$$\Delta i_a = i_{maswa} - i_{maa}$$ Δi_a 35136.80 J/kg

$$\Delta i_b = i_{maswb} - i_{mab}$$ Δi_b 28733.92 J/kg

$$\Delta i_c = i_{maswc} - i_{mac}$$ Δi_c 26091.57 J/kg

$$\Delta i_d = i_{maswd} - i_{mad}$$ Δi_d 25020.87 J/kg

Substitution into the Chebyshev-integral yields:

$$Me_{CT} = \frac{c_{pwm} \cdot (T_{wi} - T_{wo})}{4} \cdot \left(\frac{1}{\Delta i_a} + \frac{1}{\Delta i_b} + \frac{1}{\Delta i_c} + \frac{1}{\Delta i_d} \right)$$ Me_{CT} 1.712333 #

This value must be basically identical to the value obtained by adding the transfer coefficients of the three wet zones together, which in turn means that the determined T_{wo} is correct.

The error regarding the Merkel numbers is (equation (B-2)):

E_{Me} 2.48E-8 %

Energy Balance

The heat rejected by the cooling tower is given by

$$Q_w = m_w \cdot c_{pwi} \cdot (T_{wi} - 273.15) - [m_w - m_a \cdot (w_5 - w_q)] \cdot c_{pwo} \cdot (T_{wo} - 273.15)$$ Q_w 886.169 MW

The correctness of the chosen temperature of the saturated air leaving the spray zone, T_{a5}, can be confirmed from the relation

$$Q_a = m_a \cdot (i_{ma5} - i_{ma1})$$ Q_a 886.169 MW

The values of Q show an error of (equation (B-2)):

E_Q -4.69E-8 %

Loss coefficients

The loss coefficients due to the tower supports referred to the fill is determined from:

$$K_{ts} = \frac{C_{Dts} \cdot L_{ts} \cdot n_{ts} \cdot d_{ts}}{\pi \cdot d_3 \cdot H_3}$$ K_{ts} 0.181433 #

$$K_{tsfi} = \left[\frac{C_{Dts} \cdot L_{ts} \cdot n_{ts} \cdot d_{ts} \cdot A_{fr}^{\ 2}}{(\pi \cdot d_3 \cdot H_3)^3} \right] \cdot \left(\frac{\rho_{av15}}{\rho_{av1}} \right) \cdot \left(\frac{m_{av1}}{m_{av15}} \right)^2$$ K_{tsfi} 0.870369 #

The specified loss coefficient due to the fill support structure and the contraction loss into the fill is referred to the mean density through the fill, i.e.:

$$K_{fsfi} = K_{fs} \cdot \left(\frac{\rho_{av15}}{\rho_{av1}} \right) \cdot \left(\frac{m_{av1}}{m_{av15}} \right)^2$$ K_{tsfi} 0.470735 #

According to the specified fill loss coefficient

$$K_{fsfi} = 1.851 \cdot L_{fi} \cdot G_w^{\ 1.2752} \cdot G_a^{\ -1.0356}$$ K_{fdm} 16.47852 #

The actual fill loss coefficient applicable to the cooling tower is given by

$$K_{fi} = K_{fdm} + \left(\frac{G_{av5}{}^2}{\rho_{av5}} - \frac{G_{av1}{}^2}{\rho_{av1}} \right) \cdot \frac{\rho_{av15}}{G_{av15}{}^2}$$ K_{fi} 16.59759 #

The expansion loss coefficient after the fill is given by

$$K_{ctefi} = \left(1 - \frac{A_{fr}}{A_3} \right)^2 \cdot \left(\frac{\rho_{av15}}{\rho_{av5}} \right) \cdot \left(\frac{m_{av5}}{m_{av15}} \right)^2$$ K_{ctefi} 0.000426 #

The loss coefficient through the spray zone is given by

$$K_{spfi} = L_{sp} \cdot \left[0.4 \cdot \left(\frac{G_w}{G_a} \right) + 1 \right] \cdot \left(\frac{\rho_{av15}}{\rho_{av5}} \right) \cdot \left(\frac{m_{av5}}{m_{av15}} \right)^2$$ K_{spfi} 2.611692 #

For the water distribution system, it follows from the specified loss coefficient that

$$K_{wdfi} = K_{wd} \cdot \left(\frac{\rho_{av15}}{\rho_{av5}} \right) \cdot \left(\frac{m_{av5}}{m_{av15}} \right)^2$$ K_{wdfi} 0.530270 #

The loss coefficient for a type c drift eliminator based on the fill is given by

$$Ry = \frac{m_{av5}}{A_{fr} \cdot \mu_{av5}}$$ Ry 1.064390E+05 #

$$K_{defi\_C} = K_{de}(Ry) \cdot \left(\frac{\rho_{av15}}{\rho_{av5}} \right) \cdot \left(\frac{m_{av5}}{m_{av15}} \right)^2$$ K_{defi_C} 5.603748 #

The sum of all the loss coefficients in the vicinity of the fill is

$$K_{ct\_fi} = K_{fsfi} + K_{fi} + K_{ctefi} + K_{spfi} + K_{wdfi} + K_{defi}$$ K_{ct_fi} 25.81446 #

The inlet-loss coefficient for a circular cooling tower with splash type isotropic fill operating in the absence of a rain zone and based on fill conditions can be determined according to the following applicable equation, presented by Kröger (2004).

$$A_{ctfi1} = 0.011266 \cdot e^{\frac{0.093 \cdot d_3}{H_3}} \cdot K_{ct\_fi}{}^2 - 0.3105 \cdot e^{\frac{0.1085 \cdot d_3}{H_3}} \cdot K_{ct\_fi}$$ A_{ctfi1} -4.095318 #

$$A_{ctfi2} = -1.7522 + 4.5614 \cdot e^{\frac{0.131 \cdot d_3}{H_3}}$$ A_{ctfi2} 13.49887 #

$$A_{ctfi3} = \frac{10970.2 \cdot e^{-0.2442 \cdot K_{ct\_fi}} + 1391.3}{\frac{d_3}{H_3} - 15.7258} + 1205.54 \cdot e^{-0.23 \cdot K_{ct\_fi}} + 109.314$$ A_{ctfi3} -104.2408 #

$$A_{ctfi4} = \frac{2 \cdot r_i}{d_3} - \frac{0.01942}{\frac{d_3}{H_3} - 27.929} - 0.016866$$ A_{ctfi4} -0.015828 #

$$K_{ctfinorz} = \left(A_{ctfi1} + A_{ctfi2} + a\sinh\left(A_{ctfi3} \cdot A_{ctfi4}\right)\right) \cdot \left[\left(\frac{\rho_{av15}}{\rho_{av1}}\right) \cdot \left(\frac{m_{av1}}{m_{av15}}\right)^2 \cdot \left(\frac{4 \cdot A_{fr}}{\pi \cdot d_3{}^2}\right)^2\right]$$

$K_{ctfinorz}$	9.654751	#

This value must be multiplied by a correction factor C_{rz} as given by the following equation to obtain the correct inlet-loss coefficient in the presence of the rain zone.

$$A_{crz1} = 0.2394 + 80.1 \cdot \left(\frac{0.0954}{\frac{d_3}{H_3}} + d_d\right) \cdot e^{0.395 \cdot \frac{G_w}{G_{av1}}} - 0.3195 \cdot \frac{G_w}{G_{av1}}$$

A_{crz1}	2.066767	#

$$A_{crz2} = 966 \cdot \left(\frac{d_d}{\frac{d_3}{H_3}}\right) \cdot e^{0.686 \cdot \frac{G_w}{G_{av1}}}$$

A_{crz2}	1.623944	#

$$A_{crz3} = \left(1 - 0.06825 \cdot G_w\right) \cdot K_{ct\_fi}{}^{0.09667} \cdot e^{8.7434 \cdot \left(\frac{1}{d_3} - 0.01\right)}$$

A_{crz3}	1.100798	#

$$C_{rz} = \left(A_{crz1} - A_{crz2}\right) \cdot A_{crz3}$$

C_{rz}	0.487458	#

Due to reasons discussed in section 5.3.4, C_{rz} = 1, thus

$$K_{ctfi} = C_{rz} \cdot K_{ctfinorz}$$

K_{ctfi}	9.654751	#

The loss coefficient for the rain zone referred to the fill conditions is calculated using the following equation, which also makes use of the identical α-coefficients defined for the rain zone transfer coefficient equation used above.

$$B_{rz1} = \left(0.22460 - 0.31467 \cdot a_\rho \cdot \rho_{av1} + 5263.04 \cdot a_\mu \cdot \mu_{av1}\right)$$

B_{rz1}	0.001050	#

$$B_{rz2} = 0.775526 \cdot \left(1.4824163 \cdot e^{71.52 \cdot a_L \cdot d_d} - 0.91\right)$$

B_{rz2}	0.961899	#

$$B_{rz3} = \left(0.39064 \cdot e^{0.010912 \cdot a_L \cdot d_3} - 0.17\right) \cdot \left[2.0892 \cdot \left(a_v \cdot v_{av3}\right)^{-1.3944} + 0.14\right]$$

B_{rz3}	0.849058	#

$$B_{rz4} = e^{\left(0.8449 \cdot \ln\left(a_L \cdot \frac{d_e}{2}\right) - 2.312\right) \cdot \left(0.3724 \cdot \ln\left(a_v \cdot v_{av3}\right) + 0.7263\right) \cdot \ln\left[206.757 \cdot \left(a_L \cdot H_3\right)^{-2.8344} + 0.43\right]}$$

B_{rz4}	0.810150	#

$$K_{rz} = 3 \cdot a_v \cdot \left(\frac{G_w}{\rho_{wo}}\right) \cdot \left(\frac{H_3}{d_d}\right) \cdot \left(B_{rz1} + B_{rz2} \cdot B_{rz3} \cdot B_{rz4}\right)$$

K_{rz}	10.99179	#

$$K_{rzfi} = K_{rz} \cdot \left(\frac{\rho_{av15}}{\rho_{av1}}\right) \cdot \left(\frac{m_{av1}}{m_{av15}}\right)^2 \cdot \left(\frac{4 \cdot A_{fr}}{\pi \cdot d_3{}^2}\right)^2$$

K_{rzfi}	9.937799	#

The effective diameter in the absence of the rain zone can be determined from

$$d_{e3} = d_3 \cdot \left[\begin{array}{l} 1.27 - 0.16722 \cdot \ln\left(\frac{d_3}{H_3}\right) + \\ \left(0.043653 \cdot \ln\left(\frac{d_3}{H_3}\right) - 0.062658\right) \cdot \ln\left(K_{ct\_fi}\right) \end{array}\right]$$

d_{e3}	88.416	m

The corresponding effective frontal area is:

$$A_{fre} = \frac{\pi \cdot d_{e3}{}^2}{4}$$

A_{e3}	6139.81	m^2

At this stage it is possible to confirm the values of p_{a3} and p_{a5} according to the equations

$$p_{a3} = p_{a1} \cdot \left(1 - \frac{0.00975 \cdot H_3}{T_{a1}}\right)^{3.5 \cdot (1+w_1) \cdot \left(\frac{w_1}{w_1 + 0.62198}\right)} - \left(K_{tsfi} + K_{rzfi} + K_{fsfi} + K_{ctfi}\right) \cdot \frac{\left(\frac{m_{av15}}{A_{fr}}\right)^2}{2 \cdot \rho_{av15}}$$

p_{a3}	83358.5	N/m^2

$$p_{a5} = p_{a1} \cdot \left(1 - \frac{0.00975 \cdot \left(H_3 + \frac{L_{fi}}{2}\right)}{T_{a1}}\right)^{3.5 \cdot (1+w_1) \cdot \left(\frac{w_1}{w_1 + 0.62198}\right)}$$

p_{a5}	83302	N/m^2

This value for pa5 must also be in agreement with the previously determined value for this parameter. The error in this case is (equation (B-2)):

E_{pa5}	-3.01E-8	%

The temperature lapse rate in the tower is determined from

$$A_{\xi Ta51} = w_5{}^2 \cdot p_{a5} \cdot e^{\frac{5406.1915}{T_{a5}}}$$

$A_{\zeta Ta51}$	5.159E+09	#

$$A_{\xi Ta52} = \left(w_5 + 0.622\right) \cdot R_a \cdot T_{a5}$$

$A_{\zeta Ta52}$	56990.1	#

$$i_e = i_{fg}\left(273.15\right) - \left(\begin{array}{l} c_{pw}\left(\frac{T_{a5} + 273.15}{2}\right) - \\ c_{pv}\left(\frac{T_{a5} + 273.15}{2}\right) \end{array}\right) \cdot \left(T_{a5} - 273.15\right)$$

i_e	2.432630E+06	J/kg

$$c_{pma\,5} = c_{pa}\left(T_{a5}\right) + w_5 \cdot c_{pv}\left(T_{a5}\right)$$

c_{pma5}	1069.80	J/kg.K

These equations are substituted into the following equation to obtain the temperature lapse rate inside the tower:

$$\xi_{T_{a5}} = \frac{-(1+w_5)\cdot g\cdot\left(1+\dfrac{0.42216\cdot 10^{-11}\cdot A_{\xi Ta51}\cdot i_e}{A_{\xi Ta52}}\right)}{\left(C_{pma5}+3.6693\cdot 10^{-8}\cdot A_{\xi Ta51}\cdot\dfrac{i_e}{T_{a5}^{\ 2}}\right)}$$ ζ_{Ta5} -0.00321 K/m

The temperature lapse rate in the tower is determined from

$$T_{a6} = T_{a5} + \xi_{Ta5}\cdot(H_6 - H_3 - L_{fi} - L_{sp})$$ T_{a6} 302.531 K

The corresponding density of the air-vapour mixture at this temperature is (equation (A-12):

$$\rho_{av6} = \rho_{av}(w_5, p_{a6}, T_{a6})$$ ρ_{av6} 0.92608 kg/m^3

The ambient temperature at elevation (7) can be calculated from the Dry-Adiabatic Lapse Rate (DALR), as follows with $H_7 = H_6$

$$T_{a7} = T_{a1} - 0.00975\cdot H_6$$ T_{a7} 285.658 K

The pressure at (7) can be determined from

$$p_{a7} = p_{a1}\cdot\left(1-0.00975\cdot\frac{H_6}{T_{a1}}\right)^{3.5\cdot(1+w_1)\cdot\left(\frac{w_1}{w_1+0.62198}\right)}$$ p_{a7} 81991.2 Pa

The corresponding density of the ambient air at elevation (7), assuming a uniform ambient humidity ratio w_1, is (equation (A-12):

$$\rho_{av7} = \rho_{av}(w_1, p_{a7}, T_{a7})$$ ρ_{av7} 0.994826 kg/m^3

With no cold inflow, these values yield the following densimetric Froude number:

$$Fr_D = \frac{1}{\rho_{av6}\cdot(\rho_{av7}-\rho_{av6})\cdot g\cdot d_6}\cdot\left(\frac{m_{av5}}{A_6}\right)^2$$ Fr_D 0.74371 #

The pressure at (6) can then be determined from

$$p_{a6} = p_{a7} + \left(0.02\cdot Fr_D^{\ -1.5} - \frac{0.14}{Fr_D}\right)\cdot\left(\frac{1}{\rho_{av6}}\right)\cdot\left(\frac{m_{av5}}{A_6}\right)^2$$ p_{a6} 81986.9 Pa

This value should be in agreement with the previously-stated value. The error in this case is (equation (B-2)):

E_{pa6} -5.16E-8 %

Draft equation

The draft equation may now be solved using the above values. Upon substitution, the left side of the equation yields

$$A_{LS1} = p_{a1} \cdot \left[1 - \frac{0.00975 \cdot \left(H_3 + \frac{L_{fi}}{2} \right)}{T_{a1}} \right]^{3.5 \cdot (1+w_1) \cdot \left(\frac{w_1}{w_1 + 0.62198} \right)}$$

A_{LS1} 83389.368385 #

$$A_{LS2} = \left[1 + \frac{\xi_{Ta5} \cdot \left(H_6 - H_3 - \frac{L_{fi}}{2} \right)}{T_{a1}} \right]^{\frac{-0.02123 \cdot (1+w_5)}{\xi_{Ta5} \cdot (w_5 + 0.62198)}}$$

A_{LS2} 0.984355 #

$$LS_{draft} = A_{LS1} \cdot A_{LS2} - p_{a7} - (p_{a6} - p_{a7})$$

LS_{draft} 97.825 #

The total loss coefficient referred to fill conditions is obtained by adding all the appropriate loss coefficients as follows:

$$K_{total} = K_{tsfi} + K_{rzfi} + K_{fsfi} + K_{ctfi} + K_{fi} + K_{ctefi} + K_{spfi} + K_{wdfi} + K_{defi}$$

K_{total} 46.27738 #

The corresponding pressure drop is therefore

$$\Delta p_{losses} = K_{total} \cdot \frac{1}{2 \cdot \rho_{av15}} \cdot \left(\frac{m_{av15}}{A_{fr}} \right)^2$$

Δp_{losses} 87.76988 Pa

$$RS_{draft} = \Delta p_{losses} \cdot \left[1 + \frac{\xi_{Ta5} \cdot \left(H_6 - H_3 - \frac{L_{fi}}{2} \right)}{T_{a5}} \right]^{\frac{-0.021233 \cdot (1+w_5)}{\xi_{Ta5} \cdot (w_5 + 0.62198)}}$$

RS_{draft} 97.825 #

The values on the right and left of the draft equation should be equal for convergence of the air-vapour mass flow rate.

The error regarding the draft equation is (equation (B-2)):

E_{Draft} -1.88E-8 %

The approximate amount of water lost due to evaporation is given by

$$m_{w\_evap} = m_a \cdot (w_5 - w_1)$$

m_{w_evap} 276.28 kg/s

Convergence criteria

Merkel number error	E_{Me}	2.48E-8	%
Energy balance error	E_Q	-4.69E-8	%
Air pressure after the drift eliminators error	E_{pa5}	-3.01E-8	%
Air pressure at the tower outlet error	E_{pa6}	-5.16E-8	%
Draft equation error	E_{Draft}	-1.88E-8	%

B.2 DESIGN CONDITIONS WITH IMPROVEMENT DISCUSSED IN SECTION 6.5

In this sample calculation the researcher provides the results for Eskom's Majuba Power Station one-dimensional model when the design conditions and the improvement discussed in section 6.5 are employed.

NDWCT design data

Dimensions			
Tower height	H_6	153.0	m
Tower inlet height	H_3	9.5	m
Tower inlet diameter	d_3	87.532	m
Shell base cross-sectional area	A_3	6017.604	m^2
Tower outlet diameter	d_6	54.000	m
Tower outlet cross-sectional area	A_6	2290.221	m^2
Fill height	L_{fi}	1.800	m
Spray zone height	L_{sp}	1.500	m
Inlet rounding	r_i	0.000	m
Number of tower supports	n_{ts}	64.000	#
Length of tower supports	L_{ts}	9.618	m
Diameter of tower supports	d_{ts}	0.700	m
Drag coefficient of tower supports (round)	C_{Dts}	1.100	#
Shell thickness (inlet)	t_s	0.920	m
Ambient conditions			
Atmospheric pressure at ground level	p_{a1}	83492.000	Pa
Air temperature at ground level	T_{a1}	287.150 14.000	K °C
Wet-bulb temperature at ground level	T_{awb1}	283.750 10.600	K °C
Ambient Temperature gradient from ground	*DALR*	-0.00975	K/m
Operating conditions			
Inlet water temperature	T_{wi}	306.090 32.940	K °C
Water mass flow rate	m_w	17800.000	kg/s
Performance characteristics			
The cooling tower is fitted with a trickle pack fill for which the performance characteristics are:			
Effective frontal area of the fill	A_{fr}	5897.000	m^2
Mean drop diameter in the rain zone	d_d	0.0029	m
Fill support system and contraction loss coefficient based on Afr	K_{fs}	0.500	#
Water distribution loss coefficient	K_{wd}	0.500	#
Kinetic energy coefficient at tower outlet	α_{e6}	1.010	#
Constants			
Pi constant	π	3.14159	rad
Gravitation constant	g	9.80	m/s^2
Vapour gas constant	R_v	461.52	J/kg.K

Air gas constant	R_a	287.08	J/kg.K
Air molecular weight	M_a	28.970	kg/mole
Vapour molecular weight	M_v	18.016	kg/mole
Latent heat of vaporization at 273.15K	i_{fgwo}	2501598	J/kg

NDWCT Solution

Air-vapour mass flow rate through the fill	m_{av15}	11063.72	kg/s
Air pressure after the drift eliminators	p_{a5}	83298.8	Pa
Air temperatures after the drift eliminators	T_{a5}	303.354	K
Air pressure at the tower outlet	p_{a6}	81986.9	Pa
Mean re-cooled water-outlet temperature	T_{wo}	294.350 21.200	K °C

Thermo-physical properties:

The thermo-physical properties of the air at (1), employing the equations given in APPENDIX A, are as follows:

Specified air-inlet dry-bulb temperature	T_{a1}	287.15	K
Specified air-inlet wet-bulb temperature	T_{awb1}	283.75	K
Humidity ratio (equation ((A-17)))	w_1	0.008312277	*kg/kg d.a.*
Humidity ratio of saturated air at Two (equation ((A-17))	w_{s1}	0.019429020	*kg/kg d.a.*
Density (equation (A-12))	ρ_{av1}	1.00777	kg/m^3
Dynamic viscosity (equation (A-3))	μ_{av1}	1.7788E-05	Pa.s
Enthalpy (equation (A-20))	i_{ma1}	35101.41383	J/kg
Specific heat (equation (A-2))	c_{pa1}	1006.6	J/kg.K
Specific heat (equation (A-6))	c_{pv1}	1874.5	J/kg.K

If the air is assumed to be saturated immediately after the drift eliminator, the wet-bulb temperature at (5) will be equal to the given dry-bulb temperature at this elevation, therefore

Wet-bulb temperature	T_{awb5}	303.354	K

The corresponding thermo-physical properties at (5) can be determined using the equations given in Appendix A.

Vapour pressure (equation (A-5))	p_{v5}	4292.44	Pa
Humidity ratio (equation (A-16))	w_5	0.033970559	kg/kg d.a.
Density (equation (A-12))	ρ_{av5}	0.937777703	kg/m^3
Dynamic viscosity (equation (A-14))	μ_{av5}	1.82728E-05	Pa.s
Enthalpy (equation (A-20))	i_{ma5}	117307.83	J/kg
Specific heat (equation (A-2))	c_{pa5}	1007.1	J/kg.K
Specific heat (equation (A-6))	c_{pv5}	1889.1	J/kg.K
The mean pressure of the air-vapour in the fill (equation (B-1))	p_{a15}	83395.4	Pa
The approximate harmonic mean density of the air-vapour in the fill (equation (B-1))	ρ_{av15}	0.971516	kg/m^3
The mean air temperature (equation (B-1))	T_{a15}	295.252 22.102	K °C

The thermo-physical properties of water at the inlet temperature T_{wi} are as follows:

Specific heat (equation (A-22))	c_{pwi}	4177.599	J/kg.K

The thermo-physical properties of water at the outlet temperature T_{wo} are as follows:

Density (equation (A-21))	ρ_{wo}	997.907	kg/m^3
Specific heat (equation (A-22))	c_{pwo}	4184.072	J/kg.K
Surface tension (equation (A-27))	σ_{wo}	0.072592	N/m
The mean water temperature (equation (B-1))	T_{wm}	300.220 27.070	K °C
Specific heat at T_{wm} (equation (A-22))	c_{pwm}	4180.0	J/kg.K

Flow rates:

The dry air mass flow rate can be determined from the following relation:

$$m_a = \frac{2 \cdot m_{av15}}{2 + w_1 + w_5}$$ m_a 10834.7 kg/s

The respective flow rates upstream and downstream of the fill are thus

Upstream:	$m_{av1} = m_a \cdot (1 + w_1)$	m_{av1}	10924.7	kg/s
Downstream:	$m_{av5} = m_a \cdot (1 + w_5)$	m_{av5}	11202.7	kg/s

The corresponding mass velocities are: $G_{av15} = \frac{m_{av15}}{A_{fr}}$ G_{av15} 1.87616 kg/m^2.s

$$G_a = \frac{m_a}{A_{fr}}$$ G_a 1.83731 kg/m^2.s

$$G_{av1} = \frac{m_{av1}}{A_{fr}}$$ G_{av1} 1.85258 kg/m^2.s

$$G_{av5} = \frac{m_{av5}}{A_{fr}}$$ G_{av5} 1.89973 kg/m^2.s

$$G_w = \frac{m_w}{A_{fr}}$$ G_w 3.01848 kg/m^2.s

Transfer coefficients or Merkel numbers:

The transfer coefficient of the rain zone of this particular tower is approximated. The α-coefficients appearing in this equation for the rain zone transfer coefficient and the pressure drop, required later on, are as follows:

$$a_\mu = 3.061 \cdot 10^{-9} \cdot \left(\frac{\rho_{wo}^{\ 4} \cdot g^9}{\sigma_{wo}} \right)^{0.25}$$ α_μ 0.999975 #

$$a_\rho = \frac{998}{\rho_{wo}}$$ α_ρ 1.000094 #

$$a_\mu = 73.298 \cdot \left(\frac{\sigma_{wo}^{\ 3} \cdot g^5}{\rho_{wo}^{\ 3}} \right)^{0.25}$$ α_v 1.001093 #

$$a_\mu = 36.122 \cdot \left(\frac{\sigma_{wo} \cdot g}{\rho_{wo}} \right)^{0.25}$$ α_L 1.000345 #

The values of these values are close to unity.

The diffusion coefficient at air-inlet conditions is:

$$D_1 = \frac{0.04357 \cdot T_{a1}^{1.5} \cdot \left(\frac{1}{28.97} + \frac{1}{18.016}\right)^{0.5}}{p_{a1} \cdot \left(29.9^{0.333} + 18.8^{0.333}\right)^2}$$

D_1 2.29903E-05 m^2/s

The Schmidt number is: $Sc_1 = \frac{\mu_{av1}}{\rho_{av1} \cdot D_1}$

Sc_1 0.767740 #

The air-vapour velocity before the fill: $v_{av3} = \frac{m_{av1}}{\rho_{av1} \cdot A_{fr}}$

v_{av3} 1.89973 m/s

With these values find

$$A_{rz1} = 12 \cdot \left(\frac{D_1}{v_{av3} \times d_d}\right) \cdot \left(\frac{H_3}{d_d}\right) \cdot \left(\frac{p_{a1}}{\rho_{wo} \cdot R_v \cdot T_{a1}}\right) \cdot Sc_1^{0.33} \cdot \left(\frac{\ln\left(\frac{w_{s1} + 0.622}{w_1 + 0.622}\right)}{w_{s1} - w_1}\right)$$

A_{rz1} 0.149273 #

$A_{rz2} = 0.90757 \cdot a\rho \cdot \rho_{av1} - 30341.04 \cdot a_\mu \cdot \mu_{av1} - 0.37564$ A_{rz2} -0.000625 #

$A_{rz3} = 0.55 + 41.7215 \cdot (a_L \cdot d_d)^{0.80043}$ A_{rz3} 0.938425 #

$A_{rz4} = \left(3.11 \cdot e^{0.15 \cdot a_v \cdot v_{av3}} - 3.13\right) \cdot \left[3.741 \cdot (a_L \cdot H_3)^{-1.23456} + 0.713\right]$ A_{rz4} 0.951451 #

$A_{rz5} = e^{5.3759 \cdot e^{-0.2092 \cdot a_L \cdot H_3} \cdot \ln\left(0.3719 \cdot e^{0.0019055 \cdot a_L \cdot d_3} + 0.55\right)}$ A_{rz5} 0.992206 #

The substitution of the above equations into the following equation yields the transfer coefficient applicable to the rain zone, the rain zone Merkel number is:

$$Me_{rz} = A_{rz1} \cdot \left(A_{rz2} + 4.04016 A_{rz3} \cdot A_{rz4} \cdot A_{rz5}\right)$$

Me_{rz} 0.53418 #

The transfer coefficient applicable to the fill, the fill Merkel number is:

$$Me_{fi} = 0.25575 \cdot L_{fi} \cdot G_w^{-0.094} \cdot G_a^{0.6023}$$

Me_{fi} 1.252034 #

The transfer coefficient applicable to the spray zone, the spray zone Merkel number is:

$$Me_{sp} = 0.2 \cdot L_{sp} \cdot \left(\frac{G_a}{G_w}\right)^{0.5}$$

Me_{sp} 0.234056 #

The overall transfer coefficient is the sum of the transfer coefficients of the rain, fill and spray zones respectively.

$$Me_{CT} = Me_{rz} + Me_{fi} + Me_{sp}$$

Me_{CT} 2.02027 #

If the four-point form of the Chebyshev integral is applied to this relation, the integral on the right-hand side can be determined as follows:

The enthalpy differentials are dependent on the following intermediate temperatures:

$$T_{wa} = T_{wo} + 0.1 \cdot (T_{wi} - T_{wo})$$ T_{wa} 295.524 K

$$T_{wb} = T_{wo} + 0.4 \cdot (T_{wi} - T_{wo})$$ T_{wb} 299.046 K

$$T_{wc} = T_{wo} + 0.6 \cdot (T_{wi} - T_{wo})$$ T_{wc} 301.394 K

$$T_{wd} = T_{wo} + 0.9 \cdot (T_{wi} - T_{wo})$$ T_{wd} 304.916 K

The humidity ratios of saturated air at the intermediate water temperatures are (equation (A-18)):

$$w_{sa} = f(T_{wa}, p_{a15}, p_v(T_{wa}))$$ w_{sa} *0.02094* kg/kg d.a.

$$w_{sb} = f(T_{wb}, p_{a15}, p_v(T_{wb}))$$ w_{sb} *0.02608* kg/kg d.a.

$$w_{sc} = f(T_{wc}, p_{a15}, p_v(T_{wc}))$$ w_{sc} *0.03012* kg/kg d.a.

$$w_{sd} = f(T_{wd}, p_{a15}, p_v(T_{wd}))$$ w_{sd} *0.03727* kg/kg d.a.

From these intermediate temperatures and humidity ratios the enthalpies of saturated air at the intermediate water temperatures are determined as follows (equation (A-19) :

i_{maswa} 75790.6 J/kg

i_{maswb} 92571.0 J/kg

i_{maswc} 105368 J/kg

i_{maswd} 127433 J/kg

The intermediate air enthalpies are also calculated using these values.

$$i_{maa} = \frac{m_w \cdot c_{pwm} \cdot (T_{wa} - T_{wo})}{m_a} + i_{ma1}$$ i_{maa} 42996.59 J/kg

$$i_{mab} = \frac{m_w \cdot c_{pwm} \cdot (T_{wb} - T_{wo})}{m_a} + i_{ma1}$$ i_{mab} 66682.13 J/kg

$$i_{mac} = \frac{m_w \cdot c_{pwm} \cdot (T_{wc} - T_{wo})}{m_a} + i_{ma1}$$ i_{mac} 82472.48 J/kg

$$i_{mad} = \frac{m_w \cdot c_{pwm} \cdot (T_{wd} - T_{wo})}{m_a} + i_{ma1}$$ i_{mad} 106158.0 J/kg

Find the difference in enthalpies as the difference in the above two values

$$\Delta i_a = i_{maswa} - i_{maa}$$ Δi_a 32794.01 J/kg

$$\Delta i_b = i_{maswb} - i_{mab}$$ Δi_b 25888.85 J/kg

$$\Delta i_c = i_{maswc} - i_{mac}$$ Δi_c 22896.02 J/kg

$$\Delta i_d = i_{maswd} - i_{mad}$$ Δi_d 21275.09 J/kg

Substitution into the Chebyshev integral yields:

$$Me_{CT} = \frac{c_{pwm} \cdot (T_{wi} - T_{wo})}{4} \cdot \left(\frac{1}{\Delta i_a} + \frac{1}{\Delta i_b} + \frac{1}{\Delta i_c} + \frac{1}{\Delta i_d} \right)$$ Me_{CT} 2.02027 #

This value must be basically identical to the value obtained by adding the transfer coefficients of the three wet zones together, which in turn means that the determined T_{wo} is correct.

The error regarding the Merkel numbers is (equation (B-2)):

E_{Me}	-2.91E-8	%

Energy Balance

The heat rejected by the cooling tower is given by

$$Q_w = m_w \cdot c_{pwi} \cdot (T_{wi} - 273.15) - [m_w - m_a \cdot (w_5 - w_q)] \cdot c_{pwo} \cdot (T_{wo} - 273.15)$$

Q_w	890.678	MW

The correctness of the chosen temperature of the saturated air leaving the spray zone, T_{a5}, can be confirmed from the relation

$$Q_a = m_a \cdot (i_{ma5} - i_{ma1})$$

Q_a	890.678	MW

The values of Q show an error of (equation (B-2)):

E_Q	1.156E-8	%

Loss coefficients

The loss coefficients due to the tower supports referred to the fill is determined from

$$K_{ts} = \frac{C_{Dts} \cdot L_{ts} \cdot n_{ts} \cdot d_{ts}}{\pi \cdot d_3 \cdot H_3}$$

K_{ts}	0.181433	#

$$K_{tsfi} = \left[\frac{C_{Dts} \cdot L_{ts} \cdot n_{ts} \cdot d_{ts} \cdot A_{fr}^{\,2}}{(\pi \cdot d_3 \cdot H_3)^3}\right] \cdot \left(\frac{\rho_{av15}}{\rho_{av1}}\right) \cdot \left(\frac{m_{av1}}{m_{av15}}\right)^2$$

K_{tsfi}	0.868965	#

The specified loss coefficient due to the fill support structure and the contraction loss into the fill is referred to the mean density through the fill, i.e.:

$$K_{fsfi} = K_{fs} \cdot \left(\frac{\rho_{av15}}{\rho_{av1}}\right) \cdot \left(\frac{m_{av1}}{m_{av15}}\right)^2$$

K_{fsfi}	0.469976	#

According to the specified fill loss coefficient

$$K_{fsfi} = 1.851 \cdot L_{fi} \cdot G_w^{\,1.2752} \cdot G_a^{\,-1.0356}$$

K_{fdm}	16.59668	#

The actual fill loss coefficient applicable to the cooling tower is given by

$$K_{fi} = K_{fdm} + \left(\frac{G_{av5}^{\,2}}{\rho_{av5}} - \frac{G_{av1}^{\,2}}{\rho_{av1}}\right) \cdot \frac{\rho_{av15}}{G_{av15}^{\,2}}$$

K_{fi}	16.71889	#

The expansion loss coefficient after the fill is given by

$$K_{ctefi} = \left(1 - \frac{A_{fr}}{A_3}\right)^2 \cdot \left(\frac{\rho_{av15}}{\rho_{av5}}\right) \cdot \left(\frac{m_{av5}}{m_{av15}}\right)^2$$

K_{ctefi}	0.000427	#

The loss coefficient through the spray zone is given by

$$K_{spfi} = L_{sp} \cdot \left[0.4 \cdot \left(\frac{G_w}{G_a}\right) + 1\right] \cdot \left(\frac{\rho_{av15}}{\rho_{av5}}\right) \cdot \left(\frac{m_{av5}}{m_{av15}}\right)^2$$

K_{spfi}	2.64027	#

For the water distribution system, it follows from the specified loss coefficient that

$$K_{wdfi} = K_{wd} \cdot \left(\frac{\rho_{av15}}{\rho_{av5}}\right) \cdot \left(\frac{m_{av5}}{m_{av15}}\right)^2$$ K_{wdfi} 0.531086 #

The loss coefficient for a type c drift eliminator based on the fill is given by

$$Ry = \frac{m_{av5}}{A_{fr} \cdot \mu_{av5}}$$ Ry 1.039652E+05 #

$$K_{defi\_C} = K_{de}(Ry) \cdot \left(\frac{\rho_{av15}}{\rho_{av5}}\right) \cdot \left(\frac{m_{av5}}{m_{av15}}\right)^2$$ K_{defi_C} 5.631197 #

The sum of all the loss coefficients in the vicinity of the fill is

$$K_{ct\_fi} = K_{fsfi} + K_{fi} + K_{ctefi} + K_{spfi} + K_{wdfi} + K_{defi}$$ K_{ct_fi} 25.99185 #

The inlet loss coefficient for a circular cooling tower with splash type isotropic fill operating in the absence of a rain zone and based on fill conditions can be determined according to the following equation, presented in Kröger (2004).

$$A_{ctfi1} = 0.011266 \cdot e^{\frac{0.093 \cdot d_3}{H_3}} \cdot K_{ct\_fi}^{\ 2} - 0.3105 \cdot e^{\frac{0.1085 \cdot d_3}{H_3}} \cdot K_{ct\_fi}$$ A_{ctfi1} -4.001091 #

$$A_{ctfi2} = -1.7522 + 4.5614 \cdot e^{\frac{0.131 \cdot d_3}{H_3}}$$ A_{ctfi2} 13.49887 #

$$A_{ctfi3} = \frac{10970.2 \cdot e^{-0.2442 \cdot K_{ct\_fi}} + 1391.3}{\frac{d_3}{H_3} - 15.7258} + 1205.54 \cdot e^{-0.23 \cdot K_{ct\_fi}} + 109.314$$ A_{ctfi3} -104.2374 #

$$A_{ctfi4} = \frac{2 \cdot r_i}{d_3} - \frac{0.01942}{\frac{d_3}{H_3} - 27.929} - 0.016866$$ A_{ctfi4} -0.015828 #

$$K_{ctfinorz} = \left(A_{ctfi1} + A_{ctfi2} + a\sinh\left(A_{ctfi3} \cdot A_{ctfi4}\right)\right) \cdot \left[\left(\frac{\rho_{av15}}{\rho_{av1}}\right) \cdot \left(\frac{m_{av1}}{m_{av15}}\right)^2 \cdot \left(\frac{4 \cdot A_{fr}}{\pi \cdot d_3^{\ 2}}\right)^2\right]$$ $K_{ctfinorz}$ 9.72421 #

This value must be multiplied by a correction factor C_{rz} as given by the following equation to obtain the correct inlet loss coefficient in the presence of the rain zone.

$$A_{crz1} = 0.2394 + 80.1 \cdot \left(\frac{0.0954}{\frac{d_3}{H_3}} + d_d\right) \cdot e^{0.395 \cdot \frac{G_w}{G_{av1}}} - 0.3195 \cdot \frac{G_w}{G_{av1}}$$ A_{crz1} 2.090085 #

$$A_{crz2} = 966 \cdot \left(\frac{d_d}{\frac{d_3}{H_3}} \right) \cdot e^{0.686 \cdot \frac{G_w}{G_{av1}}}$$ A_{crz2} 1.667085 #

$$A_{crz3} = (1 - 0.06825 \cdot G_w) \cdot K_{ct\_fi}^{\ 0.09667} \cdot e^{8.7434 \cdot \left(\frac{1}{d_3} - 0.01 \right)}$$ A_{crz3} 1.101527 #

$$C_{rz} = (A_{crz1} - A_{crz2}) \cdot A_{crz3}$$ C_{rz} 0.465946 #

Due to reasons discussed in section 5.3.4, C_{rz} = 1, thus

$$K_{ctfi} = C_{rz} \cdot K_{ctfinorz}$$ K_{ctfi} 9.72421 #

The loss coefficient for the rain zone referred to the fill conditions is calculated using the following equation, which also makes use of the identical α-coefficients defined for the rain zone transfer coefficient equation used above.

$$B_{rz1} = (0.22460 - 0.31467 \cdot a_\rho \cdot \rho_{av1} + 5263.04 \cdot a_\mu \cdot \mu_{av1})$$ B_{rz1} 0.001070 #

$$B_{rz2} = 0.775526 \cdot (1.4824163 \cdot e^{71.52 \cdot a_L \cdot d_d} - 0.91)$$ B_{rz2} 0.961899 #

$$B_{rz3} = (0.39064 \cdot e^{0.010912 \cdot a_L \cdot d_3} - 0.17) \cdot \left[\begin{array}{l} 2.0892 \cdot (a_v \cdot v_{av3})^{-1.3944} \\ + 0.14 \end{array} \right]$$ B_{rz3} 0.849058 #

$$B_{rz4} = e^{\left(0.8449 \cdot \ln\left(a_L \cdot \frac{d_e}{2} \right) - 2.312 \right) \cdot (0.3724 \cdot \ln(a_v \cdot v_{av3}) + 0.7263) \cdot \ln\left[206.757 \cdot (a_L \cdot H_3)^{-2.8344} + 0.43 \right]}$$ B_{rz4} 0.810150 #

$$K_{rz} = 3 \cdot a_v \cdot \left(\frac{G_w}{\rho_{wo}} \right) \cdot \left(\frac{H_3}{d_d} \right) \cdot (B_{rz1} + B_{rz2} \cdot B_{rz3} \cdot B_{rz4})$$ K_{rz} 10.99212 #

$$K_{rzfi} = K_{rz} \cdot \left(\frac{\rho_{av15}}{\rho_{av1}} \right) \cdot \left(\frac{m_{av1}}{m_{av15}} \right)^2 \cdot \left(\frac{4 \cdot A_{fr}}{\pi \cdot d_3^{\ 2}} \right)^2$$ K_{rzfi} 13.52186 #

The effective diameter in the absence of the rain zone can be determined from

$$d_{e3} = d_3 \cdot \left[\begin{array}{l} 1.27 - 0.16722 \cdot \ln\left(\frac{d_3}{H_3} \right) + \\ \left(0.043653 \cdot \ln\left(\frac{d_3}{H_3} \right) - 0.062658 \right) \cdot \ln(K_{ct\_fi}) \end{array} \right]$$ d_{e3} 88.437 m

The corresponding effective frontal area is:

$$A_{fre} = \frac{\pi \cdot d_{e3}^{\ 2}}{4}$$ A_{e3} 6142.67 m^2

At this stage it is possible to confirm the values of p_{a3} and p_{a5} according to the equations:

$$p_{a3} = p_{a1} \cdot \left(1 - \frac{0.00975 \cdot H_3}{T_{a1}}\right)^{3.5\cdot(1+w_1)\cdot\left(\frac{w_1}{w_1+0.62198}\right)} - \left(K_{tsfi} + K_{rzfi} + K_{fsfi} + K_{ctfi}\right)\cdot\frac{\left(\frac{m_{av15}}{A_{fr}}\right)^2}{2\cdot\rho_{av15}}$$

p_{a3}	83353.7	N/m^2

$$p_{a5} = p_{a1} \cdot \left(1 - \frac{0.00975 \cdot \left(H_3 + \frac{L_{fi}}{2}\right)}{T_{a1}}\right)^{3.5\cdot(1+w_1)\cdot\left(\frac{w_1}{w_1+0.62198}\right)}$$

p_{a5}	83298.8	N/m^2

This value for p_{a5} must also be in agreement with the previously-determined value for this parameter. The error in this case is (equation (B-2)):

E_{pa5}	3.2E-8	%

The temperature lapse rate in the tower is determined from

$$A_{\xi Ta51} = {w_5}^2 \cdot p_{a5} \cdot e^{\frac{5406.1915}{T_{a5}}}$$

$A_{\zeta Ta51}$	5.279E+09	#

$$A_{\xi Ta52} = \left(w_5 + 0.622\right)\cdot R_a \cdot T_{a5}$$

$A_{\zeta Ta52}$	57126.4	#

$$i_e = i_{fg}(273.15) - \left(c_{pw}\left(\frac{T_{a5}+273.15}{2}\right) - c_{pv}\left(\frac{T_{a5}+273.15}{2}\right)\right)\cdot\left(T_{a5} - 273.15\right)$$

i_e	2.431775E+06	J/kg

$$c_{pma5} = c_{pa}(T_{a5}) + w_5 \cdot c_{pv}(T_{a5})$$

c_{pma5}	1070.31	J/kg.K

These equations are substituted into the following equation to obtain the temperature lapse rate inside the tower

$$\xi_{T_{a5}} = \frac{-(1+w_5)\cdot g\cdot\left(1 + \frac{0.42216\cdot10^{-11}\cdot A_{\xi Ta51}\cdot i_e}{A_{\xi Ta52}}\right)}{\left(C_{pma5} + 3.6693\cdot10^{-8}\cdot A_{\xi Ta51}\cdot\frac{i_e}{{T_{a5}}^2}\right)}$$

ζ_{Ta5}	-0.00319	K/m

The temperature lapse rate in the tower is determined from

$$T_{a6} = T_{a5} + \xi_{Ta5}\cdot\left(H_6 - H_3 - L_{fi} - L_{sp}\right)$$

T_{a6}	302.906	K

The corresponding density of the air-vapour mixture at this temperature is (equation (A-12):

$$\rho_{av6} = \rho_{av}(w_5, p_{a6}, T_{a6})$$

ρ_{av6}	0.92455	kg/m^3

The ambient temperature at elevation (7) can be calculated from the Dry-Adiabatic Lapse Rate (DALR) as follows with $H_7 = H_6$

$$T_{a7} = T_{a1} - 0.00975\cdot H_6$$

T_{a7}	285.658	K

The pressure at (7) can be determined from

$$p_{a7} = p_{a1} \cdot \left(1 - 0.00975 \cdot \frac{H_6}{T_{a1}}\right)^{3.5 \cdot (1+w_1) \cdot \left(\frac{w_1}{w_1 + 0.62198}\right)}$$

p_{a7}	81991.2	Pa

The corresponding density of the ambient air at elevation (7), assuming a uniform ambient humidity ratio w_1, is (Equation (A-12):

$$\rho_{av7} = \rho_{av}(w_1, p_{a7}, T_{a7})$$

ρ_{av7}	0.994825	kg/m^3

With no cold inflow, these values yield the following densimetric Froude number:

$$Fr_D = \frac{1}{\rho_{av6} \cdot (\rho_{av7} - \rho_{av6}) \cdot g \cdot d_6} \cdot \left(\frac{m_{av5}}{A_6}\right)^2$$

Fr_D	0.695896	#

The pressure at (6) can then be determined from

$$p_{a6} = p_{a7} + \left(0.02 \cdot Fr_D^{-1.5} - \frac{0.14}{Fr_D}\right) \cdot \left(\frac{1}{\rho_{av6}}\right) \cdot \left(\frac{m_{av5}}{A_6}\right)^2$$

p_{a6}	81986.9	Pa

This value should be in agreement with the previously-stated value. The error in this case is (equation (B-2)):

E_{pa6}	4.11E-8	%

Draft equation

The draft equation may now be solved using the above values. Upon substitution, the left side of the equation yields

$$A_{LS1} = p_{a1} \cdot \left[1 - \frac{0.00975 \cdot \left(H_3 + \frac{L_{fi}}{2}\right)}{T_{a1}}\right]^{3.5 \cdot (1+w_1) \cdot \left(\frac{w_1}{w_1 + 0.62198}\right)}$$

A_{LS1}	83389.36	#

$$A_{LS2} = \left[1 + \frac{\xi_{Ta5} \cdot \left(H_6 - H_3 - \frac{L_{fi}}{2}\right)}{T_{a1}}\right]^{\frac{-0.02123 \cdot (1+w_5)}{\xi_{Ta5} \cdot (w_5 + 0.62198)}}$$

A_{LS2}	0.984381	#

$$LS_{draft} = A_{LS1} \cdot A_{LS2} - p_{a7} - (p_{a6} - p_{a7})$$

LS_{draft}	100.032	#

The total loss coefficient referred to fill conditions is obtained by adding all the appropriate loss coefficients as follows:

$$K_{total} = K_{tsfi} + K_{rzfi} + K_{fsfi} + K_{ctfi} + K_{fi} + K_{ctefi} + K_{spfi} + K_{wdfi} + K_{defi}$$

K_{total}	50.10689	#

The corresponding pressure drop is therefore

$$\Delta p_{losses} = K_{total} \cdot \frac{1}{2 \cdot \rho_{av15}} \cdot \left(\frac{m_{av15}}{A_{fr}} \right)^2$$

Δp_{losses}	90.77319	Pa

$$RS_{draft} = \Delta p_{losses} \cdot \left[1 + \frac{\xi_{Ta5} \cdot \left(H_6 - H_3 - \frac{L_{fi}}{2} \right)}{T_{a5}} \right]^{\frac{-0.021233 \cdot (1+w_5)}{\xi_{Ta5} \cdot (w_5 + 0.62198)}}$$

RS_{draft}	100.032	#

The values on the right and left of the draft equation should be equal for convergence of the air-vapour mass flow rate.

The error regarding the draft equation is (equation (B-2)):

E_{Draft}	3.61E-8	%

The approximate amount of water lost due to evaporation is given by

$$m_{w\_evap} = m_a \cdot (w_5 - w_1)$$

m_{w_evap}	277.99	kg/s

Convergence criteria

Merkel number error	E_{Me}	-2.91E-8	%
Energy balance error	E_Q	1.16E-8	%
Air pressure after the drift eliminators error	E_{pa5}	3.20E-8	%
Air pressure at the tower outlet error	E_{pa6}	4.11E-8	%
Draft equation error	E_{Draft}	3.61E-8	%

APPENDIX C
ARTIFICIAL NEURAL NETWORKS

C.1 INTRODUCTION

The term 'neural network' has its origin in attempts to find mathematical representations of information processing in biological systems (Bishop, 2006). An Artificial Neural Network (ANN) is a mathematical/ computational model based on biological neural networks that simulates a combination of neural cells through a connectionist approach. The purpose of ANNs is to acquire the features of these specific cells in order to build an intelligent model.

In more practical terms neural networks are non-linear statistical data modelling tools. It can be used to model complex relationships between predictor (independent) variables, or inputs, and predicted (dependent) variables, or outputs, even when the relationship is complex and not easily articulated in the usual terms of correlations. It can also be implemented to find patterns in data. These relationships or patterns are determined and modelled by means of training data. This means that the network can be trained to recognise outputs given a certain set of inputs (Beale & Jackson, 1990). The more training data is used, the better the predictive capabilities of the network.

A wide range of problem domains, including finance, medicine, engineering, geology and physics have benefitted from the successful implementation of neural networks. This is because all of these areas have certain fields where prediction, classification or control is required. Prediction can be divided into two categories, namely classification and regression. In classification, the objective is to determine to which of a number of discrete classes a given input case belongs, while with regression the aim is to predict the value of a continuous variable.

The reasons for this successful implementation are power and ease-of-use. Neural networks have the power to model extremely complex models or functions (Bishop, 2006). This is accomplished statistically, without any knowledge of the mathematical relationships between variables and the objective function. The level of user knowledge needed to successfully apply neural networks in a specified field is much lower than what would be the case using some more traditional nonlinear statistical methods. The user does, however, need some knowledge of how to select and prepare data; how to select an appropriate neural network and how to interpret the results. Using inaccurate data will result in useless and meaningless results, while the incorrect neural network will result in a slow convergence.

In this appendix the researcher investigates the fundamentals of neural networks. This includes an evaluation of the different activation functions used in neural networks, and an overview of network architectures. A discussion regarding neural network data follows, after which neural network training and convergence criteria are discussed.

C.2 THEORY

C.2.1 The neuron

The human brain consists of approximately 10 billion interconnected neural cells or neurons. In the ANN context these cells are mimicked and known as neurons. A neuron is the most simplistic component of an ANN, as is the case with neural cells in the human brain. Figure C-1 shows a simple neuron with 3 inputs and the single output.

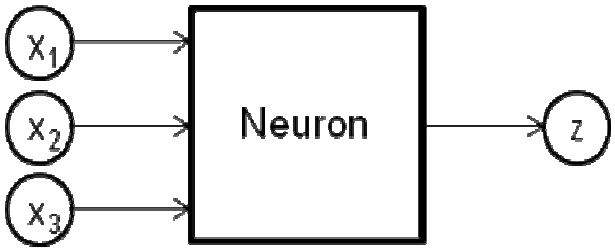

Figure C-1: The basic neuron showing the input and output variables

In the brain the inputs to the neuron simulate the stimuli, or signals, that the neural cells receive. The output simulates the response, or signal, generated by the neural cell. Neurons can have a number of inputs (two or more) that originate either from original data or from outputs of other neurons in a neural network. The inputs are normally scaled to form numbers between 0 and 1. These inputs each have a signal strength, or weight, assigned to them that are initially chosen to be normalised (scaled) random numbers. All the inputs are mathematically manipulated to form only one output per neuron.

Figure C-2 and equation (C-1) explain the mathematical manipulation of the inputs, which includes multiplication of each input with a specific weight. These manipulated inputs are then summed and a firing threshold of the specific neuron is subtracted from this summation to form the activation- or firing signal of the neuron. The firing threshold, more commonly known as the threshold, is the resistance a neuron has to firing (firing points to the release of an output from the neuron or in other words to the activation signal of the neuron). A neuron fires only if the total manipulated input signal explained above exceeds the threshold. The above entails that the activation function is actually a simple linear function of the inputs.

The activation signal is passed through an activation function (or transfer function) to produce the output of the neuron. This activation function is one-dimensional and has the purpose of scaling the output signal to ensure that the signal has a value between 0 and 1. This scaling is, however, more complex than the normal scaling methods. A number of these activation functions will be discussed in this Appendix.

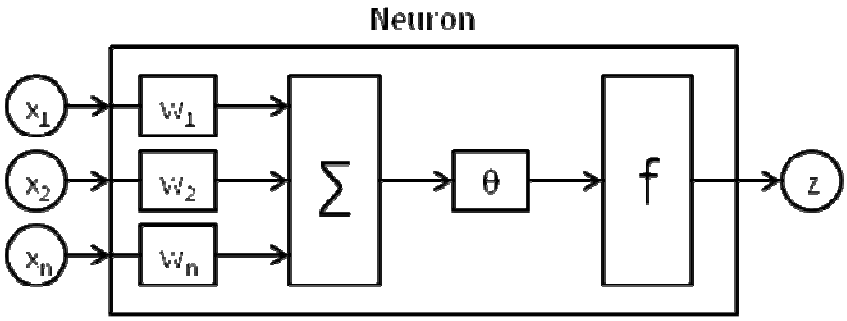

Figure C-2: The internal mathematical manipulations of a basic neuron

$$z = f(d - \theta) \tag{C-1}$$

where

d = $\sum x_i \times w_i \sum x_i \times w_i$

θ = Threshold (number between 0.25 and 1)

f = Activation function

The above equation states that the output is entirely dependent on the chosen activation function, as well as the threshold and the weights used to manipulate the inputs. The biggest challenge with neural networks is to determine the correct values for the weights and the threshold. This is done by means of complex training algorithms that are explained in section C.5.

C.2.2 Neural networks

As the name suggests, a neural network is an arrangement of neurons that are interconnected, and may be compared to the vast network of neurons in the human brain. It is important to realise that for a neural network to be of any use, it should have predictor (independent) variables as well as a predicted (dependant) variable. Within this network each neuron will have its own predictor and predicted variables. Every output (predicted variable) from a specific neuron is connected to all the downstream neurons and in this way form a predictor (independent) variable for the downstream neurons.

The predictor variables can be compared to the sensory nerves in the brain, whereas the predicted variables can be compared with the brains' motor nerves that react to the sensory nerves. It is intuitive that the brain has other nerves that also play a role in the response of the motor nerves. These other nerves are accounted for in neural networks in the form of hidden layer neurons. These hidden neurons together with the input- and output neurons are all connected together.

The amount of neurons in the input- and output layers corresponds to the amount of inputs and outputs of the data respectively. The amount of hidden layers and neurons per hidden layer can, however, not be optimised in advance. These

amounts can change per network configuration and type of data. In general, the addition of a hidden layer can allow the network to learn more complex patterns, but the downside is that the network performance decreases because of the added computational complexity. It is formally proven that any network can be trained with as little as two hidden layers, but it is generally good practice to start with a single hidden layer and add more when it is noticed that the network is not learning as well as was expected (Bharath & Drosen, 1994).

The connection of the neurons to those downstream can be done in a number of ways. The most common connection regime or structure is the feed-forward structure. This structure has a distinct layered topology and the signal flows forward from the inputs, through the hidden layer neurons eventually reaching the output layer neuron that provides the output signal. This structure has proven to be very stable and is depicted in Figure C-3. This structure is more commonly known as the Back Propagation Network or the Multilayer Perceptron, which is discussed in section C.5 (Bishop, 2006).

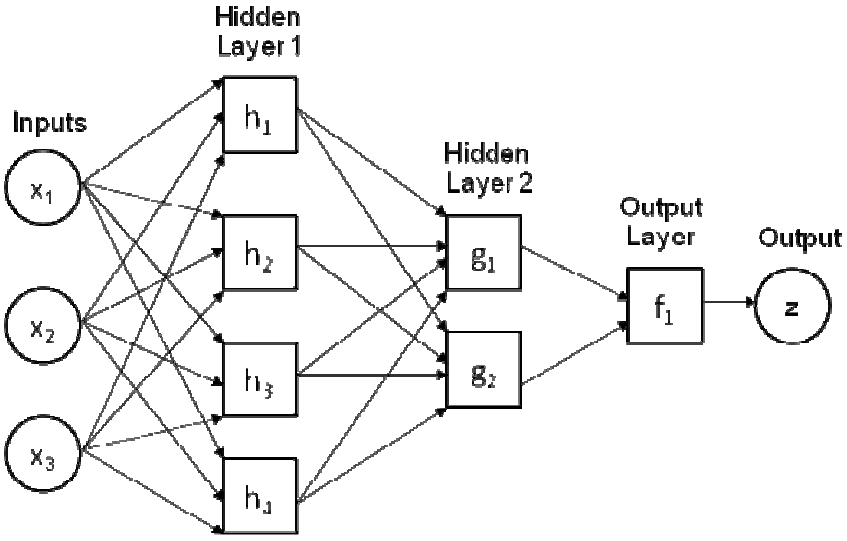

Figure C-3: Neural network feed-forward structure

C.2.3 Activation functions

As explained in section C.5, the activation or firing signal is passed through an activation function in order to generate an output that is scaled (it has a squashing effect). The combination (dot product) of a multi-dimensional linear input function and a one-dimensional transfer function results in a one-dimensional output. These transfer functions need to be non-linear. Linear functions are limited as the output is simply proportional to the input. A number of transfer functions exist. Figure C-4 depicts the main transfer functions.

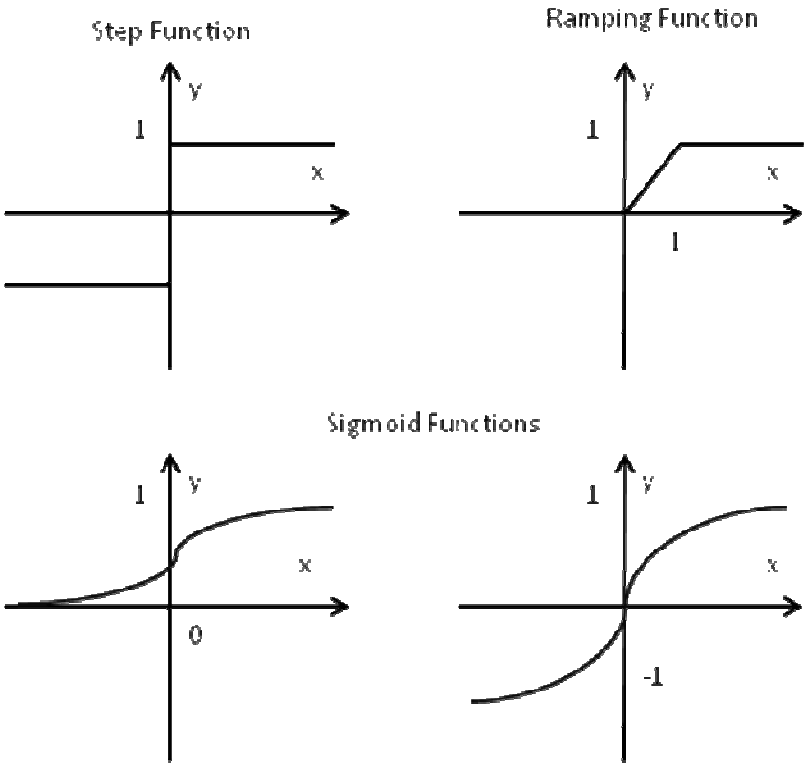

Figure C-4: Main ANN activation functions

The step function provides an output of 1 when the input is more than 0, and an output of negative one (-1) when the input is less than 0 The ramping function is actually a linear function that is clipped to minimum and maximum values, making it a non-linear function. It thus still acts as a hard limiter outside the specified range.

The Sigmoid or S-shaped curve is often the transfer function of choice. One reason for this is the mathematical advantage that lies in the fact that both the function and its derivative are continuous. The curve approaches a minimum and maximum value at the asymptotes. The curve is commonly called a sigmoid when it ranges between 0 and 1, and a hyperbolic tangent when it ranges between negative one (-1) and 1. The sigmoid function has the following corresponding equation:

$$s(x) = 1/(1 + e^{-ax}) \qquad \textbf{(C-2)}$$

where

a = Real number constant between 0.5 and two (starting point: use a = 1)

x = Input value

C.3 NETWORK ARCHITECTURES

Network architectures are defined as the basic design that executes the functions of a neural network. A number of different architectures exist, all of which display a strong similarity to the concepts of neurons, interconnections and activation- or transfer functions. The most common architecture is the multi-layer feed forward network, which is mainly used for pattern recognition. Such a network is also known as a Multilayer Perceptron (Bishop, 2006).

The development of this architecture was conducted in 1986 by Rumelhart, Hilton & Williams. The architecture has a feed-forward topology as explained earlier. The network thus has a simple interpretation as a form of input-output model with the weights and threshold the free parameters of the model. The function complexity is determined by the number of layers in the model as well as the number of units in each layer. Other important issues with this architecture are the number of hidden layers and units in these layers. It is standard practice to start with one hidden layer and a number of units equal to half of the sum of the overall ANN input and -output units.

C.4 NEURAL NETWORK DATA

A dataset is made up of a number of cases consisting of a set of values that represent the relevant inputs and output. These sets should preferably be filled with numeric data. A few problems areas exist with datasets; the most significant of which is that the data should be representative of the underlying model being modelled. This should be the case for the training data and for the verification and test data. A neural network's worth can at best be compromised if the datasets are not representative, and at worst it may be completely useless. Other problems that occur with datasets can be summarised as follows:

- Data is in an unusable range;
- Some cases have missing data; and
- Some data is non-numeric.

The solutions to these problems include:

- Scaling (linear- or non-linear) the data into an appropriate range for the network;
- Substituting missing values with the mean value of the specific variable;
- Data cases that have missing values can be deleted if a sufficient amount of training cases exist; and/ or
- Techniques may be used to convert non-numeric data into numeric data.

Acquiring a reliable dataset to be used for training purposes is often very tricky. Two major problems exist in this regard and are explained in the next section.

C.4.1 Variable selection

One approach of selecting data for training purposes is to do so by intuition. Some expertise in the specific domain will, however, be vital to provide some guidance into which variables to choose. The best way to employ this technique is to select all the relevant variables that have an influence of the output. During the design process the dataset will then have to be whittled down, deleting the variables that do not have an influence on the output. This process can, however, cause substantial delays and can be extremely expensive on a computational level if a number of unnecessary variables are included.

A more efficient approach to data selection is to perform a thorough sensitivity analysis on the data. This analysis will provide information that will basically eliminate the re-work that is necessary when following the intuition approach discussed above.

C.4.2 Required training cases

The amount of training cases will naturally increase substantially with an increase in the amount of variables. This increase is exponential and this problem is known as “the curse of dimensionality” (Vanderplaats, 2007). Heuristic guidelines exist for approximating the amount of cases required. Factors such as noisy data can, however, not be accounted for accurately when employing these approaches. It is recognised that the amount of training cases will be a few hundreds or thousands, but a specific value cannot be determined with a great degree of accuracy.

It is extremely important to verify the data for any outliers, missing- and unrealistic data before the data is used for training purposes. This means that the amount of training cases should take into account that a certain percentage of the data will be discarded because of undesired data.

C.5 NEURAL NETWORK TRAINING

Once the neural network architecture has been established for a specific application, the training can commence. The purpose of the training is to determine the correct values for the weights and threshold for each specific neuron in order for the network to provide the correct outputs. These weights are initially chosen randomly (between zero and one). Training can be divided into both supervised and unsupervised training (Vanderplaats, 2007). With unsupervised training the dataset excludes the outputs. Here the network has to make sense of the inputs without the help of the specific outputs to give the training guidance. This is often referred to as self-organisation or adaption.

With supervised learning the dataset used for training includes the specific outputs. The network compares the trained outputs to the desired outputs. The difference between the two values creates an error. This is used to adjust the weights and threshold that control the network in order to minimise the error, which is also known as the function value, F(X), in optimisation terms. This process is repeated until the weights and thresholds are adequately refined.

The adjustment to the weights and threshold is done by the chosen optimisation algorithm. There are three basic types of approximation algorithms, namely zero-order, first-order and second order algorithms. All three of these algorithms aim to minimise the error (objective function F(X)) discussed above. The X-values are the design variables (weights and the threshold) used in the optimisation, in vector form, denoted by [X].

Zero-order algorithms are the simplest algorithms. These algorithms minimise the objective function *F(X)* by randomly selecting a large number of candidate X-vectors and evaluating F(X) for each of them. The X-vector corresponding to the minimum value for F(X) is then deemed the optimum solution X^*. A great amount of X vectors will naturally be necessary to determine the precise optimum solution.

Second-order algorithms use the first and second derivatives of the objective function F(X) to determine the optimum solution. These algorithms are substantially faster than the zero- or first-order algorithms. Some of these algorithms include the "Conjugate Gradient Decent" algorithm as well as the "Levenberg-Marquardt" algorithm (Vanderplaats, 2007). These methods are not used in this study due to their extreme complexity and consequently not discussed.

First-order algorithms present a more difficult but efficient approach to the optimisation problem (compared to zero-order algorithms) through the use of gradient information in looking for the optimum solution. The gradient information ΔF(X) reveals the steepest descent direction, which can be used to determine a new X-vector that will be closer to the global optimum than the previous X-vector. The step size in this direction is denoted by α (scaling parameter). The following equation explains this:

$$X^1 = X^0 - \alpha \Delta F\left(X^0\right) \qquad \textbf{(C-3)}$$

where

X^0 = original/ old X-vector

α = scaling parameter

$-\Delta F(X^0)$ = steepest decent direction vector

X^1 = new X-vector

With first-order algorithms one is forced to limit oneself to a specific search direction rather than searching the entire design space, as is the case with the zero-order algorithms. The first-order algorithms are the most popular algorithms because of their ease of use and speed. The most common and widely used first-order approximation algorithm for multi-layer feed-forward neural networks is the back-propagation algorithm (Vanderplaats, 2007).

With this back-propagation algorithm, the steepest decent direction is determined as explained above. The step size in this direction is proportional to the slope as

well as the learning rate. Too big a step size might cause the algorithm to overstep/exceed the optimum solution in this search direction or deviate in the wrong direction. Too small a step size will eventually supply the desired result, but will use a great amount of iterations to get to the result. The learning rate is a numeric value, between 0 and 1, which is application-dependant. This value is typically chosen by experiment.

The back-propagation algorithm is usually also modified to have a momentum term. This term encourages movement in a fixed direction, so that if several steps are taken in the same direction, the algorithm will pick up momentum in this direction (Vanderplaats, 2007). This gives the algorithm the ability to escape local minima as well as to move rapidly over flat spots and plateaus in the design space.

The algorithm progresses through a number of epochs (functional evaluations). After each epoch, the target and actual outputs are compared and an error value created. This error value, together with the steepest decent direction, is used to adjust the design variables, which are the weights and threshold as explained above. These weights are modified from the output layer backwards through the hidden layers to the input layer. This process of proceeding backwards is what constitutes the name "back propagation". The process is then repeated until the optimum solution is obtained.

Back propagation mostly provides a quick and accurate solution. This algorithm is a good choice for when the dataset is very large and contains a great deal of redundant data (Bishop, 2006). The case-by-case error adjustment approach that this algorithm follows ensures that redundant data does not harm it at all. The process of changing the design variables varies for the output and hidden layers. These two processes are discussed below, with the following in mind:

- λ is the learning rate: It is usually 0.2 for output layer neurons and 0.15 for hidden layer neurons.

When determining the design variables (weights and threshold) for the output layer, the following process is followed. Firstly, the error is calculated:

$$e = z \times (1 - z) \times (y - z) \qquad \textbf{(C-4)}$$

where

z = calculated output.

y = desired output

After the error is calculated, it is used to calculate the change in the threshold as well as the weights (design variables):

$$\Delta\theta = \lambda \times e \tag{C-5}$$

$$\Delta w_i = \Delta\theta \times x_i \tag{C-6}$$

where

i denotes the specific input to the neuron

The hidden layer training is a bit more complex as the hidden layer has more than one output, and the outputs of the hidden layer are used as inputs for the next layer. For this reason the following approach is used with the help of Figure C-5:

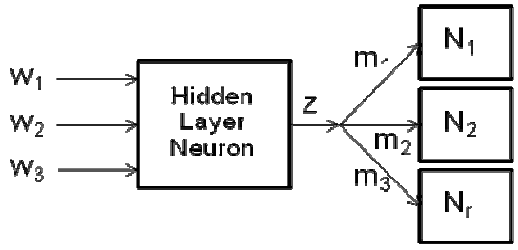

Figure C-5: Hidden layer training

$$g = \sum m_i \times e_i \tag{C-7}$$

Where

m_i = weight of the downstream neurons for i=1 to r

r = number of downstream neuron i

e_i = error of the downstream neuron i

It is important to notice that in calculating g, the errors and weights for the downstream layer should already have been determined. This means that one needs to start downstream from the output layer and work backwards. After calculating g, the specific neurons' error can be calculated:

$$e = z \times (1 - z) \times g \tag{C-8}$$

With this error the design variables of the hidden layer can be altered similar to the output layers' variables as discussed above.

C.6 CONVERGENCE CRITERIA

The total network error is normally determined by means of a sum squared error of all the individual neuron errors. This error is inherently minimised through the backwards minimisation of the individual neurons in the network as explained above. The errors create an error surface of which the global minimum needs to be determined, as explained above. The problem with achieving this is that you can never be sure whether a global minimum has been reached because of the inability

to display an n-dimensional space, where n is larger than three (curse of dimensionality (Bishop, 2006)).

The n-dimensional error surfaces are normally extremely complex, and are characterised by a number of unhelpful features including local minima, flat-spots and plateaus, saddle-points, and long narrow ravines (Vanderplaats, 2007).

It is normally recommended that the network be optimised from a few different starting positions to be sure that the global optimum is reached, but this introduces more computations, and therefore expenses. A fine line thus exists in ensuring that the final results are actually a global minimum and the cost involved in obtaining the global minimum this.

The training is normally stopped when the error level reaches a pre-determined acceptance level; when a preset number of function evaluations (epochs) have elapsed, or when the error stops improving.

C.7 CONCLUSION

This section provides the reader with theoretical knowledge of ANNs. This includes the fundamentals of a neuron, neural network, ANN architectures, activation functions, ANN training, convergence criteria and neural network datasets. The knowledge gained in this section is used in section 5.4 where a NDWCT at Eskom's Majuba Power Station is modelled through the use of an ANN.

APPENDIX D
MAJUBA POWER STATION's WEAHTER MAST EQUIPMENT – PHOTOGRAPHS, CALIBRATION CERTIFICATES AND ADDITIONAL DATALOGGER INFORMATION

Figure D-1: YSI44203 thermistor with radiation shield installed on Majuba Power Station's weather mast

Figure D-2: RM Young 41372 humidity sensor installed on Majuba Power Station's weather mast

Figure D-3: RM Young 41372 humidity sensor radiation shield installed on Majuba Power Station's weather mast

Figure D-4: RM Young 61101 SENTRA barometric pressure transducer installed on Majuba Power Station's weather mast

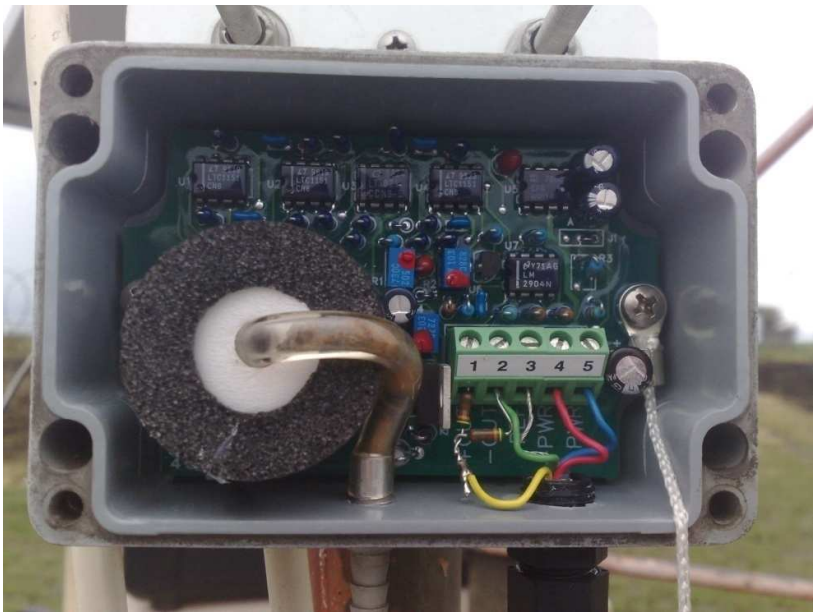

Figure D-5: RM Young 61101 SENTRA barometric pressure transducer installed on Majuba Power Station's weather mast - internals

Figure D-6: Texas Electronics tipping bucket rain gauge installed on Majuba Power Station's weather mast

Figure D-7: Texas Electronics tipping bucket rain gauge, installed on Majuba Power Station's weather mast - internals

Figure D-8: RM Young 05103 wind anemometer installed on Majuba Power Station's weather mast

Calibration Certificate SANAS 1145

INTELTRONICS
P.O. BOX 181
BRITS
<0250>
e-mail: itronics@icon.co.za
Vat Reg. No. 4210123651

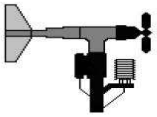

SANAS ACCREDITED LABORATORY 1549

UITSIG
DE KROON
BRITS
TEL 012 250 2403
FAX 012 250 2809
CEL 082 445 2531

Eskom Holdings (Pty) Ltd
Majuba Power Station
Private Bag X9001, Volksrust
2470

TEL 017 799 3257
FAX 017 799 3259
DATE 2009.08.28

CUSTOMER NUMBER	REPORT BY:	CALIBRATION DATE	Page No.
535.4	CJP LE ROUX	2009.08.18	1 OF 1

STATION NAME CALIBRATION SITE	INSTRUMENT TYPE	SERIAL NO.	PARAMETER MEASURED	REFERENCE	FIELD READING	UNITS
Majuba	R.M. YOUNG	76781	WINDSPEED	0.0	0.0	m/s
	MODEL 05103	10meter	WINDSPEED	30.4	30.0	m/s
			WIND DIR	0-360	0-355	°
			TORQUE	1.0	<1.0	m/s
Secondary Std	R.M. YOUNG	76789	WINDSPEED	0.0	0.0	m/s
DCP5	MODEL 05103	20meter	WINDSPEED	30.4	30.0	m/s
			WIND DIR	0-360	0-355	°
True North			TORQUE	1.0	<1.0	m/s
It was confirmed	R.M. YOUNG	76787	WINDSPEED	0.0	0.0	m/s
that the instrument/s	MODEL 05103	40meter	WINDSPEED	30.4	30.0	m/s
measuring wind			WIND DIR	0-360	0-355	°
direction was oriented			TORQUE	1.0	<1.0	m/s
True North	R.M. YOUNG	76788	WINDSPEED	0.0	0.0	m/s
	MODEL 05103	65meter	WINDSPEED	30.4	30.0	m/s
			WIND DIR	0-360	0-355	°
			TORQUE	1.0	<1.0	m/s

CALIBRATION METHODS:

1. **TEMPERATURE**: THE TEMPERATURE PROBE UNDER CALIBRATION WAS COMPARED AGAINST THE SECONDARY STANDARD IN ICE AND AMBIENT WATER HOUSED IN DEWAR FLASKS.
2. **PRESSURE**: THE PRESSURE SENSOR UNDER CALIBRATION WAS COMPARED AGAINST THE SECONDARY STANDARD UNDER AMBIENT PRESSURE
3. **HUMIDITY**: THE HUMIDITY SENSOR UNDER CALIBRATION WAS CALIBRATED WITH SATURATED SALT SOLUTIONS (LITHIUM CHLORIDE AND SODIUM CHLORIDE)
4. **WIND SPEED**: A WIND SPEED OF 30 METER PER SECOND WAS SIMULATED ON THE R.M. YOUNG MODEL 18801 ANEMOMETER DRIVE AND APPLIED TO THE SENSOR UNDER CALIBRATION.
5. **WIND DIRECTION**: The Windvane under test was held in positions of 0,90,180,270 and 355 degrees and readings taken: **0, 90, 180, 270, 355 (76781); 1, 90, 180, 270, 355 (76789); 0, 90, 181, 270, 355 (76787); 0, 90, 180, 270, 360 (76788).**
6. **SOLAR RADIATION**: THE SENSOR UNDER CALIBRATION WAS COMPARED AGAINST THE SECONDARY STANDARD VALUE UNDER SUNLIT CONDITIONS.
7. **RAIN**: The tips were counted while running the measured volume of water into the rain gauge.
8. **STATEMENT OF TRACEABILITY**: THE SECONDARY STANDARD IS COMPARED AGAINST THE PRIMARY STANDARD ON A 4 MONTHLY SCHEDULE. LAST PRIMARY STANDARD CALIBRATION DATE: MAY 2009 AND WAS TRACEBLE TO NATIONAL STANDARDS
9. **THE RESULTS** OF THESE CALIBRATIONS RELATE ONLY TO THE ABOVE SENSORS.
10. **THIS REPORT** SHOULD ONLY BE REPRODUCED IN FULL
11. **ENVIRONMENTAL CONDITIONS** FOR DURATION OF CALIBRATION:

TEMPERATURE: 11.8 ºC
HUMIDITY: 50 % RH

12. **Uncertainties of Measurements**: The estimated uncertainty of measurements were based on standard uncertainties multiplied by the appropriate factor as indicated by k=2.00 for a 95% confidence level.

A) TEMPERATURE: +/- 0.394 ºC
B) HUMIDITY: +/- 6.0 % RH
C) PRESSURE: +/- 2.08 mB
D) SOL RAD: +/- 60.8 W/m^2
E) W Speed +/- 0.2032m/s W Direction +/- 6.06°
F) RAINFALL +/- 0.04 mm/5mm Rain

GPS LOCATION OF STATION: 27°05.23" S 29°46.52" E

CSANAS1145.535.4.20090828

Figure D-9: Calibration certificate (1 of 2) for Majuba Power Station's weather mast – 2009-08-28

TEST CERTIFICATE SANAS 1145

INTELTRONICS
P.O. BOX 181
BRITS
<0250>
e-mail: itronics@icon.co.za
Vat Reg. No. 4210123651

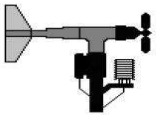

SANAS ACCREDITED LABORATORY 1549

UITSIG
DE KROON
BRITS
TEL 012 250 2403
FAX 012 250 2809
CEL 082 445 2531

Eskom Holdings (Pty) Ltd
Majuba Power Station
Private Bag X9001, Volksrust
2470

TEL 017 799 3257
FAX 017 799 3259
DATE 2009.08.28

CUSTOMER NUMBER 535.4 | REPORT BY: CJP LE ROUX | CALIBRATION DATE 2009.08.18 | Page No. 2 OF 2

STATION NAME CALIBRATION SITE	INSTRUMENT TYPE	SERIAL NO.	PARAMETER MEASURED	REFERENCE	FIELD READING	UNITS
Majuba	LI-200SA	27883	SOLAR RAD	**750.0**	**720.0**	W/m^2
			SOLAR RAD '0'	**0.0**	**-0.3**	W/m^2
	R.M. YOUNG	0883	HUMIDITY	**13.0**	**14.0**	% RH
	MODEL 41372 VC			**75.0**	**73.0**	% RH
	ECO RAINGAUGE		RAINFALL	**3.2**	**4.0**	mm RAIN
	R.M. YOUNG	01141	PRESSURE	**835.0**	**835.0**	mB
	MODEL 61201					
	YSI	1.2 meter	TEMP	**0.2**	**0.1**	°C
	MODEL 44203		TEMP	**14.8**	**14.7**	°C
	YSI	2.5 meter	TEMP	**0.1**	**0.3**	°C
	MODEL 44203		TEMP	**14.7**	**14.9**	°C
	YSI	5 meter	TEMP	**0.2**	**0.1**	°C
	MODEL 44203		TEMP	**14.8**	**14.9**	°C
	YSI	10 meter	TEMP	**0.1**	**0.9**	°C
	MODEL 44203		TEMP	**14.8**	**14.8**	°C
	YSI	20 meter	TEMP	**0.2**	**0.1**	°C
	MODEL 44203		TEMP	**14.8**	**14.7**	°C
	YSI	40 meter	TEMP	**0.2**	**0.2**	°C
	MODEL 44203		TEMP	**14.8**	**14.6**	°C
	YSI	65 meter	TEMP	**0.1**	**0.2**	°C
	MODEL 44203		TEMP	**14.8**	**14.9**	°C
	YSI	65 meter	TEMP	**0.1**	**0.2**	°C
	MODEL 44203		TEMP	**14.8**	**14.9**	°C

CSANAS1145.535.4.20090828

Figure D-10: Calibration certificate (2 of 2) for Majuba Power Station's weather mast – 2009-08-28

Gemini DATA LOGGERS

Tinytag Plus 2 Dual Channel Temperature/Relative Humidity (-25 to +85°C/0 to 100% RH)

TGP-4500

Issue 7 : 14th August 2009 (E&OE)

Features

Total Reading Capacity	32,000 readings
Memory type	Non Volatile
Trigger Start	Magnetic Switch
Delayed Start	Relative / Absolute (up to 45 days)
Stop Options	When full After n Readings Never (overwrite oldest data)
Reading Types	Actual, Min, Max
Logging Interval	1 sec to 10 days
Offload	While stopped or when logging in minutes mode
Alarms	2 fully programmable; latchable

Reading Specification

Temperature

Reading Range	-25°C to +85°C (-13°F to +185°F)
Sensor Type	10K NTC Thermistor (Internally mounted)
Response Time	25 mins to 90% FSD in moving air
Reading Resolution	0.01°C or better
Accuracy	

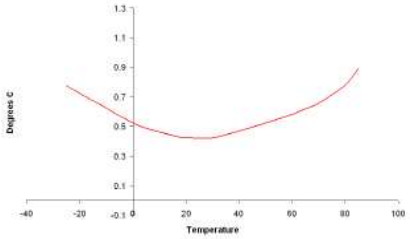

Relative Humidity

Reading Range	0% to 100% RH
Sensor Type	Capacitive
Accuracy	±3.0% at 25°C / 77°F
Reading Resolution	Better than 0.3% RH
Sensor Location	Externally mounted
Response Time	10 seconds to 90%

RH Sensor Working Range

The working range for the RH sensor is shown in terms of relative humidity / temperature limits.

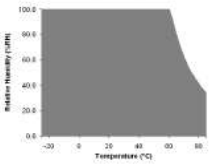

Physical Specification

IP Rating	IP68 water-proof (see notes)
Operational Range*	-40°C to +85°C (-40°F to +185°F)
Case Dimensions	
Height	34mm / 1.34"
Width	57mm / 2.25"
Depth	80mm / 3.15"
Weight	110g / 3.9oz

*The Operational Range indicates the physical limits to which the unit can be exposed, not the reading range over which it will record.

Notes

Battery Type SAFT LS14250 or LST14250; Tekcell SBAA02P

The logger will operate with other ½AA 3.6V Lithium (Li-SOCl2) batteries but performance cannot be guaranteed.

Replacement Interval Annually

Before replacing the battery the data logger must be stopped.

Data stored on the logger will be retained after a battery is replaced.

If used at low temperatures the data logger should be allowed to warm to room temperature before it is opened to avoid condensation forming inside the unit.

The IP68 rating is valid only when the unit's connector cap is fitted and is valid to a depth of 15m (50ft). The IP68 rating does not apply to the unit's RH sensor.

If moisture forms on the unit's RH sensor readings will become unpredictable. Once the sensor has dried out, and provided no residue is left behind, the unit should return to normal reading within 30 minutes.

Any dust or residue that is allowed to build up on the RH sensor will affect the unit's reading accuracy.

The sensor may be cleaned with de-ionised water or pure isopropanol, but not with abrasive detergents, as scratches or residue will affect the accuracy.

The RH sensor will resist small amounts of the following chemicals: formaldehyde, ammonia, carbon monoxide, sulphur dioxide, ethylene oxide, hydrogen chloride, hydrogen fluoride, hydrogen peroxide, nitrogen dioxide, methyl chloride, chlorine, freon, methanol, ethanol, isopropanol and ozone.
It also offers resistance to ultraviolet rays.

Salt solutions may cause permanent damage as crystals forming within the porous layers affect moisture levels there.

The position of the unit's trigger start switch is indicated by the • • • label on the back of the logger. When the "Wait until trigger event" option is selected in the Tinytag Explorer software, the green LED on the unit will flash once every eight seconds, indicating that the unit is waiting to log. When a magnet is held next to the label, the green LED will light until the magnet is removed to show that the switch is closed. After the magnet has been removed, the green LED will flash every four seconds to indicate that the logger is recording.

data sheet

www.tinytag.info sales@tinytag.info

Figure D-11: Tinytag data logger data sheet

REFERENCES

Allen, R.G.; Walter, I.A.; Elliot, R.L.; Howell, T.A.; Itenfusi, D.; Jensen, M.E. & Snyder, R.L. 1990. *The ASCE Standardized Reference Evapotranspiration Equation*. 176-177. Virginia: ASCE.

Anfossi, D., Bacci, P. & Longhetto, A. 1976. Forecasting of vertical temperature profiles in the atmosphere during nocturnal radiation inversions from air temperature trend at screen height. *Quarterly Journal of the Royal Meteorological Society*. 102: 173-180.

Beale, R. & Jackson, T. 1990. *Neural Computing: An Introduction.* Bristol: Institute of Physics Publishing.

Benton, D. & Mirsky, G.R. 1993. *Impact of Atmospheric Lapse Rate on Power Plant Performance.* American Power Conference. 55-2: 1427-1431.

Bharath, R. & Drosen, J. 1994. *Neural Network Computing.* New York: McGraw-Hill.

Bishop, C.M. 2006. *Pattern Recognition and Machine Learning.* Cambridge: Springer Science and Business Media.

Bourillot, C.; Grange, J. & Lecoeuvre, J.M. 1980. *Effect of wind on the performance of a natural wet cooling tower.* Fifth IAHR Cooling Tower Conference. Monterey

BS 4485: Water cooling towers, Part 2 - Methods for performance testing. British Standards Institution. 1988. UK: British Standards Institution.

Civil Time. 2010. Wikipedia. [Online]. Available: http://en.wikipedia.org/wiki/Civil_time. [01 July 2010].

Çengel, Y.A. 2003. *Heat Transfer: A Practical Approach.* Second Edition. New York: McGraw-Hill.

Counihan, J. 1975. Adiabatic atmospheric boundary layers: A review and analysis of the data from the period 1880-1972. *Atmospheric Environment*. 9: 871-905.

CTI ATC-105: CTI Code Tower Standard Specifications, Acceptance Test Code for Water Cooling Towers. Cooling Technology Institute. 2000. USA: Cooling Technology Institute.

Ding, E. 1992. *Air Cooling Techniques in Power Plants.* Beijing: Water and Electrical Power Press.

Elliot, D.L.; Hooladay, C.G.; Barchet, W.R.; Foote, H.P. & Sandusky, W.F. 1986. *Wind Energy Recources Atlas of the United States*. Richland: Pacific Northwest laboratory/ Solar Energy Research Institute.

Gao, M.; Sun, F.Z.; Zhou, S.J.; Shi, J.T; Zhao, Y.B & Wang, N.H. 2008. Performance prediction of wet cooling tower using artificial neural network under cross-wind conditions. *International Journal of Thermal Sciences*. 48: 583-589.
Golder, D. 1972. Relations among stability parameters in the surface layer. *Boundary Layer Meteorology*. 13: 47-58.

Gorchakov, G.I.; Kadygrov, E.N.; Kortunuva, Z.V.; Isakov, A.A.; Karpov, A.V.; Kopeikin, V.M. & Miller 1975. Eclipse effects in the atmospheric boundary layer. *Izvestiya Atmospheric and Oseanic Physics*. 44: 100-106.

Herberholz, P. & Schulz, S. 1979. The Influence of Atmospheric Precipitation on the Operation of a Natural-Draught Indirect-Contact Cooling Tower. *German Chemical Engineering*. 2-1: 352-360.

Hoffmann, J.E. 1997. *The influence of Temperature Stratification in the Lower Atmospheric Boundary Layer on the Operating Point of Natural Draft Cooling Tower.* South Africa, University of Stellenbosch, Stellenbosch (Ph.D. Thesis).

Hozos, M.; Ertunc, H.M. & Bulgurcu, H. 2007. Performance prediction of a cooling tower using artificial neural network. *Energy Conversion and Management*. 48, Issue 4: 1349-1359.

Hsu, S.A.; Meindl, E.A. & Gilhousen, D.B. 1994. Determining the Power-Law Wind-Profile Exponent under Near-Neutral Stability Conditions at sea. *Journal of Applied Meteorology*. 33:757-765.

*ISO-2533. International Organisation of Standarisation, Standard Atmosphere.*1975. Geneva: ISO.

Kloppers, J.C. 2003. *A critical evaluation and refinement of the performance prediction of wet-cooling towers.*South Africa, University of Stellenbosch, Stellenbosch (Ph.D. Thesis).

Kloppers, J.C. & Kröger, D.G. 2005. Influence of Temperature Inversions on Wet-Cooling Tower Performance. *Applied Thermal Engineering*. 28: 1325-1336.

Kröger, D.G. 1998. *Air-cooled Heat Exchangers and Cooling Towers - Thermal-flow Performance Evaluation and Design.* Begell House Inc., New York.

Kröger, D.G. 2004. *Air-cooled Heat Exchangers and Cooling Towers - Thermal-Flow Performance Evaluation and Design.* Oklahoma: PennWell Corporation.

Kůrková, V.; Steele, N.C.; Neruda, R. & Kárný, M. 2001. *Artificial neural nets and genetic algorithms.* Austria: Springer-Verlag.

Lander, M. 1991. *An emperical method to calculate atmospheric wind and temperature profiles.* Eskom Engineering Group - Engineering Investigations, TRR/P91/023. Location: Eskom.

Lauraine, H.; Lemmens, P. & Monjoie, M. 1988. *Experimental Data Coupling Atmospheric Temperature Inversions and Cooling Tower Performances:* 6th IAHR Cooling Tower Workshop. Italy. 1988.

Louth, W. 1996. *Summary of Weather Conditions obtained from a 65 m Weather Mast at Majuba Power Station: October 1995 - February 1996.* Johannesburg: Eskom.

Lutgens, F.K. & Tarbuck, E.J. 1995. *The Atmosphere: An Introduction to Meteorology.* Sixth Edition. New York. Prentice Hall.

Merkel, F. 1925. *Verdunstungskuhlung.* Berlin: VDI Forschungsarbeiten.

Moore, F.K. 1976. *Dry Cooling Towers, Advances in Heat Tansfer.* Vol 12. Location: Academic Press.

Ohya, Y. & Uchida, T. 2004. Turbulence Structure of Stable Boundary Layers with a Near-Linear Temperature Profile. *Boundary-Layer Meteorology*. 108: 19-38

Oke, T.R. 1987. *Boundary layer climates.* Cambridge: University Press.

Rumelhart, D.E.; Hilton, G.E. & Williams, R.J. 1986. *Learning internal representations be error propagation*. MIT Press. MIT

Peterson, E.W. & Hennessey, J.P. 1978. On the use of power laws for estimates of wind power potential. *Journal of Applied Meteorology.* 17: 390-394.

Shoda, T.; Murakami, S. & Yoshino, H. 1975. *Experimental Studies on Hot-Water Supply in Apartment House and Methods for Sizing of Service Water Heating Equipment.* Japan: Tohoku University.

Solar Time. 2010. [Online]. Available: http://www.encyclopedia.com/topic/solar_time.aspx. [02 July 2010].

Soler, M.R.; Infante, C.; Buenestado, P. & Mahrt, L. 2002. Observations of nucturnal drainage flows in a shallow gully. *Boundary Layer Meteorology*. 105: 253-273.

Surridge, A.D. 1986. *Extrapolation of the Nocturnal Temperature Inversion from Ground-based Measurements,* Atmospheric Environment.Vol. 20: 4:803-806.

Talay, T.A. 1975. *Introduction to the Aerodynamics of Flight,* Washington D.C.: NASA.

Terblanche, R.; Reuter, H.C.R. & Kröger, D.G. 2009. Drop size distribution below different wet-cooling tower fills. *Applied Thermal Engineering*. 29: 1552-1560.

Touma, J.S. 1977. Dependence of the wind profile power law on stability for various location. *Journal for AirPollution Control Association.* 27: 863-866.

Vanderplaats, G.N. 2007. *Multidicipline Design Optimization.* California : Vanderplaats Research and Development.